UNIVERSITÉ DE GRENOBLE

THÈSE

Pour obtenir le grade de

DOCTEUR DE L'UNIVERSITÉ DE GRENOBLE

Spécialité : **Physique appliquée**

Arrêté ministériel : 7 août 2006

Présentée par

Eric SAGE

Thèse dirigée par **Laurent DURAFFOURG**
codirigée par **Sébastien HENTZ**

préparée au sein du **Laboratoire des composants microcapteurs (LCMC) du CEA/LETI-MINATEC**
dans **l'École Doctorale de Physique - Grenoble**

Nouveau concept de spectromètre de masse à base de réseaux de nanostructures résonantes

Thèse soutenue publiquement le **13/12/13**,
devant le jury composé de :

M. Vincent BOUCHIAT
Professeur, UJF (Grenoble), Président
M. Bernard LEGRAND
Directeur de recherche, LAAS (Toulouse), Rapporteur
M. Jean-Claude TABET
Professeur émérite, UPMC (Paris VI), Rapporteur
M. Michael ROUKES
Professeur, CALTECH (Pasadena), Examinateur
M. Adrian BACHTOLD
Professeur, UAB (Barcelone), Examinateur
M. Christophe MASSELON
Chercheur HDR, CEA (Grenoble), Examinateur
M. Laurent DURAFFOURG
Chercheur HDR, CEA (Grenoble), Directeur de thèse
M. Sébastien HENTZ
Chercheur HDR, CEA (Grenoble), CoDirecteur de thèse

Université Joseph Fourier / Université Pierre Mendès France / Université Stendhal / Université de Savoie / Grenoble INP

ACKNOWLEDGMENTS

Ces trois années de recherches où je me suis beaucoup investi furent particulièrement intenses avec leurs lots de déceptions et de frustrations mais également de succès inespérés et de bons moments. Ces derniers ont été rendus possibles grâce aux personnes que je souhaite saluer ici et qui ont su me tendre la main, me prodiguer de précieux conseils ou simplement me redonner le sourire dans les moments difficiles.

Je tiens en premier lieu à remercier Laurent Duraffourg pour m'avoir convaincu de postuler à ce sujet de thèse, d'avoir défendu avec vigueur l'aspect thèse de mon travail au sein du laboratoire et de m'avoir donné une grande liberté pour développer mon sujet tout en me fournissant les clés pour développer mes compétences de chercheur. J'ai particulièrement apprécié les visites à l'improviste qui débouchaient toujours sur des discussions intéressantes et je l'encourage à faire de même avec ses futurs doctorants. Je remercie également Sébastien Hentz pour son soutien irréprochable lors de moments critiques comme la rédaction du manuscrit, les répétitions de soutenance de thèse ou de conférences, etc. Malgré certaines irrémédiables divergences en termes de couleurs de courbe ou de série TV (☺), j'ai pris un réel plaisir à travailler à ses cotés et énormément appris en termes de rédaction de papiers scientifiques (entre autres). Je tiens également à exprimer ma gratitude envers Guillaume Jourdan, notre gourou officieux des thésards du laboratoire. En plus de nous faire exploser de rire avec ses plaisanteries, inattendues, dirons nous, il sait se rendre toujours disponible pour des conseils extrêmement techniques quelque soit sa charge de travail du moment. Et pour ce double soutien moral/scientifique indéfectible, il mérite notre respect et notre reconnaissance. Un énorme merci également à Eric Colinet pour m'avoir aiguillé avec succès sur le thème des réseaux de NEMS et pour son rôle de mentor lors de mon séjour à Caltech. Que ce soit pour ses précieux conseils techniques, son soutien moral ou son enthousiasme communicatif, sa présence a été déterminante pour un séjour fructueux et agréable. A vrai dire, mis à part les réussites scientifiques et autres relations que j'ai pu nouer sur place, cette rencontre se suffirait à elle-même pour justifier l'intérêt du séjour. Encore merci.

Lors des moments de découragements pendant la rédaction du manuscrit, il n'est pas rare de se demander si ce dernier va réellement être lu et intéresser quelqu'un. Je tiens à remercier le jury de thèse pour m'avoir prouvé que rien n'est plus faux. Leur intérêt pour mon travail et leur présence lors de ma soutenance m'honore. Je tire mon chapeau à Bernard Legrand pour son impressionnant travail de relecture, exhaustif et minutieux, qui m'a permis d'améliorer notablement la version finale du manuscrit. Que ce soit lors de l'IFCS 2013 à Prague, par téléphone ou lors de ma soutenance, j'ai toujours trouvé nos discussions particulièrement captivantes et j'espère sincèrement que nous aurons de nouvelles occasions de rencontres. Merci à Jean-Claude Tabet pour avoir accepté de rapporter une thèse en dehors de son domaine d'expertise, pour son intérêt et ses apports originaux. Je remercie également Vincent Bouchiat pour avoir accepté d'être président du jury, pour ses contributions sur l'aspect physique du travail et pour ses encouragements. Merci à Christophe Masselon pour

avoir suivi avec intérêt l'évolution de mes travaux et pour son aide sur les aspects spectrométrie de masse conventionnelle. I am honored to count Adrian Bachtold among my jury and thank him for his enthusiasm and his keen interest for this work. I am grateful as well to Michael Roukes for his presence at the defense, for following my progress throughout these years, as well as for welcoming me at Caltech for a period of 6 months. I learnt a lot there and I would like to salute Scott Kelber, Selim Hanay for including me in the NEMS-MS team and Peter Hung, Luis Guillermo Villanueva, J-S Moulet, Rassul Karabalin, Warren Fon, Su Naing and Hugues Metras for their help. I also send my warm regards to my campus buddies with whom I spent my time at ISP lunches, Cats' parties and other social events: Jenny, Nicolas, Fabien, Allan, Manan, Bassam, Mark, Niko, Patrick, Bruno, Christine, Stephen, Jay, Hao, Yanan, Michel, Scott, Eric, John, Paraj, Utkarsh Vicky, Tom, Xavier, Matthieu etc. For that matter, I would like to thank the Fulbright commission for making this exchange possible.

La majorité de mon travail a consisté à étudier et manipuler des résonateurs NEMS en silicium et rien n'aurait donc été possible sans le travail de fabrication de Carine Marcoux et Cécilia Dupré. Je les remercie pour la qualité des dispositifs fournis mais surtout pour leur disponibilité, leur bonne humeur et leur aide, que ce soit pour comprendre les masques ou pour la formation à la microscopie à balayage électronique. Je salue Julien Arcamone qui m'a prodigué bien des conseils utiles en caractérisation électrique. J'ai eu également un grand plaisir à collaborer avec Christophe Leblanc et Nicolas Delorme (Asygn) et je salue leurs travaux sur les cartes d'acquisition électronique et sur la documentation associée qui m'ont permis d'obtenir une grande partie des mesures présentée dans cette thèse. Je voudrais également remercier infiniment Ariel Brenac et Robert Morel pour m'avoir accueilli à bras ouvert et m'avoir permis de modifier et utiliser leur banc de déposition de nanoparticules métalliques. La possibilité de mesurer la masse de particules uniques en temps réel a clairement été un tournant dans ma thèse en termes de résultats et j'ai pris un réel plaisir à faire de « la science qui tâche » en modifiant un bâti sous ultravide ou en manipulant du refroidissement à l'azote liquide. Ariel et moi avons formé un binôme particulièrement complémentaire, chacun ayant son propre domaine d'expertise, et je le remercie encore et encore d'avoir partagé avec moi une même volonté d'avancer et d'améliorer ce banc à chaque nouvel essai ainsi que mes horaires pas vraiment syndicaux. Je tiens de même à saluer Lucien, Céline, Jérémie et les autres membres de l'INAC qui m'ont immédiatement adopté en salle café et contribué à rendre ces journées de manip' bien agréables.

Je remercie Philippe Robert pour m'avoir accueilli au sein de son laboratoire ainsi que tous mes compagnons de salle café : Pierre-Patrick, JPP, J-S, Audrey, Aude, François, Marie-Hélène, Brigitte, Fanny, Cathy, Jean-Louis, Nicolas, Sophie, Amy, Christine, Arnaud, Eric, Caroline, Marjolaine, Manu et bien d'autres avec qui j'ai eu le plaisir de partager café/chocolats/croissants/gateaux de Nicolas et des éclats de rire. Je n'oublierai pas les sorties de labo, pic-nic, laser-game, via-ferrata et autres activités où j'ai pu apprécier leur compagnie et je ne manquerai pas de venir les saluer à l'occasion. Je me dois quand même de faire une dédicace spéciale à Christine Courtois et ses pouvoirs magiques capables de faire disparaître le moindre de nos soucis administratifs. Bravo et merci !

Merci à Rémi Pérénon, ainsi que Pierre Grangeat, pour leurs apports sur le traitement Bayesien des données. Travailler avec Rémi a vraiment été plaisant. Je souhaite une bonne continuation à Olivier Martin et une excellente fin de thèse à Julien Philippe. Son inébranlable optimisme, sa bonne humeur, sa curieuse conception de la réservation d'équipement et ses talents cachés ont rendu ces longues heures passées en salle de caractérisation toute de suite plus sympathiques. Dans le même registre, je souhaite également bonne route à Alexandra Koumela et Gregory Arndt qui ont partagé avec moi la même quête de courbe de résonance (cette petite bosse là, à ton avis c'est une résonnance ou bien?). Merci à Kevin Benedetto pour avoir été particulièrement arrangeant avec la réservation d'équipement et les discussions techniques. Je souhaite bien du courage et le meilleur à Ludovic Laurent que j'ai eu la chance d'encadrer pour son stage de fin d'étude et à Thomas Alava qui est un grand bonhomme, oui oui, et avec qui j'ai eu plaisir à partager mes connaissances mais aussi de bonne pintes de Chouffe. Un grand merci à Thomas Bordy pour son aide prompt sur l'aspect bruit secteur. I am grateful to Ann-Katrin Stark for her thorough review of my MS introduction, allowing me to avoid the wrath of MS specialists!

Mes hommage aux potos de l'étage Bob, Toby, Alisée, Oliv' et Croc pour leur potentiel infini de déconne. Je salue également mes ex collègues du LTPI dont Arnaud Pouydebasque, Sébastien Bolis, Patrice Jacquet, Claudine Bridoux, Damien Saint-Patrice, Sophie Verrun et Christophe Bouvier.

On en vient maintenant aux co-bureaux et affiliés! Je salue donc mes amis Jérémie Ruellan, Yannick Deimerly, Antoine Niel, Jareck Czarny, Rémi Dejaeger, Nils Rambal, Julie Abergel, J-S Moulet, Luca Leoncino et Sofiane Soulimane, Fabrice Terry. Je garde un souvenir nostalgique (ou pas ?) de nos débats sur des termes qu'il faut aller chercher sur wikipédia (ils comprendront), la naissante d'une idylle entre deux hommes, l'élevage de chats, les descriptions de vidéos du web, ou les mots fléchés force 1 de la salle café. Merci à Yannick de m'avoir supporté presque trois ans dans le même bureau, pour ses craquages après 18h, pour ses baskets fluo et ses fantastiques pulls à col roulés. Merci à Jérémie pour m'avoir tiré plus d'une fois d'un mauvais pas (saleté de Raymonde…) et d'avoir été mon acolyte au labo (cours, conf', discussions « scientifiques »…) mais également en dehors (badminton, lan, bière…). Je salue au passage son amusante volonté de raisonner l'irraisonnable, surtout quand c'est cause perdue. Je pense que Nils et Rémi se sont déjà reconnus plus haut. Merci à Jarek pour sa bonne humeur, sa vodka, ses coupes de cheveux improbables et sa bogôssitude ! Merci à J-S pour ses « conseils de l'ancien » et ses briefings voyage qui feraient honte au Routard ! Merci à Fabrice pour faire baisser la moyenne d'âge et bonne route à Luca ! Merci à Julie pour sa distribution de shots de bonne humeur et son accueil 5 étoiles au « H6 » avec Matthieu et Polin. Ce fut formidable de partager joies et peine de cette aventure de trois ans avec vous tous et la solidarité de notre petit groupe m'a fait chaud au cœur et permis de tenir bon. Je salue aussi Henri Blanc pour ses révélations inattendues et distrayantes, ses sources d'informations originales et pour avoir alimenté bien des discussions de déjeuners.

Je considère que « l'épreuve » du doctorat n'est pas seulement scientifique mais également personnelle. Parfois, il faut y croire pour s'accrocher et voir la lumière au bout du long tunnel et ça, ce n'est pas possible sans le soutien des proches. Impossible donc d'oublier

la chaleureuse colloc' du 50B avec Sim' et Crazy Johny! Merci à eux pour les craquages, les soirées « limite », la tyrannie culinaire etc., bref le sentiment d'appartenir à une mini-tribu qui fait tout ensemble. Poi vorrei ringraziare tutta la "famiglia italiana": Chiara, Lia, Giada, Vera, Ramona, Clio, Carlo, Gianni, Ricchi, Cus, Gan, Stefano e Lorenzo; per tutti i buoni momenti. So che sono stato fortunato di partecipare alla vita de la famiglia durante questi tre anni memorabile e spero che saremo reuniti molto presto. Grazie mille! L'élégance m'oblige malheureusement à mentionner mes compagnons de ~~bistrot~~ toujours qui supportent ma présence bon gré, mal gré, lors de toutes ces soirées, nouvel ans européens et autres voyages. C'est donc en me pinçant le nez que je salue Yvon qui décidément saura nous distraire jusqu'au bout, quelques fois (qui a dit litote ?) à ses dépends. Mais je retiens surtout son cœur en or et promis, si j'ai un chien il sera le parrain. Mes prières vont à Gouze[1], notre unique prophète (même s'il est plusieurs), qui m'a montré bien des fois la lumière (celle qu'on voit avant de mourir) à l'aide de ses fameux « raccourcis » en montagne et tour d'hélico. Rien de tel que la peur de la mort pour oublier le stress de la rédaction ! Merci à Grunge pour m'avoir probablement inconsciemment sauvé la vie maintes fois. Merci à Mr Max, dit le Cat Killer, pour l'ensemble de son œuvre, sa mauvaise fois et pour avoir, avec succès, fait semblant de s'intéresser à ma thèse. Merci François pour nous fournir un support d'expression artistique (au marqueur indélébile) pour les fins de soirée et pour le sous-titrage en VC (version catalane). Pour ne choquer la sensibilité de personne je ne m'attarderai pas sur Yaaaaaaaaaan ! Bravo à Salah pour avoir su incarner à merveille le rôle du hispter. Quand à 'Tonin, ce fut un honneur de faire un bout de route ensemble mais je suis bien obligé de révéler ce que tout le monde refuse de voir : tu es l'être le plus méchant que je connaisse. Mes vœux de bonheur à la petite famille de Valou et Céline qui s'agrandit de plus en plus ! A sa majorité, Sylvain sera obligé de lire ce manuscrit avant interrogation orale. Et bien sûr je n'oublie pas le reste de la fine équipe : Moskito, Peyro, Tinmar, Manue, Fanny, Simon et Bastoune.

Evidement, je ne serai jamais allé aussi loin dans mes études sans le soutien inconditionnel et l'amour de ma famille. Si je me sens fort aujourd'hui c'est grâce à vous, papa, maman, Sophie et Stéphane ; grâce à une enfance heureuse et des voyages qui m'ont donné le virus de la bougeotte, grâce à une éducation libérale qui m'a poussé vers la science et grâce à des valeurs qui me servent désormais de boussole pour le reste de mon court voyage sur cette planète…

Enfin, j'ai une tendre pensée pour celle qui a le courage de me supporter, me réconforter et de m'accompagner dans mes pérégrinations autour du monde. Merci de faire de moi un homme chanceux ma petite Caroline.

[1] *Vigouroux et al. Proc. 30th Gocad Meeting, Nancy,2010*
Vigouroux et al. Proc. 3rd FEFLOW User Conference, Berlin, 2012

General introduction

Following the trend of downscaling in accordance with Moore's law, the micro-electronics industry has been able to shrink CMOS-circuits with physical features down to tens of nanometers thanks to tremendous progress in micro and nano fabrication processes. Yet, downscaling has reached a physical limit implying important leakage currents for sub-10nm CMOS technology [1]. Hence a new trend, generally referred to as "More than Moore", has emerged where focus is now on the integration of a multitude of functions on a silicon wafer: actuators, sensors, energy harvesting, light emission, photovoltaic cells etc… [2]. Integrating a sensor directly on a silicon wafer has many advantages as sensing cells fully integrated with their associated electronics suffer less from capacitive loss of electrical connections and their batch fabrication is far cheaper. As the micro-electronics industry has already developed a full set of fabrication and characterization tools, VLSI (Very Large Scale Integration) CMOS compatible design enables to imagine millions of micro/nano-sized devices easily coupled with appropriate electronics [3]–[5].

For that matter, Nano-Electro-Mechanical Systems (NEMS) form a new class of sensors that would greatly benefit from Very Large Scale Integration. NEMS devices are extremely interesting objects of study as their minute size makes them very sensitive to excessively small physical variations occurring at the micro and nanoscale. Hence, astute engineering of nanosized devices may provide a variety of exotic tools to sense the quantum world by measuring physical quantities such as force [6], [7], molecular weight [8], gas concentration [4], surface stress [9] or molecule shapes [10] that would be otherwise impossible to measure with traditional instruments. However, obstacles to real world implementations of NEMS have yet not been completely breached as their extremely reduced size, albeit being the source of their outstanding properties, makes them difficult to interface with the physical quantities to be measured. In addition, the small signals provided by these sensors are generally extremely attenuated by electrical connections before reaching conventional tabletop instruments. Therefore, integrating NEMS sensors directly with their electronic read-out would circumvent this issue and allow for dense areas of millions of sensors easily coupled with interfaces with the macro world such as gas capillaries, microfluidics etc.

In the past decade, there has been a growing interest in mass detection based on monitoring the resonance frequency variations of a nanomechanical resonator. As their sizes are reduced, nanomechanical resonators are increasingly sensitive to mass adsorption but also increasingly difficult to monitor as transducing mechanical motion at this scale can be challenging. However, tremendous effort in the design of efficient transduction means [11] and device shrinking has led to the demonstration of attogram resolution [12] (one attogram=$10^{-18}g$) down to yoctogram resolution [8] (one yoctogram=$10^{-24}g$). This extreme mass sensitivity enabled the measurement of golden mass standards such as the mass of gold atoms [13] or Xe atoms [14] using carbon nanotube devices (CNT). At this point, one could

wonder if resonant NEMS can be used for mass spectrometry applications and weigh individual particles of a complex mixture. But what could be the contribution of Nanomechanical Mass Spectrometry (NEMS-MS) to the mature field of Mass Spectrometry (MS)?

Mass Spectrometry is a universal technique to determine the chemical composition of a given substance. It is widely used in broad range of domains such as medicine, biology, material science, geology etc. The molecular weight of each compound composing the analyzed mixture is deduced from their mass-to-charge ratios (m/z): samples are vaporized and ionized into small charged particles that are separated by a mass analyzer using electromagnetic fields. An ion detector sends an electrical signal proportional in amplitude to the number of incoming charges for each m/z ratio and a so called "mass spectrum" is built by displaying the abundance with respect to m/z. Introduction of the ElectroSpray Ionization (ESI) source in the mid 1980s revolutionized the field of MS as it enabled the introduction of biomolecules in the gas phase without fragmentation (soft ionization) and with a large number of charge states [15], [16], lowering the molecules m/z to values falling in the mass range of common mass analyzers whose resolution drops beyond a few tens of kDa (one Dalton=$1.66 \times 10^{-24} g$) [17]. This benefitted to the development of the field of proteomics. Proteomics is an emerging technique for the analysis of biomolecules: proteins, macroleculars complexes, viruses, bacterias etc. that relies on the weighing of intact molecules before structural analysis using successive fragmentation and MS steps. While the rapid growth of MS techniques and technologies offer now a broad range of instruments with outstanding mass resolution, most commercial MS equipments still have difficulties measuring particles over 100kDa (One Dalton = 1 Da = 1.660×10^{-27} kg= 1 proton mass) because of the large required electromagnetic fields for ion acceleration and poor resolving power (ability to separate two different m/z peaks) at these mass ranges. MS of high mass molecules is thus extremely arduous, requiring the use of ultra high magnetic field FTICR mass spectrometer [18] or modification of common instruments at the cost of lower dynamic range and resolving power [19]. To date, the highest weighed mass is a 18MDa virus assembly provided extensive modification of a quadrupole time-of-flight instrument [20]. Before then, the record lied in the 200kDa range [21]. For higher mass ranges, technologies such as Surface Plasmon Resonance (SPR) [22] and Surface Accoustic Wave (SAW) or Bulk Acoustic Wave (BAW) [23] cover mass ranges of 1-100GDa (SPR) and 10-100TDa (SAW/BAW). Therefore the mass range 100kDa-1GDa remains an unmet challenge and cannot be routinely acquired with current instruments.

NEMS resonators, with their demonstrated close to Dalton resolution [8], have the potential to fill in this mass range and provide increasing resolving power with higher mass range whereas it decreases for conventional ion MS. Plus, they offer a wide dynamic range (up to GDa) and the unique ability to measure neutral particles, circumventing issues with low ionization yield or peak overlap caused by multi charge states [24]. However, the capture surface of a resonant NEMS is extremely low (~µm²), making detection of a large number of particles extremely difficult. To address this challenging issue, Caltech and CEA-Leti, in the framework of the Alliance for nanosystems VLSI [25], are pushing toward large scale

integration of top-down NEMS arrays for large capture surfaces and ultra-fast NEMS-MS measurements. A major milestone for the Alliance consisted in the first demonstration of single protein nanomechanical mass spectrometry in real time [26]. With a mass resolution around 100kDa, human antibodies (IgM) in the MDa range were successfully weighed one-by-one. However, given the difficulty to focus the ionized particles on the tiny NEMS surface, this generation of NEMS-MS bench is not adapted to measure high flux of particles and the resulting low event rate yields very high acquisition times (up to tens of hours). Plus, to date, NEMS-MS spectra have been acquired "blindly" insofar as no mass calibration of the sensors could be performed: their high mass operating range forbids using golden mass standards such as atom masses. Further progression toward a compact and robust ultra-fast MS system implies addressing several points:

- Deeper understanding of the mechanisms limiting our mass resolution to adapt future designs for targeted mass sensing applications.
- High throughput handling. Focalized and faster mass delivery in combination with ultra-fast event tracking ability is required for high event rate acquisitions.
- Larger capture surface. Large arrays of individually addressed resonant NEMS are necessary to enhance the mass event probability.
- Comparison of NEMS-MS with conventional ion-MS for calibration and validation of the technique.

The work described in the present manuscript proposes to address these issues. A first critical point lies in the phenomena limiting the mass resolution of our sensors that initiated a thorough study to determine our expected mass resolution and noise source identification. With the expected mass resolution in mind, we built a MS bench providing both NEMS-MS and conventional ion-MS with an ion source delivering particles comprised in a mass range overlapping on those of both NEMS-MS and ion-MS. In parallel, an electrical scheme and a post-processing algorithm were developed for fast event rate handling. After validation and calibration of NEMS-MS with a single device, instrument control and fast readout scheme were developed for arrays of individually addressed NEMS. Final validation of the concept of nanomechanical mass spectrometry based on resonant NEMS arrays was performed in our MS bench by confrontation with conventional ion-MS. This manuscript is organized as follows:

The first chapter provides an introduction on the subject with the background of the thesis, a brief description of conventional MS and the potential contribution of NEMS-MS to the MS field. A review of NEMS based mass sensing is presented, describing the race for lower mass resolutions and the emergence of single molecule NEMS-MS. Finally, the model of nanomechanical resonators, the scaling effects on their performances and the devices used in this work are described.

The second chapter covers the experimental study of the devices mass resolution, strongly dependent on the frequency stability of the resonant sensor. After explaining that

thermomechanical noise should be limiting our frequency stability, the expected frequency stability is computed before experimental verification. Using frequency stability characterization tools such as the Allan Deviation (ADEV) or the Power Spectral Density (PSD), we evidence the presence of a 1/f colored noise orders of magnitude more important that the expected white noise. Further investigations are carried out to identify the nature of this noise.

The third chapter covers the comparison of nanomechanical mass spectrometry with conventional ion-MS. After explanation of the motivation of this approach, we detail the electrical setup and post-processing algorithm developed to handle high mass event rates and build a NEMS-MS spectrum from multi-mode resonance acquisition on a doubly clamped beam. The MS bench delivering metallic nanoclusters measurable either by NEMS-MS, TOF-MS or with a QCM is presented before description of a mass sensitivity calibration procedure. Then, we provide the expected Limit of Detection (LOD) and mass resolution considering the experimental conditions and our post-processing algorithm. The experimental results that follow feature comparisons of spectra from both techniques supported by simulations, investigation of different mass ranges, weighing of multicharged particles and the first evidence of neutral particle nanomechanical mass spectrometry.

The fourth chapter addresses the capture cross-section issue and presents the principle of frequency-addressed NEMS arrays. The fabrication processes to build such arrays as well as their architecture is detailed. Then, we present the characterization results before proceeding to actual implementation of the frequency-addressing technique on a small array of cantilevers (20 devices). Potential applications in mass and gas sensing are demonstrated, either by considering the array as a single device averaging the contributions of individual devices or by tracking the frequency jumps induced by electrostatic force on all individual devices of the array. Signal averaging provides noise reduction by the square root of the number of devices in the array which is promising for gas sensing. On the other hand, successful detection of frequency jumps on all 20 devices with a 40ms response time is a first step toward NEMS-MS with arrays.

The fifth chapter exhibits the first proof-of-concept of an array of nanomechanical mass spectrometers. An array of 20 doubly-clamped arrays controlled with the frequency-addressing technique, developed in Chapter IV, is introduced in the MS bench built for the experiments of Chapter III. Aided with the tools developed in Chapter II for noise characterization, the optimal operating points (drive and polarization voltages) can be set. After collective mass sensitivity calibration, we demonstrate successful multi-mode monitoring of single particle deposition events on every individual device within the array. Mass spectra built from the contribution of all devices are compared with TOF-MS and with single NEMS-MS. Finally, we highlight the ability of our arrays of nanomechanical spectrometer to perform MS imaging by placing it at the rim the nanocluster beam, evidencing dissymmetry of the mass event rates along the array.

After a summary of the main contributions of this work, we conclude on future developments of NEMS-MS and its potential for biomolecules analysis.

BIBLIOGRAPHY

[1] K. Roy, S. Mukhopadhyay, and H. Mahmoodi-meimand, “Leakage current mechanisms and leakage reduction techniques in deep-submicrometer CMOS circuits,” *Proc. IEEE*, vol. 91, no. 2, pp. 305–327, 2003.

[2] B. Vigna, “More than Moore: micro-machined products enable new applications and open new markets.,” in *International Electron Device Meeting (IEDM)*, 2005, p. 8.

[3] P. Andreucci, “Very Large Scale Integration (VLSI) of NEMS based on top down approaches, Nanomechanics for NEMS : Scientific and technological issues,” in *an international state-of-the-art workshop by OMNT 26 & 27 June 2008, Grenoble-Minatec, France www.nanovlsi.org*.

[4] J. Arcamone, A. Niel, V. Gouttenoire, M. Petitjean, N. David, R. Barattin, M. Matheron, F. Ricoul, T. Bordy, H. Blanc, J. Ruellan, D. Mercier, N. Pereira-Rodrigues, G. Costa, V. Agache, S. Hentz, J. Gabriel, F. Baleras, C. Marcoux, T. Ernst, L. Duraffourg, E. Colinet, E. B. Myers, M. L. Roukes, P. Andreucci, E. Ollier, and P. Puget, “VLSI silicon multi-gas analyzer coupling gas chromatography and NEMS detectors,” in *International Electron Devices Meeting (IEDM)*, 2011, pp. 29.3.1–29.3.4.

[5] I. Bargatin, E. B. Myers, J. S. Aldridge, C. Marcoux, P. Brianceau, L. Duraffourg, E. Colinet, S. Hentz, P. Andreucci, and M. L. Roukes, “Large-Scale Integration of Nanoelectromechanical Systems for Gas Sensing Applications,” *Nano Lett.*, vol. 12, pp. 1269–1274, 2012.

[6] G. Tosolini, L. G. Villanueva, F. Perez-Murano, and J. Baussels, “Fast on-wafer electrical, mechanical, and electromechanical characterization of piezoresistive cantilever force sensors,” *Rev. Sci. Instrum.*, vol. 83, p. 015002, 2012.

[7] Z. Xiong, B. Walter, E. Mairiaux, M. Faucher, L. Buchaillot, and B. Legrand, “MEMS piezoresistive ring resonator for AFM imaging with pico-Newton force resoluation,” *J. Micromechanics Microengineering*, vol. 23, p. 035016, 2013.

[8] J. Chaste, A. Eichler, J. Moser, G. Cballos, R. Rurali, and A. Bachtold, “A nanomechanical mass sensor with yoctogram resolution,” *Nat. Nanotechnol.*, vol. 7, pp. 301–304, 2012.

[9] J. Fritz, M. K. Baller, H. P. Lang, H. Rothuizen, P. Vettiger, E. Meyer, H.-J. Güntherodt, C. Greber, and J. K. Gimzewski, “Translating biomolecular recognition into nanomechanics,” *Science (80-.).*, vol. 288, p. 316, 2000.

[10] B. Walter, E. Mairiaux, Z. Xiong, M. Faucher, L. Buchaillot, and B. Legrand, “DNA ORIGAMI IMAGING WITH 10.9 MHZ AFM MEMS PROBES,” in *Micro Electro Mechanical Systems (MEMS)*, 2012, pp. 555–558.

[11] E. Mile, G. Jourdan, I. Bargatin, S. Labarthe, C. Marcoux, P. Andreucci, S. Hentz, C. Kharrat, E. Colinet, and L. Duraffourg, “In-plane nanoelectromechanical resonators based on silicon nanowire piezoresistive detection.,” *Nanotechnology*, vol. 21, no. 16, p. 165504, Apr. 2010.

[12] M. Li, H. X. Tang, and M. L. Roukes, “Ultra-sensitive NEMS-based cantilevers for sensing, scanned probe and very high-frequency applications.,” *Nat. Nanotechnol.*, vol. 2, no. 2, pp. 114–20, Feb. 2007.

[13] K. Jensen, K. Kim, and A. Zettl, “An atomic-resolution nanomechanical mass sensor.,” *Nat. Nanotechnol.*, vol. 3, pp. 533–537, Sep. 2008.

[14] H.-Y. Chiu, P. Hung, H. W. C. Postma, and M. Bockrath, “Atomic-scale mass sensing using carbon nanotube resonators.,” *Nano Lett.*, vol. 8, no. 12, pp. 4342–6, Dec. 2008.

[15] J. B. Fenn, M. Mann, C. K. Meng, S. F. Wong, and C. M. Whitehouse, “Electrospray Ionization for Mass Spectrometry of Large Biomolecules,” *Science (80-.).*, vol. 246, no. 4926, pp. 64–71, 1989.

[16] S. Banerjee and S. Mazumdar, “Electrospray ionization mass spectrometry: a technique to access the information beyond the molecular weight of the analyte,” *Int. J. Anal. Chem.*, vol. 2012, no. Article ID 282574, p. 40 pages, 2012.

[17] D. H. Russell and R. D. Edmondson, “High-resolution Mass Spectrometry and Accurate Mass Measurements with Emphasis on the Characterization of Peptides and Proteins by Matrix-assisted Laser Desorption / Ionization Time-of-flight Mass Spectrometry,” *J. mass Spectrom.*, vol. 32, pp. 263–276, 1997.

[18] N. L. Kelleher, M. W. Senko, M. M. Siegel, and F. W. McLafferty, “Unit resolution mass spectra of 112 kDa molecules with 3 Da accuracy,” *J. Am. Soc. Mass Spectrom.*, vol. 8, no. 4, pp. 380–383, 1997.

[19] R. H. H. Van den Heuvel, E. van Duijn, H. Mazon, S. Synowsky, K. Lorenzen, C. Versluis, S. J. J. Brouns, D. Langridge, J. van der Oost, J. Hoyes, and A. J. R. Heck, “Improving the Performance of a Quadrupole Time-of-Flight Instrument for macromolecualr Mass Spectrometry,” *Anal. Chem.*, vol. 78, pp. 7473–7483, 2006.

[20] J. Snijder, R. J. Rose, D. Veesler, J. E. Johnson, and A. J. R. Heck, “Studying 18 Mda virus assemblies with native mass spectrometry,” *Angew. Chemie*, vol. 52, pp. 4020–4023, 2013.

[21] K. Breuker, M. Jin, X. Han, H. Jiang, and F. W. McLaffertey, “Top-down identification and characterization of biomolecules by mass spectrometry,” *J. Am. Soc. Mass Spectrom.*, vol. 19, pp. 1045–1053, 2008.

[22] J. Homola, “Surface Plasmon Resonance Sensors for Detection of Chemical and Biological Species,” *Chem. Rev.*, vol. 108, pp. 462–493, 2008.

[23] S. Fanget, S. Hentz, P. Puget, J. Arcamone, M. Matheron, E. Colinet, P. Andreucci, L. Duraffourg, E. Myers, and M. L. Roukes, “Gas sensors based on gravimetric detection—A review,” *Sensors Actuators B Chem.*, vol. 160, pp. 804–821, 2011.

[24] E. van Duijn, “Current limitations in native mass spectrometry based structural biology,” *J. Am. Soc. Mass Spectrom.*, vol. 21, no. 6, pp. 971–978, 2010.

[25] “http://www.nanovlsi.com/.” .

[26] M. S. Hanay, S. Kelber, A. K. Naik, D. Chi, S. Hentz, E. C. Bullard, E. Colinet, L. Duraffourg, and M. L. Roukes, “Single protein nanomechanical mass spectrometry in real time,” *Nat. Nanotechnol.*, vol. 7, pp. 602–608, 2012.

“It always seems impossible until it’s done”

Nelson Mandela

Table of contents

ACRONYMS

ADEV	Allan deviation
APN	Anomalous phase noise
BAW	Bulk acoustic wave
CMOS	Complementary metal-oxide-semiconductor
ESI	Electrospray ionization
FTICR	Fourier transform ion cyclotron resonance
FWHM	Full width at half maximum
JPDF	Joint probability density function
LIA	Lock-in amplifier
LOD	Limit of detection
MALDI	Matrix-assisted laser adsorption/desorption
MFN	Mechanical frequency noise
MS	Mass spectrometry
NEMS	Nano-electro-mechanical -system
NEMS-MS	Nano-electro-mechanical –system mass spectrometry
PDF	Probability density function
PLL	Phase-locked loop
QCM	Quartz microbalance
Q-TOF	Quadrupole/time-of-flight
TOF-MS	Time-of-flight mass spectrometry
SAW	Surface acoustic wave
SBR	Signal to background ratio
SNR	Signal to noise ratio
SPR	Surface Plasmon resonance
TEM	Transmission electron microscopy
VLSI	Very large scale integration

Chapter I: Introduction

1. Background

This thesis was performed in the framework of the Alliance for nanosystems VLSI [1], an alliance between the California Institute of Technology (Caltech) and Leti-Minatec. Caltech-KNI and Leti-Minatec have joined their expertise to transition from the era of "nanocraft" to very large-scale integration (VLSI) of nanosystems. Transitioning the recent advances from nanoscience into large-scale nanotechnology remains a largely unmet challenge worldwide. To date, very few beachheads have been attained in this domain, largely due to the monumental challenge of merging the separate methodologies of nanoscale bio/chemical sensor device fabrication with state-of-the-art, foundry-scale microelectronics processing. LETI/Minatec researchers are now collaborating with Caltech/KNI scientists to transform nanotechnology-based prototypes into robust, complex sensing systems. Caltech's team, led by Prof. Roukes, is a pioneer in the nanoscale device field and has already demonstrated a wide range of NEMS based applications while Leti-Minatec researchers have developed NEMS VLSI tools including in particular electromechanical simulation and circuit design in order to predict the performances of NEMS embedded with their control electronics [2]. Moreover, a 200mm wafer, CMOS compatible, NEMS fabrication process is now available [3] and CEA-LETI is now able to massively produce NEMS devices (Fig. I.1).

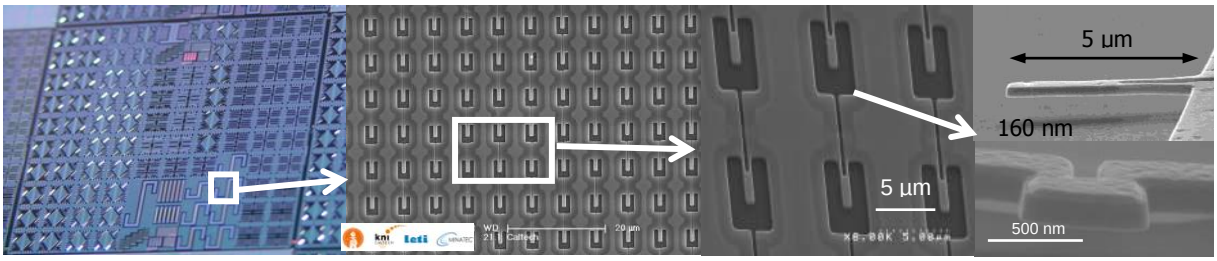

Fig. I.1: Very Large Scale integration of NEMS on 200 mm wafer produced by LETI (Alliance for Nanosystems VLSI) . Each wafer corresponds to 3,000,000 NEMS devices comprising far more NEMS than the total created during the preceding ~15 years of this field.

The alliance is driven by three main thrusts, namely chemical sensing (gaseous phase), biochemical sensing (liquid phase) and mass spectrometry (vacuum). The work presented in this thesis is focused on NEMS based mass spectrometry and was essentially performed at CEA-Leti of Grenoble within the LETI/DCOS/SCMS/LCMC laboratory. Most electrical measurements were performed at the LETI/DCOS/S3D/LCFC laboratory in the M&NEMS characterization room while mass measurements were acquired in the nanocluster deposition bench of the DSM/INAC/SP2M/NM laboratory. In the framework of collaborative research within the alliance and thanks to a Fulbright scholarship, 6 months were spent at Caltech along with Prof. Roukes' team for electrical characterizations and instrument control development for NEMS arrays and noise studies.

The work described in this thesis attempt to achieve three main objectives:

- Study the current limitation on the device mass resolution
- Evaluate NEMS-MS by comparing it with traditional ion-MS
- Demonstrate the feasibility of NEMS-MS with frequency-addressed arrays

This work was carried out in continuity of Dr. Ervin Mile and Dr. Sébastien Labarthe's doctoral research within the LCMC laboratory. They developed the NEMS resonator currently known as the "cross-beam" that achieves outstanding transduction efficiency [4] with a focus on design and simulation for Dr. Labarthe [5] and a focus on experimental characterizations for Dr. Mile [6]. For that matter, the author strongly encourages the reader willing to further broaden their knowledge on the device fundamental principles to read the oft cited thesis manuscripts as it will be evoked only briefly in this present document. Another building block essential to this work is the implementation of the nanosystem control loop performed during Chady Kharrat's doctoral work [7]. By the time this document was written, my collaborators from Caltech Dr. Sélim Hanay and Dr. Scott Kelber have now defended their thesis that lay the base of NEMS-MS and whose reading is also warmly recommended. Dr. Hanay developed the multimode operation that is critical for NEMS-MS and performed NEMS-MS acquisition essentially with an Electro-Spray Ionization (ESI) source while Dr. Kelber built from a to z a complete bench of NEMS-MS coupled with a Matrix Assisted Laser Desorption/Ionization (MALDI).

The demonstration of the concept of nanomechanical mass spectrometry with resonant nanostructure arrays presented in this manuscript was carried out in parallel with the doctoral work of Julien Philippe, Olivier Martin and Rémi Pérénon with whom fruitful exchanges were developed. Rémi Pérénon implemented a bayesian approach to post-process NEMS-MS raw data with the aim of reducing the current mass resolution, automate frequency jumps detection and implement a robust algorithm for real time acquisitions [8]–[10]. Olivier Martin's focus was on the design of cantilever arrays for gas sensing and on the simulation and design of the co-integrated control loop electronics to transition from tabletop controlled sensors to a fully wafer-level integrated sensing system. Julien Philippe is working on process integration toward a 3D co-integration of NEMS arrays enabling in situ amplification and addressing of a large number of devices.

Assembling the main building blocks constructed at Caltech and Leti-Minatec, the ambition is to obtain massively parallel NEMS arrays with thousands of devices for ultra-fast proteomics analysis.

2. NEMS-MS and Mass Spectrometry

2.1. Mass spectrometry: a diversity of techniques, a unique concept

Mass spectrometry (MS) is a widely used technique in analytical laboratories and represents today the only universal technique for determining chemical composition. Initially conceived for isotopic composition determination, MS is used today in a great variety of domains such as medicine, biology, pharmacology organic and inorganic chemistry, electronic, material science, surface physics, environment, geology and nuclear sciences. For instance MS can be used for carbon dating or for the detection of pesticides traces. Even some satellites or spacecrafts are equipped with mass spectrometers to analyse encountered particles or perform specific analysis (the SOHO satellite uses a MS device to analyse solar winds). Actually, the rover Curiosity (controlled by the Jet Propulsion Laboratory on Caltech's campus), currently in mission on Mars, embarks a Quadrupole Mass spectrometer (QMS) as well. Used in combination with a gas chromatograph, it analyzes the Martian atmosphere in search of evidence of the possibility of life. A broad range of commercial mass spectrometers exists based on diverse type of instruments. However, all rely on three basic components: First, samples are vaporised and ionized into small charged particles. Then, a so-called mass analyzer sorts these charged by-products according to their mass-to-charge ratios (*m/z*) by influencing their trajectory by using electromagnetic fields. And finally, a detector estimates the number of particles of different mass-to charge ratio (Fig. I.2). By comparing the obtained mass spectra to databases, it is then possible to determine the chemical structure of the analysed compound.

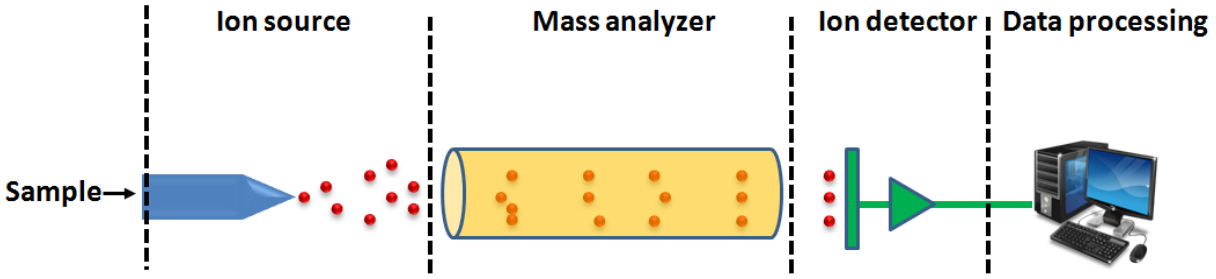

Fig. I.2: Particle separation is obtained according to the mass-to-charge ratio in a mass analyzer.

The performance of a MS apparatus is defined by its ability to accurately deduce the actual mass of the molecule from *m/z* ratios and its ability to distinguish between ions differing in the quotient *m/z* by a small increment. We define here the resolving power as $R = \frac{M}{\Delta m}$ where M is the measured mass [11]. Δm is defined either with the peak width, generally the Full Width at Half Maximum (FWHM), or the closest spacing of two peaks whose valley between them is at 10% or 50% of the smallest peak. We will use here the FWHM definition. Mass accuracy denotes the deviation between the measured mass and the actual value.

Ion sources

Despite the vast diversity of ion sources, mass analyzer and detectors that can be used to perform a MS analysis, the concept of separation according to m/z remains to date the golden rule of MS. Therefore, a crucial parameter of a MS system is the good ionization rate of the ion source as neutral molecules are simply not transmitted to the detector. The most popular ion sources for biomolecular MS are:

- ElectroSpray Ionization (ESI)

ESI [12]–[14] is now a widely used ionization technique in which the sample, mixed with a solvent, is ejected from the tip of a capillary where a high voltage is applied. The charged droplets repel each other as a result of Coulombic force and form a supercharged cone shape (known as the Taylor cone) before being expelled in the evaporation chamber. As the solvent gradually evaporates and given the Coulombic repulsion, the droplets split up until single molecules are finally gathered at the outlet of the ion source (Fig. I.3 a). ESI is a source of choice for MS of large masses (>1kDa) as most molecules remain intact during the process, making ESI a soft ionization method. Plus, ESI is known to produce highly charged molecules leading to *m/z* ratios below the maximal measurable *m/z* of the mass analyzers. However, the multiple *m/z* peaks engendered by multiple charging can complicate analysis of heterogeneous samples.

- Matrix Assisted Laser Desorption/Ionization (MALDI)

With the MALDI technique [15], the sample is embedded in a solid organic matrix and desorbed by a laser pulse. Vibrational excitation within the matrix cause local disintegration and ejection of analytes in the gas-phase (Fig. I.3 b). MALDI is considered as a soft ionization method as well and the localization of the sample desorption allows for MS imaging (a tissue section for example): a spatial mapping for different *m/z* levels can be generated. The main drawbacks of this technique are the matrix signal background that can be problematic for molecules below 700 Da and the molecule degradation relative to matrix interaction or photo-absorption [16]. MALDI produces far less multiple charged molecules than ESI yielding ions with higher *m/z*.

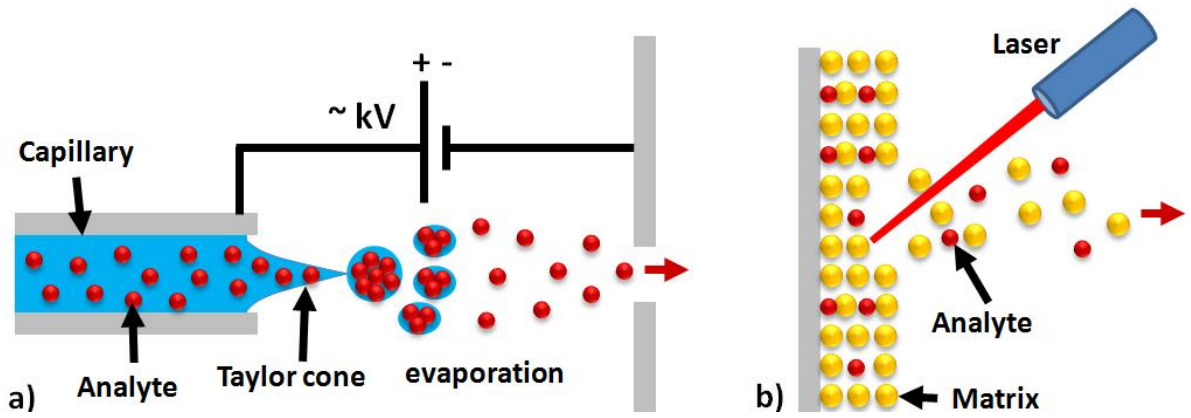

Fig. I.3: Schematic of the two most popular ion sources for biomolecule analysis, namely the ESI technique (a) using a highly charged capillary tip and MALDI (b) based on laser desorption.

Mass analyzers

Once they become ionized (negatively or positively), the molecules of interest are then transferred to a mass analyzer. Most commonly used techniques analyzers:

- Time-Of-Flight (TOF)

In TOF-MS [17], [18], molecules are accelerated with a pulsed electromagnetic field before travelling across a drift zone where light (or highly charged) ions with high kinetic energy come out first while heavy ions (or with low number of charges) come out last. The time of arrival of ions colliding with the ion detector, usually of Micro Channel Plate (MCP), directly translates to a *m/z* ratio.

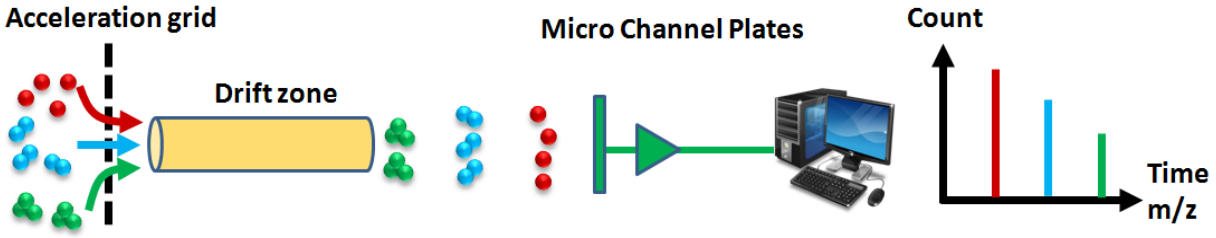

Fig. I.4: Schematic of the Time-of-Flight mass spectrometry principle. Accelerated ions have a different velocity depending on *m/z*: for a given charge state, lighter ions hit the MCP first while the heavy ones are detected last. Each ion count per time-of-flight can then be translated to *m/z*.

- Quadrupole mass analyzer

A quadrupole mass analyzer [20] consists in four metallic rods connected in parallel with a DC and Radio Frequency (RF) source that act as a band-pass mass filter for ions travelling between the four rods. The RF field and DC offset are tuned to allow ions at a chosen *m/z* to be transmitted across the device while all other ions have unstable trajectories. A detector counts the number of ions passing though the mass filter while scanning the desired *m/z* range.

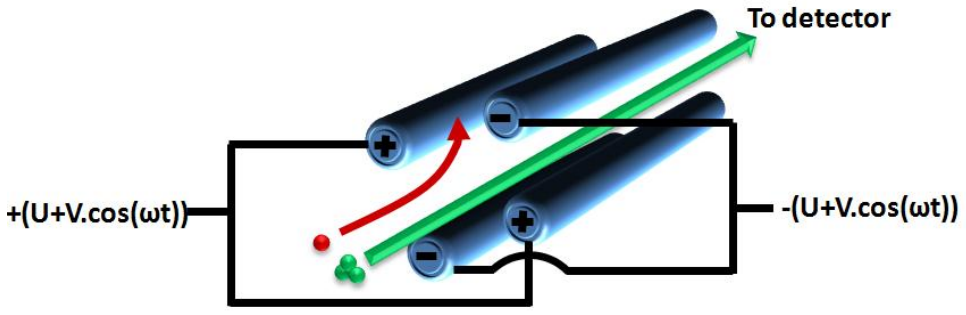

Fig. I.5: Schematic of the quadrupole mass analyzer. The applied RF field on the rods determines the *m/z* ratio allowed to travel across the mass filter.

The quadrupole may also be used in combination with different ion sources and/or mass analyzers as a mass filter to null out signal from undesired mass ranges or to select a specific molecule for tandem MS. Because of the different functions they provide and their low cost, quadrupoles are present in most tandem MS equipments.

Tandem Mass Spectrometry consists in combining multiple stage of mass spectrometry separated by fragmentation steps or ion selection for enhanced sensitivity or structural analysis. For instance, after a first *m/z* separation stage, one can select an ion of interest to enter a collision cell where the ion is fragmented before analysis of the byproducts. This may be done with a triple quadrupole mass spectrometer where the ions travel across three quadrupoles placed in series, each of which has a specific function. The first and the third, denoted as Q1 and Q3, operate in a "conventional' mode i.e. by filtering *m/z* or scanning across the *m/z* range. The second one, Q2, operated in so-called RF-only mode that allows the transmission of a broad *m/z* range, and is used as a Collision-Induced Dissociation (CID) cell: ions are accelerated to higher kinetic energies in presence of a neutral gas generating collision events and ion fragmentation. By scanning Q1 mass range and selecting a given *m/z* on Q3, one can study which precursor ion is composed of the selected product ion. On the other hand, it is possible to select a precursor ion with Q1 and scan Q3 to analyze its product ions. Tandem MS has a broad range of applications and has become increasingly important in the domain of proteomics for life sciences.

- Fourier Transform Ion Cyclotron Resonance (FTICR)

FTICR relies on the measurement of ions' orbiting motion trapped in a magnetic field of an analyzer cell [19]. An RF field is applied to excite ions to higher cyclotron orbits and the current gathered at the ends of a capacitor during relaxation is analyzed by Fast Fourier Transform (FFT) to reveal the ions cyclotron frequency that depends on *m/z* (Fig. I.6).

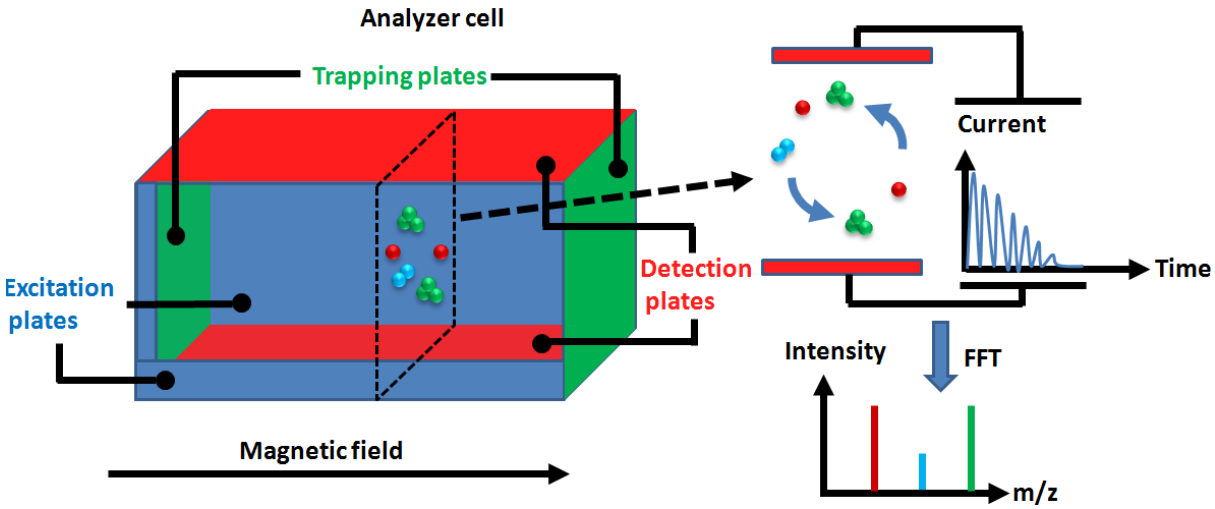

Fig. I.6: Schematic of the FTICR mass spectrometry principle. Ions are trapped in an analyzer cell where they are set in orbital motion with a magnetic and RF electrostatic field. As the ions get closer to the top or bottom electrode of the detection plates, a current is generated at the cyclotron frequency. A FFT analysis enables to separate all cyclotron frequencies precisely and deduce the corresponding *m/z* spectra.

FTCIR is a very expensive system as it generally requires superconducting magnets. Nevertheless, FTICR offers outstanding resolving power with respect to the other techniques mentioned above.

Typical mass analyzers performances

The resolving power of MS instruments depends on the mass range of measurement, generally decreasing with higher mass ranges. For instance in the case of FTICR-MS, the resolving power decreases linearly with mass. We list in Table I.1 the typical mass range of operation and resolving power of common mass analyzers at 1000Da/charge [21]. Values are in *m/z* ratios.

Mass analyzer	TOF	Quadrupole	FTICR
Mass range	10^6	$10^3 - 10^4$	10^5
Resolving Power	$10^3 - 10^4$	10^3	10^6

Table I.1: Typical mass range and resolving power of common mass analyzers

2.2. Mass Spectrometry for life sciences

Life sciences are devoted to the study of living organisms and the comprehension of the mechanisms governing their behaviors. This implies extensive study of life main building blocks that are DNA, RNA or proteins. Genes coded by the DNA are considered as the minimum level of biological information and contain all the instructions for the development and functioning of a living organism. Found in the nucleus of every cell, they provide the blueprint to the ribosomes for the synthesis of proteins. Today, the use of tools such as DNA microarrays combined with Polymerase Chain Reaction (PCR) allow easy identification of specific DNA strands and DNA sequencing can now be performed almost routinely [22]. Yet, DNA sequencing is not sufficient for extensive comprehension of biological phenomenon as many additional processes intervene during gene transcription and protein synthesis such as DNA methylation, gene silencing or Post-Translational Modification (PTM). The latter will determine the final shape of the protein and by extension its function. Indeed, the structural shape (at various levels) of a protein is essential for its function whether it defines chemical reaction sites for an enzymatic catalyzer, rigidity for a structural protein or the porosity of ion channel proteins. Therefore, there is a necessity to study these proteins in a state as close as possible to their native one.

The field of proteomics has been developed to study the structure and functions of proteins. While DNA sequencing consists in analyzing the genome of a cell, proteomics aims at defining its proteome i.e. identify the proteins contained in a cell. Proteomics is often synonym of protein Mass Spectrometry where the analysis relies on peptide or protein identification by their molecular weight. Protein complexes can be composed of several "subcomplexes" non convalently bound which are themselves formed by protein chains where each protein is a chain of peptide. Hence, a good understanding of proteins machinery requires the ability to probe the various levels of the pyramid of protein organization states [23] described in Fig. I.7.

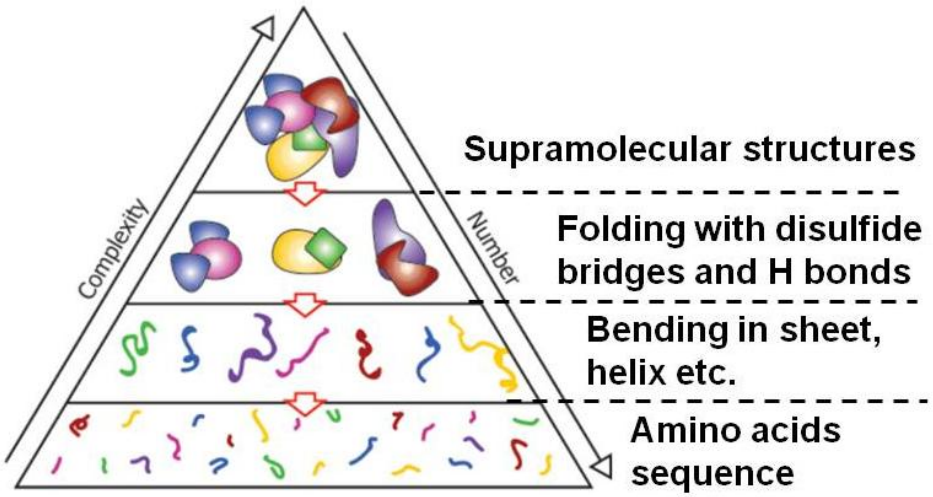

Fig. I.7: Pyramid of protein organization states. There are various levels of protein organization which can be probed in proteomic analyses by means of MS. A protein complex may be comprised of several subcomplexes, which themselves are composed of individual protein chains. Source: [23]**.**

Mass Spectrometry for proteomics application can be divided in two categories: Bottom-up Proteomics and Top-down Proteomics. Bottom-up proteomics is the most mature technique and deals with the two lower levels of the pyramid. It relies on digestion of the protein into small protein fragments that are introduced into a MS instrument. Measured fragments are then matched against a DNA-predicted protein database. Some instruments feature tandem MS where a specific peptide can be isolated and fractioned into amino acids for peptide identification. Thousands of peptides are necessary to deduce the protein with a good confidence level which requires resolving powers of 10^5.While bottom-up proteomics has proven very reliable for rapid DNA-predicted protein identification in complex mixtures; it suffers from information loss caused by neutral fragments, does not provide any structural information and cannot evidence PTMs or mutations of the precursor molecule as the information is lost in the digestion [24]. Top-down Proteomics, on the other hand, deals with intact proteins and probes the upper two levels of the pyramid in Fig. I.7. It has emerged since the invention of soft ionization techniques such as ESI or MALDI allowing for introduction of large biomolecule complexes without covalent bond breaking. The high number of charges of molecules vaporized by ESI extended the mass range to tens of kDa as the ratios m/z could be lowered below the mass analyzers limits. However, dissociation from a liquid phase to a gas phase in an ESI solvent may denature the native state of the protein and modify its shape conformation because of the buffer solution used for ESI [25]. The proteins can be affected by several factors such as pH of the solution, concentration of non-volatile salts and fraction of organic solvents [26].

This motivated the development of native-MS that allows introduction of the proteins in their native or near-native states into the gas phase for MS analysis. The ESI solvent is generally aqueous, at physiological PH and appropriate ionic strength for minimum denaturation of the protein [26], [27]. Given the high mass ranges involved, mass analyzers are chosen amongst TOF, Q-TOF for tandem MS and FTICR. However, it is reported that quadrupoles have a maximum *m/z* of 4000 restricting ion selection for proteins below 60kDa [26], [27] while mass analyzers have trouble measuring proteins above 100kDa [28]. Van den

Heuvel *et al.* modified a Q-TOF to provide ion isolation up to 12800 *m/z* and detection up to 38150Da to extend the mass range for macromolecular MS at the cost of lower resolving power. Yet, the record of measured protein mass still lies within the 100kDa range: Han *et al.* measured the mycocerosic acid synthase (229kDa) by fragmenting the initial complex using prefolding dissociation (PFD) [29] while Karabacak *et al.* identified the Thyroglobulin (~670kDa) using funnel skimmer dissociation but reported no possible weighing of the entire complex [30]. Clearly, the effort put into instrumentation modification for higher mass ranges and molecule fragmenting strategies denote the importance of finding a solution for routine mass measurement above 100kDa.

Esther van Duijn reported the current limits in Native-MS [31]. Along with the difficulty of measuring weakly charged or large molecules, a concern is reported about peak splitting caused by the different molecule charge states that may overlap with those of another molecule. As the analysis point toward bigger macromolecules, fragmenting lead to extremely complex tandem MS spectra caused by multiple charge states. Yet, highly charged species are necessary for tandem MS as effective fragmentation is correlated with a high number of charges. Because of the asymmetric charge distribution upon dissociation, the initial macromolecular complex loses most of its charges after several fragmentations and the remaining structure simply cannot be studied. Therefore, a highly charged molecule ion is desirable but can be difficult to obtain for folded proteins structure: as injection of charges seems to essentially occur at the protein surface that presents possible chemical interaction sites, proteins introduced in the gas phase in their native states presents higher m/z ratios than their unfolded counterparts [23].

In summary, Top-down proteomics is limited by the finite mass ranges and decreasing mass resolution of current MS equipment above 100kDa, the requirement of highly charged particles and interpretation complexity of spectra from tandem MS. Some emerging technologies based on Surface Plasmon Resonance (SPR) [33] or Surface Accoustic Wave (SAW) or Bulk Acoustic Wave (BAW) [34] offer solutions in mass ranges of 1-100GDa (SPR) and 10-100TDa (SAW/BAW) but cannot be considered for MS of MDa proteins.

2.3. Bridging the gap with NEMS-MS

NEMS-based Mass Spectrometry (NEMS-MS) is a completely new paradigm that relies on direct mass measurements without ionization or separation. The inertial mass of molecules landing on a resonant nanostructure is deduced from the inferred frequency shifts generated by mass loading (Fig. I.8). While atomic resolution has been demonstrated [35], the upper mass range limit is set by the mass sensing linear range up to ~1GDa: NEMS-MS has the potential to fill in the current mass range gap.

Moreover, particles can be sent directly onto a large number of NEMS devices enabling parallel measurements.

Such a paradigm has tremendous potential advantages over conventional spectrometers:

- Highly simplified architecture (no ionization source, no analyzer)
- Much larger dynamic range: this system can detect particles as large as ~1GDa or more according to the device size and maintains the same masse resolution for all mass ranges, whereas conventional spectrometers show a resolution proportional to the detected mass
- Orders of magnitude improvement in yield; ionization yields in conventional techniques can be extremely low [36]. This system weighs any particle, ionized or not, landing on the surface of the NEMS.
- Possibility of massively parallel architectures with a large number of devices and interfacing with microfluidics
- Lower costs thanks to microfabrication and transportability

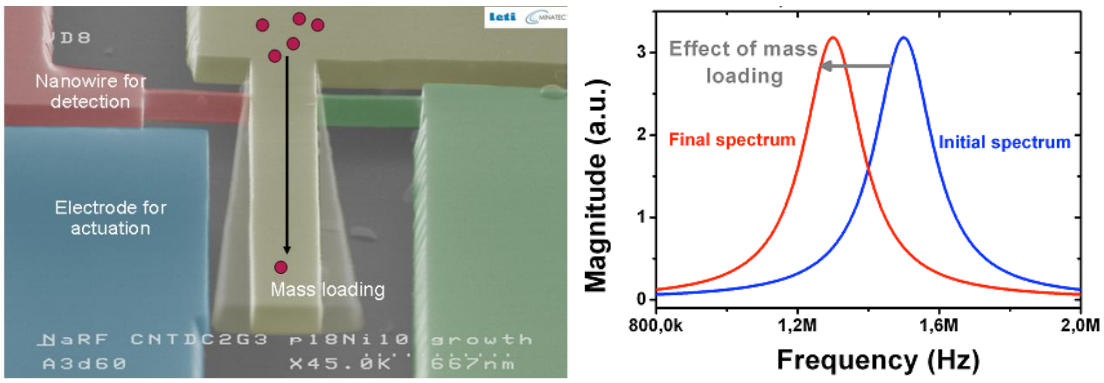

Fig. I.8: Working principle of a NEMS using electrostatic forces for actuation and piezoresistive nanowires for detection. An added mass on the nanobeam will be detected through the resonance frequency shift.

Transitioning from the proof of principle experiment [37] to a robust, high-throughput system will require significant efforts in the following critical areas:

- Design and fabrication NEMS devices with optimum mass resolution (down to a few Dalton)
- Very Large scale integration of NEMS devices to develop NEMS arrays
- Co-integration of NEMS devices with CMOS circuitry
- System architecture of these co-integrated device arrays with some pre-processing system and sample preparation.

Each of these efforts would enable realization of high throughput single molecule NEMS based mass spectrometry (MS) with unprecedented mass sensitivity. Each NEMS array device could process hundred of molecules per second. Thanks to their high integration capability, combining this very short time response with multiple parallel channels (up to

several thousands), high throughput analysis (for eg. millions of proteins in a few hundreds seconds) could be performed with NEMS-MS (Fig. I.9).

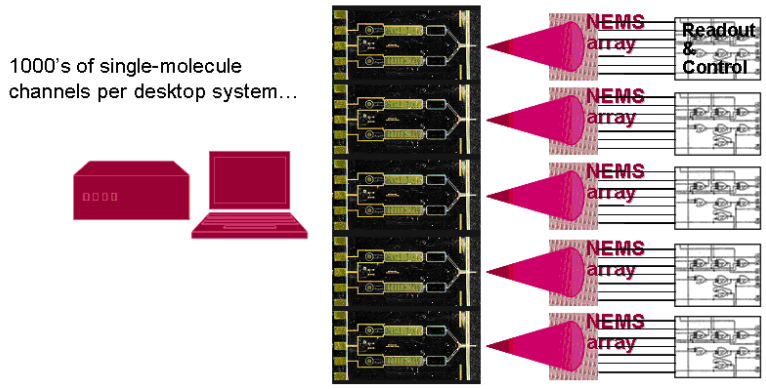

Fig. I.9: Single-Molecule NEMS-Mass Spectrometry on Chip. Microfluidics channel are used to spread analysed particles on a NEMS array for high throughput biological analysis. Courtesy of Michael Roukes.

Considering NEMS-based sensors for MS applications has been made possible thanks to great progress with their mass resolution as well as the use of several resonance modes.

3. Review of NEMS-based mass sensing

The fundamental principle of mass sensing with resonant nanostructures is based upon the observed frequency variation of a resonator following a mass adsorption upon its resonant surface. For an added mass that is significantly smaller than the total resonant mass and that does not induce any stiffness change, a linear relationship can be established between the frequency shift and the mass shift. A harmonic oscillator can be described by a simple model:

$$f = \frac{1}{2\pi}\sqrt{\frac{k}{M}} \qquad \textbf{(I.1)}$$

where f is the resonance frequency, k the stiffness and M the resonant mass.

We now consider an addition of a minute mass $\Delta m \ll M$ along the resonator surface that does not affect the resonator's stiffness. This leads to a frequency shift:

$$\Delta f = \frac{1}{2\pi}\left[\sqrt{\frac{k}{M}} - \sqrt{\frac{k}{M\left(1+\frac{\Delta m}{M}\right)}}\right] \qquad \textbf{(I.2)}$$

Since $\Delta m \ll M$, we can use Taylor expansion to write:

$$\Delta f = \frac{1}{2\pi}\left[\sqrt{\frac{k}{M}} - \sqrt{\frac{k}{M}}\left(1 - \frac{\Delta m}{2M}\right)\right] = \frac{1}{2\pi}\sqrt{\frac{k}{M}}\,\frac{\Delta m}{2M} \qquad \textbf{(I.3)}$$

The relative frequency response of a resonator to the mass adsorption is therefore described as:

$$\frac{\Delta f}{f} = \frac{\Delta m}{2M} \qquad \textbf{(I.4)}$$

The resonator mass sensitivity is defined as:

$$\frac{\Delta f}{\Delta m} = \frac{f}{2M} \qquad \textbf{(I.5)}$$

Therefore, the resonator mass sensitivity increases with lower masses and higher frequencies. An accreted mass will be detected if the induced relative frequency shift steps out of the relative frequency fluctuations and the mass resolution σ_m is calculated for a one sigma deviation as:

$$\sigma_m = 2M\sigma_{\delta f} \qquad \textbf{(I.6)}$$

where $\sigma_{\delta f}$ is the deviation of the resonator relative frequency

The relative frequency fluctuation deviation depends on the measurement integration time and generally decreases with higher integration for a dominant white noise.

3.1. NEMS mass sensing: from attogram to yoctogram resolutions

In the last decade, the potential extreme mass sensitivity of NEMS resonators has raised a growing interest in the NEMS/NEMS community and a race toward lower mass resolutions lead to successive demonstrations of resolutions of the order of the attogram [38], zeptogram [39]–[41] and more recently yoctogram [35]. Mass measurements are always performed in high vacuum for maximal device quality factor and minimum environmental pollution.

Prof. Roukes' group is a pioneer in the domain of electromechanical systems and pushed forward lower mass resolutions with suspended doubly-clamped beams. In 2004, Ekinci *et al.* [38] exposed a doubly-clamped SiC resonator cooled at 17K under a flux of gold nanoparticles at successive time intervals and observed frequency shifts as shown in Fig. I.10.

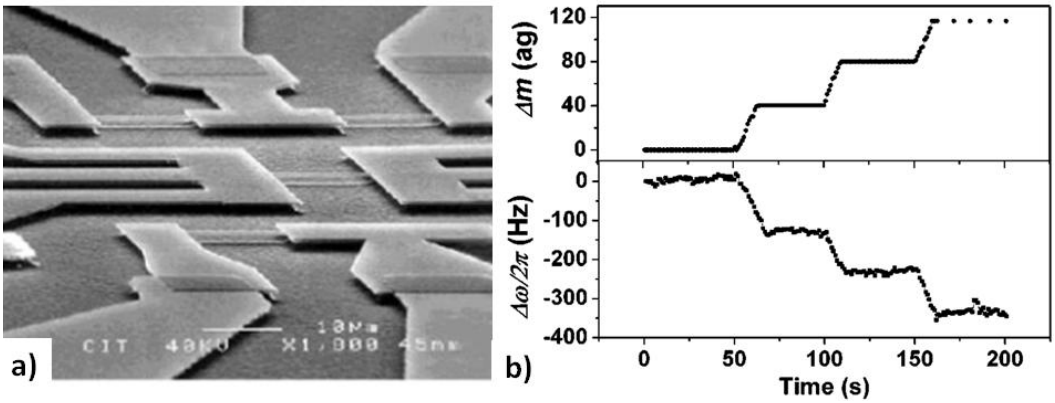

Fig. I.10: Attogram sensing experiment. SEM image of the suspended SiC structure (a) and mass sensing experiment (b) with frequency shifts detected on the NEMS upon exposure to gold particle flux (bottom) compared with the Quartz Crystal Microbalance (QCM) reference (top).

The device resonated at 72MHz with dimensions of 10µm*650nm*260nm (length, width and thickness respectively). Thanks to QCM calibration, the mass sensitivity was extracted and estimated at 2.56Hz/ag (one attogram = $1 \times 10^{-18} g$). For a relative frequency stability of 2×10^{-7} at the integration time $\tau = 2ms$, this yields a mass resolution of 2.53ag. This work demonstrated a first NEMS-based real time measurement of mass deposition showing the potential for smaller devices and higher quality factors.

The experiment was repeated in 2006 by Yang *et al.* with smaller devices. Best results were obtained on a (2.3µm*150nm*70nm) doubly-clamped SiC beam resonating at 133Mhz and featuring a quality factor of 5000. At 37K, Xe and N_2 molecules were projected on the resonator at successive interval using a mechanical shutter (Fig. I.11).

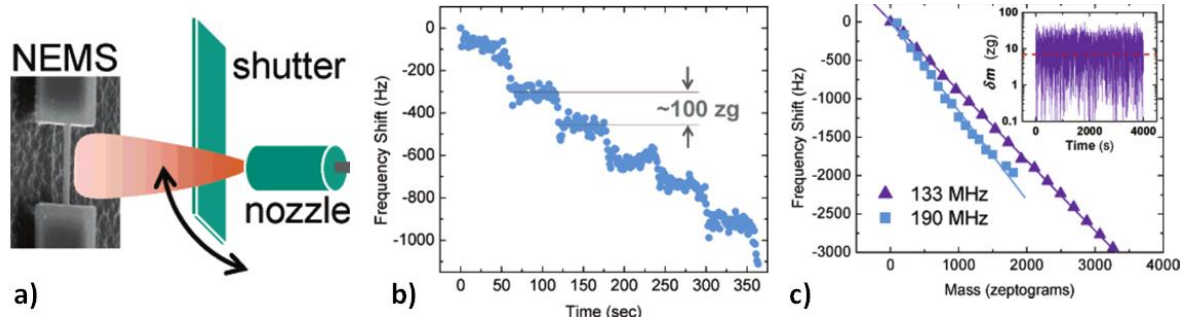

Fig. I.11: Zeptogram sensing experimental setup (a) where a gas nozzle combined with a shutter projects Xe or N_2 molecules on the resonator at the desired time. Mass induced frequency jumps are acquired in real time with a Phase Locked Loop (b). The mass sensitivity is deduced from observed frequency shifts at increasing adsorbed masses (c).

With a mass sensitivity estimated at 0.89Hz/zg (one zeptogram = $1 \times 10^{-21} g$) and a relative frequency fluctuation of 5×10^{-8} at 1s, a mass resolution of 7zg is reached. Hence, as particles down to 4kDa could be measured, the next step consisted in weighing biomolecules and proteins with resonant NEMS.

The race for lower mass resolution went on with bottom-up devices such a Carbon Nanotubes (CNT). CNTs are folded graphene sheets composed of Carbon atoms assembled in a honeycomb crystal lattice. They are currently well known objects in the nanoscience field as

they exhibit exquisite properties such as one dimensional electron transport [42] or outstanding stiffness [43]. To date, despite their great promise in many fields and great technological effort, no real VLSI processes has been demised to fabricate such devices in a robust and reproducible manner. In 2008, both Roukes' group and Zettl's group demonstrated that using CNT's could lower the mass resolution down to atomic resolutions. Chiu *et al.* used a single wall doubly clamped CNT with a 1nm diameter and a 400nm length resonating at 300MHz [40]. Cooled at 6K, it featured a quality factor of 200 and allowed to measure the atomic mass of Ar as 0.085zg, close to the 0.066zg mass reference. Jensen *et al*. used a singly clamped double-walled CNT with a 254nm length, a 1.75nm inner diameter and a 2.09nm outer diameter [41]. It resonated at 325MHz and featured a quality factor of 1000. Gold particles were evaporated on the nanotube and a reference QCM at room temperature (Fig. I.12).

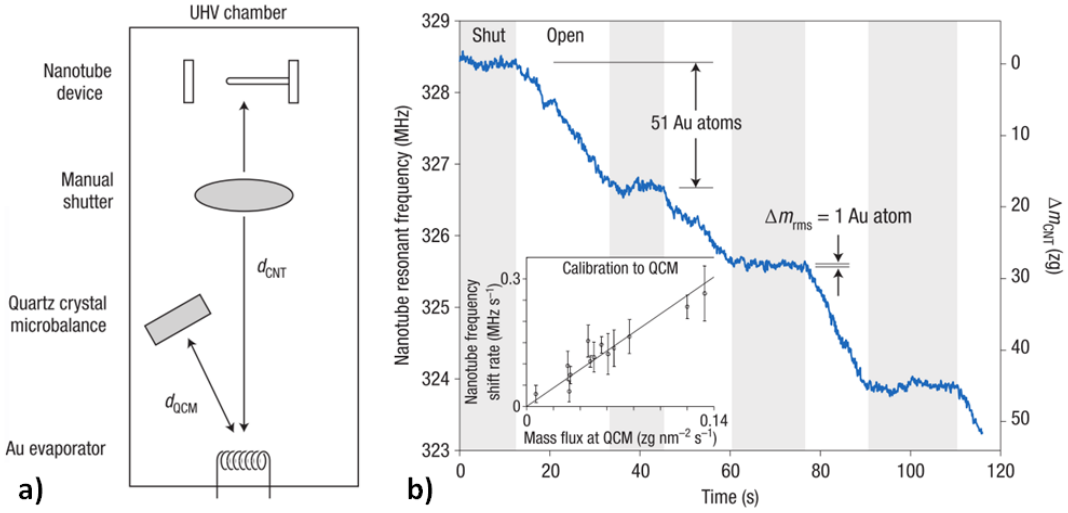

Fig. I.12: Nanotube based MS setup where gold atoms are evaporated toward a QCM or the nanotube device (a). Frequency shifts during mass loading for a nanotube mass sensor and quartz crystal microbalance (b) as the manual shutter is shut or opened.

Using either a statistical approach of the measured frequency shifts or spectral density comparison when the manual shutter was opened or shut, the atomic mass of gold was evaluated at 0.29zg, close to the 0.327zg reference. Both CNT based experiments relied on indirect mass determination and frequency shifts upon accretion of an individual atom was not clearly evidenced but they demonstrated the feasibility of measuring a mass standard that is the mass of an atom.

The current mass record is held by Bachtold's group that demonstrated close-to yoctogram resolution (one yoctogram = $1 \times 10^{-24} g$) in 2012 [35]. They measured frequency jumps on a 150nm long doubly clamped CNT with a 1.7nm diameter resonating around 2 GHz and cooled at 5.5K. Upon device annealing by passing a large current across the CNT, they reduced the device relative frequency fluctuations down to 2.8×10^{-6} for a 2s integration time. Given the outstanding mass sensitivity of 3.1MHz/yg, a mass resolution down to 1.7yg is achieved (Fig. I.14).

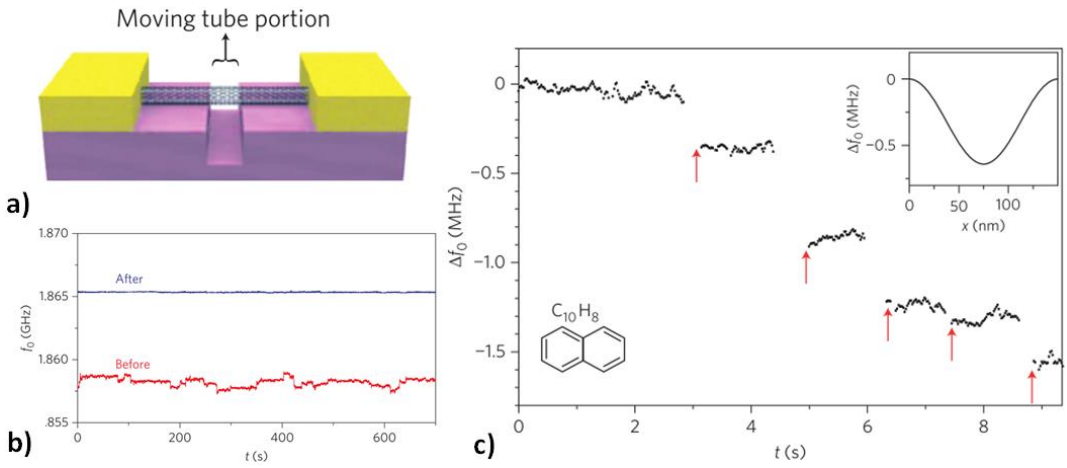

Fig. I.13: Yoctogram sensing achieved with a doubly clamped CNT (a) whose thermal annealing provided enhanced frequency stability (b) that allowed for sensing of individual naphthalene molecules (c).

The CNT sensed adsorption of Xe atoms as well as naphthalene molecules. For the latter, frequency shifts consistent with single molecule loading were observed. However, no individual mass attribution could be made as frequency shifts depend on the molecule landing position. For both acquisitions, upward shifts occurred during mass loading time intervals. They are attributed to molecules either desorbing in vacuum or diffusing along the nanotube toward the clamping regions. Therefore, engineering trapping sites on the CNT surface will be required to move toward nanomechanical spectrometry applications. Nevertheless, the extreme mass sensitivity of the device allowed demonstrating the thermal dependence of the process of Xe adsorption on the nanotube surface and a binding energy of 131MeV was extracted. Hence, the application of CNTs might be extended to atom binding energy to nanotubes measurements and diffusion processes studies.

Results of the previously discussed papers are summarized in Table I.2.

Paper	[38]	[39]	[40]	[41]	[35]
Group	Roukes	Roukes	Roukes	Zettl	Bachtold
Publication	2004	2006	2008	2008	2012
Device	Doubly-clamped beam	Doubly-clamped beam	Doubly-clamped CNT	Single-clamped CNT	Doubly-clamped CNT
Frequency	72MHz	133MHz	300MHz	325MHz	1.862GHz
Dimensions	L=10µm w=650nm t=260nm	L=2.3µm w=150nm t=70nm	L=400nm d=1nm	L=254nm d=2.1nm	L=150nm d=1.7nm
M_{eff}	7.2e-12g	7.3e-14g	1.6e-18g	2.3e-18g	3e-19g
Q	3000	5000	200	1000	/
Temperature	17K	37K	6K	300K	5.5K
τ	2ms	1s	/	/	
$\sigma_{\delta f}$	2e-7	5e-8	/	/	2.8e-6
Mass sensitivity	2.56e+18Hz/g	8.9e+20Hz/g	9.3e+25Hz/g	9.1e+25Hz/g	3.1e+30Hz/g
Mass resolution	2.53ag	7zg	85yg	290yg	1.7yg

Table I.2: Summary of NEMS-based sensing experiments toward lower mass resolution.

In less than 10 years, NEMS-based mass sensing experiments have demonstrated the feasibility to sense molecules down to 1.7yg i.e. almost the mass of a hydrogen atom. The recipe for low mass resolution resides in resonant mass shrinking for larger mass sensitivity, low frequency fluctuations and low temperature. At this point where the Da resolution has been experimentally proved, it is clear that NEMS-based sensing has a promising future for mass spectrometry applications given that we are able to weight individually each impinging molecules.

3.2. Emergence of single particle nanomechanical mass spectrometry

In 2009, Naik *et al.* exposed for the first time an association of resonant NEMS sensing with conventional mass spectrometry components [37]. They built a hybrid MS setup using an ESI ion source and quadripole focusing to project proteins such as Bovine Serum Albumine (66kDa) and β–amylase (200kDa) on a resonant NEMS cooled at 40K (Fig. I.14). The device was a 1.7µm long and 120nm wide doubly-clamped SiC beam composed on three layers of SiC (100nm), Al (40nm) and Ti (5nm) and featured a quality factor of 2000.

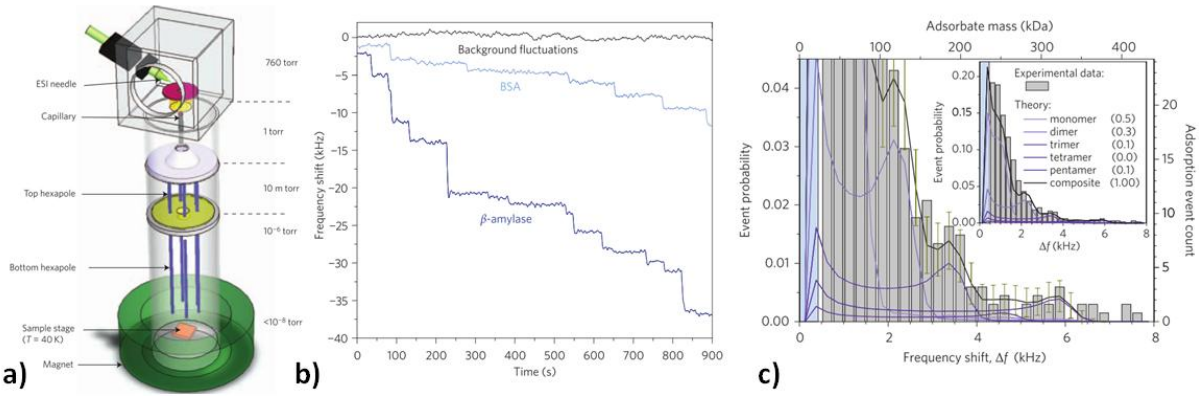

Fig. I.14: Schematic of the protein mass sensing setup shown the ESI ion injection, the three stage differential pumping and the two stage ion optics (a). Real time records of single molecule adsorption events on the NEMS mass sensor (b). Histogram of frequency jumps from protein acquisitions with 250Hz bins compared with theory (c).

They observed a mass sensitivity of 12Hz/zg along with a relative frequency fluctuation of 3.5×10^{-7} over 5s integration time yielding a mass resolution of 17zg (10kDa). This time, they were able to record events associated with the adsorption of a single molecule: each frequency jump observed on the PLL acquisition can be attributed to the adsorption of a protein. However, because the magnitude of the frequency jumps not only depends on the protein mass but also on the landing position, the individual mass of a molecule cannot be retrieved as the molecules positions could not be known. The idea here consisted in accumulating enough statistical events to suppose homogeneous deposition along the NEMS surface and compare frequency shifts histogram with theoretical ones. For

homogeneous deposition of molecules such as gold nanoparticles, the population's mean mass was found. This first step toward hybrid NEMS Mass Spectrometry (NEMS-MS) is very important as it proved that an experimental setup could be built to measure biomomecules, instead of gas atoms or nanoparticles previously used so far for mass sensing. Yet, it still lacks the possibility to individually weight each particle in real time which requires finding a way to determine the particles' landing positions.

The dependence of the frequency shifts on the particle's landing position has been thoroughly studied by Boisen's group. In 2007, Dohn *et al.* derived an analytical expression to relate mass and position of a particle attached on a cantilever to the frequency shift observed on a cantilever [44] before verifying it experimentally for the 4th first bending modes as show in Fig. I.15.

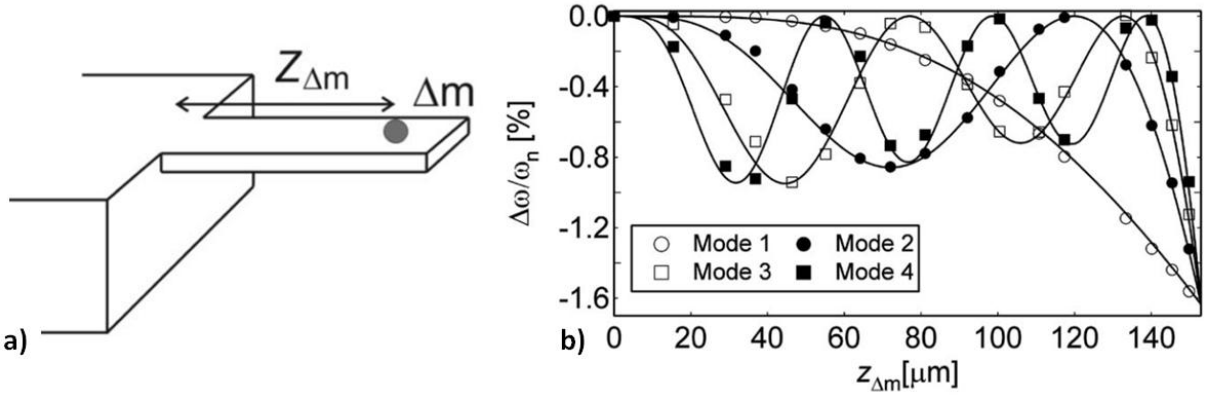

Fig. I.15: Mass localization on a cantilever. A schematic of a cantilever with a single bead of mass Δm positioned at $Z_{\Delta m}$ is depicted in (a) while (b) shows measured relative resonant frequency change of the first four modes as a function of the position of the attached gold bead. Curves denotes the theoretical values calculated from the model.

Measuring the four first bending modes enabled them to determine the position of a gold bead with good precision on most portions of the beam. Clearly, this seems to be an interesting lead for nanomechanical mass spectrometry of individual particles. Moreover, the method was extended in 2010 to the determination of the mass and position of multiple particles attached to a cantilever [45]. Measuring the first 7 modes of a cantilever with a laser-Doppler vibrometer, they were able to locate and weigh 3 different particles attached to the cantilever. Therefore, measuring a maximum of resonance frequency should be sought for in flexural beam resonant sensing applications.

In 2012, the Alliance for nanosystems VLSI was able to demonstrate the first nanomechnical spectrometry of single molecules using multiple resonance mode monitoring [46]. Hanay *et al.* modified their electrical scheme to monitor in real time the first two resonance modes of a Leti doubly-clamped Si beam. Thanks to the symmetric properties of the doubly-clamped beam, monitoring the first two resonance frequencies was sufficient to deduce the molecules position. Frequency fluctuations on mode 1 and mode 2 can translate into uncertainty on mass and position of the detected particle. Therefore a complex error model (detailed in Chapter III) was built to calculate the Joint Probability Density Function (JPDF) of the mass of each particle according to mode 1 and mode 2 frequency noises and by

extension defines the mass resolution in terms of mass spectrometry (when using the FMHW definition). Mass acquisition was performed on two different setups using either ESI or MALDI ionization source, the two most popular ionization sources in Top-down proteomics and Native MS. To demonstrate the utility of NEMS-based MS, they acquired mass spectra of human IgM (Immunoglobulin M), an antibody in the MDa range (Fig. I.16).

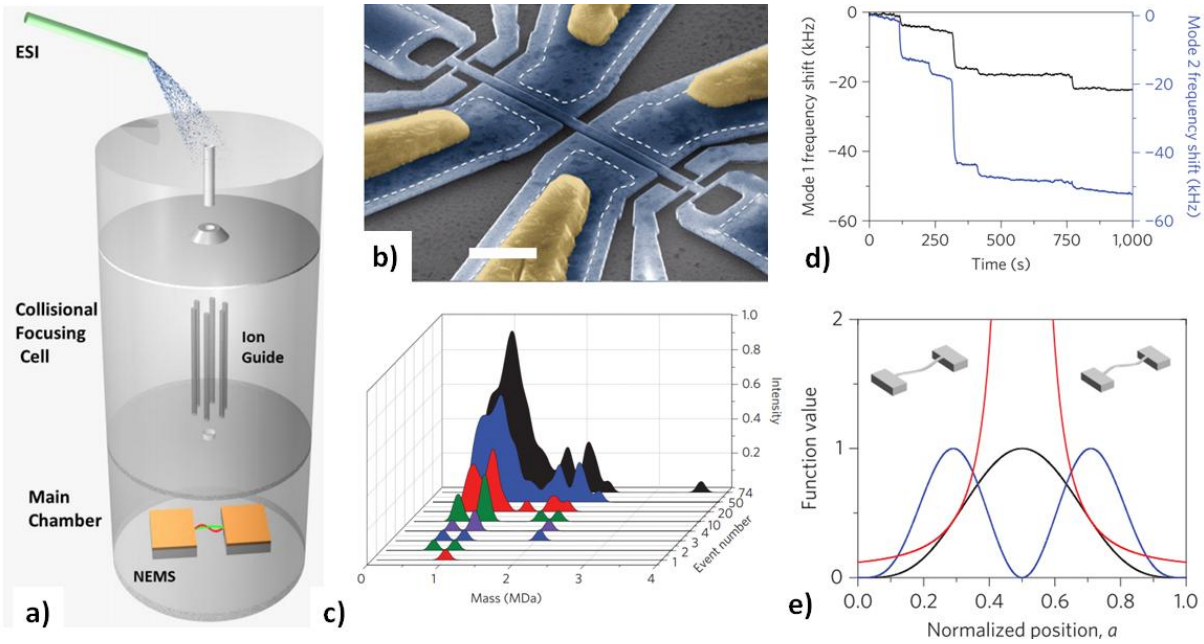

Fig. I.16: Nanomechanical mass spectrometry of single molecule. The ESI setup is schematized in (a) showing the ESI ionization source, the collisional focusing cell and the NEMS chamber. A colorized SEM image displays the doubly-clamped resonator with its four electrostatic actuation pads and nanogauge bridge placed close to each anchor for motion transduction (b). The system allowed acquiring a mass spectrum event-by-event of human IgM molecules (b): when single molecules are adsorbed on the cooled device, they induced frequency shifts on mode 1 and mode 2 resonances (c). Thanks to symmetric properties of the doubly-clamped beam, the ratio between shifts on mode 1 and mode 2 is sufficient to deduce its normalized position on the beam relative to the center (e). The black and blue curves are the response function of mode 1 and mode 2 respectively while the red curve denotes the ratio mode2/mode1.

They were able to differentiate the different IgM isoforms on ranges from 0.5MDa to 2.5MDa on a spectrum built event per event rending possible further inquisition of the underlying structure of the composite intensity curve. Plus, mass resolution depends only on the NEMS frequency noise and remains constant on all the NEMS mass dynamic range: while conventional MS displays decreasing resolution for high masses, NEMS-MS is more efficient as measured masses get heavier. The possibility to weigh neutral molecules as well as further prospects with VLSI arrays of NEMS co-integrated with CMOS highlights the great potential of NEMS-MS for MS of large protein macromolecules.

4. Mechanical resonators

4.1. Mechanical resonance of flexural beams

A mechanical resonator is described as a simple harmonic oscillator where energy is successively transferred from kinetic energy to potential energy stored in the spring. As damping or energy loss in the anchors lead to energy loss for each cycle, an undriven resonator will eventually see its oscillations decrease until it becomes motionless as all energy has been dissipated. We consider here the in-plane mechanical resonance of flexural beams being either cantilevers or doubly-clamped beams with a length L, a width w and a thickness t as defined in Fig. I.17. While both design have been fabricated and characterized, doubly-clamped beams have been extensively used for mass detection experiments. In consequence, most discussions will focus on this design.

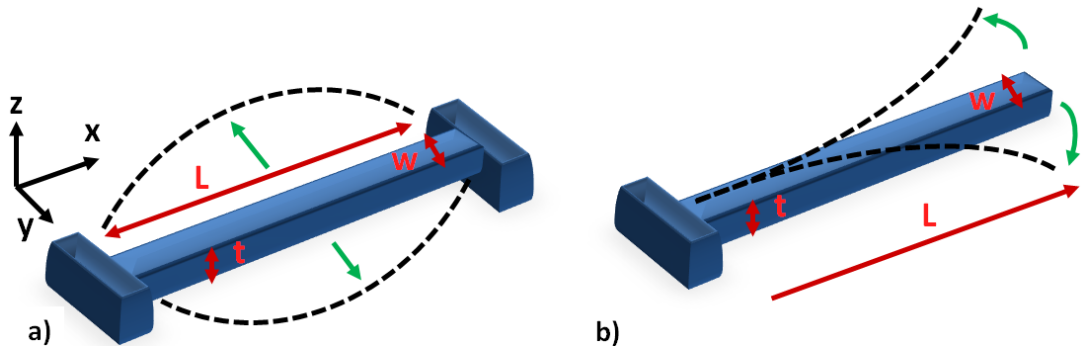

Fig. I.17: Illustration of a doubly-clamped beam (a) and a cantilever (b) showing the dimensions notation that will be used throughout the manuscript (in red). Black dashed lines and green arrows describe the beams in-plane motion at resonance (1st mode). Position on the beam is defined by the x axis while in-plane motion is done along the y axis.

For a ratio $\frac{L}{t} \gg 1$ and small deflections, the motion of a flexural beam can be described using the Euler-Bernoulli beam theory [47]. Boundary conditions (clamping) and dimensions of the geometry will determine the allowed eigen frequency resonance modes. The eigen frequencies are obtained for the ideal case where the beam is not subjected to damping or an external driving force:

$$EI\frac{\partial^4 y(x,t)}{\partial^4 x} + \rho S\frac{\partial^2 y(x,t)}{\partial^2 t} = 0 \qquad \text{(I.7)}$$

where E is Young's modulus, S=$w.t$ the beam section and $I = \frac{t.w^3}{12}$ the inertial moment in flexion. The position along the beam is denoted with x, equal to 0 at one anchor, while y denotes the beam deformation along the y axis, equal to 0 at null deformation.

We need to separate position and temporal dependence of $y(x,t)$ by using Galerkin's decomposition method:

$$y(x,t) = \sum_{n=1}^{+\infty} y_n(t).\varphi_n(x) \qquad \textbf{(I.8)}$$

where $\varphi_n(x)$ is solution of equation (I.7) and should thereby satisfy:

$$\frac{\partial^4 \varphi_n(x)}{\partial^4 x} = \lambda_n^4.\varphi_n(x) \qquad \textbf{(I.9)}$$

where λ_n is the eigenvalue of mode *n*.

Thus, the beam deformation at a point *x* at a given time *t* is an infinite addition of the possible orthogonal resonance modes: $\varphi_n(x)$ denotes the mode shape of mode *n* while $y_n(t)$ reflects the temporal oscillation of this mode shape. We define the mode shapes $\varphi_n(x)$ as forming a dimensionless orthonormal base satisfying the normalisation condition:

$$\frac{1}{L}\int_0^L \varphi_n(x).\varphi_m(x)dx = \delta_{mn} \qquad \textbf{(I.10)}$$

where *x* is the normalized position along the beam and $\delta_{mn} = 1$ if m=n, 0 otherwise.

Inserting equation (I.8) into equation (I.9) yields:

$$\sum_{n=1}^{+\infty} EI.y_n(t).\lambda_n^4.\varphi_n(x) + \rho S.\varphi_n(x)\frac{\partial^2 y_n(t)}{\partial^2 t} = 0 \qquad \textbf{(I.11)}$$

Given that the modes are orthogonal, the projection on mode *n* is obtained by multiplying equation (I.11) by $\varphi_n(x)$ and integrating along *x* from 0 to L:

$$EI.y_n(t).\lambda_n^4 + \rho S\frac{\partial^2 y_n(t)}{\partial^2 t} = 0 \qquad \textbf{(I.12)}$$

By expressing $y_n(t) = Ae^{-j\omega_n t}$ where ω_n is the resonance pulsation of the n^{th} mode, we can translate to the frequency domain and use the Fourier transform to write:

$$y_n(\omega_n)\frac{EI.\lambda_n^4}{\rho S} - {\omega_n}^2.y_n(\omega_n) = 0 \qquad \textbf{(I.13)}$$

Therefore the resonance frequency of the n^{th} mode is calculated as:

$$f_n = \frac{\omega_n}{2\pi} = \frac{\lambda_n^2}{2\pi}\sqrt{\frac{EI}{\rho S}} = \frac{\lambda_n^2 . w}{4\pi}\sqrt{\frac{E}{3\rho}} \quad \textbf{(I.14)}$$

The eigenvalue λ_n is obtained by solving equation (I.9) using boundary conditions and the general solution:

$$\varphi_n(x) = A_n\, sinh(\lambda_n x) + B_n\, cosh(\lambda_n x) + C_n\, sin(\lambda_n x) + D_n\, cos(\lambda_n x) \quad \textbf{(I.15)}$$

Boundary conditions of a cantilever anchored at x=0 and free at its extremity at x=L are:

$$\begin{aligned} y_n(x=0,t) &= 0 \quad & \frac{\partial^2 y_n}{\partial^2 x}(x=L,t) &= 0 \\ \frac{\partial y_n}{\partial x}(x=0,t) &= 0 \quad & \frac{\partial^3 y_n}{\partial^3 x}(x=L,t) &= 0 \end{aligned} \quad \textbf{(I.16)}$$

Boundary conditions of a doubly-clamped beam are:

$$\begin{aligned} y_n(x=0,t) &= 0 \quad & y_n(x=L,t) &= 0 \\ \frac{\partial y_n}{\partial x}(x=0,t) &= 0 \quad & \frac{\partial y_n}{\partial x}(x=L,t) & \end{aligned} \quad \textbf{(I.17)}$$

For a doubly clamped beam, we obtain the following system of equation:

$$\begin{aligned} A_n + C_n &= 0 \\ B_n + D_n &= 0 \\ A_n(sinh(k) - sin(k)) + B_n(cosh(k) - cos(k)) &= 0 \\ A_n(cosh(k) - cos(k)) + B_n(sinh(k) + sin(k)) &= 0 \end{aligned} \quad \textbf{(I.18)}$$

where $k = \lambda_n L$

Solving the matrix for non trivial solutions leads to the transcendental equation:

$$(sinh(k) - sin(k)).(sinh(k) + sin(k)) - (cosh(k) - cos(k))^2 = 0 \quad \textbf{(I.19)}$$

The equation is solved numerically on Matlab by displaying the function and looking for f(λL)=0.

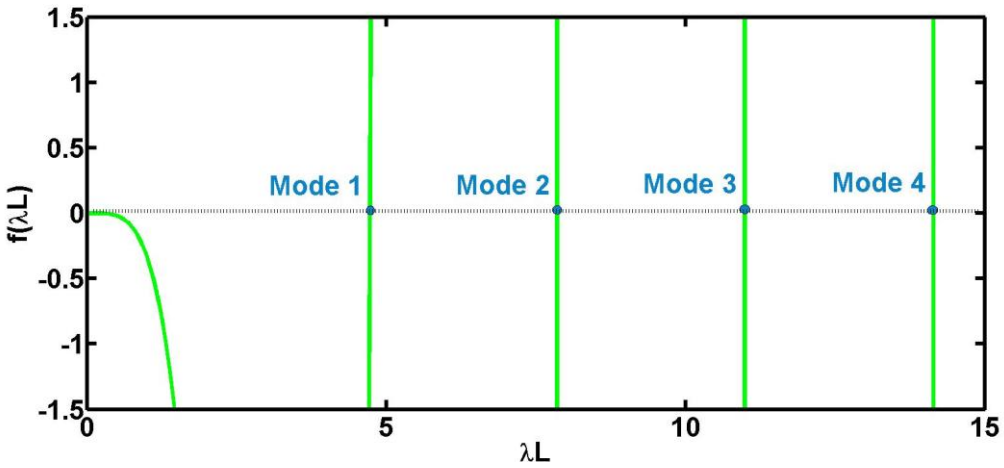

Fig. I.18: Numerical solutions of equation (I.19). The solutions of f(λL)=0 provide the eigenvalues of the resonance modes.

Eigenvalues found for cantilevers and doubly clamped beam are listed in Table I.3 for the first four modes.

	$\lambda_1 L$	$\lambda_2 L$	$\lambda_3 L$	$\lambda_4 L$
Cantilever	1.875	4.694	7.854	10.995
Doubly clamped beam	4.73	7.853	10.995	14.14

Table I.3: Eigenvalues for cantilevers and doubly clamped beams up to mode 4

It is interesting to note the similarities of the eigenvalues $\lambda_n L$ of doubly clamped beams with $\lambda_{n+1} L$ of cantilevers. Therefore, if our instrumentation allows us to measure n modes of a doubly clamped beam, this means we are able to measure n+1 modes of a cantilever of equal length. As detailed further in this thesis, the ability to measure several resonance mode of a resonator may prove to be useful for mass sensing.

Given equation (I.14), we can deduce, for example, the 1st resonance mode of a doubly clamped beam:

$$f_1 = \frac{w}{L^2} \frac{4.73^2}{4\pi} \sqrt{\frac{E}{3\rho}} \qquad \textbf{(I.20)}$$

We observe that the resonance frequency of a flexural beam does not depend on its vibrating thickness but on its ratio width over length squared. Therefore, length is the most sensitive parameter to tune to design resonators with different resonance frequencies.

When measuring the resonance modes of a resonator, it is extremely useful to know the expected ratio between successive modes, which makes it way easier to find the higher modes after having found the fundamental one. According to equation (I.14) the ratios between two successive modes of a beam resonator are the square of the ratios between their respective eigenvalues. Hence ratios between two successive resonance frequencies are:

	$\frac{f_2}{f_1}$	$\frac{f_3}{f_2}$	$\frac{f_4}{f_3}$
Cantilever	6.27	2.8	1.96
Doubly clamped beam	2.76	1.96	1.65

Table I.4: Ratios between two successive resonance frequencies up to mode 4

For each $\lambda_n L$, equation (I.18) is solved with Matlab to calculate the coefficients A_n, B_n, C_n, and D_n. The resulting normalized mode shapes $\varphi_n(x)$ of a doubly-clamped beam are displayed in Fig. I.19.

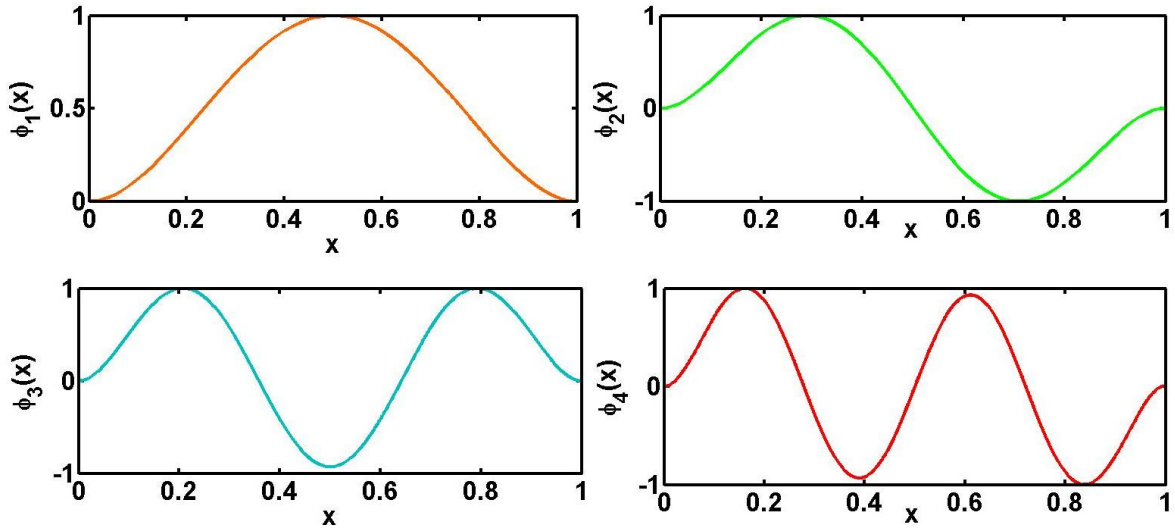

Fig. I.19: Normalized mode shapes versus normalized beam length for the first four resonance mode of a doubly clamped beam. The number of nodes increases with higher modes.

4.2. The driven harmonic oscillator model

We now consider a resonator subject to damping and driven by a force $F(x,t) = g(x)f(t) = g(x).F_0.e^{-i\omega_d t}$, directed along the y axis, where $g(x)$ is the position dependent force per unit length and ω_d the frequency of excitation:

$$EI\frac{\partial^4 y(x,t)}{\partial^4 x} + \rho S\frac{\partial^2 y(x,t)}{\partial^2 t} + b\frac{\partial y(x,t)}{\partial t} = g(x)f(t) \qquad \text{(I.21)}$$

where b is the damping coefficient

By projecting equation (I.21) on mode n, we obtain:

$$EI.y_n(t).\lambda_n^4 L + \rho SL\frac{\partial^2 y_n(t)}{\partial^2 t} + bL\frac{\partial y_n(t)}{\partial t} = f(t)\int_0^L \varphi_n(x)g(x)dx \qquad \text{(I.22)}$$

We can rearrange it as:

$$\ddot{y}_n(t) + \dot{y}_n(t)\frac{b}{\rho S} + y_n(t)\ \frac{EI.\lambda_n^4}{\rho S} = \frac{f(t)\eta}{M} \qquad \textbf{(I.23)}$$

where $M = \rho SL$ is the resonator mass and $\eta = \int_0^L \varphi_n(x)g(x)dx$ is a coefficient depending on the electrode length facing the beam. For the case of electrostatic force we generally consider $g(x) = cst = 1$ for the sake of simplicity.

This equation can be identified to a lumped spring-mass system whose behavior is described as simple harmonic oscillator resonating at $\omega_0 = \sqrt{\frac{k}{m}}$:

$$\ddot{Y} + \frac{c}{m}\dot{Y} + \frac{k}{m}Y = \frac{F}{m} \qquad \textbf{(I.24)}$$

where Y is the displacement, m the mass of the system, k the stiffness and c the viscous damping coefficient

Q is the quality factor of the system defined as:

$$Q = 2\pi\ \frac{energy\ stored\ in\ the\ system}{energy\ lost\ per\ cycle} = \frac{\omega_0}{\gamma} \qquad \textbf{(I.25)}$$

where $\gamma = \frac{c}{m}$ is the damping coefficient of the system

Equation (I.24) can be rewritten as:

$$\ddot{Y} + \frac{\omega_0}{Q}\dot{Y} + \omega_0^2 Y = \frac{F}{m} \qquad \textbf{(I.26)}$$

By identification with $\frac{b}{\rho S} = \frac{\omega_0}{Q}$ and $\frac{EI.\lambda_n^4}{\rho S} = \omega_0^2$, Equation (I.23) is equivalent to (I.26) and the transfer function of our system is written as:

$$H(\omega) = \frac{y(\omega)}{F(\omega)} = \frac{\eta}{M\left(\omega_0^2 - \omega + j\frac{\omega\omega_0}{Q}\right)} \qquad \textbf{(I.27)}$$

At resonance, we obtain the following gain and phase:

$$|H(\omega_0)| = \frac{Q\eta}{M\omega_0^2}$$
$$arg\big(H(\omega_0)\big) = -\frac{\pi}{2} \qquad \textbf{(I.28)}$$

Resonators with a high quality factor yield a high gain at resonance and resonate on a narrow bandwidth $\Delta f = \frac{f}{Q}$. The resonator acts as bandpass filter where a 3dB loss of gain is found at $\omega = \omega_0 \left(1 \pm \frac{1}{2Q}\right)$ as shown in Fig. I.20.

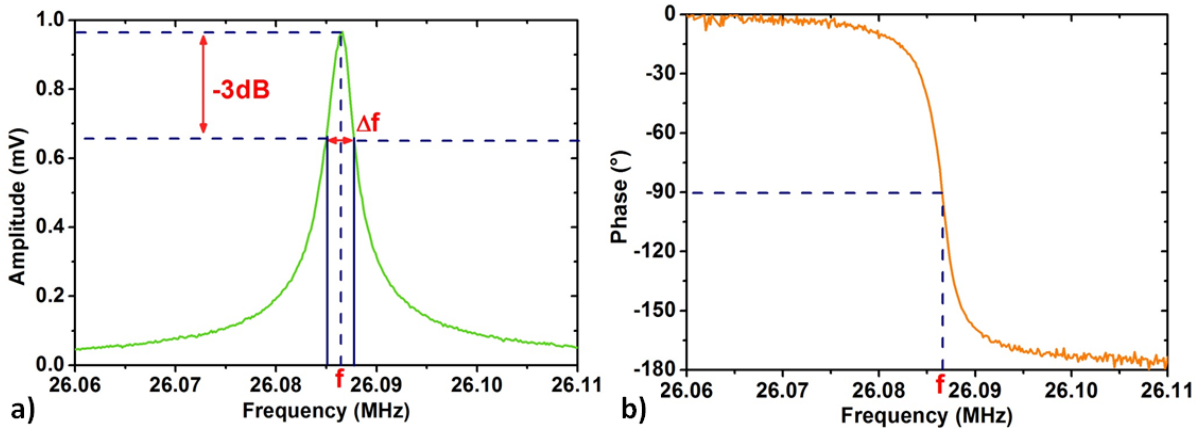

Fig. I.20: Amplitude (a) and phase (b) of a resonator transfer function. A phase of $-\frac{\pi}{2}$ is observed at resonance. The bandwidth at -3dB of the maximum gain defines the resonator bandwidth.

5. Mass induced frequency shift of a single particle

5.1. Concept of resonant effective mass

We previously associated the mechanical resonance of a flexural beam with a lumped spring-mass model. Yet, while the lumped model considers the oscillation of a punctual mass with a punctual kinetic energy, the matter composing the beam does not carry the same kinetic energy along the beam: almost null close to the anchors, it becomes maximal at the point of maximum deflection. The concept of effective mass was introduced to translate this homogeneity of deformation, hence kinetic energy, to a punctual mass considered at the maximum of deflection [37]. With this definition, the effective mass M_{eff} is a fraction of the actual mass M. The effective mass is identified by equalizing the kinetic energy (K.E) of the flexural beam model and the lumped spring-mass model of mass M_{eff} and stiffness K_{eff} with deflections equal to those at maximum deflection of the beam, i.e. where $\varphi_n(x) = 1$. For a doubly-clamped beam, the displacement at a point x along the beam can be expressed as:

$$y(x) = y_{max} \times \varphi_n(x) \qquad \textbf{(I.29)}$$

The kinetic energy of the flexural beam is calculated as:

$$K.E = \frac{1}{2}\int \dot{y}^2 dm = \frac{1}{2}\int_0^L \rho.t.w.\left(\dot{y}_{max} \times \varphi_n(x)\right)^2 dx \qquad \textbf{(I.30)}$$

Equation (I.30) can be reshaped as the kinetic energy of a lumped model $K.E = \frac{1}{2}mv^2$:

$$K.E = \frac{1}{2}M\int_0^L \varphi_n(x)^2\, dx\, .\dot{y}_{max}{}^2 \qquad \textbf{(I.31)}$$

By identification, the effective mass of the resonator at a given harmonic n is obtained as:

$$M_{effn} = M.\int_{x=0}^{x=1} \varphi_n^2(x)dx = M\alpha_n \qquad \textbf{(I.32)}$$

The coefficients α_n of the nth mode are given in Table I.5 for a doubly clamped beam.

n	1	2	3	4
α_n	0.3964	0.4390	0.4371	0.4367

Table I.5: coefficient for effective mass calculation of a doubly clamped beam for the first four modes.

5.2. Punctual mass addition

Assuming the beam stiffness and the mode shapes remain constant, we now consider the adsorption of a punctual mass Δm at a position x_0 on a resonator of effective mass M_{effn} resonating at f_n for the mode n. The kinetic energy is now:

$$\begin{aligned} K.E &= \frac{1}{2}M_{effn}.\dot{y}_{max}{}^2 + \frac{1}{2}\Delta m.\dot{y}_{max}{}^2.\varphi_n(x_0)^2 \\ &= \frac{1}{2}\left[M_{effn} + \Delta m.\varphi_n^2(x_0)\right].\dot{y}_{max}{}^2 \end{aligned} \qquad \textbf{(I.33)}$$

Therefore, the new resonance frequency is:

$$f_n' = \sqrt{\frac{k_{effn}}{M_{effn} + \Delta m.\varphi_n^2(x_0)}} \qquad \textbf{(I.34)}$$

For a mass $\Delta m \ll M_{effn}$, the mass induced frequency shift is given by:

$$\frac{\Delta f}{f_n} = \frac{f_n - f_n'}{f_n} \approx \frac{\Delta m.\varphi_n^2(x_0)}{2M_{effn}} \qquad \textbf{(I.35)}$$

Hence, the relative frequency shift induced by a punctual particle landing on the NEMS resonator strongly depends on the landing position and the mode shape of the considered mode. Deducing the particle mass implies prior knowledge of the particle position. One solution, detailed in Chapter III and used in [46], consists in observing several resonance modes to deduce the particle position.

6. Resonator scaling effects for mass sensing

For the sake of simplicity, scaling effects are studied for uniform mass deposition described by equation (I.4). We consider scaling laws by studying the effects the geometric NEMS dimensions L, t and w on the device properties denoted by the factor l.

As observed in equation (I.20), the resonance frequency scale as $f_0 \propto \frac{w}{L^2} \propto \frac{1}{l}$. As smaller device are used, the electronics needs to be able to drive and read the NEMS at higher frequencies. For frequencies above the GHz, capacitive losses make signal detection very challenging.

Stiffness scales as $\propto w\left(\frac{t}{L}\right)^3 \propto \frac{1}{l}$: smaller devices are stiffer, hence more difficult to actuate. Yet, with efficient transduction means, this parameter is generally not a problem for the first harmonics but may play an important role for higher harmonics. Stiffness of higher modes are related as $k_{n+1} = k_n\left(\frac{\lambda_{n+1}}{\lambda_n}\right)^4$ and thus depends only on boundary conditions of the flexural beam. Yet, while the first mode of a doubly clamped beam may be easy to drive, mode 4 is $\left(\frac{14.14}{4.73}\right)^4 = 80$ times stiffer. For devices designed to operate at higher harmonics, stiffness engineering becomes increasingly important.

Driving the resonator at high amplitudes is essential to obtain high Signal to Background Ratio (SBR) and Signal to Noise Ratio (SNR). Yet, when efficiently driven, resonators may feature non-linearity effects such as electrostatic spring softening or mechanical spring hardening. The thresholds at which these effects appear limit the ability to improve the SBR and SNR. These effects were extensively studied in the doctoral work of Najib Kacem [48]. The critical amplitude, i.e. the maximal deflection amplitude in linear regime, is estimated as $A_c = 1.685w/\sqrt{Q}$ for a doubly-clamped beam and $A_c = 6.3L/\sqrt{Q}$ for a cantilever (set by the mechanical NL). Hence, tiny device are more prone to suffer from nonlinear effects. Yet, as only one dimension is concerned, device design may be optimized for linear operation by favoring reduction of the other two dimensions.

We define the mass sensitivity of a resonator as:

$$S = \frac{\Delta f}{\Delta m} = \frac{f}{2M_{eff}} \quad \textbf{(I.36)}$$

Therefore, the mass sensitivity described with geometric terms is written as:

$$S = \frac{1}{t.L^3} \frac{(\lambda_n L)^2}{\rho 8\pi} \sqrt{\frac{E}{3\rho}} \quad \textbf{(I.37)}$$

where $\lambda_n L$ is a constant

Mass sensitivity scales as $S \propto \frac{1}{l^4}$. Scaling down devices leads to a tremendous gain in term of absolute detected resonance frequency shift. Yet, it must be kept in mind that the mass resolution depends on the ability to resolve a frequency shift from the frequency noise floor (equation (I.6)). The physical phenomena playing a role in this noise are still misunderstood as detailed in Chapter II. Nevertheless, we believe the relative frequency fluctuations $\sigma_{\delta f}$ increase with smaller devices. We can write the LOD as:

$$\Delta m = \frac{1}{S_r} \sigma_{\delta f} \quad \textbf{(I.38)}$$

where S_r is the relative sensitivity written as:

$$S_r = \frac{\Delta f}{f \Delta m} = \frac{1}{2M} = \frac{1}{2\rho.t.w.L} \quad \textbf{(I.39)}$$

Relative mass sensitivity scale as $S_r \propto \frac{1}{l^3}$. Scaling laws of relative frequency noise are still unclear. However, it has been experimentally proved in the literature that smaller devices detect increasingly smaller molecules [35], [39], [49]. Therefore, resonator relative frequency fluctuations should probably have a scaling law $\sigma_{\delta f} \propto l^{\alpha}$ with $\alpha \in]0,3[$.

A better understanding of internal frequency fluctuations is required to obtain predictive scaling laws of the mass resolution. Nevertheless, for a given $\sigma_{\delta f}$ it is clear that shrinking the devices bring enhanced relative sensitivity. For doubly-clamped beams, L and t should be reduced in priority as lower w favors early non-linear effects. Plus, reducing w also reduces the capture cross section for single mass detection in vacuum. L can be shrunk in the limit of the transduction setup bandwidth and also needs to fulfill the $L \gg t$ condition for the Euler-Bernoulli equation to remain valid. Fabricating thinner device is an excellent way to improve the relative mass sensitivity without increasing the resonance frequency, reducing the capture cross section or provoking early non-linearity effects but it increase substantially the stiffness, unless L is scaled accordingly. Plus, the reduced capacitive surface offered for electrostatic actuation may require higher drive voltages. Hence a trade-off needs to be made by taking into account the electronics bandwidth, actuation efficiency and non-linear effects.

7. NEMS devices for mass sensing

The CEA-Leti capitalizes on an advanced experience of silicon based device and a state-of-the-art cleanroom for micro-electronics and is dedicated to industrial transfer. In the framework of the Alliance for nanosystems VLSI, we favor the production of VLSI CMOS compatible devices. Therefore, the roadmap was naturally set for top-down fabricated crystalline silicon resonators. Dr. Sébastien Labarthe and Dr. Ervin Mile developed designs of in-plane resonators for mass sensing applications [4], [6], [50]. The produced devices featured Signal to Background Ratios (SBR) up to 67dB and Signal to Noise Ratios (SNR) up to 100dB. Their outstanding transduction efficiency along with their small resonant mass (hundreds of fg) make these devices excellent candidate for mass sensing.

The device fabrication steps use state-of-the-art microelectronics fabrication processes following a top-down approach on a 200mm silicon-on-insulator (SOI) of (100) orientation with a p-doped top silicon layer (from 9.10^{18} cm^{-3} to 5.10^{19} cm^{-3}). The top silicon layer is intended to form the resonant area as well as electrical accesses while the buried oxide is used as a sacrificial layer released by vapor HF. The resonant beam is patterned by a hybrid deep UV/electron beam lithography technique. AlSi metal lines are deposited on the existing Si electrical access to minimize electrical access resistance and form metallic pads adapted to device wirebonding. The resonator beam is released by vapor HF.

While a variety of flexural beam designs has been produced (tuning forks, free-free beams, etc.), for now the focus has been on simple cantilevers and doubly-clamped beams based on electrostatic actuation and piezoresistive detection as shown in Fig. I.21.

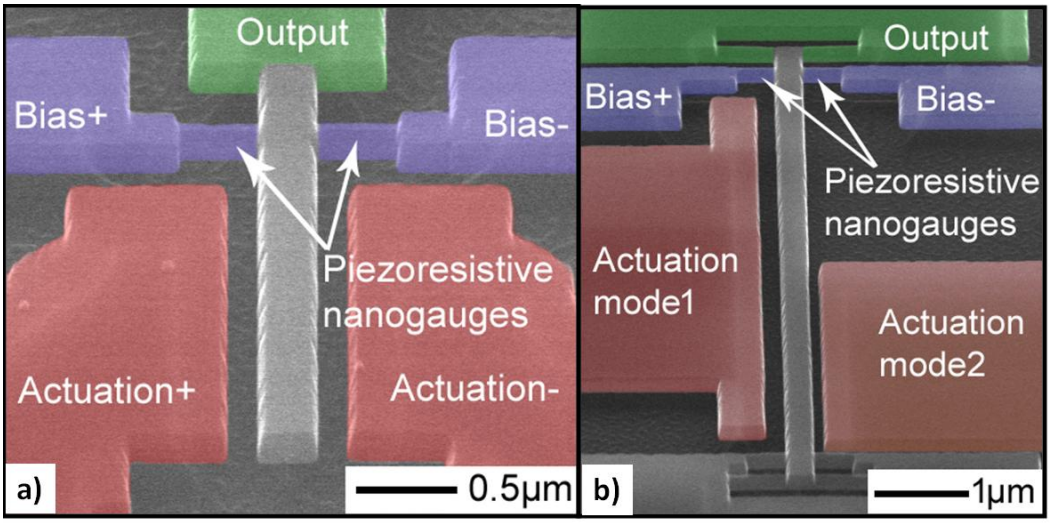

Fig. I.21: Colorized SEM image of typical suspended in-plane resonators studied in this work: cantilevers are designed for gas sensing (a) while doubly clamped beams are designed for NEMS-MS (b). Actuation pads are in red or orange, bias gauges in blue and output in green.

The first mode resonance frequencies are designed in the tens of MHz range. The beams are set in motion by capacitive force thanks to electrodes patterned along the beam

length. Two piezoresistive nanogauges are disposed on both sides of the beams at a position 0.15L where the lever effect is maximized. As the beam resonates, it induces compressive strain on one gauge and dilatation strain on the other one. Strain is converted to electrical signal trough piezoresistive effect. Using two different transduction means for actuation and detection, referred to as orthogonal transduction, is an excellent way to minimize cross-talking between signals.

7.1. Actuation

Actuation is performed through capacitive force. The energy stored in a capacitor is $E = \frac{C.V_d^2}{2}$ where C is the capacitance formed by the actuation electrode surface and the beam surface facing the electrode. V_d is the actuation voltage applied on the electrode. Force applied on the beam is the derivative of the stored energy:

$$F = -\frac{1}{2}\frac{\delta c}{\delta y}V_d^2 = -\frac{1}{2}\frac{A\varepsilon_0}{(g-y)^2}V_d^2 = -\frac{A\varepsilon_0}{2g^2\left(1-\frac{y}{g}\right)^2}V_d^2 \qquad \textbf{(I.40)}$$

where A is the capacitor surface, ε_0 the permittivity, y the displacement in the y direction and g the gap between the electrode and the beam.

Assuming that small displacements in the y direction are negligible with respect to the gap ($y \ll g$), we have:

$$F \cong -\frac{A\varepsilon_0}{2g^2}V_d^2 \quad (1st\ order) \qquad \textbf{(I.41)}$$

A static force can be applied with a DC source or the beam can be driven into oscillation with an AC voltage. Let us consider the general case where the actuation voltage is composed of an AC signal with a DC offset $V_d = V_{AC}\cos(\omega t) + V_{DC}$. The force is then:

$$F(\omega) = -\frac{A\varepsilon_0}{2g^2}\left(\underbrace{\frac{V_{AC}^2}{2}cos(2\omega t)}_{2\omega} + \underbrace{2V_{DC}V_{AC}\,cos(\omega t)}_{\omega} + \underbrace{V_{DC}^2 + \frac{V_{AC}^2}{2}}_{DC}\right) \qquad \textbf{(I.42)}$$

Thus, the frequency spectrum of the actuation force is composed of DC, 1ω and 2ω.

If $V_{DC} = 0$, we operate with a so called 2ω actuation scheme: the 1ω component is null and the device resonance at ω_0 is actuated with an voltage at $\frac{\omega_0}{2}$ with a force magnitude proportional to $\frac{A\varepsilon_0}{2g^2}\frac{V_{AC}^2}{2}$.

If $V_{DC} \neq 0$, we drive the device with a 1ω actuation scheme: V_d is set at $\omega_0$and the applied force is proportional to $\frac{A\varepsilon_0 2V_{DC}V_{AC}}{2g^2}$.

We note here that 2ω actuation has a quadratic dependence on V_{AC} while 1ω actuation has a linear dependence with $V_{DC}V_{AC}$. 2ω actuation provides lower background signal as cross-talk is quasi absent for the actuation signal is at $\frac{\omega_0}{2}$ while the polarization signal in the piezoresistive nanogauges is at ω_0. 1ω actuation enables stronger actuation than 2ω as RF sources generally struggle to deliver high voltages at high frequency while DC voltage is very accessible. Operation in environment with viscous damping such as air requires 1ω actuation.

Applying an electrostatic force on a mechanical resonator leads to a downward shift of its resonance frequency caused by the second order (spring softening). Developing equation (I.40) to the second order we get:

$$F \cong -\frac{A\varepsilon_0}{2g^2}\, V_d^2 \left(1 + 2\frac{y}{g}\right) \quad (2nd\ order) \qquad \textbf{(I.43)}$$

Inserting this force in (I.26), we obtain:

$$m\ddot{y} + c\dot{y} + ky = -\frac{A\varepsilon_0}{2g^2}\, V_d^2 \left(1 + 2\frac{y}{g}\right) \qquad \textbf{(I.44)}$$

This can be rearranged as:

$$m\ddot{y} + c\dot{y} + \left(k - \frac{A\varepsilon_0}{g^3}\, V_d^2\right) y = \frac{A\varepsilon_0}{2g^2}\, V_d^2 \qquad \textbf{(I.45)}$$

Thus the second order component of the force induces negative stiffness in the resonant system. It is observed for small gap devices and for large applied drive voltage. Negative stiffness can be used as a practical tool to tune the resonance frequency or simulate frequency jumps with DC steps.

7.2. Motion transduction

As the resonator is driven into oscillation, its motion in the y axis generates compression on one nanogauge and dilation on the other one. Applying strain on a piezoresistive conductor modulates its resistivity as a result of two effects: geometrical deformation and electrical carrier mobility modulation. The geometrical effect, exploited in metallic piezoresistors, results from the definition of resistance $R = \rho\frac{L}{t.w}$: variation of dimensions translates to resistance variation. The second effect, dominant in semiconductor piezoresistors, is based on the strain induced deformation of the atomic lattice that affects bandgaps causing a redistribution of the carriers between conducting valleys with different carrier mobility. Piezoresistive effects occurring in the nanogauges of our devices is extensively studied here [50]. A bias current is applied on the nanogauges to read the resistance variations.

The piezoresistive nanogauges are disposed in a bridge configuration for background cancellation. The bias current is either applied to the nanogauges ends with a 180° phase shift and the output signal is read at the center of the bridge or applied at the center of the bridge and the output signal is read by an operational amplifier subtracting the signal coming out of the nanogauges. This scheme cancels out-of-plane resonance signals and amplifies in-plane resonance signals. To circumvent signal attenuation caused by parasitic capacitances in the circuitry, the NEMS output is downmixed at several 10 kHz by a heterodyne scheme and read by a Lock-In Amplifier (LIA) [4].

In this case, beam motion induces resistance modulation $\delta r = \frac{\Delta R}{R}\cos(\omega_0 t)$ while a bias current $I = I_0 \cos((\omega_0 - \Delta\omega)t)$ is applied on the nanogauges. Downmixing occurs in the nanogauges, generating an output voltage:

$$V_0 = \frac{1}{2}\frac{\Delta R}{R} I_0 \left[\cos(\Delta\omega t) + \cos\left((2\omega_0 - \Delta\omega)t\right)\right] \qquad \textbf{(I.46)}$$

The resistance variation, initially modulated at ω_0 (a few tens of MHz), is now carried by a signal at a chosen $\Delta\omega$ (a few tens of kHz), weakly attenuated by parasitic capacitances of the circuitry. The component modulated at $(2\omega_0 - \Delta\omega)$, if not attenuated, is filtered out by the low pass filter (LPF) of the LIA.

The device can be modeled by a simple electrical representation:

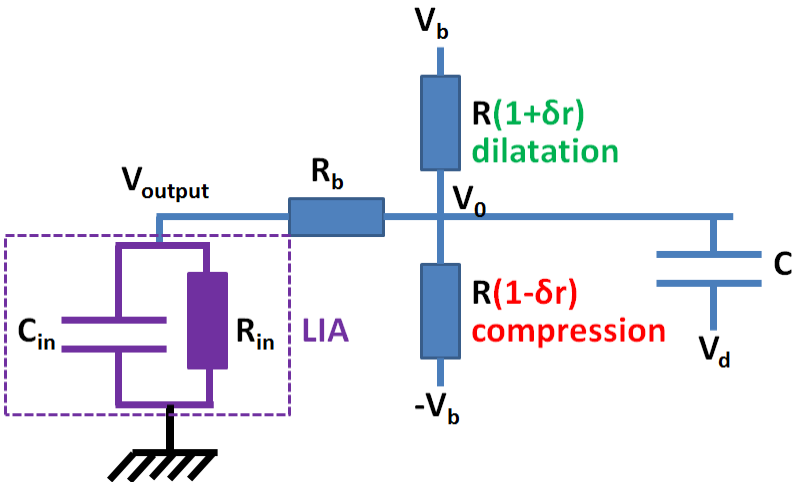

Fig. I.22: Electrical model of single resonant NEMS. Nanogauges resistances are modeled by R while Rb is the resistance from the Bias pad to the middle of the nanogauge bridge. A capacitor models the electrostatic actuation. δr is the piezoresistive resistance variation. The input impedance of the LIA is modeled by a resistance and a capacitor in parallel.

The LIA input impedance is $Z_{in} = \left(\frac{1}{R_{in}} + jC_{in}\omega\right)^{-1}$.

For the configuration where 180° dephased signals are applied at both end of the nanogauges, the voltage at the middle of the bridge is obtained with Millman's theorem:

$$V_0 = \frac{V_b \delta r}{1 + \frac{R}{2(Z_{in} + R_b)}} \quad \textbf{(I.47)}$$

where V_0 is the voltage at the middle of the nanogauge bridge, V_b the polarization voltage, R the nanogauge nominal resistance and δr the relative resistance variation in a nanogauge subjected to mechanical strain. We considered here that the current leaking through drive capacitance can be neglected.

The output voltage is then:

$$V_{output} = \frac{V_b \delta r}{1 + \frac{R_b}{Z_{in}} + \frac{R}{2Z_{in}}} \quad \textbf{(I.48)}$$

In the ideal case with infinite LIA input impedance we have:

$$V_{output} = V_b \times \delta r \quad \textbf{(I.49)}$$

The output voltage is proportional to the resistance variation and applied polarization V_b. Given its modulation at $\Delta\omega$, a LIA is used to detect at this given frequency. A LIA measurement requires a reference signal that will be used to determine the in-phase and out-of-phase components of the input signal. Usually, the drive signal of the studied system (here the NEMS) is used as a reference for the output of the system. However, this cannot be done with the downmixing configuration as the output is a low frequency signal ($\Delta\omega$) whereas the input is at high frequency (ω or $\omega/2$). This is why we use a mixer and a LPF (Low Pass Filter) to generate a reference for the LIA. The complete electrical setup for a 1ω actuation scheme and 180° dephased polarization signals applied at both end of the nanogauges is shown in Fig. I.23.

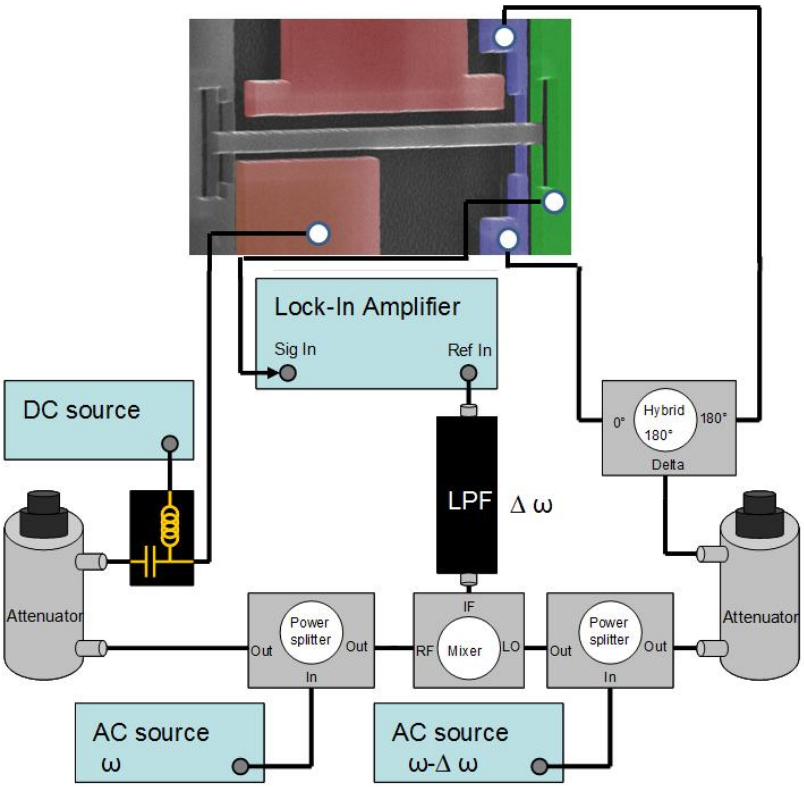

Fig. I.23: Downmixing setup using an AC+DC actuation: a bias tee is added to generate an AC+DC drive voltage enabling the 1f mode.

The Lock-in Amplifier plays an important role in the detection of the output signal and it needs to be finely tuned. An internal oscillator is locked onto the Δω reference signal that we built by mixing our two AC source. The oscillator is used by the LIA to detect the Δω component of the LIA input signal. Detection of a given spectral component can be simply made by signal mixing (multiplication) and low pass filtering: the reference internal oscillator signal $Ref\cos(\Delta\omega t)$ is multiplied with the input $A\cos(\Delta\omega t+\varphi)$, φ accounting for phase difference between the two signals, which yields:

$$V_{mix}=\frac{1}{2}A.Ref[\cos(\varphi)+\cos(2\Delta\omega t+\varphi)] \qquad \textbf{(I.50)}$$

An important parameter is the LIA low pass filter time constant, denoted as τ_{LIA}, that needs to be chosen high enough to rule out the $2\Delta\omega$ component. For instance, for $\frac{\Delta\omega}{2\pi}=50kHz$, τ_{LIA} should be chosen above 100µs to place to LPF cut-off frequency below 10kHz and filter the component $\frac{2\Delta\omega}{2\pi}=100kHz$. After filtering, we obtain a DC signal $X=\frac{1}{2}A.Ref.\cos(\varphi)$. The very same procedure is simultaneously applied with a 90° phase shifted reference to obtain a DC signal $Y=\frac{1}{2}A.Ref.\sin(\varphi)$. X is called the in-phase component of the signal (in phase with the reference) while Y denotes the quadrature signal. Magnitude and phase of the input signal can be extracted:

$$A = \frac{2}{Ref}\sqrt{X^2 + Y^2}$$

$$\varphi = tan^{-1}\left(\frac{Y}{X}\right) \quad \textbf{(I.51)}$$

7.3. Device used for mass sensing & characterization benches

As mentioned in the previous section, cantilevers can be driven at much larger amplitudes than doubly-clamped beams before reaching the non-linear regime. Cantilevers are preferred for regular mass sensing applications where the analyte is deposited uniformly on the sensor such as concentration gas sensing. However, for single molecule mass sensing, monitoring a minimum of three resonant modes is required to extract the particle position needed to retrieve its mass [44]. Doubly-clamped beams, on the other hand, can resolve the position and mass of the adsorbed particles using only the frequency shifts of the first two modes thanks to their longitudinal symmetry. The method to do so is detailed in Chapter III. As a consequence, cantilevers are specifically designed as gas sensors operating in air environment while doubly-clamped beams are designed for NEMS-MS in vacuum.

Estimation of gas sensing performances has been published here [51]. For a cantilever dimensioned as 3.2µm*300nm*160nm (length, width and thickness respectively) and resonating around 42Mhz, the mass sensitivity is 17zg/Hz. With a frequency noise floor $\sigma(\Delta f)$ measured around 40Hz ($\sigma\left(\frac{\Delta f}{f}\right) = 9.5 \times 10^{-7}$) a mass resolution of 700zg is estimated.

The doubly-clamped beams that were used for NEMS-MS experiments are all 300nm wide and 160nm thick unless stated otherwise. A schematic of the design is presented in Fig. I.24.

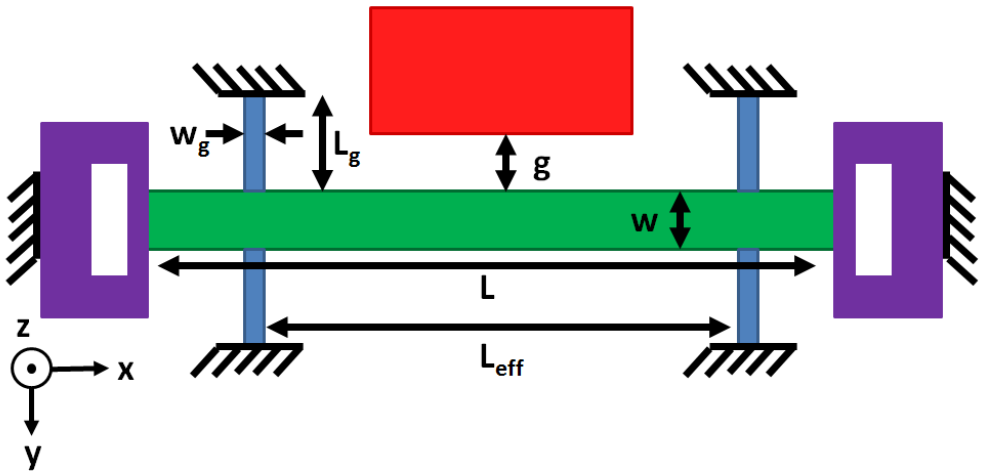

Fig. I.24: Schematic of the resonant doubly-clamped structure. The resonant flexural beam is in green, the electrostatic actuation electrode in red, the beam anchors are in purple and the piezoresistive nanogauges are in blue.

Dimensions of a typical device are given below.

Dimension	L	L_{eff}	w	g	L_g	w_g
Value	10µm	9.2µm	300nm	200nm	400nm	80nm

Table I.6: Typical dimensions of a doubly clamped beam.

The beam anchors are designed with suspension springs that allow axial elongation of the beam while in transverse vibration, pushing the onset of nonlinearity to higher displacement values. Nevertheless, for modeling considerations, they will be considered as regular doubly clamped beams in this manuscript: We define L_{eff} as the beam length between the nanogauges. FEM simulations showed that negligible beam displacement is found between the nanogauges and the resonant beam anchors. Therefore, we only consider the resonant mass between the two nanogauges. The resonant effective mass is evaluated around 0.4pg for the dimensions reported in Table I.6. Equation (I.6) provides the 1 sigma mass resolution for a given relative frequency noise. [4] reported a relative frequency noise $\sigma_{\delta f} = 1 \times 10^{-6}$ at 1s integration time for a similar device. This would lead here to a 480kDa mass resolution. Nevertheless, the actual frequency stability of these devices needs to be properly characterized to deduce their mass resolution.

In the framework of single particle mass sensing in vacuum, almost all device characterizations were performed in vacuum (~$10^{-5} mbar$). A prober station under vacuum enables quick characterization of devices for selection while a vacuum chamber can receive chips wirebonded on a PCB Fig. I.25.

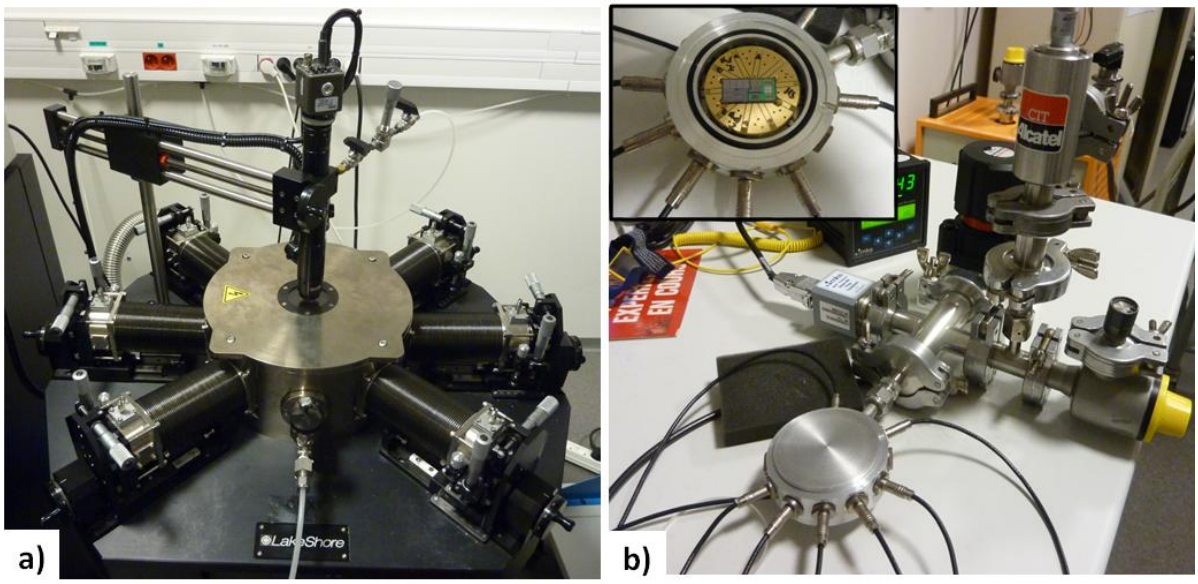

Fig. I.25: Probe station under vacuum for fast selection of devices of interest (a) and vacuum chamber bench (b) used to characterize the selected devices, wirebonded on a PCB. The chip and the PCB placed in the chamber are shown in the inset.

8. Conclusion

In this chapter, we presented the ultimate goal of this work, that is propose a new paradigm of mass spectrometry based on arrays of resonant nanostructures for biomolecules mass spectrometry applications. NEMS-based MS operates on larger mass ranges than conventional ion-MS and directly measures the molecule inertial mass instead of a m/z ratio which leads to simple spectra and potential neutral molecule mass spectrometry. The Alliance developed devices with outstanding transduction efficiencies for that purpose and one of the main challenges is the identification of the noise limiting our mass resolution. Chapter II presents an experimental study of this noise.

BIBLIOGRAPHY

[1] "http://www.nanovlsi.com/." .

[2] E. Colinet, L. Duraffourg, S. Labarthe, S. Hentz, P. Robert, and P. Andreucci, "Self-oscillation conditions of a resonant nanoelectromechanical mass sensor," *J. Appl. Phys.*, vol. 105, no. 12, p. 124908, 2009.

[3] P. Andreucci, "Very Large Scale Integration (VLSI) of NEMS based on top down approaches, Nanomechanics for NEMS : Scientific and technological issues," in *an international state-of-the-art workshop by OMNT 26 & 27 June 2008, Grenoble-Minatec, France www.nanovlsi.org*.

[4] E. Mile, G. Jourdan, I. Bargatin, S. Labarthe, C. Marcoux, P. Andreucci, S. Hentz, C. Kharrat, E. Colinet, and L. Duraffourg, "In-plane nanoelectromechanical resonators based on silicon nanowire piezoresistive detection.," *Nanotechnology*, vol. 21, no. 16, p. 165504, Apr. 2010.

[5] S. Labarthe, "Conception et modélisation d'un nanocapteur de masse par détection piezorésistive," 2010.

[6] E. Mile, "Systèmes électromécaniques nanométriques à base de nanofils de silicium et nanotubes de carbone," 2010.

[7] C. Kharrat, "Application des techniques de contrôle sur les réseaux de micro et nanostructures," 2009.

[8] R. Pérénon, "Traitement de l'information en mode comptage appliqué aux détecteurs spectrométriques," 2013.

[9] R. Pérenon, E. Sage, A. Mohammad-Djafari, L. Duraffourg, S. Hentz, A. Brenac, R. Morel, and P. Grangeat, "Bayesian inversion of multi-mode mass spectrometry Signal," in *The 2012 European Signal Processing Conference*, 2012.

[10] R. Pérenon, A. Mohammad-Djafari, E. Sage, L. Duraffourg, S. Hentz, A. Brenac, R. Morel, and P. Grangeat, "MCMC-based inversion algorithm dedicated to NEMS Mass-Spectrometry," in *32nd International Workshop on Bayesian Inference and Maximum Entropy Methods in Science and Engineering*, 2012.

[11] C. Dass, *Fundamentals of contemporary mass spectrometry*. Chichester: John Wiley & Sons, 2007.

[12] J. B. Fenn, M. Mann, C. K. Meng, S. F. Wong, and C. M. Whitehouse, “Electrospray Ionization for Mass Spectrometry of Large Biomolecules,” *Science (80-.).*, vol. 246, no. 4926, pp. 64–71, 1989.

[13] M. Wilm, “Principle of Electropray Ionization,” *Mol. Cell. Proteomics*, vol. 10, pp. 1–8, 2011.

[14] P. Kebarle and U. H. Verkerk, “ELECTROSPRAY: FROM IONS IN SOLUTION TON IONS IN THE GAS PHASE, WHAT WE KNOW NOW,” *Mass Spectrom. Rev.*, vol. 28, no. 6, pp. 898–917, 2009.

[15] M. Karas, D. Bachmann, U. Bahr, and F. Hillenkamp, “Matrix-assisted ultraviolet laser desoprtion of non-volatile compounds,” *J. Mass Spectrom. Ion Process.*, vol. 78, pp. 53–68, 1987.

[16] “http://masspec.scripps.edu/mshistory/whatisms_details.php#.” .

[17] M. M. Wolff and W. E. Stephens, “A Pulsed Mass Spectrometer with Time Dispersion,” *Rev. Sci. Instrum.*, vol. 24, p. 616, 2004.

[18] V. H. Dibeler, D. F. Eggers, M. Wolff, W. E. Stephens, and S. S. Friedland, “Time-of-Flight Mass Spectrometer with Improved Resolution,” *Rev. Sci. Instrum.*, vol. 26, no. 12, 1955.

[19] M. B. Comisarow and A. G. Marshall, “Fourier transform ion cyclotron resonance spectroscopy,” *J. Mass Spectrom.*, vol. 31, no. 6, pp. 586–587, 1996.

[20] W. Paul and H. Steinwedel, “APPARATUS FOR SEPARATING CHARGED PARTICLES OF DIFFERENT SPECIFIC CHARGES,” 1960.

[21] G. Siuzdak, *Mass Spectrometry for biotechnology*. Academic Press, 1996.

[22] M. B. Miller and Y. Tang, “Basic Concepts of Microarrays and Potential Applications in Clinical Microbiology,” *Clin. Microbiol. Rev.*, vol. 22, no. 4, p. 611, 2009.

[23] J. L. P. Benesch, B. T. Ruotolo, D. A. Simmons, and C. V. Robinson, “Protein Complexes in the Gas Phase: Technology for Structural Genomics and Proteomics,” *Chem. Rev.*, vol. 107, pp. 3544–3567, 2007.

[24] T. Wehr, “Top-Down versus Bottom-Up Approaches in Proteomics,” *LCGC NORTH Am.*, vol. 24, no. 9, 2006.

[25] K. Breuker and F. W. McLaffertey, “Stepwise evoluation of protein native structure with electrospray into the gas phase, 10-12 to 10+02s,” *PNAS*, vol. 105, no. 47, pp. 18145–18152, 2008.

[26] H. Zhang, W. Cui, M. Gross, and R. Blankenship, “Native mass spectrometry of photosynthetic pigment–protein complexes,” *FEBS Lett.*, pp. 1–9, 2013.

[27] R. van den Heuvel and A. J. Heck, “Native protein mass spectrometry: from intact oligomers to functional machineries,” *Curr. Opin. Chem. Biol.*, vol. 8, pp. 519–526, 2004.

[28] N. L. Kelleher, M. W. Senko, M. M. Siegel, and F. W. McLafferty, “Unit resolution mass spectra of 112 kDa molecules with 3 Da accuracy,” *J. Am. Soc. Mass Spectrom.*, vol. 8, no. 4, pp. 380–383, 1997.

[29] X. Han, M. Jin, K. Breuker, and F. W. McLafferty, “Extending Top-Down Mass Spectrometry to Proteins with Masses Greater Than 200 Kilodaltons,” *Science (80-.).*, vol. 314, p. 109, 2006.

[30] N. M. Karabacak, L. Li, A. Tiwari, L. J. Hayward, P. Hong, M. L. Easterling, and J. N. Agar, “Sensitive and Specific Identification of Wild Type and Variant Proteins from 8 to 669 kDa Using Top-down Mass Spectrometry,” *Mol. Cell. proteomics*, vol. 8, no. 4, pp. 846–856, 2009.

[31] E. van Duijn, “Current limitations in native mass spectrometry based structural biology,” *J. Am. Soc. Mass Spectrom.*, vol. 21, no. 6, pp. 971–978, 2010.

[32] Y. Zhong, S. Hyung, and B. Ruotolo, “Ion mobility–mass spectrometry for structural proteomics,” *Expert Rev. Proteomics*, vol. 9, no. 1, pp. 47–58, 2012.

[33] J. Homola, “Surface Plasmon Resonance Sensors for Detection of Chemical and Biological Species,” *Chem. Rev.*, vol. 108, pp. 462–493, 2008.

[34] S. Fanget, S. Hentz, P. Puget, J. Arcamone, M. Matheron, E. Colinet, P. Andreucci, L. Duraffourg, E. Myers, and M. L. Roukes, “Gas sensors based on gravimetric detection—A review,” *Sensors Actuators B Chem.*, vol. 160, pp. 804–821, 2011.

[35] J. Chaste, A. Eichler, J. Moser, G. Cballos, R. Rurali, and A. Bachtold, “A nanomechanical mass sensor with yoctogram resolution,” *Nat. Nanotechnol.*, vol. 7, pp. 301–304, 2012.

[36] J. S. Page, R. T. Kelly, K. Tang, and R. D. Smith, “Ionization and Transmission Efficiency in an Electrospray Ionization-Mass Spectrometry Interface,” *Am. Soc. Mass Spectrom.*, vol. 18, no. 9, pp. 1582–1590, 2007.

[37] A. K. Naik, M. S. Hanay, W. K. Hiebert, X. L. Feng, and M. L. Roukes, “Towards single-molecule nanomechanical mass spectrometry,” *Nat. Nanotechnol.*, vol. 4, no. June, p. 445, 2009.

[38] K. L. Ekinci, X. M. H. Huang, and M. L. Roukes, “Ultrasensitive nanoelectromechanical mass detection,” *Appl. Phys. Lett.*, vol. 84, no. 22, p. 4469, 2004.

[39] Y. T. Yang, C. Callegari, X. L. Feng, K. L. Ekinci, and M. L. Roukes, “Zeptogram-scale nanomechanical mass sensing.,” *Nano Lett.*, vol. 6, no. 4, pp. 583–6, Apr. 2006.

[40] H.-Y. Chiu, P. Hung, H. W. C. Postma, and M. Bockrath, “Atomic-scale mass sensing using carbon nanotube resonators.,” *Nano Lett.*, vol. 8, no. 12, pp. 4342–6, Dec. 2008.

[41] K. Jensen, K. Kim, and A. Zettl, “An atomic-resolution nanomechanical mass sensor.,” *Nat. Nanotechnol.*, vol. 3, pp. 533–537, Sep. 2008.

[42] J.-C. Charlier, X. Blase, and S. Roche, “Electronic and transport properties of nanotube,” *Rev. Mod. Phys.*, vol. 79, no. 2, pp. 677–732, 2007.

[43] T. Filleter, R. Bernal, S. Li, and H. D. Espinosa, “Ultrahigh Strength and Stiffness in Cross-Linked Hierarchical Carbon Nanotube Bundles,” *Adv. Mater.*, vol. 23, no. 25, pp. 2855–2860, 2011.

[44] S. Dohn, W. Svendsen, A. Boisen, and O. Hansen, “Mass and position determination of attached particles on cantilever based mass sensors.,” *Rev. Sci. Instrum.*, vol. 78, no. 10, p. 103303, Oct. 2007.

[45] S. Dohn, S. Schmid, F. Amiot, and A. Boisen, “Position and mass determination of multiple particles using cantilever based mass sensors,” *Appl. Phys. Lett.*, vol. 97, p. 044103, 2010.

[46] M. S. Hanay, S. Kelber, A. K. Naik, D. Chi, S. Hentz, E. C. Bullard, E. Colinet, L. Duraffourg, and M. L. Roukes, “Single protein nanomechanical mass spectrometry in real time,” *Nat. Nanotechnol.*, vol. 7, pp. 602–608, 2012.

[47] S. Timoshenko, D. Young, and J. W. Weaver, *Vibration problems in engineering, Wiley, New York*. 1974.

[48] N. Kacem, “Nonlinear dynamics of m&nems resonant sensors: design strategies for performance enhancement,” 2010.

[49] M. Li, H. X. Tang, and M. L. Roukes, “Ultra-sensitive NEMS-based cantilevers for sensing, scanned probe and very high-frequency applications.,” *Nat. Nanotechnol.*, vol. 2, no. 2, pp. 114–20, Feb. 2007.

[50] S. Labarthe, “Conception et modélisation d’un nanocapteur de masse par détection piézoresistive,” 2010.

[51] J. Arcamone, A. Niel, V. Gouttenoire, M. Petitjean, N. David, R. Barattin, M. Matheron, F. Ricoul, T. Bordy, H. Blanc, J. Ruellan, D. Mercier, N. Pereira-Rodrigues, G. Costa, V. Agache, S. Hentz, J. Gabriel, F. Baleras, C. Marcoux, T. Ernst, L. Duraffourg, E. Colinet, E. B. Myers, M. L. Roukes, P. Andreucci, E. Ollier, and P. Puget, “VLSI silicon multi-gas analyzer coupling gas chromatography and NEMS detectors,” in *International Electron Devices Meeting (IEDM)*, 2011, pp. 29.3.1–29.3.4.

Chapter II: Study of nanomechanical sensors mass resolution

This Chapter presents an experimental study of the mass resolution of our sensor. First, we show the importance of the resonator's frequency stability in the mass resolution and demonstrate that thermomechanical noise should limit our frequency stability. After computation of the expected frequency stability, we proceed to experimental validation. However, an excess noise of unknown origin is encountered. We present the experiments that investigate the nature of this source and propose a first hypothesis on the noise origin, laying the base of future researches.

1. Theoretical nanomechanical mass sensing resolution

1.1. Expression of the mass resolution for resonant systems limited by additive white noise

We have seen in Chapter I that the mass of punctual particle landing of the resonator is written as:

$$\Delta m = \frac{\Delta f}{f}\frac{2M_{eff}}{\varphi(x)^2} \qquad \textbf{(II.1)}$$

where is $\varphi(x)$ the normalized mode shape, M_{eff} the resonator effective mass and $\frac{\Delta f}{f}$ the observed relative frequency shift.

Thus, the minimum measurable mass depends on the ability to resolve a mass induced frequency shift from the resonator frequency fluctuations. The mass resolution (σ_m) at 1-sigma deviation can then be defined as:

$$\sigma_{\mathrm{m}} = \sigma_{\delta f}(\tau)\frac{2M_{eff}}{\varphi(x)^2} \qquad \textbf{(II.2)}$$

where $\sigma_{\delta f}(\tau)$ is the relative frequency deviation at a given integration time τ.

A wide range of noise processes can affect the measurement of a resonators' relative frequency and they have been thoroughly studied as they impose the sensing limit of detection of the physical quantities to be measured [1]. Their analysis in the framework of mass sensing

demonstrated theoretical achievable mass resolutions down to the Dalton ($1Da = 1.66 \times 10^{-27} kg$) [2] before experimental demonstration [3] and their influence within a PLL scheme has been analyzed [4]. Noise in the measurement of the relative frequency can be affected by external noise like electronics noise or basic noises arising from the device such as:

- Johnson noise from the nanogauges
- 1/f resistance noise from nanogauges
- Thermomechanical noise from the resonator Brownian motion

Other source of noises can be temperature fluctuations and adsorption-desorption.

For a system resonating at f_0 dominated by additive white noise, the angular frequency spectral density is given by Robin's formula [5]:

$$S_f(f) = \left(\frac{f_0}{2Q}\right)^2 \frac{S_n(f_0)}{P_0} \quad \textbf{(II.3)}$$

where ω_0 is the angular resonance frequency, Q the quality factor, $S_n(f)$ the noise spectral density and P_0 the carrier power.

The relative frequency deviation can then be estimated as:

$$\sigma_{\delta f} = \frac{1}{2Q} \frac{S_n^{1/2}(f_0)\sqrt{B}}{A_0} = \frac{1}{2Q.SNR} \quad \textbf{(II.4)}$$

where B is the measurement bandwidth, A_0 the measured output signal and SNR the signal to noise ratio. SNR depends on the bandwidth as $SNR = \frac{A_0}{S_n^{1/2}(f_0)\sqrt{B}}$.

This expression can be simply derived from the effect of white noise on the transfer function of the resonator phase close to resonance as explained in Appendix A. It relies on the relationship between phase and frequency close to resonance:

$$\frac{\Delta f}{f} = -\frac{\Delta \varphi}{2Q} \quad \textbf{(II.5)}$$

where $\Delta\varphi$ is the phase deviation and Δf the frequency deviation.

For a punctual particle landing at the maximum sensitivity of the response mode ($\varphi(x) = 1$), the mass sensing resolution can then be expressed as:

$$\sigma_m = \frac{M_{eff}}{Q} \frac{S_n(f_0)\sqrt{B}}{A_0} = \frac{M_{eff}}{Q.SNR} \quad \textbf{(II.6)}$$

This expression has been the starting point to direct the effort carried out in the last decade to decrease the mass resolution of nanomechanical mass sensors: engineering of

smaller (hence lighter) devices with a high quality factor and high SNR (see Chapter I). For the latter, efficient transduction means were developed to produce important output signals for optimum SNR [6].

1.2. Basic noise sources and effect on SNR

The basic noise sources identified in mechanical resonators were investigated to identify those who limit the mass resolution.

1/f-noise from resistors

Motion transduction of our resonator is performed thanks to piezorestive nanogauges disposed in bridge configuration. Generally 1/f noise generated by resistance fluctuations is the main noise source in piezoresistors. Yet, our devices are weakly affected as we operate at relatively high frequencies (≈20MHz). The PSD of the 1/f noise in a resistor can be described using Hooges' empirical model ([4-5]):

$$S_H(f) = \frac{HV_{bias}^2}{N|f - f_{bias}|} \quad [V^2/Hz] \qquad \textbf{(II.7)}$$

where N is the total number of carriers within the gauge, V_{bias} and f_{bias} the voltage and frequency of the signal applied on the resistor while H denotes Hooge's constant.

Dr. Ervin Mile performed extractions of Hooge's constant from the nanogauges used for nanomechanical motion transduction of our device ([6]). For nanogauges with dimensions of 500nm*80nm*160nm (length, width and thickness respectively), H was found to be close to 10^{-6} which yielded an estimated noise of a few nv/√Hz at 20MHz quasi negligible with respect to other sources of noise (see below). The nanogauges found in the devices used in this thesis are 80nm wide and 160nm thick while their lengths can vary from 500nm to 300nm i.e. a maximum ratio of only 1.6 with respect to the nanogauges studied by Dr Mile. Therefore, we considered the 1/f-noise from nanogauges as negligible for 300nm long nanogauges as well. While 1/f-noise is usually dominant at low frequencies, its influence decreases with increasing frequencies until the white Johnson-Nyquist noise floor is reached.

Johnson-Nyquist noise

Johnson-Nyquist noise arises from thermal agitation of electrical carriers in electrical conductors and depends on resistance R and temperature T. It is a white noise whose PSD is written as:

$$S_J = 4k_bTR \quad [V^2/Hz] \qquad \textbf{(II.8)}$$

where k_b is Boltzmann's constant

Johnson-Nyquist is an important source of noise for our resonators when weakly driven. Johnson noise is minimized with lower temperatures or lower device equivalent

resistances attained with higher doping levels or parallel architectures (array configuration, see Chapter IV). For a doping level of $2 \times 10^{-19} cm^{-3}$, our devices equivalent resistances are found around 12kΩ yielding a Johnson noise of $14.1 nV/\sqrt{Hz}$.

Thermomechanical noise

Thermomechanical noise comes from the coupling of the resonator with its environment by a stochastic force accounting for its thermalization. It derives from the theorem of fluctuation-dissipation that states that any system dissipating energy is noisy. $S_f(\omega)$ is defined as the thermomechanical force spectral density with a white spectrum being equal to ([2]):

$$S_f(\omega) = \frac{4 M_{eff} \omega_0 k_b T}{Q} \qquad \textbf{(II.9)}$$

The spectral density of displacement y of the beam is given by:

$$S_y(\omega) = \frac{1}{M_{eff}^2} \frac{S_f(\omega)}{(\omega^2 - {\omega_0}^2)^2 + \left(\frac{\omega \omega_0}{Q}\right)^2} \qquad \textbf{(II.10)}$$

The resonator acts as a band-pass filter and only the force noise within the resonator bandwidth will actually affect the system. Given a resonator transfer function $H(\omega)$ the spectral density of displacement y around resonance is [9]:

$$S_y(\omega) = \frac{4 k_b T Q}{M_{eff {\omega_0}^3}} \qquad \textbf{(II.11)}$$

Displacement noise is minimized with low dissipating resonators i.e. with a high quality factor Q, low mass and low temperature and high resonance frequency. Displacement noise is translated to signal noise via piezoresistive detection. It is interesting to note here that cooling the device has the potential to decrease both Johnson-Nyquist and thermomechanical noise.

Dr Ervin Mile measured the thermomechanical noise of a cantilever beam of dimensions 5µm*300nm*160nm with a doping level of $1 \times 10^{-19} cm^{-3}$, a Q of 5000 and an effective mass of 140fg. The thermomechanical noise was evaluated around $25 nV/\sqrt{Hz}$, beyond the Johnson noise measured at $11.2 nV/\sqrt{Hz}$ [6]. Therefore, thermomechanical noise was identified as the limiting noise. A SNR up to 100dB for a 1Hz bandwidth was obtained which yielded a theoretical mass resolution of 0.28zg (170Da) according to equation (II.6) and a theoretical Allan Deviation of 1×10^{-9} for a 1s integration time according to equation (II.4). However the experimental Allan Deviation for a 1s integration time was found at 1.5×10^{-6}, orders of magnitude more important than expected. This frequency stability level corresponds to a actual mass resolution of 0.42ag (253kDa).

We decided to initiate an experimental study to apprehend the observed discrepancy as this unexplainably high frequency noise level degrades our mass resolution from hundreds of Da to hundreds of kDa. This is of critical importance as it prevents us from covering a mass range overlapping with mass ranges of traditional ion MS. A first step consisted in reproducing the thermomechanical noise measurements.

1.3. Thermomechanical noise measurement

We measured the thermomechanical noise of a cantilever resonator p-doped at $1.9\times10^{19}cm^{-3}$ with dimensions of 5µm*300nm*160nm (length, width and thickness respectively).

We employed the downmixing technique described by Bargatin *et al.* ([10]) where the polarization voltage of the nanogauges is swept across a bandwidth centered on the resonance frequency and no actuation voltage is applied. The LIA reference Δf is internal and set to 20kHz. When the polarization frequency f_{bias} is a few tens of kHz away from the nominal resonance frequency f_0 then the thermomechanical displacement is downmixed and the setup picks up the noise induced by Brownian motion of the resonator. Therefore, we expect noise detection at both $f_0 - f_{bias}$ and $f_0 + f_{bias}$. The setup scheme is show in Fig. II.1.

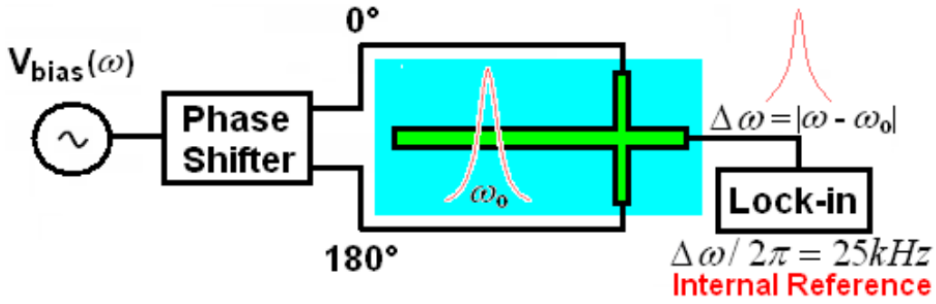

Fig. II.1: Thermomechanical noise measurement setup. Source: [11]

The obtained voltage noise is displayed in Fig. II.2.

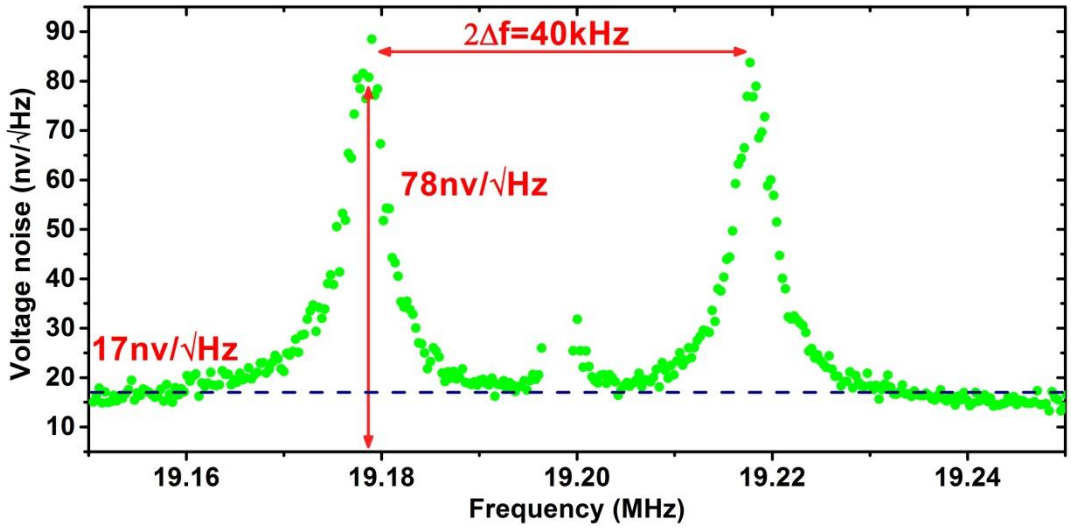

Fig. II.2: Thermomechanical noise spectral density obtained with the downmixing scheme. $V_{bias=3.67\,Vpp}$

Two peaks emerge at 19.1787MHz and 19.2187Hz: they are separated by $2\Delta f = 40kHz$ which yields a nominal resonance frequency at 19.1987MHz. What happened at $f_{bias} = f_0$ has not been explained yet.

We measure a noise floor $S_{floor}^{1/2} = 17nV/\sqrt{Hz}$ and deduce a thermomechanical peak $S_{th}^{1/2} = 76nV/\sqrt{Hz}$. The equivalent resistance of the device is estimated at 15kΩ yielding a Johnson noise $S_j^{1/2} = 15.7nV/\sqrt{Hz}$. Therefore the electronic noise is estimated as $S_{el}^{1/2} = \sqrt{S_d - S_j} = 6.3nV/\sqrt{Hz}$ which is close the 5nV/√Hz input noise specified by our LIA documentation.

Because the spectrum has to be swept point-per-point, the downmixing technique for thermomechanical noise detection can prove to be very long to acquire and is usually performed overnight. We have designed a different detection scheme based on spectral analysis to quickly study parametric variations: the LIA is replaced by an amplifier and an acquisition board. A Fast Fourier Transform (FFT) is applied on the acquired time-series to analyze the device output. The frequency difference Δf between f_{bias} and f_0 will determine where the thermomechanical peak will show up in the spectrum as shown in Fig. II.3.

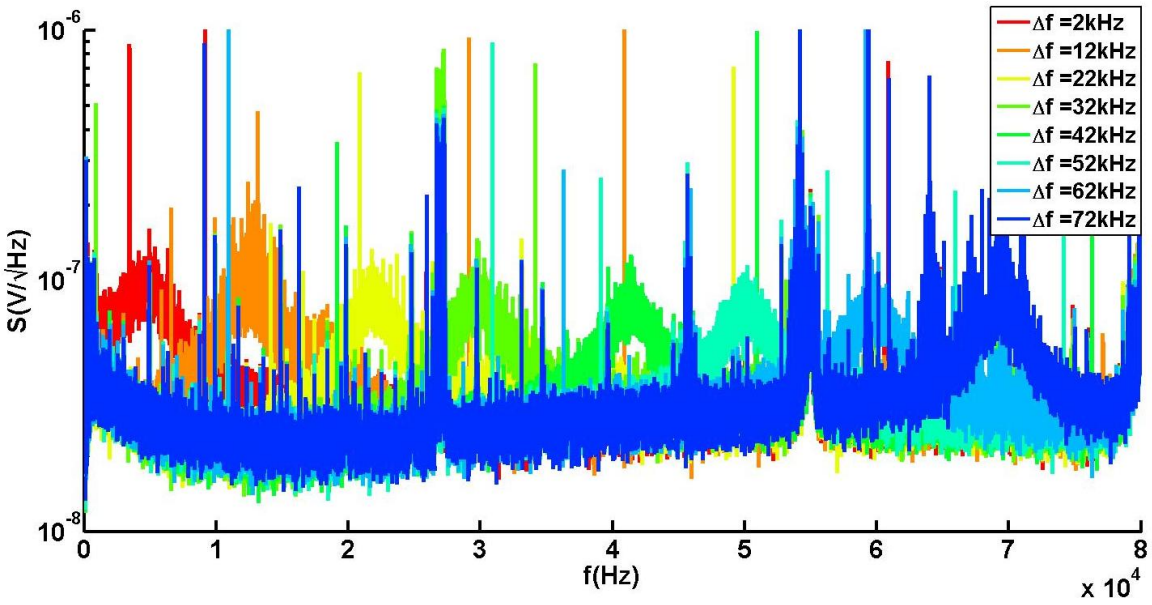

Fig. II.3: Illustration of the FFT technique with a spectrum of the device output with different polarization frequency f_{bias}. f_0 is estimated at 17.845MHz.

We note that that spectrum features some noise spikes that depend on the type of signal generator used for polarization. Further inquiries with different equipments can be made to build a setup with equipments noise as low as possible. Given that the acquisition takes a few minutes, we have the possibility to change parameters such as polarization voltage and observe the effects as shown in Fig. II.4.

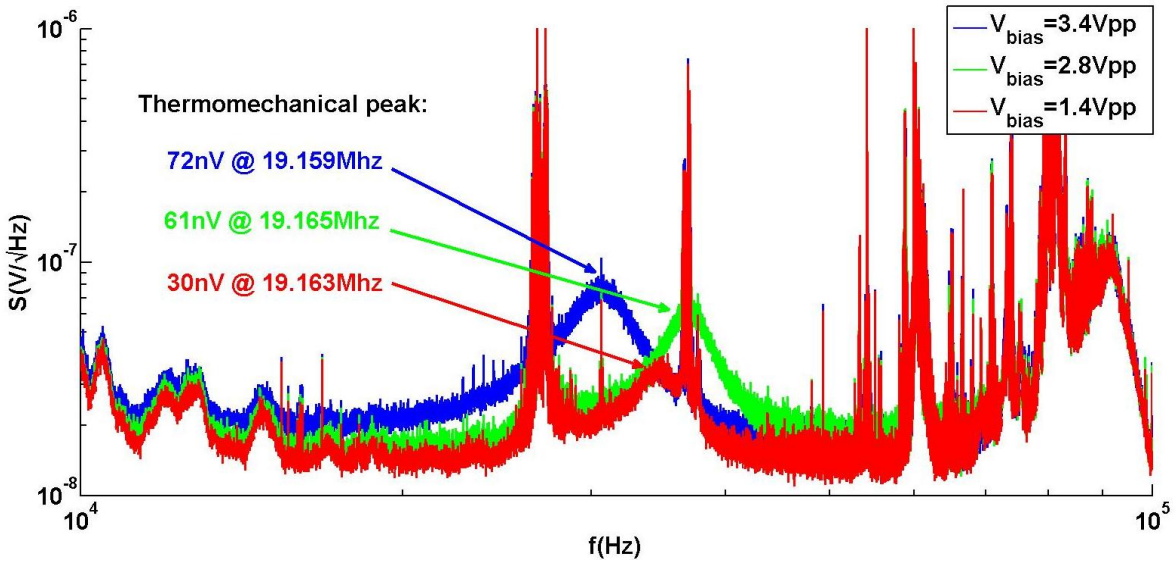

Fig. II.4: Spectrum of the device output with different polarization voltage V_{bias} . A voltage of 1.4/2.8/3.4 Vpp leads to a thermomechanical peak of 30/61/72 nV/√Hz respectively. Higher V_{bias} increases the temperature and induces a shift of the resonance frequency. Why this shift is not monotonous has not been explained yet.

A higher V_{bias} voltage means a larger transduced signal: we observe that an increase of the nanogauge polarization voltage is passed on to the thermomechanical peak. Similarly as [6] and provided noiseless transduction, the intrinsic thermomechanical noise will be limiting the mass resolution of our resonators.

For a system limited by white noise, we calculate S_{noise} as:

$$S_{noise} = \sqrt{\int_{f_0-\delta f/2}^{f_0+\delta f/2} S_n(f)\, df} \approx \sqrt{S_{th}(f_0) \times B} = S_n^{\frac{1}{2}}(f_0) \times \sqrt{B} \qquad \textbf{(II.12)}$$

where $B = \frac{1}{\tau}$ is the measurement bandwidth and $S_n^{\frac{1}{2}}(f_0)$ the voltage noise per $\sqrt{Hz}$ at f_0

We measured $S_n^{\frac{1}{2}}(f_0)$ around $50nV/\sqrt{Hz}$ while our output signals are generally in the mV order of magnitude. For a 1Hz bandwidth, we estimate a SNR of 86dB. For a measured Q=5200, we can expect frequency fluctuations down to 4.8×10^{-9} according to equation (II.4). We now proceed to experimental validation of this expected frequency fluctuation. While our devices design present a wide range of geometric variations and boundary conditions leading to different values of frequency fluctuations, we can assume similar orders of magnitudes as they only differ by their boundary conditions (cantilever or doubly-clamped beams) and their length. Therefore ADEVs in the 10^{-9} or 10^{-8} range are to be expected, yielding mass resolutions around hundreds of Daltons.

2. Experimental measurement of the frequency stability

The frequency stability of our resonators is acquired by monitoring the frequency resonance frequency of our device either in Open or Closed loop and applying analytical algorithm on these acquisitions to characterize the noise of our system

2.1. Analytical tools

We characterized the frequency fluctuations of our resonators with a statistical tool called the Allan Deviation (ADEV).

The Allan Deviation

The Allan Deviation, introduced by David W. Allan [12], is a well-known statistical tool mainly used in scientific domains such as frequency synthesis, crystal oscillators, resonators, atomic clocks, etc. for characterization of the frequency stability of the object of interest. Among other reasons, it was developed to compensate weaknesses of the standard deviation that does not converge for various noise sources [13]. The Allan deviation allows the separation of different noise sources and provides visualization of the signal deviation according to the instrument bandwidth, leading to the selection of the optimum system response time. In simple terms, the Allan Deviation is the quadratic mean of the frequency deviation between two successive frequencies:

$$\sigma_y(\tau) = \sqrt{\frac{1}{2(M-1)} \sum_{i=1}^{M-1} (\bar{y}_{i+1} - \bar{y}_i)^2} \qquad \textbf{(II.13)}$$

where M is the number of sample, τ the integration time and $\bar{y}_i$ the averaged fractional frequency.

Details of its computation are covered in Appendix B.

The Allan Deviation gives us an estimation of the frequency instability between two successive points at a given integration time. Hence it provides us a first evaluation of the minimum resolvable mass of our resonating sensors as well as the optimum bandwidth as illustrated in Fig. II.5. According to the aimed application, it guides us on the best trade-off on frequency stability and measurement speed (determined by the bandwidth).

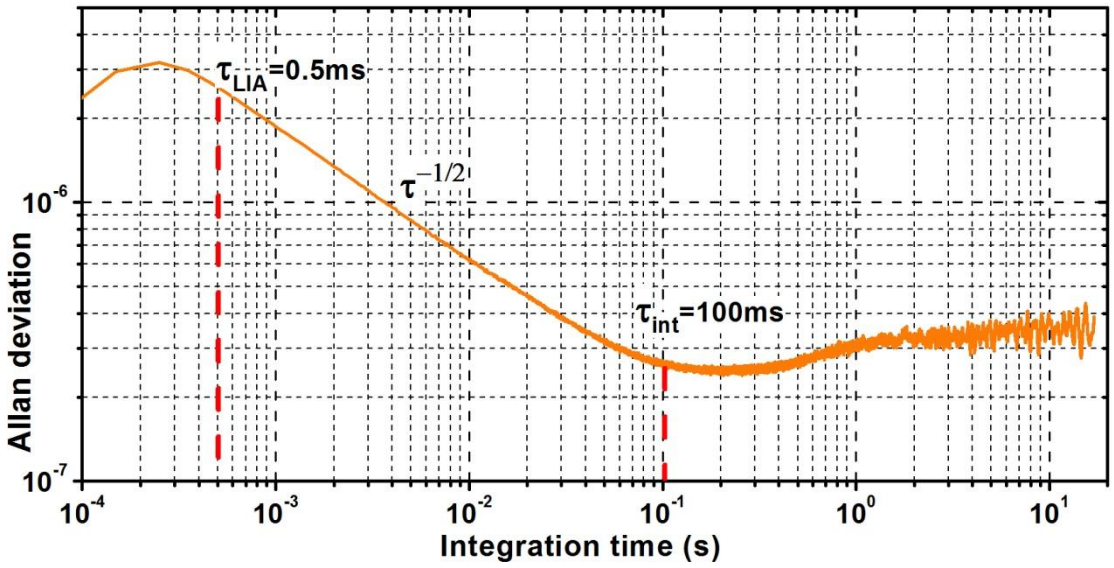

Fig. II.5: Typical Allan Deviation of a resonator limited by amplitude white noise ($\tau^{-1/2}$ slope). As the acquisition was performed with a $\tau_{LIA} = 0.5ms$, we may not pick an integration time below this value. As the integration time increases, the white noise limiting the frequency stability is averaged yielding a noise reduction up to a certain limit, here 100ms. Above 100ms, further integration of the signal does not provide any gain as another source of noise, other than white, dominates. Thus, an integration time of 100ms provides the fastest response time for best frequency stability (2.7×10^{-7}) available.

We observe that the white noise is identified here as a $\tau^{-1/2}$ slope on the ADEV curve [14]. Indeed, the Allan Deviation plots can be used to identify the different types of noise present in our acquisition as shown in Fig. II.6.

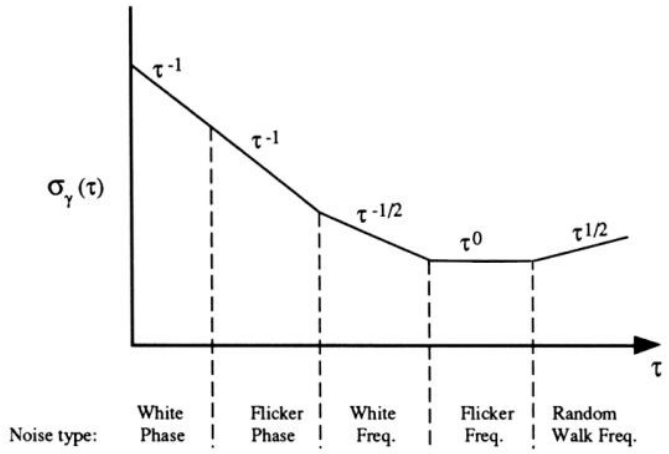

Fig. II.6: Type of noise highlighted by the Allan Deviation (source: [15]**) based on their τ dependence.**

As demonstrated later on, our acquisitions are mostly affected by white frequency noise, flicker frequency noise and frequency drifts. Frequency drifts are long timescale variations of the resonance frequency caused by environmental fluctuations (temperature, pressure, etc.) that generally appear at integration times above a few seconds.

Power Spectral Density (PSD)

The Allan deviation is meant to provide one with information at long time scales, which is why, we also compute the Power Spectral Density (PSD) of the frequency deviation from nominal frequency. It provides an alternate visualization of frequency-dependent noise sources evidenced by the ADEV and clearly shows any presence of harmonic signals. Constant plateaus indicate white frequency noise while flicker frequency noise is shown by f^{-1} behavior. The PSD is an excellent complimentary tool to evidence presence of unwanted harmonics in our signal that are difficult to interpret with the ADEV (see Fig. II.8).

Correlation factor

For some of our experiments, we were able to monitor simultaneously two frequency signals to study their potential correlation using the correlation function. The correlation function Γ_{XY} of two random vectors is the measurement of these two vectors' linear dependence. The output of this function is comprised within [-1, 1]. If X and Y are independent then $\Gamma_{XY} = 0$. It is equal to 1 when Y is a linear positive function of X, or -1 if Y is a linear negative function of X. Between these values are found lower degrees of linear dependence.

The function is defined as:

$$\Gamma_{XY} = \frac{\sigma_{XY}}{\sigma_X \sigma_Y} \qquad \textbf{(II.14)}$$

where σ_{XY} is the covariance between X and Y, σ_X the variance of X and σ_Y the variance of Y.

For two vectors $X(x_1, \dots, x_n)$ and $Y(y_1, \dots, y_n)$, the correlation is calculated as:

$$\Gamma_{XY} = \frac{\sum_{i=1}^{n}(x_i - \bar{x})(y_i - \bar{y})}{\sqrt{\sum_{i=1}^{n}(x_i - \bar{x})^2}\ \sqrt{\sum_{i=1}^{n}(y_i - \bar{y})^2}} \qquad \textbf{(II.15)}$$

We built an integration time dependent correlation function $\Gamma_{XY}(\tau)$ to study the evolution of correlation from short time scales to long time scales.

2.2. Allan deviation measurement protocol

In this work, we have measured the Allan deviation in both open and closed loop, which is equivalent.

In Open Loop operation, the device is driven at a fixed frequency (its resonance frequency), and its phase fluctuations are recorded. If the device was made to oscillate via a perfect feedback loop, it would exhibit frequency fluctuations accordingly. These frequency fluctuations can be computed using the measured quality factor (see Appendix A), in a bandwidth where the phase response is linear. The Allan Deviation algorithm previously discussed is finally applied.

In Closed Loop operation, the resonance frequency is tracked with a Phase Locked Loop (PLL) adjusting the drive signal to minimize deviation from the phase reference. The coefficients of the PLL transfer function are calculated with a robust H∞ controller thanks to the extracted linear frequency/phase slope (usually deduced from Q) and the desired PLL response time τ_{PLL} [16]. Since we directly acquire the relative resonance, the application of the Allan Deviation Algorithm is straightforward.

In Open Loop, a drift of the mechanical resonance will translate into a signal phase drift that will eventually step out of the linear dynamic range. Therefore the Closed Loop method is compulsory for long acquisitions aiming at observing ADEVs at long integration times (>10s). Plus, it is easier to perform (i.e. less prone to user related errors) than Open Loop method and gives a confident evaluation of the sensor's performance in operation. On the other hand, an ADEV curve acquired in Closed Loop is meaningless below the PLL response time, generally around 10ms. Hence, the Open Loop method is preferred for investigation of low integration times. The lower integration time limit in Open Loop is $3 \times \tau_{LIA}$.

We proceeded to demonstrate the consistency of these methods by applying successively both of them on the same resonator with the same actuation and polarization voltages (Fig. II.7).

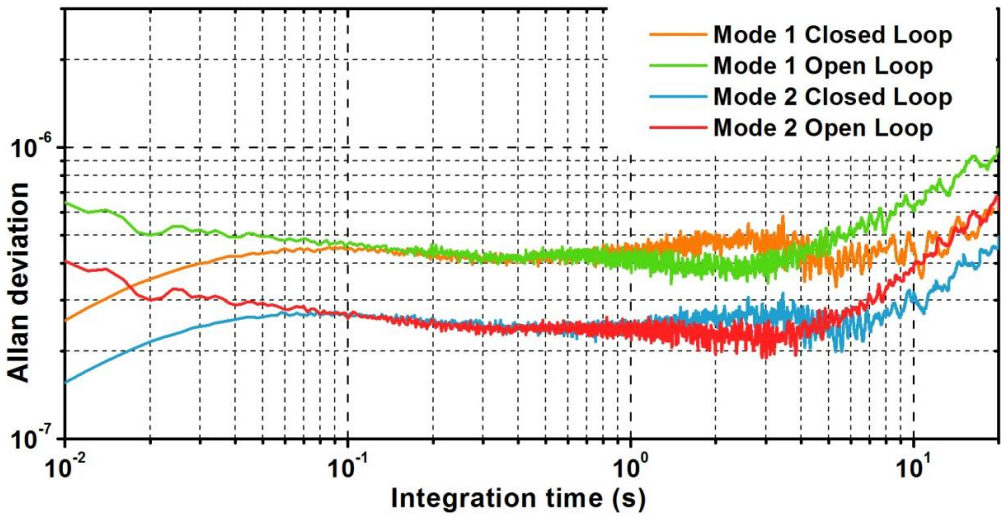

Fig. II.7: Comparison of ADEV computed from Open Loop acquisition and Closed loop acquisition ($\tau_{PLL} = 100ms$) for both mode 1 and mode 2. $\tau_{LIA} = 10ms$. The resonator is driven at its maximum amplitude in vacuum.

Computation of the PSD in parallel with the Allan deviation provided us an insightful complementary analysis of the measured noise. In some of our experiments, the PSD pointed out the presence of power line noise i.e. harmonics at multiples of 50Hz (Europe) or 60Hz (North America) as shown in Fig. II.8.

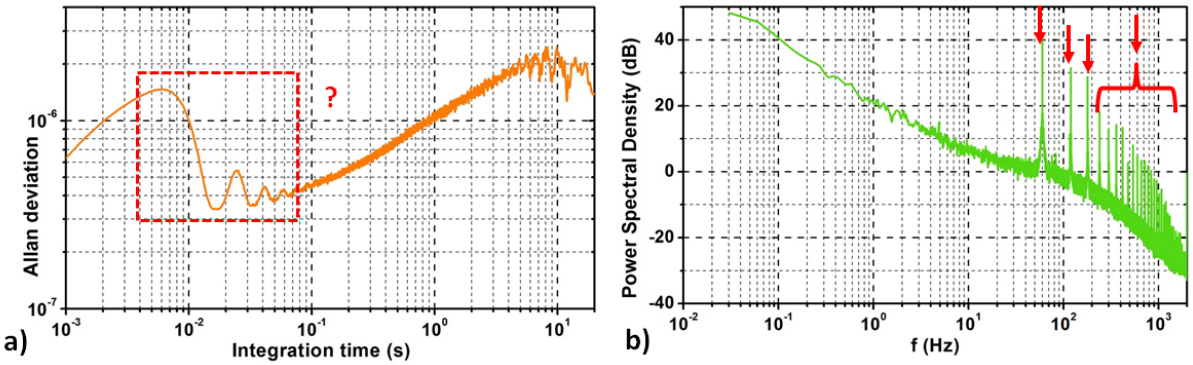

Fig. II.8: ADEV (a) and PSD (b) of a closed loop acquisition of mode 1 resonance (PLL response time=10ms). ADEV oscillations are explained by PSD peaks at multiple of 60Hz (measurement performed in north America).

An algorithm was developed by PhD student Rémi Pérénon to delete those undesired harmonics: the signal is translated to the Fourier domain where spikes at multiples of 50/60 Hz are removed and crudely interpolated with the rest of the spectrum. Translating back to the time domain yields a new signal whose ADEV does not feature oscillations at short time scales (Fig. II.9).

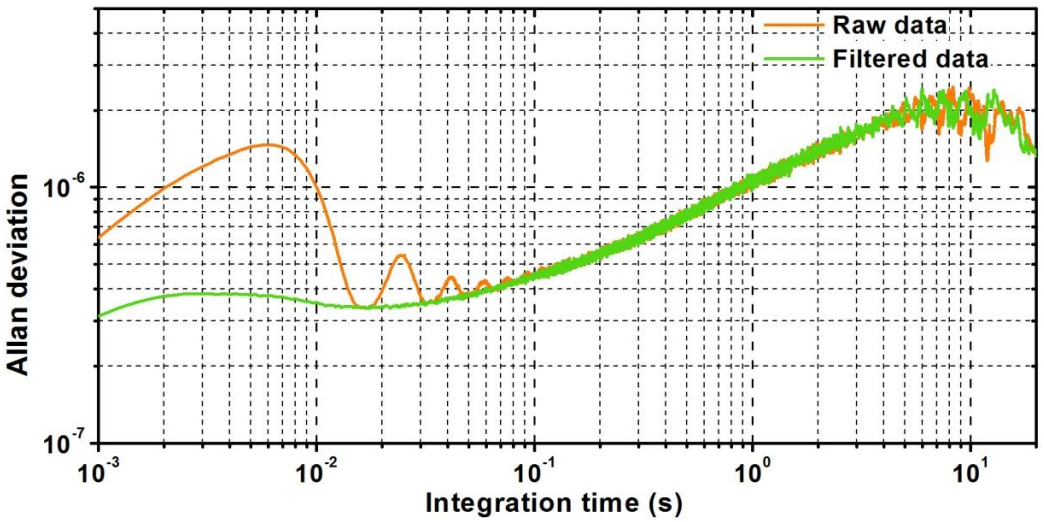

Fig. II.9: Power line noise suppression effect on the ADEV. The filtered ADEV follows the low envelope of the power line oscillations seen on the unfiltered data.

When in presence of power line noise, harmonic deletion is automatically applied for mass sensing applications.

2.3. Experimental results

To check the validity of equation (II.4) and the frequency fluctuation limit previously estimated in the 10^{-9} range, we measured the ADEV of a doubly clamped beam (doping level = $2 \times 10^{19} cm^{-3}$) with the following dimensions: 10µm*300nm*160nm for the length, width and thickness respectively. We monitored the frequency fluctuations in closed loop with $\tau_{PLL} = 1ms$ and $\tau_{LIA} = 0.5ms$ with a 2f actuation scheme. The signal detection is performed in differential mode: the bias current is applied at the center of the nanogauge bridge and the output signal is read by an operational amplifier subtracting the signal coming out of the nanogauges. The custom electronics that we used for this measurement does not provide us with an absolute value of the output voltage, preventing us from using previously calculated values of noise to compute an expected ADEV for a given signal amplitude. We will reason in term of expected behavior with respect to SNR increase or decrease.

We consider that our basic noise is composed of Johnson + thermomechanical noise + electronic noise. The signal S is proportional V_{bias} to and ${V_{drive}}^2$, the thermomechanical noise S_{th} is proportional to $V_{bias} \times \sqrt{\frac{4bTQ}{M_{eff}\omega_0^3}}$ while Johnson noise $S_j = \sqrt{4k_bTR}$. We will neglect here the influence of temperature due to Joule heating in the nanogauges as a temperature rise up to only a few tens of Kelvin has been evaluated in our operating range. At low bias we expect the Johnson noise to dominate, yielding a $SNR \propto V_{bias}\,{V_{drive}}^2$ ($V_{bias}\,V_{drive}$ for 1f actuation) while at high bias, thermomechanical noise should impose the $SNR \propto {V_{drive}}^2$ (V_{drive} for 1f actuation). Hence, increasing V_{bias} provides gain over Johnson noise only while

increasing V_{drive} provides gain on both noise sources. Progressively increasing the SNR, we expect to find relative frequency fluctuations down to the 10^{-9} range.

As a first step, we swept V_{bias} with an actuation voltage $V_{drive} = 2.75Vpp$ (Fig. II.10).

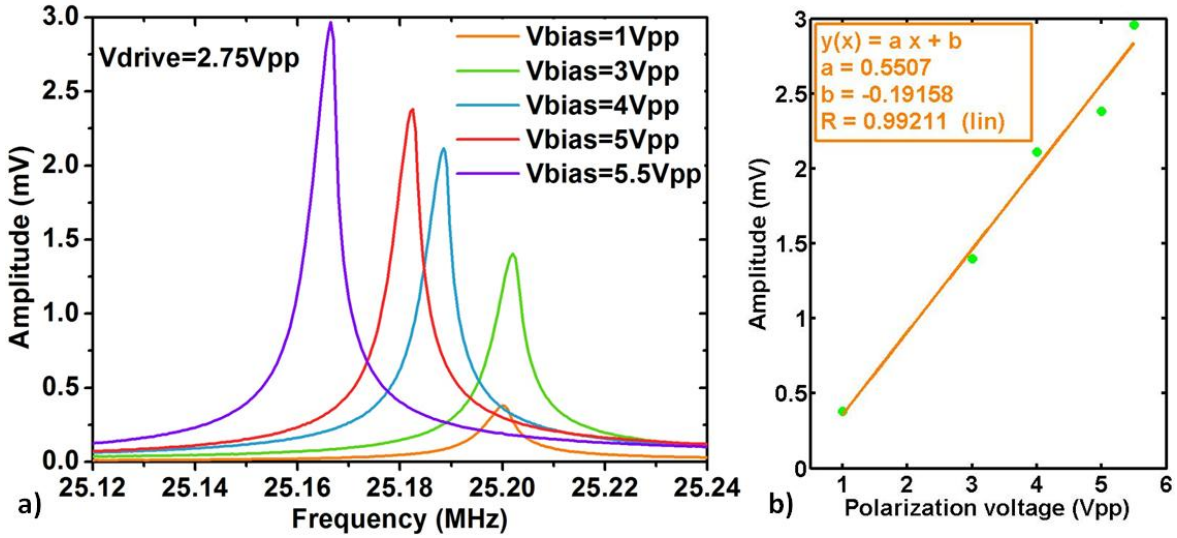

Fig. II.10: Mechanical resonance of a doubly clamped beam with increasing polarization voltages (a) and linear fit of maximum resonance versus actuation voltage (b). Amplitude values are arbitrary.

As the bias voltage becomes important, the resonance frequency shifts down probably because of the temperature rise caused by the heat dissipation in the nanogauges.

For each amplitude, we measured the corresponding relative frequency fluctuations as well as the signal PSD as shown in Fig. II.11.

If we observe the curve at $V_{bias} = 1Vpp$, the ADEV curve is composed of three main components:

- a $\tau^{-1/2}$ decreasing curve at short time scales associated with white noise
- a transition plateau
- an increasing curve at long time scales. Depending on the device or experimental conditions, the dependence goes from τ^0 to $\tau^{1/5}$

The PSD curves feature:

- a 1/f-noise behavior that decreases linearly with f.
- a white noise i.e. a constant plateau
- a cut-off frequency at 2kHz ($\tau_{LIA} = 0.5ms$)

The harmonics appearing at $V_{drive} = 2.5Vpp$ are caused by power line noise. This noise arises from other equipments connected to the power lines, the environment etc. Its presence is difficult to predict. Yet, it seems to be favored when using high AC voltages.

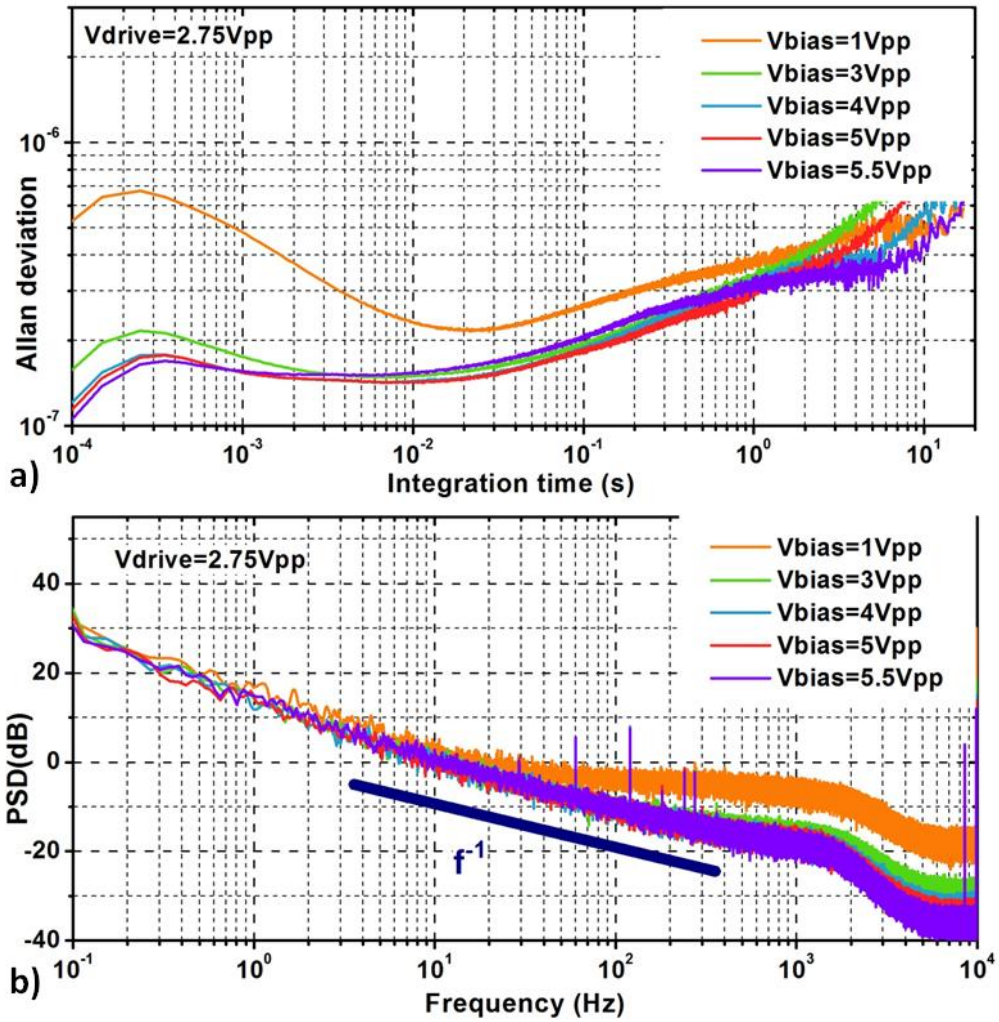

Fig. II.11: ADEV (a) and PSD (b) measured with increasing polarization voltage. While white noise is decreased with higher V_{bias} a 1/f-noise limit remains present. $\tau_{LIA} = 0.5ms$: the ADEV decrease below 0.5ms is caused by the LIA low pass filter transfer function.

Nevertheless, according to Robins law, for the ADEV we would expect a $\tau^{-1/2}$ curve accounting for white noise that decreases with higher integration. Over a few seconds we would expect frequency drifts phenomena to degrade the stability and induce a plateau or an increase in the ADEV. Yet, here for the curve at $V_{bias} = 1Vpp$, although we see the expected $\tau^{-1/2}$ curve, it seems to reach a limit at 20ms before remaining constant and increasing. If we look at the PSD, in the corresponding bandwidth [0, 50Hz] the signal noise is dominated by 1/f noise rather than white noise. On the other hand, white noise dominates on [50Hz, 2kHz]. Hence, as we reduce our bandwidth we reduce the importance of the white noise down to [0, 50Hz] where 1/f noise is dominant. Does this 1/f noise remain present for different operating conditions? Is it going to limit us at low integration time?

As V_{bias} increases, we improve our SNR for Johnson limited noise and we expect to hit a white thermomechanical noise limit i.e. we should obtain a $\tau^{-1/2}$ limit that cannot be overcome with higher bias. As we proceed with higher V_{bias}, we observe that the white noise contribution diminishes: the $\tau^{-1/2}$ dependent ADEV curve shifts down as well as the plateau of the PSD. However, rather than hitting a $\tau^{-1/2}$ limit expected in the 10^{-9} range, the same 1/f-noise plateau is reached at 1.5×10^{7} regardless of V_{bias}. Fig. II.12 shows the linear dependence of the ADEV on the amplitude at 1ms integration time before reaching the limit. Since $\tau_{PLL} = 1ms$, we plotted the amplitude dependence of the ADEV at the minimum integration time we can use for mass measurement that is 1ms.

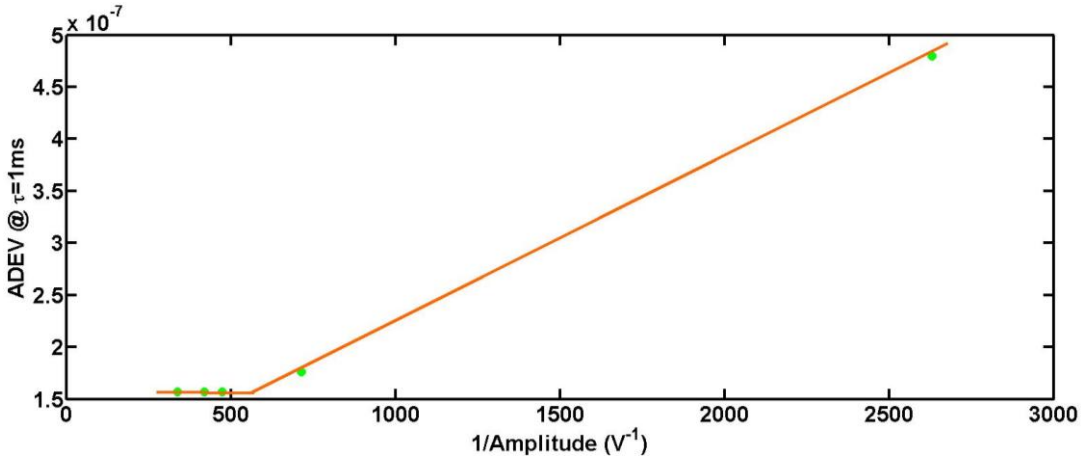

Fig. II.12: ADEV at τ=1ms with respect to the inverse of signal amplitude swept by varying V_{bias}. The ADEV linearly decreases with signal amplitude and saturates at 1.5×10^{-7}.

Hence, we are facing an unknown 1/f noise that limits frequency stability at orders of magnitude over what was expected. The curve at $V_{bias} = 1Vpp$ is probably Johnson noise limited since we were able to increase our SNR with higher V_{bias}. For higher voltages, we could not evidence thermomechanical noise as the 1/f noise already limited us.

Using a high $V_{bias} = 5Vpp$, we believe we are placed in a thermomechanical noise limited regime and we swept V_{drive} to study the impact of V_{drive} on noise. The following resonances were obtained (Fig. II.13):

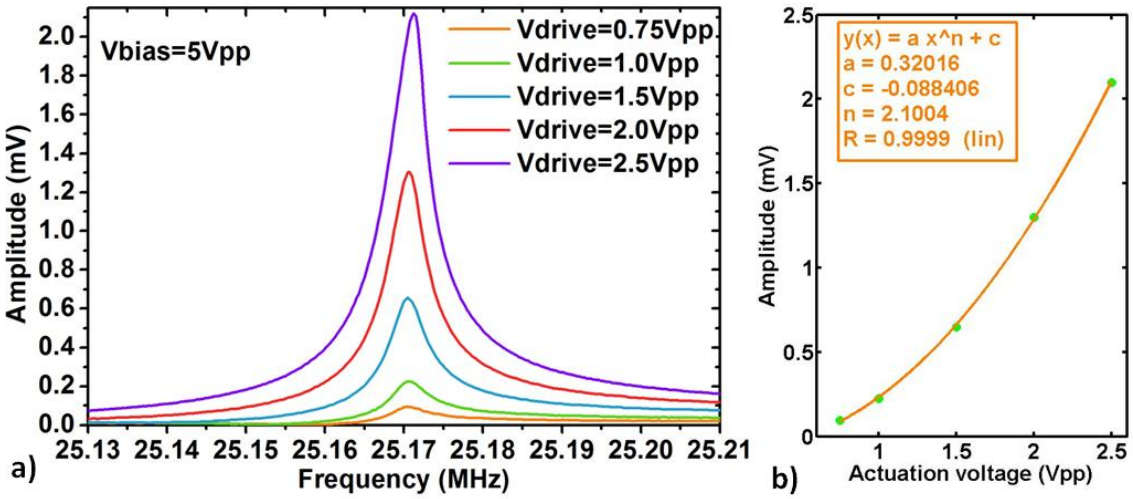

Fig. II.13: Mechanical resonance of a doubly clamped beam with increasing actuation voltages (a) and quadratic fit of maximum resonance versus actuation voltage (b). Amplitude values are arbitrary.

Like with the V_{bias} sweep, we measured the corresponding relative frequency fluctuations as well as the signal PSD (Fig. II.11). Since the thermomechanical noise dominates, increasing V_{drive} should improve our SNR.

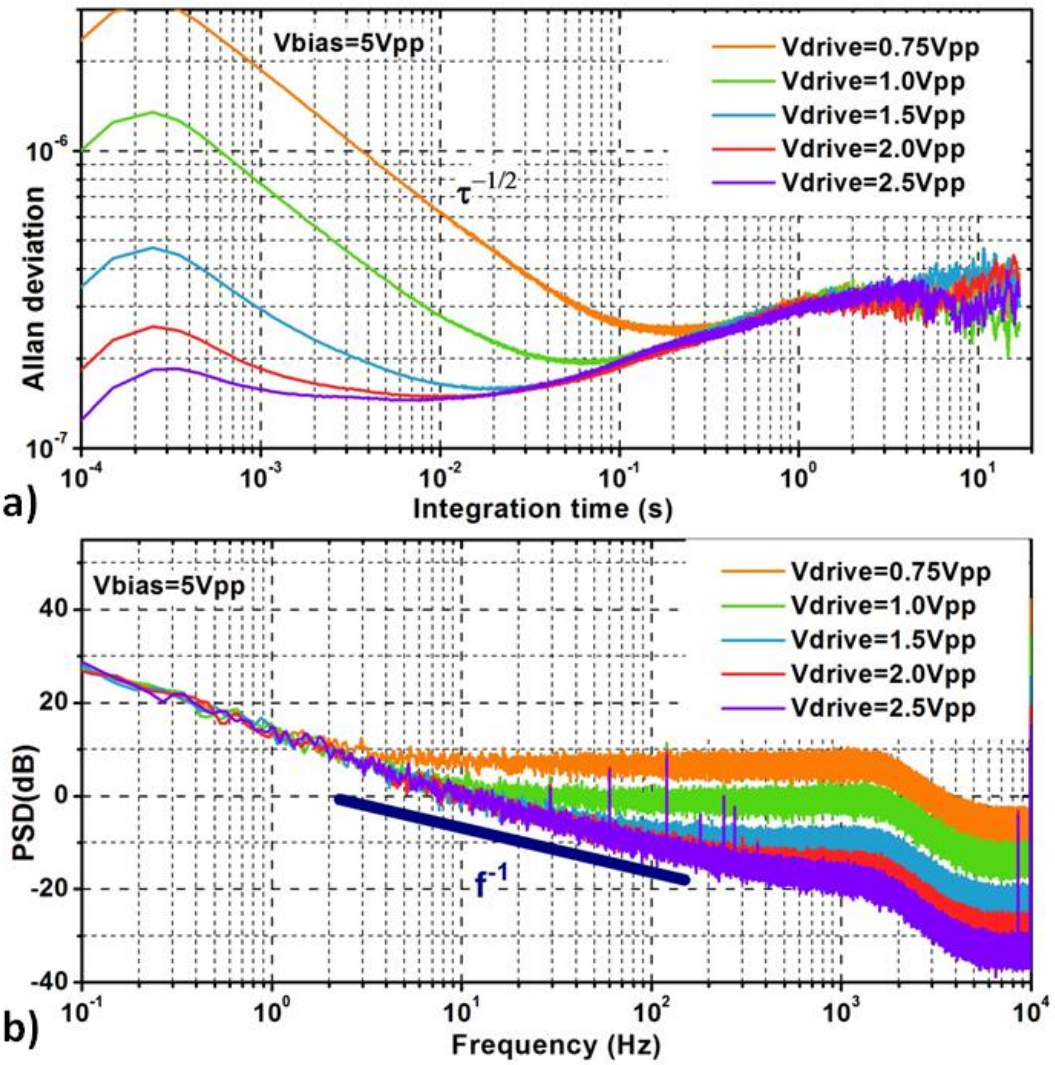

Fig. II.14: ADEV (a) and PSD (b) measured with increasing actuation voltage (2f actuation). The white noise is progressively nulled out until a 1/f-noise limit is reached. $\tau_{LIA} = 0.5ms$: the ADEV decrease below 0.5ms is caused by the LIA low pass filter transfer function.

As V_{drive} increases, we increase our SNR and observe that the white noise contribution diminishes: as expected the $\tau^{-1/2}$ dependent ADEV curve shifts down as well as the plateau of the PSD. Eventually, the same 1/f-noise plateau is reached and further increasing the actuation voltage did not bring any gain. We observe a correspondence of the integration time where a plateau is reached for the ADEV and the bandwidth limit before the white noise plateau in the PSD. The signal noise at $V_{drive} = 2.5Vpp$ is the ultimate noise limit we were able to reach. Fig. II.15 shows the linear dependence of the ADEV on the amplitude at 1ms integration time before reaching the limit.

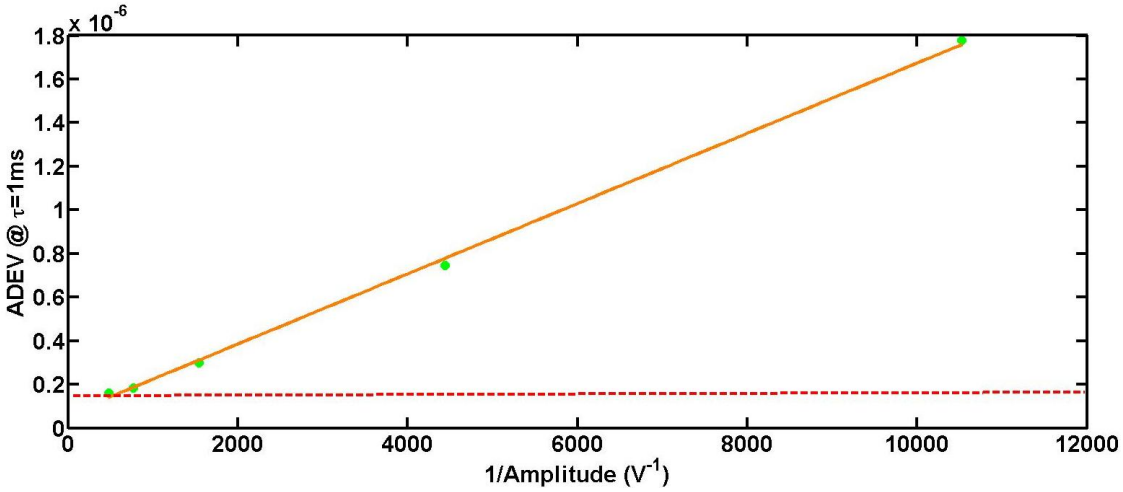

Fig. II.15: ADEV at τ=1ms with respect to the inverse of signal amplitude swept by varying V_{drive} . The ADEV linearly decreases with signal amplitude and saturates at 1.5×10^{-7}.

We note here that we did not have to push the V_{drive} up to the critical amplitude of oscillation beyond which non linear effects to observe the 1/f noise limit (see Fig. II.13). Therefore, as long as we are limited by this unknown noise, non linear effects are not limiting the mass resolution of our sensor.

Increasing either V_{drive}or V_{bias} did not allow us to reach the expected thermomechanical noise limit in the 10^{-9} range. As we increase the amplitude of resonance, we obtain a SNR improvement on the white noise only. However, after a certain limit, further increasing the amplitude also increases the quadrature noise, keeping a constant phase noise as illustrated in Fig. II.16.

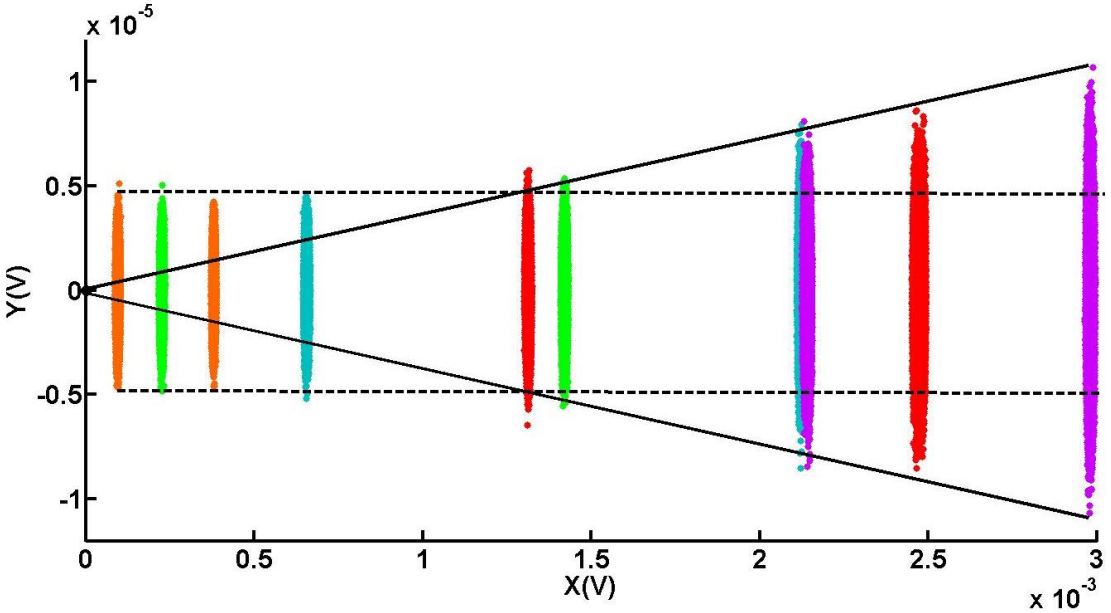

Fig. II.16: Scatter plot of quadrature signal (Y) versus in-phase signal (X) integrated at 1ms with increasing signal amplitude. The acquired data is the same as Fig. II.11 and Fig. II.14 represented in another form. The phase noise cone is decreased with increasing amplitudes in the white noise regime (dashed lines) but phase noise remains constant in the 1/f-noise regime (straight line forming the phase noise cone).

In summary, Robins law remain valid at low signals (≈ below 1mV) where white noise dominates. Indeed, the frequency fluctuations could be decreased with higher SNR and featured a $\tau^{-1/2}$ dependence (see Fig. II.14.a) as stated by equation (II.4). However, as we further tried to increase the SNR, we witnessed the presence of a 1/f excess noise that limited our minimum frequency stability to 1.5×10^{-7}: the phase noise remained constant regardless of the signal amplitude.

Given that the doubly clamped beams we plan to use for mass sensing applications have an effective mass around 0.4pg, the best mass resolution we can expect on mode 1 for a particle landing on the centre of the beam is 60zg (35kDa) (equation (II.2)) which is an order of magnitude above the expected 1kDa resolution (with $\sigma_{\delta f} = 5 \times 10^{-9}$). In order to address the ad hoc biological applications, it is important to investigate this source of excess noise and progress in its understanding.

3. Experimental investigation of the source of excess noise

To identify the origin of the excess noise, we performed series of experiments to rule out or confirm the implication of various parameters and find the location of this noise in the transduction chain. Unless stated otherwise, frequency noise is measured on the first resonance mode in vacuum at room temperature. Some experiments compare the excess noise limit according to various parameters. The excess noise limit is obtained at high polarization voltages and large driving amplitudes (close to the non linear limit). For the same design the ADEV limit can be variable and may range from 1×10^{-7} to 7×10^{-7} for 100ms integration time although they are most commonly found around $2.5 \times 10^{-7}$for mode 1 at room temperature.

The very first tests consisted in checking that our measurement protocol was not instrumentation-limited: our chain of measurement allowed us to measure experimental Allan deviations below 10^{-10} in the same frequency and signal amplitude ranges, with the same RF sources and lock-in amplifiers, cables, probes and vacuum chamber.

3.1. Actuation & motion transduction

We assumed that noise could come from physical variation affecting actuation or motion transduction of the device: for instance fluctuations of charges on the surface of the drive electrode may generate fluctuation of the driving force further transduced to signal noise or temperature fluctuations in the nanogauges may induce fluctuations of the piezoresistance measured by our detection scheme. A first step was the verification that the same limit is obtained with both 1f and 2f electrostatic actuation (cf Chapter I) as presented in Fig. II.17.

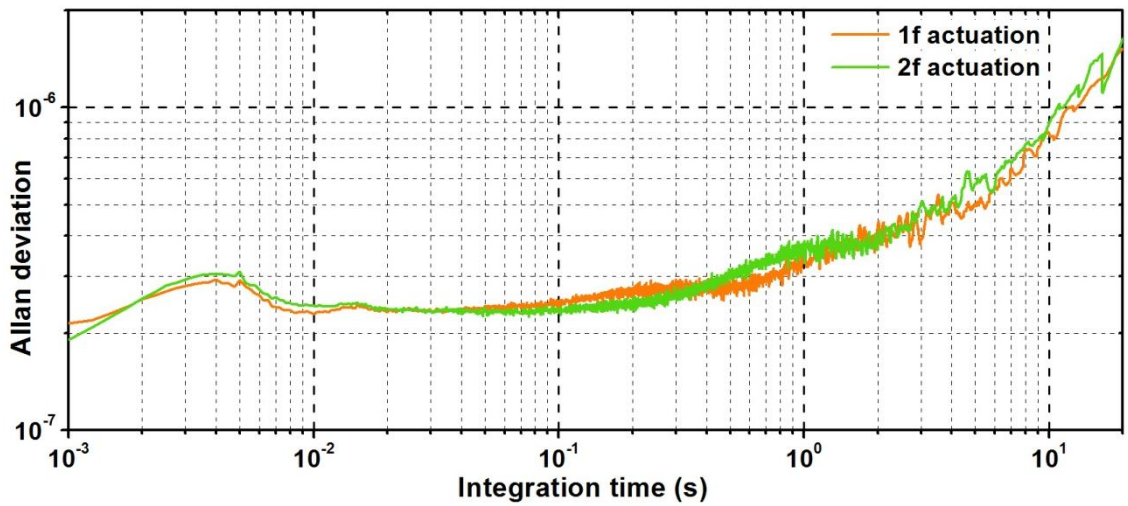

Fig. II.17: ADEV of a doubly-clamped beam with 1f and 2f actuation scheme.

Then, we decided to actuate the resonator with an alternate mean. Dr. Sébastien Hentz measured the frequency noise of a resonator actuated both conventionally and with a piezoshaker actuation [9]. The same frequency stability was obtained regardless of the actuation mean. Electrostatic actuation does not seem to be the source of the excess noise.

On the other hand, Dr. Sébastien Hentz measured the mechanical frequency stability without using the nanogauges via optical detection [9]. Both optical and electrical piezoresistive detection induced the same frequency stability: one cannot incriminate the 1/f noise in semiconductor resistances, or self-heating because of the bias voltage for example. These two experiments seem to show with no ambiguity that the excess noise manifests itself in the mechanical domain: the frequency fluctuations are present in the mechanical vibrations of the resonator, but not in the electrical signals used to drive or bias the device. The physical origin of this noise thus remains unknown, but may come from the environment or the material itself of the resonator.

3.2. Phase or frequency noise?

For white additive noises, we have seen that the expected frequency noise is obtained by calculating the appropriate phase noise before conversion to frequency noise using Robins law. Yet, it seems that our excess noise lies in the mechanical domain and clearly does not satisfy Robins law. In this regard, it is fair not consider frequency noise as a consequence of phase noise but rather the opposite. Actually, Fig. II.16 shows a phase noise that further increase at higher signal as if it was the consequence of a constant frequency noise. If so, then according to equation (II.5), phase noise should increase with higher quality factors.

Influence of Q on the excess noise

We designed an experiment where Q of the resonator can be tuned by varying the pressure of the NEMS chamber. The experiment was performed on a 5µm*300nm*160nm cantilever resonating at 17MHz with pressures varying from vacuum $3 \times 10^{-5} mbar$ to $1 \times 10^{2} mbar$. Doing so, we were able to tune the resonator quality factor from 400 to 2560

to observe its effect on the frequency fluctuations at equal resonator displacement: V_{bias} is kept constant (3.7Vpp) while V_{drive} is adjusted (from 1 to 2.6Vpp) to maintain a maximum amplitude signal as close as possible to 1mV. The challenge of the experiment resides in the difficulty to obtain equal displacements on the full pressure dynamic range. For example, we could not reach 1mV signal at ambient pressure. Results are displayed in Fig. II.18.

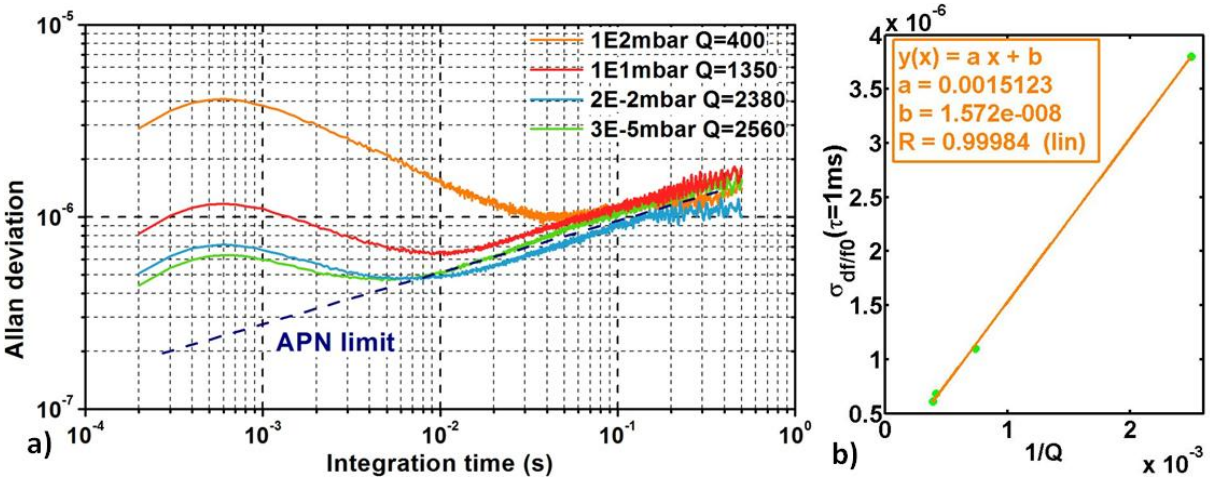

Fig. II.18: ADEV obtained from a cantilever driven for a 1mV resonance signal for different pressure conditions (a). The ADEV at 1ms is inversely proportional to Q (b).

We observe that at integration times above 40ms, the ADEV remains unaffected by Q whereas the influence of white noise increases with lower Q at short time scales as expected from equation (II.5): at an integration time of 1ms, we find a linear dependence of the white noise with respect to 1/Q. Yet, for integration times above 40ms, the same frequency fluctuation is obtained with Q ranging from 400 to 2560: the level of frequency noise seems to be constant in this quality factor range. As expected from Equation (II.5) and a constant frequency noise, the phase noise increases with higher Q.

This implies that phase noise may be a consequence of frequency noise and not the other way around: in other words, the physical source of the excess noise may well be a frequency noise source, and not an amplitude or phase noise source translating into frequency noise. As shown in Fig. II.19, frequency fluctuations will generate higher phase noise with higher Q. Hence, it seems like we may be confronted to a fluctuation of the frequency caused by unknown physical variations. From now on, we refer to this excess noise as the Mechanical Frequency Noise (MFN).

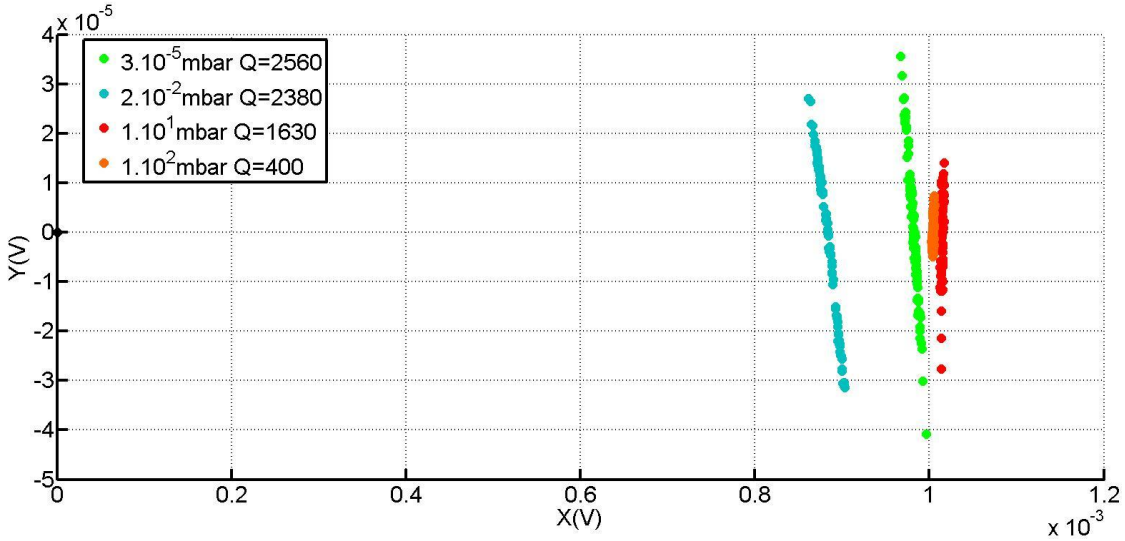

Fig. II.19: Scatter plot of quadrature signal (Y) versus in-phase signal (X) integrated at 100ms at a resonance amplitude around 1mV for different chamber pressure hence different Q . At 100ms, we are in the regime where the excess noise dominates phase fluctuations: frequency fluctuations translate to higher phase noise with higher Q. The data from the four measurements have been centered around phase=0 for easier comparison.

Fluctuation of the resonator transfer function

The MFN can be viewed as the fluctuation of the resonance peak in the frequency domain and by extension fluctuation of the phase response curve. We propose to validate this consequence by simultaneously monitoring the frequency fluctuations at two different resonance frequencies within the resonator bandwidth and study their correlation. As the fluctuation of the phase response curve should induce he same MFN at the two frequencies, a correlation of 1 is expected.

An Open Loop was performed on a doubly-clamped resonator driven at large amplitudes with two detection setups in parallel: we have two actuation signals, two polarization signals and two differential LIAs. Each setup probes a different position in the resonance peak. The LIA phase references are set for 0 at resonance. We set the transduction signal frequencies at $f_0 - 1.5kHz$ for the first detection setup and $f_0 + 1.5kHz$ for the second one. The difficulty of the experiment resides in the necessity to stay in the linear response for both setups and keep a sufficient frequency separation (here 3kHz), to minimize cross-talk between the two setups. The first setup downmixes the signal at $\Delta f_1 = 95kHz$ whereas the second one uses a carrier at $\Delta f_2 = 65kHz$. Using a high τ_{LIA} at 10ms, unwanted byproducts of the downmixing signal multiplication are filtered out. This results in the possibility to monitor phase fluctuations in Open Loop simultaneously at -15° and +15° (Fig. II.1).

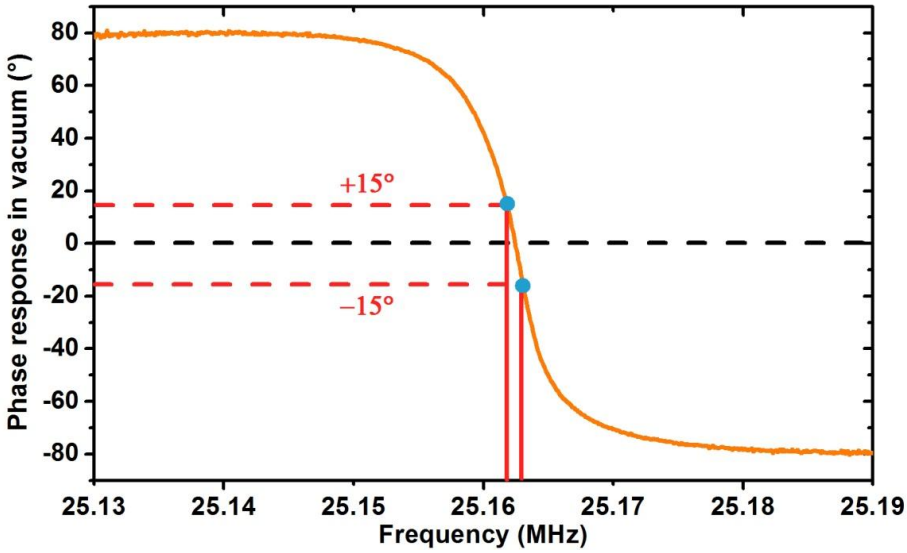

Fig. II.20: Illustration of the experimental design. Two phase fluctuations from the linear region are simultaneously monitored to demonstration noise correlation.

Whereas we usually observe phase fluctuation around 0° in conventional configurations, we obtain here two signal fluctuating around -15° and +15° that we can translate to relative frequency fluctuations as shown in Fig. II.21.

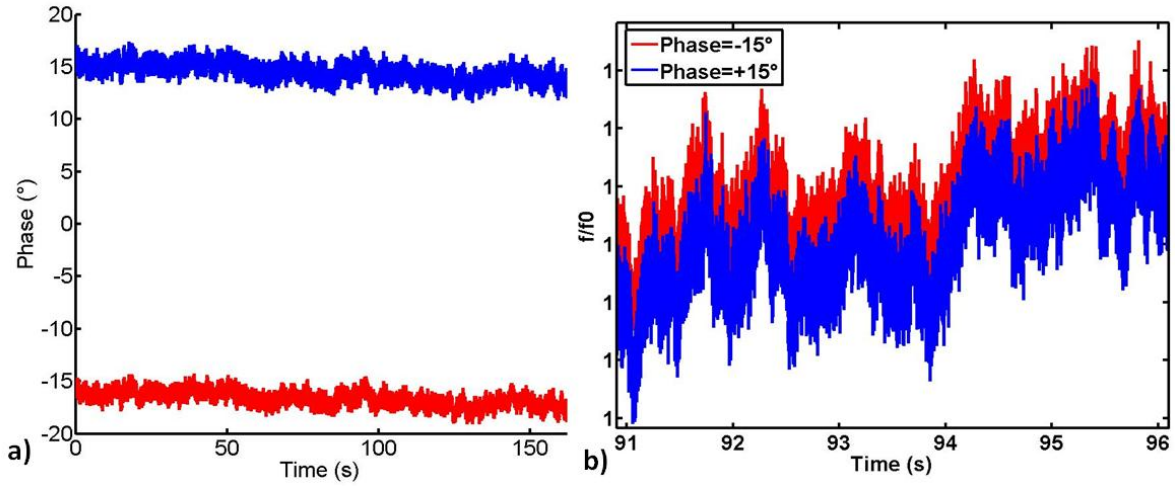

Fig. II.21: Simultaneous phase fluctuations (a) and corresponding frequency fluctuations (b) where a certain degree of correlation at long time scales can already be observed.

Looking at the relative frequency fluctuations, we can readily discern similar fluctuation patterns. For both signals, we computed the Allan Deviation and the function $\Gamma_{XY}(\tau)$ i.e. their correlation versus integration time shown in Fig. II.22.

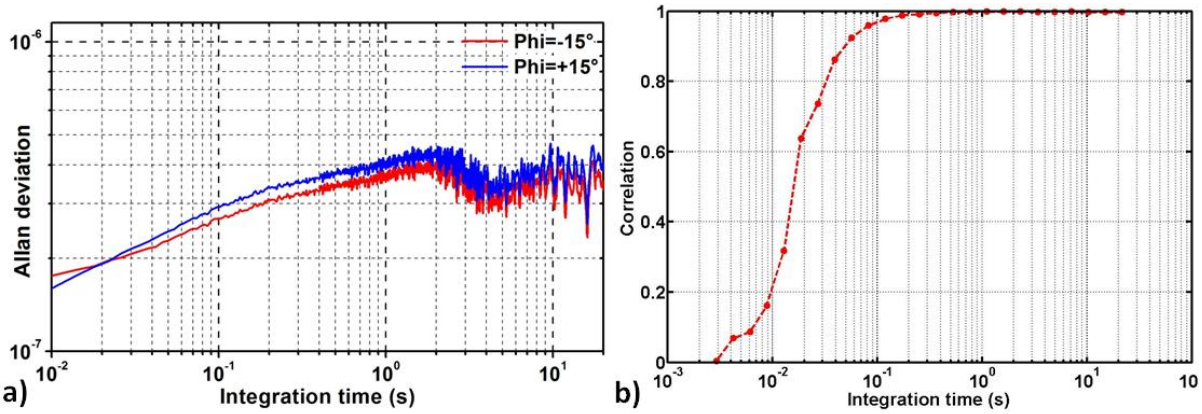

Fig. II.22: Allan deviation of both signals at -15° and +15° showing the presence of the APN (a) and correlation of the two signals with respect to integration time (b). Measurement in Open Loop with $\tau_{LIA} = 10ms$

For integration times over $5 \times \tau_{LIA}$, a correlation of 1 is evidenced: the two signals see the same noise caused by the fluctuation phase response of the system i.e. the fluctuation of the mechanical resonance frequency. Below $5 \times \tau_{LIA}$, the signals are not fully integrated and are under the influence of the LIA (two independent LIA are used for each signal). Over a few seconds, correlation could be attributed to frequency drifts. However the range from 50ms to a few seconds is clearly dominated by the MFN and displays a correlation of 1, confirming our hypothesis.

3.3. Spatial correlation of MFN

We now strongly suspect that our limiting noise is not an amplitude noise but rather a fluctuation of the resonance frequency. One could wonder if these fluctuations are the same along the resonator's dimensions or extremely localized and uncorrelated across the structure. Plus, assuming a physical variation of the environment or substrate, etc., the MFN may be correlated across several devices found on the same chip, for instance. We set up two additional experiments relying on correlation measurement to investigate if the noise is correlated at both ends of a doubly clamped beam and if a correlation is found between two different resonators.

Spatial correlation across one device

For the first one, the device is a doubly clamped beam with two symmetric sets of nanogauge bridges close to each beam anchor as shown in Fig. II.24. We monitored simultaneously the frequency fluctuations at these two extremities. Given that the resistance of the beam itself is estimated around 14kΩ and that a virtual ground should be found at the middle of each nanogauge bridge, interferences should be limited.

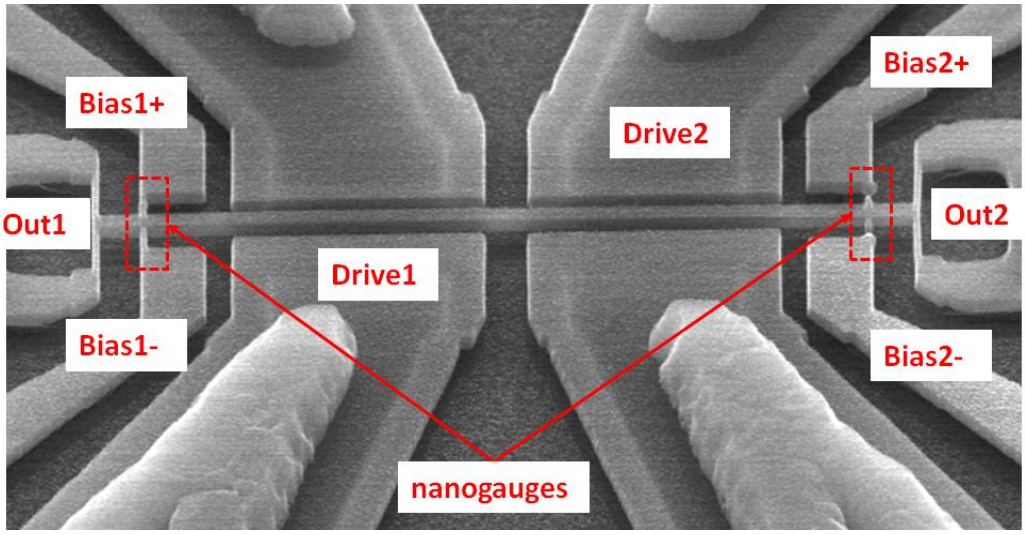

Fig. II.23: SEM image of a doubly-clamped design where a nanogauge bridge is found at each extremity.

Both ADEV and correlation functions displayed in Fig. II.24.

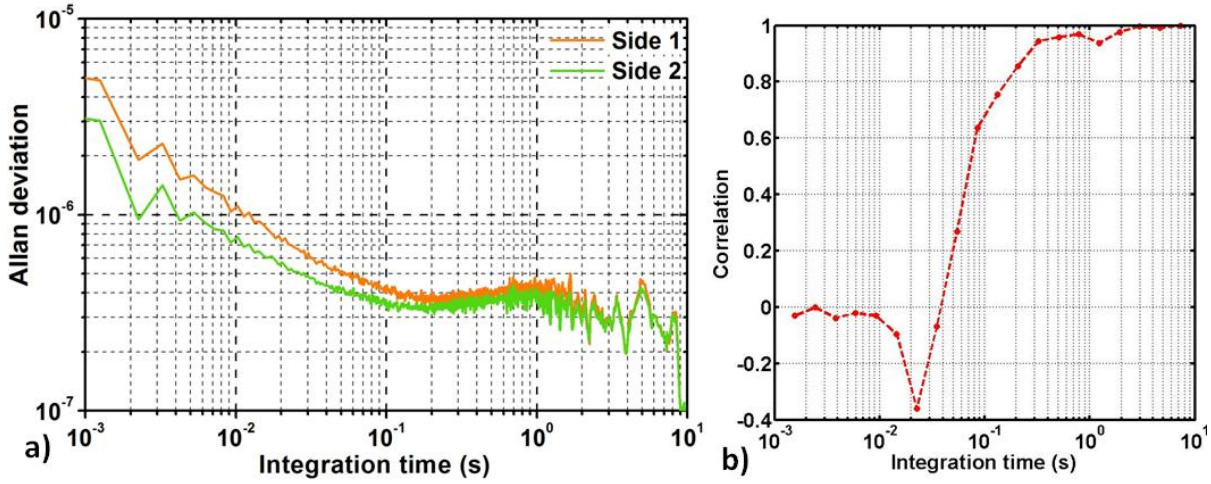

Fig. II.24: ADEV (a) and correlation (b) of two resonance frequencies measured across the device extremities in Closed Loop with $\tau_{PLL} = 10ms$.

Below 100ms integration time, we seem to have residual white noise but we notice that the MFN floor starts from100ms and that the correlation is close to 1 starting from 100ms: the MFN affects simultaneously the beam at two points (middle of the nanogauge bridge) 9µm apart. Could the MFN be caused by environmental variations affecting structures at a mm² scale or is this noise specific to a device? In other words, is there any correlation on noise from two separate devices present on the same chip?

Correlation between two spatially close devices

To investigate this, arrays of resonators were used, where 20 NEMS are interconnected in parallel with different resonance frequencies: when probing the array, we can readout a specific NEMS by reading a given frequency. Further details on arrays are found in Chapter IV. We randomly chose to read NEMS#3 and NEMS#4, separated by a

20µm pitch, and performed a simultaneous tracking of their resonance frequency (26.7MHz and 27.8MHz respectively) as shown in Fig. II.25.

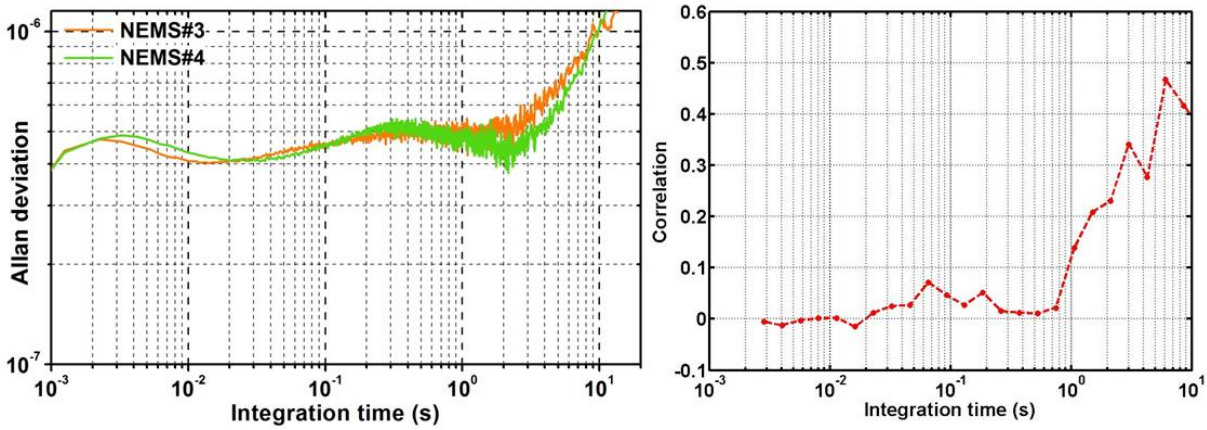

Fig. II.25: ADEV (a) and correlation function (b) of two different resonators tracked in parallel. Measurement in Closed Loop with $\tau_{PLL} = 10ms$.

We observe on the ADEV plot some remaining white noise below 10ms but anyways we are not interested in integration times below $\tau_{PLL} = 10ms$. The MFN floor is observed from 10ms to 2s. Beyond 2s, we identify a frequency drift whose τ dependence is generally around τ^1. We observe that a correlation close to 0 is found in the MFN regime, i.e.. from 10ms to 2s. On the other hand, high correlation is measured beyond 2s (where long-term drifts are expected), corresponding to a rise in ADEV and in a range where our sampling begins to be poor. The two resonators are spatially close to each other (on the order of 10µm), and it seems reasonable to think that changes in environmental temperature would induce identical frequency fluctuations. This seems to be the case beyond 2s time scale. Considering their low thermal capacitance, their thermalization time constant is on the order of a few tens of ns i.e. well below the range of the MFN regime. Yet in this regime no correlation seems apparent. This would tend to show that the MFN is not due to the temperature fluctuations of the device. More importantly, although the MFN seems to affect simultaneously the resonating structure at different positions on the beam (previous experiment), it is not correlated with the MFN of neighboring devices: the MFN of different devices are independent from one to another and are probably not caused by environmental fluctuations.

3.4. Parameters impacting the MFN

We now believe that the MFN is a noise in the mechanical domain impacting the resonator's resonance frequency probably because of some physical variations modifying some parameters inherent to the device i.e. its boundary conditions, its stiffness etc. Systematic ADEV measurements were performed on a great number of devices to highlight patterns.

Geometry

For instance we compared the ADEV of devices with difference lengths and boundary conditions (cantilever or doubly-clamped). The MFN found in cantilever beams was in the same order of magnitude than doubly-clamped beams as shown in Fig. II.26.

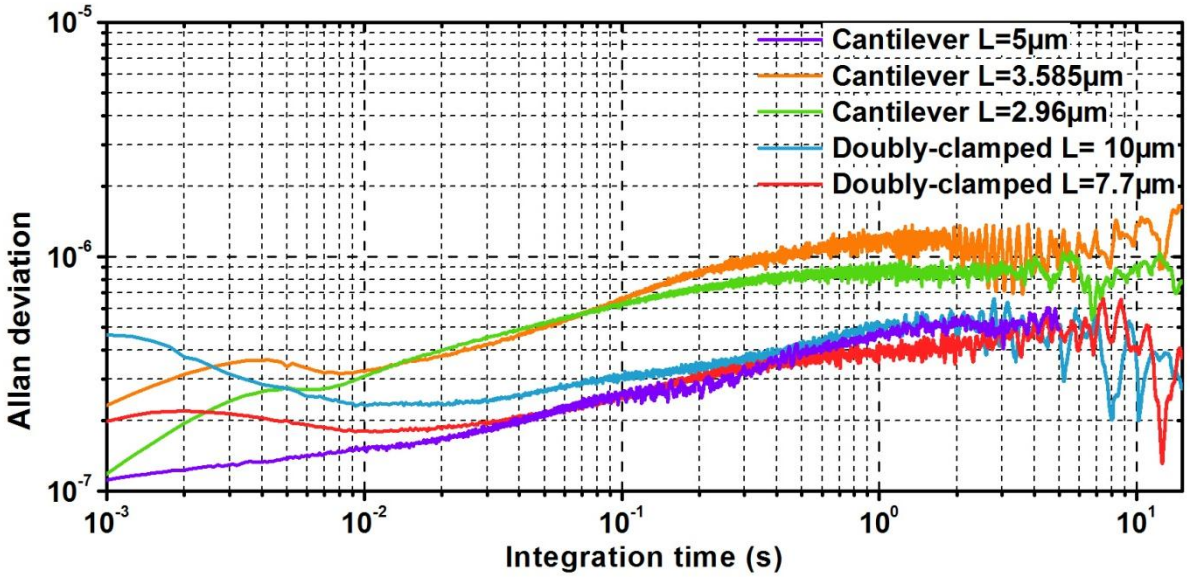

Fig. II.26: ADEV of cantilevers and doubly-clamped beams with different length. Width is 300nm and thickness is 160nm.

The APN limit is probably process dependent and the ADEV at 100ms can range from 1×10^{-7} to 7×10^{-7} for the same design. Nevertheless, it appears that the MFN does not depend on the boundary conditions. We did not find any significant trend in the MFN with respect to beam length: the differences we observe are within the range where most APN limits are found. Plus, these small length variations induce only small differences in resonant mass. Hence, new designs should feature resonant beams with significant size differences in order to investigate the APN scaling laws. For instance, Ivaldi *et al.* showed that the minimum relative frequency noise obtained for a 90µm*40µm*885nm cantilevers of different material and different transduction, i.e. with a scale roughly 10 times bigger than our devices, was 3×10^{-8} [17].

Although close in term of volume or mass, the resonance frequency of these devices ranges from ~ 20Mhz to ~40MHz. How does MFN vary with higher frequencies? This can be investigated with higher resonance modes.

Resonance mode

We measured the relative frequency fluctuations on the first three harmonics of the same doubly-clamped resonator (10µm*300nm*160nm) at 25.19MHz, 66.5MHz and 123.5MHz with measured Q of 4250, 3000and 1300 for mode 1, mode 2 and mode 3 respectively.

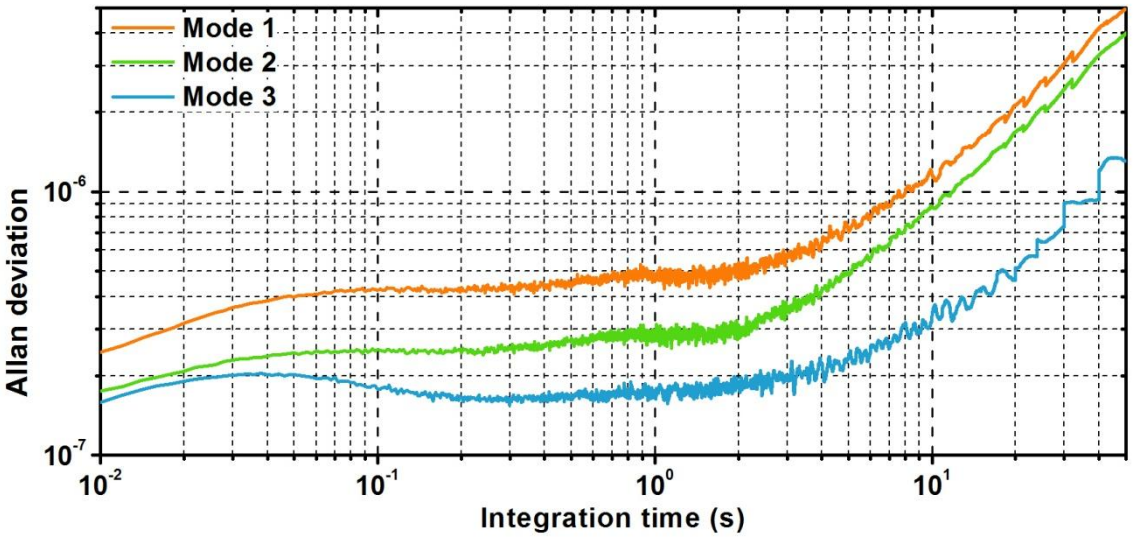

Fig. II.27: ADEV of the first three harmonics of a doubly-clamped beam performed in Closed Loop ($\tau_{PLL} = 100ms$).

Beyond 2s, we observe frequency drifts for both modes. Frequency drifts are caused by slow varying environmental variations such as temperature or pressure. Since it modifies the global physical properties of the resonator (Young's modulus etc.), all modes are influenced the same way.

Below 2s, similarly as with mode 1, mode 2 and mode 3's ADEV saturate when driven at high amplitudes, orders of magnitude above thermomechanical noise. All three resonance modes have very similar frequency fluctuations: the MFN affects relative frequency fluctuation regardless of the vibrating frequency and the mode shape. Does it mean that fluctuations of mode 1, 2 and 3 are correlated?

We investigated the correlation of the two first harmonics of a doubly-clamped device. Each detection setup is instructed to monitor a given harmonic. We obtain the following results:

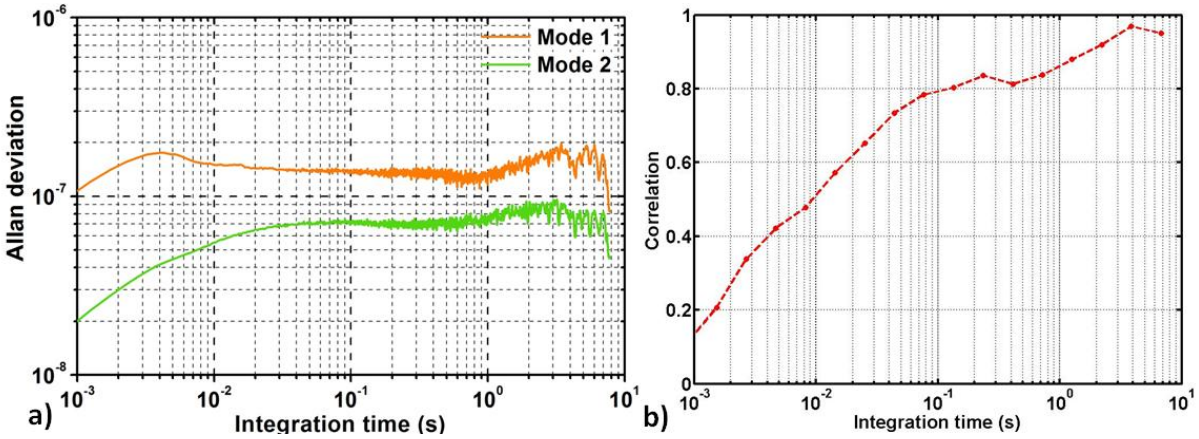

Fig. II.28: ADEV (a) and correlation (b) of the two first harmonics of a doubly clamped resonator in Closed Loop with $\tau_{PLL} = 10ms$.

The MFN floor is found from 10ms to a few seconds. It is difficult to conclude here as we cannot clearly identify a correlation of 1 of the complete domain of the MFN: it starts around 0.5 at 10ms and reach 0.9 around 2s. Additional measurements need to be performed to confirm this behavior.

Given that the MFN is a phenomenon that seems favored with smaller devices, it is possible that the MFN is caused by physical fluctuations in the whole structure volume, perturbing equally the three resonance modes. Assuming that the presence of defects in the device volume may be the cause of MFM, we can expect different saturation levels of the ADEV for different doping levels.

Doping level

We performed here a preliminary study of the impact of doping levels on the ADEV that probably deserve more effort. We used resonators with identical designs that underwent the same fabrication process except for the doping level (Boron) aimed at 9.3×10^{18}, 1.9×10^{19}, and 7.4×10^{19} dopants.cm^{-3}. Since we are interested in the MFN, we simply used actuation and polarization voltages high enough to overcome the white noise and hit the MFN floor for the three configurations. For the sake of clarity, we only display the MFN limits in Fig. II.29.

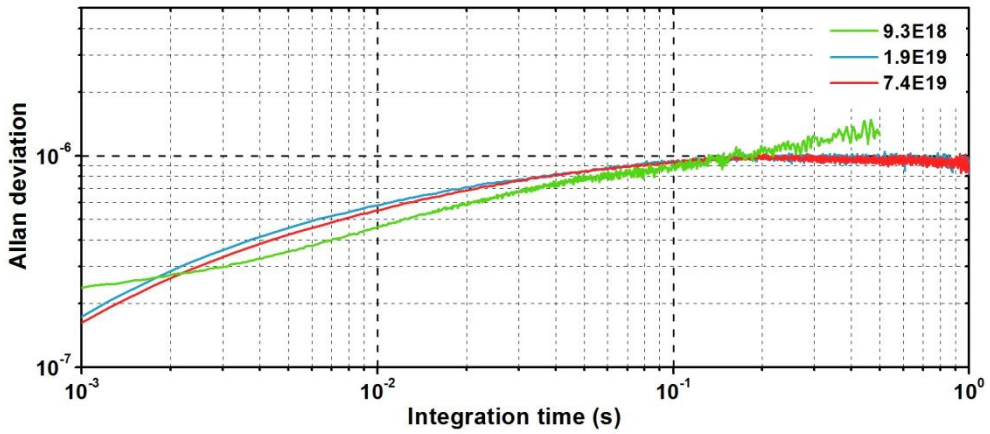

Fig. II.29: ADEV comparison of identical devices with different doping levels in atoms.cm^{-3}.

No significant APN limit difference was found for the three different levels. Additional studies with a higher dynamic range of dopant concentrations and statistical analysis need to be performed to confirm these preliminary results.

No volume effect could be shown here. Another lead is the surface effect that can be involved with adsorption desorption noise. As the devices are shrunk, their ratios surface to volume increase, making surface effects more important.

Coated resonators

We measured the MFN of devices from the same batch with different coating thickness of oxide: 0/20/30/40nm. If the source of the APN was rooted in gas-surface

interaction, some change should be apparent with change in coating. The results are displayed in Fig. II.30.

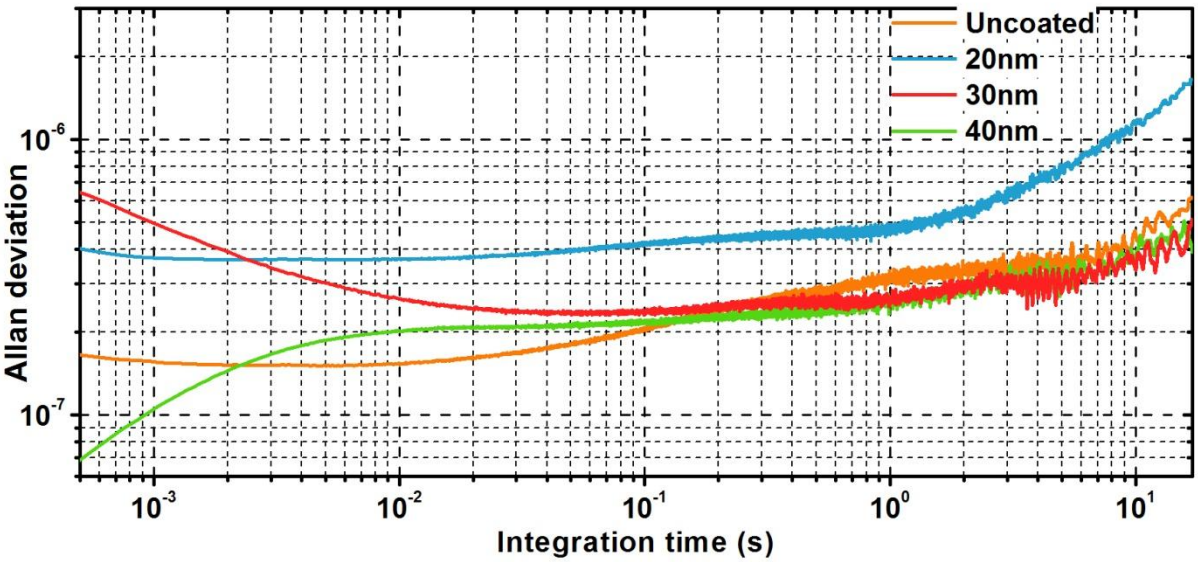

Fig. II.30: Comparison of the ADEV saturation of chips coming from the same batch with different oxide coatings. Measurement performed in Closed Loop with $\tau_{PLL} = 1ms$.

We could not evidence any significant trend in the influence of the resonator coating on frequency fluctuations. Different coatings, different viscous dampings or different resonance frequencies showed no significant impact on the observed APN. Although this would demand more experiments, a surface effect seems unlikely, like adsorbtion-desorbtion noise or charge fluctuation noise.

3.5. Temperature

We investigated the temperature dependence of the APN by using liquid Nitrogen to cool the NEMS holder described in Chapter III. Unfortunately, the setup does not feature any thermistor placed close to the NEMS or a heating plate that would have allowed for controlled temperature measurements. Hence we could only measure the MFN at room temperature and under liquid Nitrogen cooling. While theoretically at 77K, we estimated the actual NEMS temperature to be around 100K as the Argon, that has a 87K boiling point, that we projected on the NEMS surface did not condense. This may be caused by joule heating in the device nanogauges or imperfect thermal contact with the cold source. As presented in Fig. II.31, we observed improved frequency stability at low temperature.

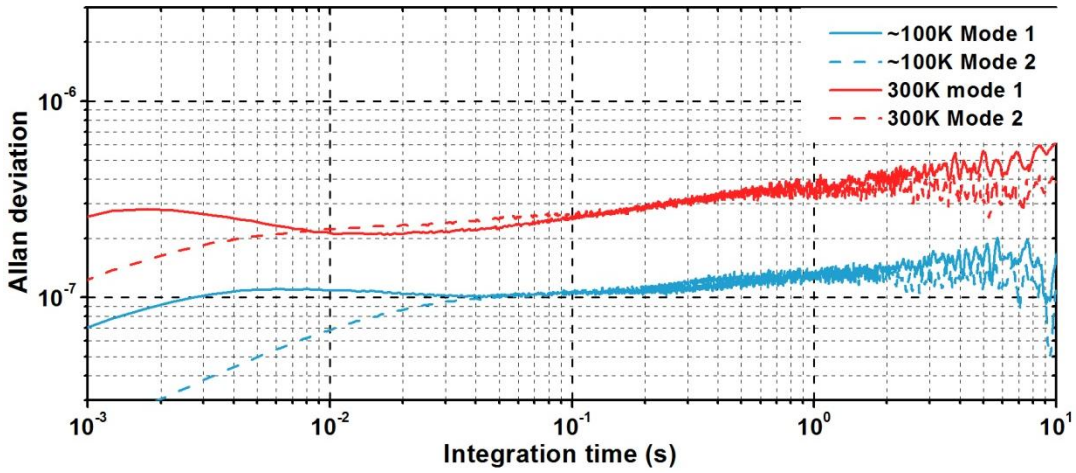

Fig. II.31: Effect of temperature on a resonator's frequency fluctuations for both mode 1 and mode 2. Measurement performed in Closed Loop with $\tau_{PLL} = 10ms$.

Cryogenic cooling provided a 2.5 factor of improvement on the frequency stability. Temperature is the only parameter that impacted the measured MFM limit in a predictive manner. All devices measured before and after cryogenic cooling presented improved frequency stability.

3.6. Excess noise facts and assumptions

Our investigation of the excess noise has experimentally demonstrated that:

- It manifests itself in the mechanical domain, upstream of the mechanical-to-electrical transduction, and downstream of the electrical-to-mechanical actuation
- It is not influenced by surface coating or doping level
- Its level changes with temperature, the only parameter we found could change the frequency stability
- The frequency noise it induces in a given bandwidth or integration time does not depend on quality factor, as opposed to the induced phase noise, whose level changes with the quality factor

A number of additional assumptions can be made about this excess noise from these measurements: they are consistent with the presence of a direct frequency noise source (as opposed to an additive amplitude noise in the signals which would increase with drive for example). It could be due to changes in the environment, generating local temperature fluctuations, inducing changes in the elastic modulus, hence frequency fluctuations. However we observed that the MFN is uncorrelated on spatially close devices and probably not caused by environmental fluctuations. We found out that the MFN limit can be decreased with lower temperature: MFM could come from thermally activated phenomena such as charge trapping or motion of crystalline defects and impurities in the Si lattice [18].

4. Conclusion

In this chapter, we have shown our mass resolution is limited by a source of noise in the mechanical domain, which is not well understood. During the course of this work, Fong *et al.* [18] performed related studies on the phase noise of ultra high Q silicon nitride resonators. Their paper leads to similar conclusions such as:

- Higher Q leads to higher phase noise
- Phase noise is independent of the actuation
- The noise spectrum is proportional to $\frac{k_b T}{f}$

They point out that temperature fluctuation [1], adsorption-desorption of molecules [13-14] or molecule diffusion along the resonator cannot account for the observed $\frac{k_b T}{f}$ noise spectrum and advocates for a model describing fluctuations with a broad spectrum of thermally activated relaxation times in the frame of the Dutta-Dimon-Horn model [21]. Their hypothesis is that the noise is caused by material defects motion. Elastic dipoles present at point defects of the crystalline lattice generate local modification of Young's modulus. The dipoles present two orientations that can be thermally switched, producing a $\frac{k_b T}{f}$ noise spectrum if we follow Dutta-Dimon-Horn model with a flat distribution of the activation energy.

Most of our experiments are in agreement with this theory except for the study of the different doping levels where a higher doping concentration should lead to a higher number of defect density hence higher frequency fluctuations. However, it is probable that the annealing step performed after doping may partially heal point defects introduced by the implantation step. Therefore, additional studies should be performed on resonators where point defect introduction is well controlled.

Progressing in the understanding of this source of noise is critical in the sense that it sets our mass resolution, and hence the future specific applications the technology we propose can address. Future experiments should include material variations, controlled defect introduction associated with Transmission Electron Microscopy (TEM) or other methods to characterize the density of defects. Then, different process steps might be optimized (implantation, annealing temperature etc.) for frequency fluctuation minimization.

Meanwhile, we made the first proof of concept of mass sensing with small arrays of flexural beam resonator as a first step toward massively parallel mass sensing with thousands of individual devices produced with VLSI fabrication processes. The first essential achievement in our progression consisted in validating the concept of NEMS-MS with an individual device. This result is reported in the upcoming Chapter III.

Bibliography

[1] A. N. Cleland and M. L. Roukes, “Noise processes in nanomechanical resonators,” *J. Appl. Phys.*, vol. 92, no. 5, p. 2758, 2002.

[2] K. L. Ekinci, Y. T. Yang, and M. L. Roukes, “Ultimate limits to inertial mass sensing based upon nanoelectromechanical systems,” *J. Appl. Phys.*, vol. 95, no. 5, p. 2682, 2004.

[3] J. Chaste, A. Eichler, J. Moser, G. Cballos, R. Rurali, and A. Bachtold, “A nanomechanical mass sensor with yoctogram resolution,” *Nat. Nanotechnol.*, vol. 7, pp. 301–304, 2012.

[4] E. Colinet, L. Duraffourg, S. Labarthe, S. Hentz, P. Robert, and P. Andreucci, “Self-oscillation conditions of a resonant nanoelectromechanical mass sensor,” *J. Appl. Phys.*, vol. 105, no. 12, p. 124908, 2009.

[5] W. P. Robins, *Phase noise in signal sources. Theory and applications.* 1984.

[6] E. Mile, G. Jourdan, I. Bargatin, S. Labarthe, C. Marcoux, P. Andreucci, S. Hentz, C. Kharrat, E. Colinet, and L. Duraffourg, “In-plane nanoelectromechanical resonators based on silicon nanowire piezoresistive detection.,” *Nanotechnology*, vol. 21, no. 16, p. 165504, Apr. 2010.

[7] F. N. Hooge, T. G. M. Kleinpenning, and L. K. J. Vandamme, “Experimental studies on 1/f noise,” *Reports Prog. Phys.*, vol. 44, p. 479, 1981.

[8] F. N. Hooge, “1/f Noise Sources,” *IEEE Trans. Electron Devices*, vol. 41, no. 11, 1994.

[9] S. Hentz, “Downscaling silicon resonant MEMS and NEMS sensors devices, trandsuction, non-linear dynamics and applications,” 2012.

[10] I. Bargatin, E. B. Myers, J. Arlett, B. Gudlewski, and M. L. Roukes, “Sensitive detection of nanomechanical motion using piezoresistive signal downmixing,” *Appl. Phys. Lett.*, vol. 86, no. 13, p. 133109, 2005.

[11] E. Mile, “Systèmes électromécaniques nanométriques à base de nanofils de silicium et nanotubes de carbone,” 2010.

[12] D. W. Allan, “Statistics of Atomic Frequency Standarts,” *Proc. IEEE*, vol. 54, no. 2, pp. 221–230, 1966.

[13] J. A. Barnes and D. W. Allan, “VARIANCES BASED ON DATA WITH DEAD TIME BETWEEN THE MEASUREMENTS,” *NIST Tech. Note*, vol. 1318, 1990.

[14] R. Levy, A. Dupret, and H. Mathias, “Phase noise analysis of the Frequency Tracking Oscillator,” in *Frequency Control Symposium*, 2010.

[15] “http://tf.nist.gov/general/glossary.htm.” .

[16] C. Kharrat, E. Colinet, and A. Voda, “H∞ Loop shaping control for PLL-based mechanical resonance tracking in NEMS resonant mass sensors,” *IEEE Sensors*, no. 4716641, pp. 1135–1138, 2008.

[17] P. Ivaldi, J. Abergel, G. Arndt, P. Robert, P. Andreucci, H. Blanc, S. Hentz, E. Defay, and C. E. A. Leti-minatec, “50 nm Thick AlN Resonant Micro-Cantilever for Gas Sensing Application,” vol. 1, pp. 81–84, 2010.

[18] K. Y. Fong, W. H. P. Pernice, and H. X. Tang, “Frequency and phase noise of ultra-high Q silicon nitride nanomechanical resonators,” *Phys. Rev. B*, vol. 85, no. 16, p. 161410, 2012.

[19] B. Gheshlaghi and S. M. Hasheminejad, “Adsorption-induced resonance frequency shift in Timoshenko microbeams,” *Curr. Appl. Phys.*, vol. 11, no. 4, pp. 1035–1041, Jul. 2011.

[20] Y. T. Yang, C. Callegari, X. L. Feng, K. L. Ekinci, and M. L. Roukes, “Zeptogram-scale nanomechanical mass sensing.,” *Nano Lett.*, vol. 6, no. 4, pp. 583–6, Apr. 2006.

[21] P. Dutta and P. M. Horn, “Low-frequency fluctuations in solids: 1/f noise,” *Rev. Mod. Phys.*, vol. 53, p. 497, 1981.

Chapter III: Comparison of nanomechanical mass spectrometry with conventional ion MS

This chapter presents the validation of the nanomechanical mass spectrometry approach by comparing it with conventional ion MS. First we will explain the motivation of this approach, detail the principle of NEMS-MS and describe the developed experimental setup. Then the procedure to evaluate the NEMS experimental sensitivity as well as its Limit Of Detection (LOD) and mass resolution will be detailed. Comparison of TOF-MS and NEMS-MS will be presented and explained thanks to simple NEMS-MS simulations. Finally we will probe our sensor's limits by measuring particles as low as possible and demonstrate its unique properties by weighing neutral species.

1. Motivation

One of the objectives of the Alliance for nanosystems VLSI is to build a robust system of NEMS-based mass spectrometry for biomolecule detection using VLSI processes easily transferable from the lab to the industry. Using scalable top-down silicon resonators described in Chapter 1, the Alliance performed the first demonstration of single-protein NEMS-MS in real time using simultaneous multi-mode tracking and complex error analysis [1]. An electrospray ionizer (ESI) was used to ionize the bioparticles and eject them in the differential pumping stages where a quadrupole guided the ions towards the NEMS (Fig. III.1.a). The detected frequency shifts (Fig. III.1.b) were then translated into a mass spectrum (Fig. III.1.c) comparable to a mass spectrum obtained by classical ion MS. However the mass data was deduced from frequency shifts using theoretical sensitivity, and no reference measurement could be used to assess the accuracy of the NEMS-based technique. The data could only be interpreted blindly. Indeed, while bottom-up devices have demonstrated yoctogram range limit of detection [2], our devices are designed for large macromolecules weighting and operate in a high-mass range where particles display a wide mass distribution and where there is no golden mass standard. A direct comparison of NEMS-MS with a reference MS measurement is therefore crucial to assess the true mass accuracy and the resolving power of NEMS-MS. This is an important step towards a real-world technology. This is challenging as it requires a complex setup, mass range overlap, ultra-fast measurements and a large number of detected particles.

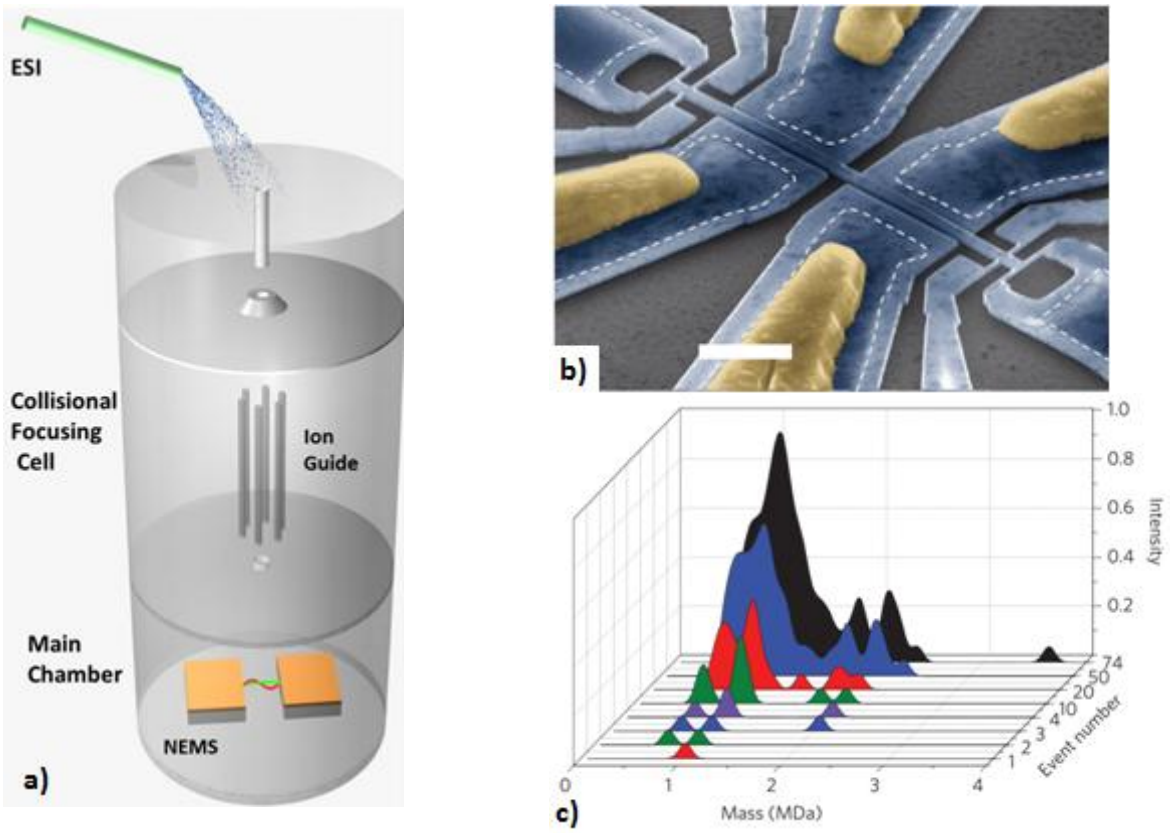

Fig. III.1: Schematic of the ESI-NEMS-MS setup (a), SEM image of the silicon resonator (b) and produced mass spectra of proteins (c)

We modified an existing nanoparticle deposition setup equipped with a QCM and a TOF mass spectrometer to allow for insertion of a NEMS sensor along with its electrical connections in the deposition chamber. Thusly, it is possible to compare NEMS-MS with TOF-MS and the QCM. The setup produces an extremely high number of particles, with respect to [1], which motivated the development of a fast electronic circuitry and post-processing algorithm able to handle thousands of events, laying the base of ultra-fast real time macromolecules measurement for future setups.

2. Building a mass spectrum with a resonator

2.1. Resonator design

The resonators that we used for NEMS-MS of individual particles are doubly clamped beams described in Chapter I. This design choice comes from the necessity to know the position of the particle of punctual mass Δm that lands on the resonating NEMS. Indeed, the frequency shift occurring on the n^{th} mode of the resonator is given by:

$$\frac{\Delta f_n}{f_n} = \frac{\Delta m}{M} \frac{\varphi_n(x)^2}{2 \times \alpha_n} \quad \textbf{(III.1)}$$

Where M is the resonator mass, f_n is the resonance frequency and $\varphi_n(x)$ the normalized mode shape of mode n. x is the normalized particle position on the beam and α_n is a numerical constant resulting of the integration of mode shape $\varphi_n(x)$ over the total length of the resonating beam:

$$\alpha_n = \int_{x=0}^{x=1} \varphi_n(x)^2 dx \quad \textbf{(III.2)}$$

Hence monitoring the relative frequency shifts of only one mode of the resonator leaves us with two unknown parameters: the analyte mass Δm and the analyte position on the beam x. Solving the equation requires extra information that can be accessed with frequency shifts of a larger number of modes. However, because of the complexity of the circuitry and the high resonances of the higher modes it is preferable to work with a minimum number of modes. Fortunately, thanks to the symmetric properties of the doubly clamped beam modes, the frequency shifts of mode 1 and mode 2 yield enough information to determine both mass and position [1]:

$$\frac{\Delta f_1}{f_1} \frac{2 \times \alpha_1}{\varphi_1(x)^2} = \frac{\Delta f_2}{f_2} \frac{2 \times \alpha_2}{\varphi_2(x)^2}$$
$$\rightarrow \; G(x) = \frac{\varphi_2(x)^2}{\varphi_1(x)^2} = \frac{\Delta f_2}{f_2} \frac{f_1}{\Delta f_1} \frac{\alpha_2}{\alpha_1} \quad \textbf{(III.3)}$$

For a doubly clamped beam, α_1 = 0.397 and α_2= 0.44. Thus provided that G is invertible, a unique solution for the particle position can be found. As presented in Fig. III.2, G(x) = y has two solutions along the complete beam length. However, since the vibrational modes of doubly clamped beams are symmetrical we can restrict the problem on the portion x = [0, 0.5] where G(x) is invertible and deduce a unique position relative to the beam centre.

Hence, although the mechanical linearity limit of doubly clamped beams are inferior to those of cantilevers, doubly clamped beams are preferred for mass spectrometry of individual particles since cantilevers require a minimum of 3 modes to determine the mass and the position of the particle.

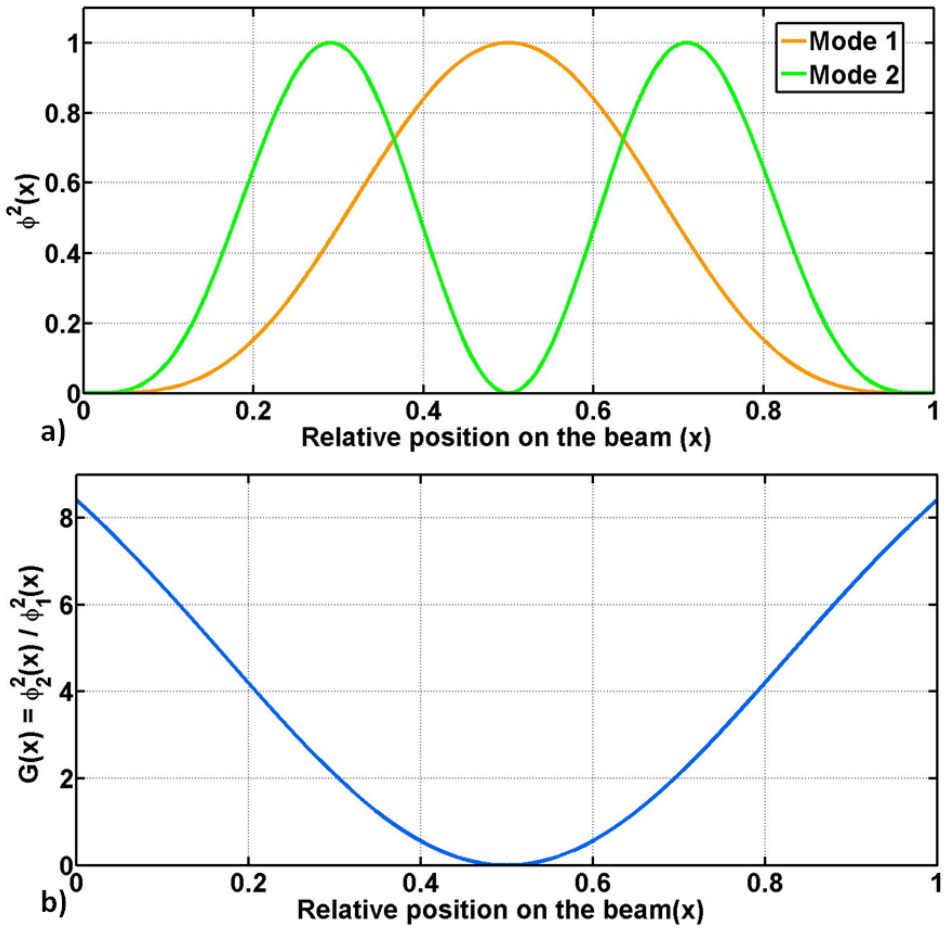

Fig. III.2: Mode 1 and mode 2 response functions (a) and their ratio versus relative position on the beam (b).

Thus the ratio between the frequency shift on mode 2 and the frequency shift on mode 1 of a doubly clamped beam yields the molecule position on the beam. Finding the molecule relative mass becomes straightforward:

$$\frac{\Delta m}{M} = \frac{\Delta f_n}{f_n} \frac{2 \times \alpha_n}{\varphi_n(x)^2} \qquad \textbf{(III.4)}$$

with n = 1 or 2

Provided the motional mass of the resonator *M* is known, the molecule mass can be eventually calculated. For better readability of the manuscript, from now on we denote:

$$\delta m = \frac{\Delta m}{M}$$
$$\delta f_n = \frac{\Delta f_n}{f_n} \qquad \textbf{(III.5)}$$

For now on, we define M as total resonant mass of the resonator, simply calculated as the material density times the volume of the resonator.

2.2. Single mode tracking

As detailed in Chapter 1, the resonator actuation is electrostatic and its motion transduction is piezoresistive. Since the devices resonate in the 10 MHz range (ω_0), the output is downmixed at several 10 kHz ($\Delta\omega$) to circumvent signal attenuation caused by parasitic impedances. A Lock In Amplifier (LIA) then measures in phase and out of phase components of the signal which yield magnitude and phase information [3]. In open loop, ω is gradually swept to detect the resonance as shown in Fig. III.3.

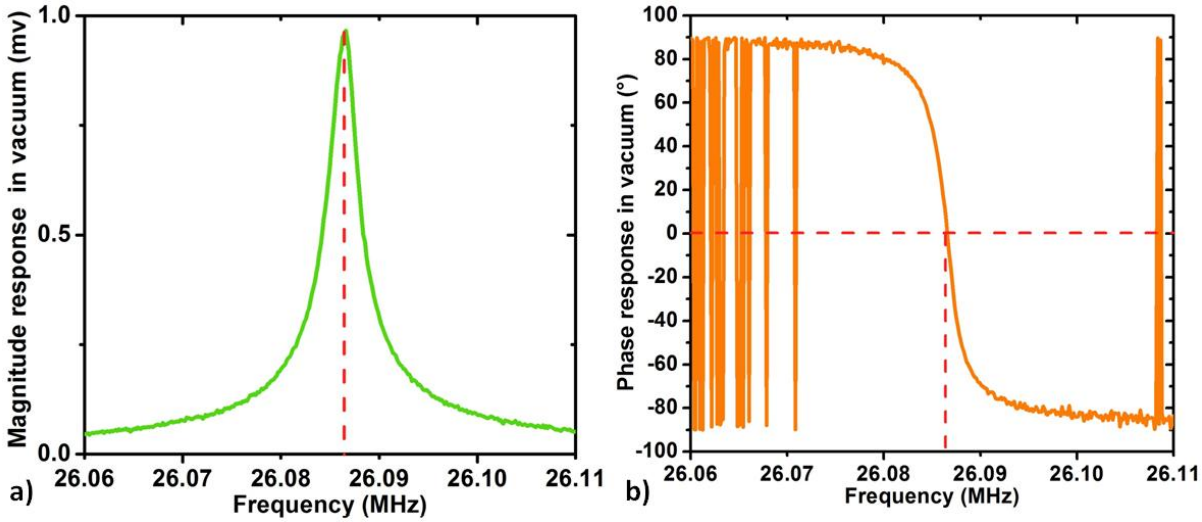

Fig. III.3: Magnitude (a) and phase (b) response of a doubly clamped beam resonating at 26.087 MHz

In Closed Loop operation, the output signal's phase difference is shaped by a corrector (CORR) that feeds a Voltage Controlled Oscillator (VCO) driving the NEMS resonator at its resonance frequency. The circuitry to track mode 1 resonance is detailed in Fig. III.4.

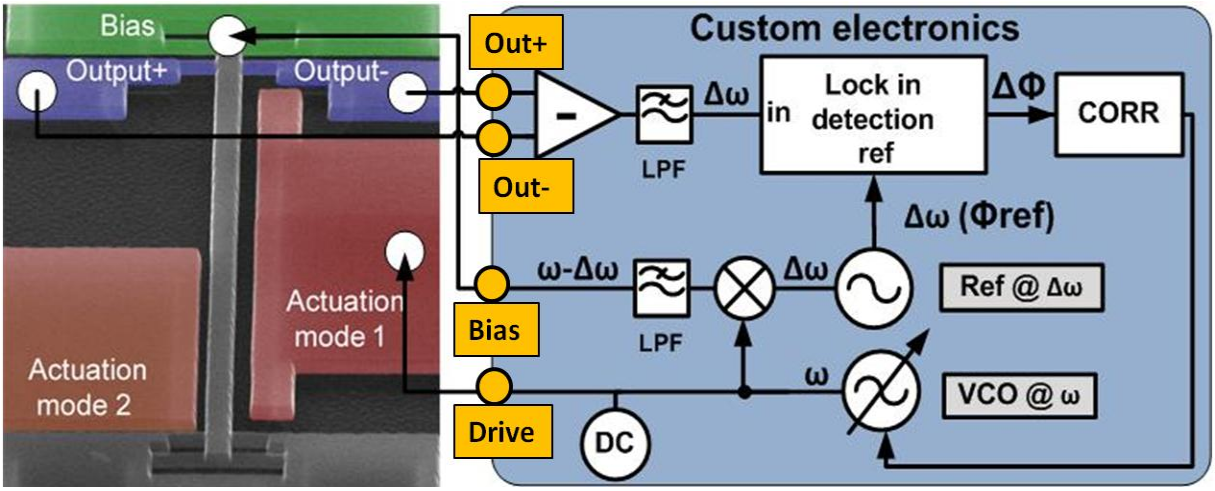

Fig. III.4: Colorized SEM image of a typical doubly clamped in-plane resonator used for NEMS-MS and its associated electronics to track mode1 with a PLL.

The corrector is a robust H∞ controller whose coefficients are calculated using a loop shaping method [4]. An experimental open loop is necessary to characterize the device transfer function and compute the coefficients accordingly. Using the open loop frequency response and appropriate LIA Sampling Rate (SR) and LIA low pass filter τ_{LIA} different PLL response time τ_{PLL} can be obtained. Generally, they are chosen to satisfy $SR_{LIA} < \frac{\tau_{LIA}}{10} < \frac{\tau_{PLL}}{100}$.

The complete setup is fully implemented in a custom electronic board [5] called the "D-Box" (see Fig. III.5.b)) that features 6 independent channels, each able to provide all the functions required for resonance tracking. This custom electronics presents several advantages over traditional equipments:

- Compactness: a single channel features both signal generation and detection functions as well as the PLL.
- Higher voltage generation at high frequencies: signals up to 10 V_{pp} can be reached (3.4 V_{pp} maximum for the Agilent N5181A signal generator)
- High speed tracking: the built-in PLL uses a robust H∞ controller that allows for PLL time response down to 1ms. Plus, an Ethernet connection with the computer overcome GPIB connection speed problems found in conventional lab equipments.

A low PLL response time is of paramount importance for our mass acquisition as we need it to be lower than the particle adsorption event rate. Indeed if two particles land on the resonator at time intervals lower than the PLL response time, we won't be able to discriminate these two particles which will generate corrupt data.

2.3. Multimode tracking

Simultaneous monitoring of mode 1 and mode 2 has been implemented in a similar way as [1] although here, we used the D-Box instead of conventional tabletop equipments for short PLL time response (down to 1ms) and compactness. Two channels of the D-Box, each being associated with a mode, were combined. High frequency signals at ω_0 are combined with appropriate power combiners while low frequency output signals at Δω are split with tees for the LIA differential input of both channels as shown in Fig. III.5.

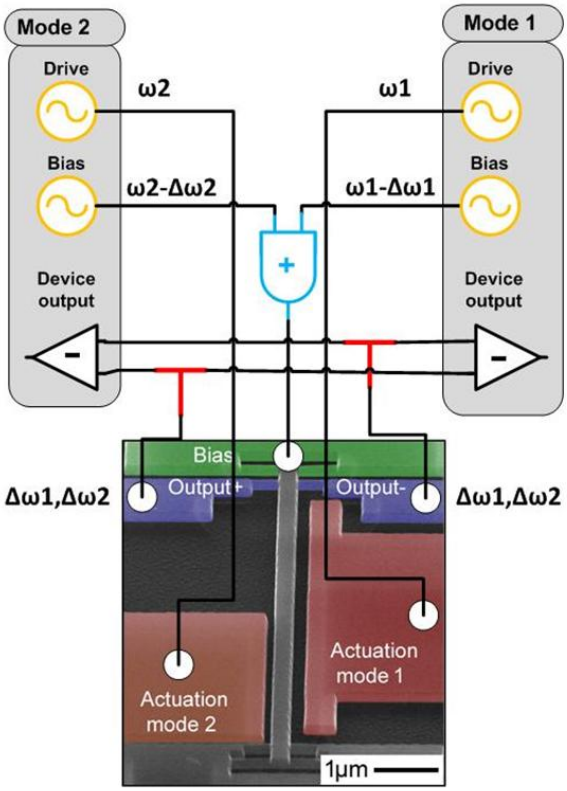

Fig. III.5: Circuitry for simultaneous mode 1 and mode 2 tracking

Simultaneous actuation of mode 1 and mode 2 is possible as resonance modes form an orthogonal base. We need to stay in a linear mechanical regime where the Euler-Bernoulli equations can be added linearly. The device nanogauges will generate two low frequency signals at $\Delta\omega 1$ and $\Delta\omega 2$, each carrying the information of mode 1 and mode 2 resonances respectively. Since the LIA inputs of each D-Box channel receive both signals, they need to be differentiated using different carrier frequency i.e. $\Delta\omega 1 \neq \Delta\omega 2$. Fig. III.6 shows how the information of mode 1 carried by $\Delta\omega 1$ is retrieved: the LIA dedicated to mode 1 monitoring detects only the component well-matched with its internal reference $\Delta\omega 1$. However, some cross-talk with $\Delta\omega 2$ may be obtained if $\Delta\omega 1$ and $\Delta\omega 2$ are not chosen carefully.

A LIA performs the detection of specific frequency component $\Delta\omega$ by multiplying the input signal to a reference at $\Delta\omega$ before filtering byproducts of the multiplication to keep a DC signal. Thus in normal operation, the time constant of the low pass filter (LPF) needs to be chosen high enough to filter out $2\Delta\omega$. In bi-mode operation, two additional multiplication byproducts are added: $\Delta\omega 1+\Delta\omega 2$ and $\Delta\omega 1-\Delta\omega 2$. In a single mode scheme where $2\Delta\omega$ is correctly filtered, $\Delta\omega 1+\Delta\omega 2$ is likely to be filtered in bi-mode scheme as well. However $\Delta\omega 1-\Delta\omega 2$ needs to be chosen high enough for efficient filtering. The lowest LPF time constant used in our experiments is 1ms and a typical $\Delta\omega$ value is 70 kHz. For bi-mode operation we used $\Delta\omega 1$ = 95 kHz and $\Delta\omega 2$ = 65 kHz to ensure that $\Delta\omega 1-\Delta\omega 2$ = 30 kHz stays out of our 1 kHz bandwidth.

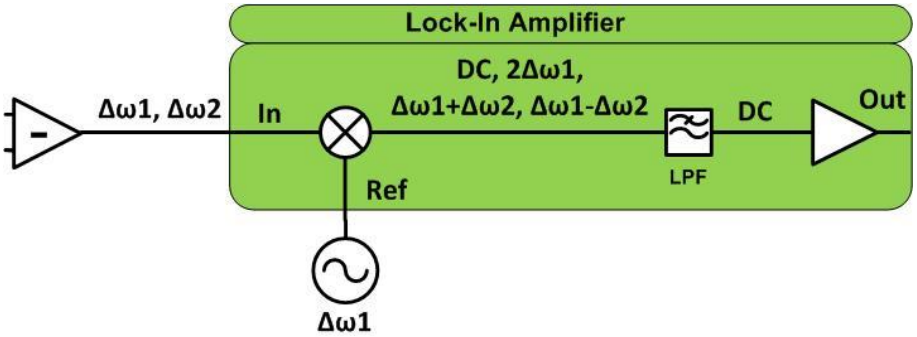

Fig. III.6: Detection of the Δω1 component in the D-Box channel associated with mode 1 tracking. Provided good filtering, we only get a DC signal proportional to Δω1.

Our multimode setup requires only 2 D-Box channels, 1 power combiner, 2 tees and 11 electrical cables while conventional lab equipments that would have required 4 HF voltage sources, 1 DC voltage source, 2 LIA, 2 frequency multipliers, 1 bias tee, 1 power combiner, 17 electrical cables and 6 GPIB connections. Our setup is way more compact than what has been previously done [1] and for faster PLL tracking.

This setup enables the simultaneous monitoring of frequency jumps on both mode 1 and mode 2 caused by particle adsorptions on the resonant beam as presented in Fig. III.7.

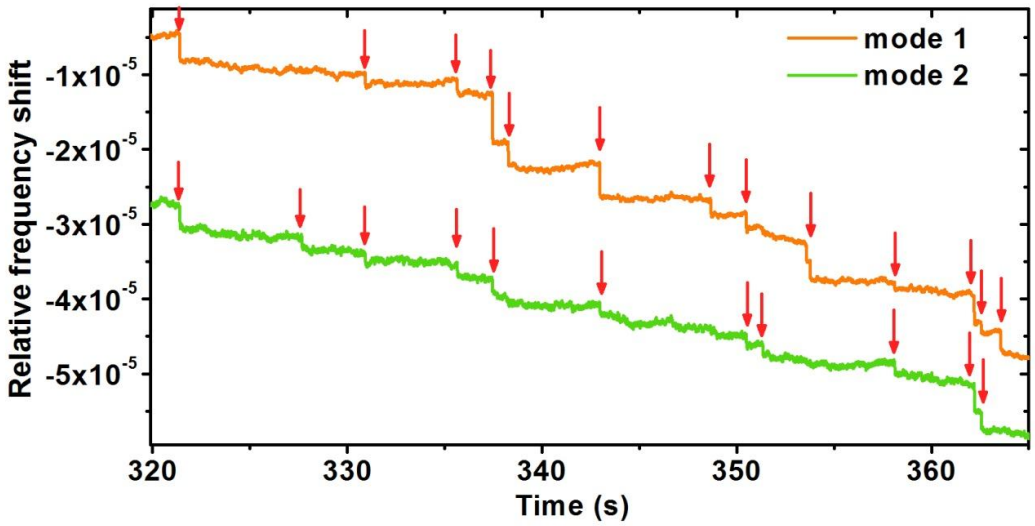

Fig. III.7: 15 mass induced frequency jumps obtained simultaneously on mode 1 and mode 2 in 25s.

It can be noted that while most mass adsorption events generate a frequency shift on both modes, some only affect one mode. This is due to the dependence of the frequency shift on the particle position. For instance a particle landing at the center of the beam will induce a frequency shift on mode 1 but none on mode 2: the middle of the beam is an antinode of the mode 1 shape but a node of the mode 2 shape (Fig. III.2).

NEMS-MS acquisition of nanoparticles presented further in this Chapter can produce up to 2000 detected events. Thus an automated algorithm for frequency jump detection and evaluation needs to be developed.

2.4. Fast and simple jump detection and quantification

Indeed, as we are progressing toward detection of an extremely high number of events, manual jump detection and quantification needs to be abandoned in favor of robust automated algorithm. A large number of step detection algorithm has been developed based on various techniques such as wavelet decomposition ([6], [7]), group fused Lasso [8], Schwarz Information Criterion [9], or the student t-test [10]. The latter was chosen for its simplicity of implementation. The student t-test is applied on a set of data points where the t function is computed successively for each point y_n:

$$t = \frac{\overline{y_1} - \overline{y_2}}{\sqrt{\frac{\sigma_1}{N} + \frac{\sigma_2}{N}}} \qquad \textbf{(III.6)}$$

where y_1 and y_2 are sets of N points right before and after point y_n. $\overline{y_1}$ and $\overline{y_2}$ are the mean of those sets while σ_1 and σ_2 are their standard deviations. N is chosen as the number of data points corresponding to the PLL response time τ_{PLL}. The t function is a good estimator of abrupt change-points and t function peaks indicate the presence of a frequency jump as shown in Fig. III.8.

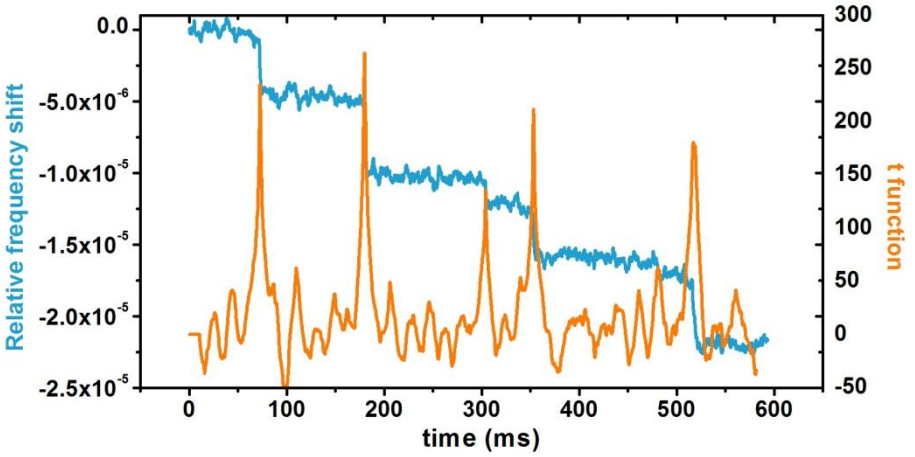

Fig. III.8: Relative frequency shift and its associated t function. Abrupt frequency shifts translate to peaks in the t function.

However this technique can be extremely long to compute especially in our situation where the data sampling rate can be very important (up to 20 kHz). In addition, the technique requires manually setting a specific threshold over which a point is considered as a change-point. The choice of this threshold is arbitrary and can prove to be difficult when the data is noisy.

We decided to develop a simple but robust step detection algorithm based on two steps: data denoising and precise step localization with the student t-test. Denoising the data reveals abrupt frequency jumps on which the student t-test is applied to localize its middle.

2.5. Noise characterization

Denoising requires a "noise multimode acquisition": the resonance frequencies of mode 1 and mode 2 are simultaneously monitored at normal operating conditions without any mass landing events. The frequency raw data points are averaged over an integration time τ_{AVG} before computation of the fractional frequency differences:

$$y_n(i) = \frac{f_n(i+1) - f_n(i)}{f_n} \qquad \textbf{(III.7)}$$

n=1 or 2 for mode 1 or 2 respectively

y_n denotes the relative frequency changes from one point to the next one. τ_{AVG} is usually a multiple of τ_{PLL}.

A scatter plot of fractional frequency differences of mode 2 with respect to mode 1 can be fitted with a bivariate Gaussian distribution defined by three parameters σ1, σ2 and ρ, respectively the standard deviation of mode1, mode 2 and the correlation factor. These parameters can be easily fitted with a Matlab function and used to obtain an elliptical contour fit calculated at a chosen multiple of σ1 and σ2. Fig. III.9 presents a fractional frequency noise distribution featuring $\sigma1 = 2 \times 10^{-7}$, $\sigma2 = 1.4 \times 10^{-7}$ and $\rho = 0.3$ with its 3 sigma contour fit.

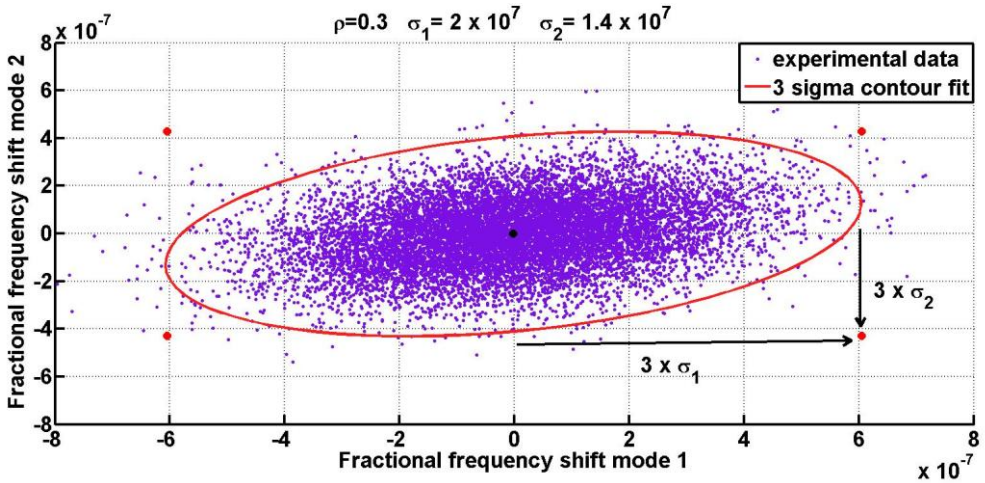

Fig. III.9: Characterization of frequency noise un multimode acquisition with a 3 sigma contour fit.

The contour fit is an ellipse defined by three parameters: the semimajor axis σ_x', the semiminor axis σ_y' and the rotation angle of the semimajor axis θ (Fig. III.10).

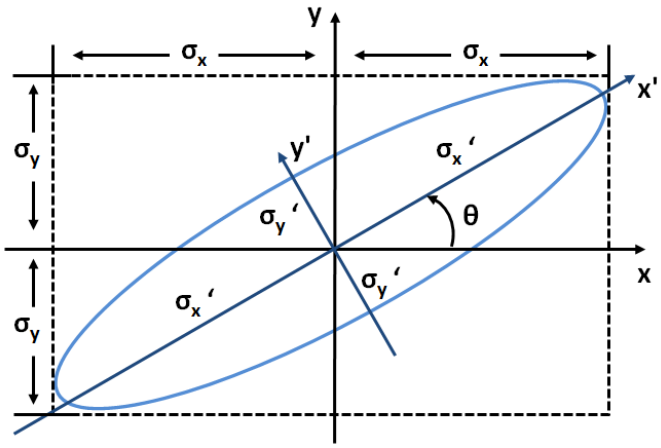

Fig. III.10: The standard error ellipse and its associated parameters.

Identifying $\sigma_x = n\sigma 1$ and $\sigma_y = n\sigma 2$ for a n-sigma standard error ellipse, these parameters can be calculated as:

$$\sigma_x' = \frac{{\sigma_x}^2 + {\sigma_y}^2}{2} + \sqrt{\frac{\left({\sigma_x}^2 - {\sigma_y}^2\right)^2}{4} + {\sigma_{xy}}^2}$$

$$\sigma_y' = \frac{{\sigma_x}^2 + {\sigma_y}^2}{2} + \sqrt{\frac{\left({\sigma_x}^2 - {\sigma_y}^2\right)^2}{4} + {\sigma_{xy}}^2} \qquad \textbf{(III.8)}$$

$$\theta = \frac{1}{2}\, tan^{-1} \frac{2\sigma_{xy}}{{\sigma_x}^2 - {\sigma_y}^2}$$

where $\sigma_{xy} = \rho\sigma_x\sigma_y$

For $\tau_{AVG} = 20ms$, typical bivariate Gaussian noise properties measured on our devices ranged around [0.25-0.5] for ρ and $[1.10^{-7} - 5.10^{-7}]$ for σ1 and σ2.

2.6. Denoising

The extracted standard error ellipse can then be used as a "denoising" tool on data acquired during a mass adsorption experiment is conducted: fractional frequency differences are plotted exactly like in Fig. III.9 (see Fig. III.11). Points outside of the standard error ellipse are considered as mass adsorption events. Points inside the ellipse are attributed to the NEMS internal noise and nulled. A 5 sigma ellipse generally deletes most noise induced fractional frequency shifts and long term drifts. An example of denoising with a 5-sigma standard error is presented in Fig. III.11.

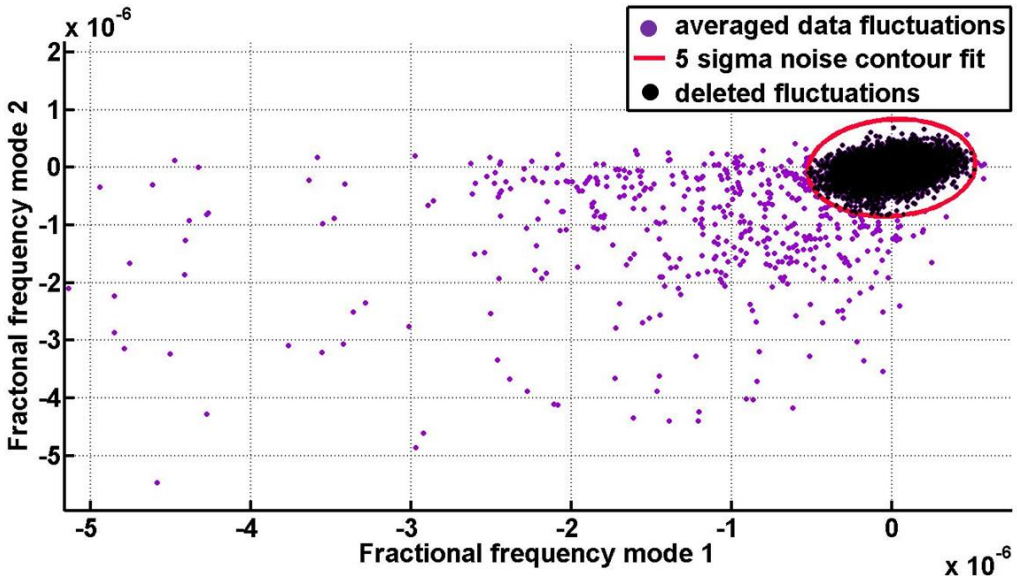

Fig. III.11: Fractional frequency scatter plot of averaged data from a cluster deposition run. Fluctuations comprised within the contour fit are "deleted" i.e. set to 0. Most points outside the ellipse are probably involved in mass induced frequency jumps.

The denoised data shows plateaus and abrupt jumps that provides a list of frequency change-point timestamps (Fig. III.12).

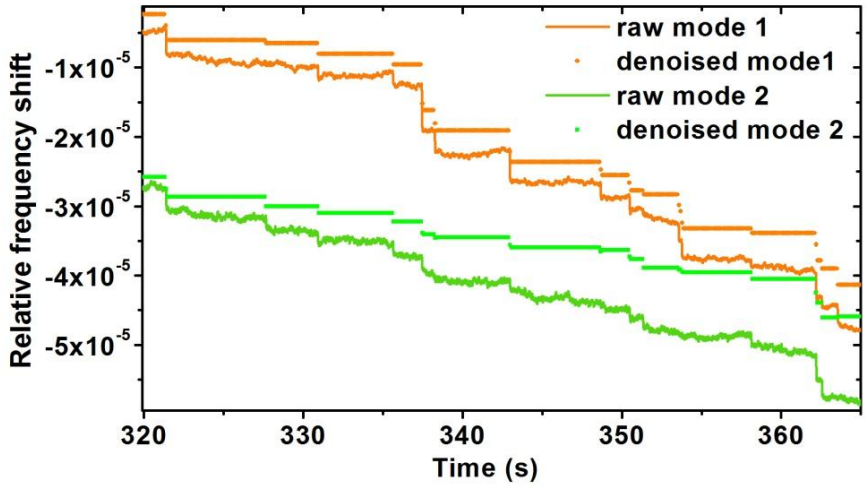

Fig. III.12: Effect of denoising on mode 1 and mode 2 relative frequencies. Mass induced frequency jumps are evidenced.

2.7. Jump detection

The student t-test is then applied on the raw frequency data over ranges centered on these change points and the maximums of the t functions computed over the chosen range provide us with a good estimation of the middle of the frequency jumps.

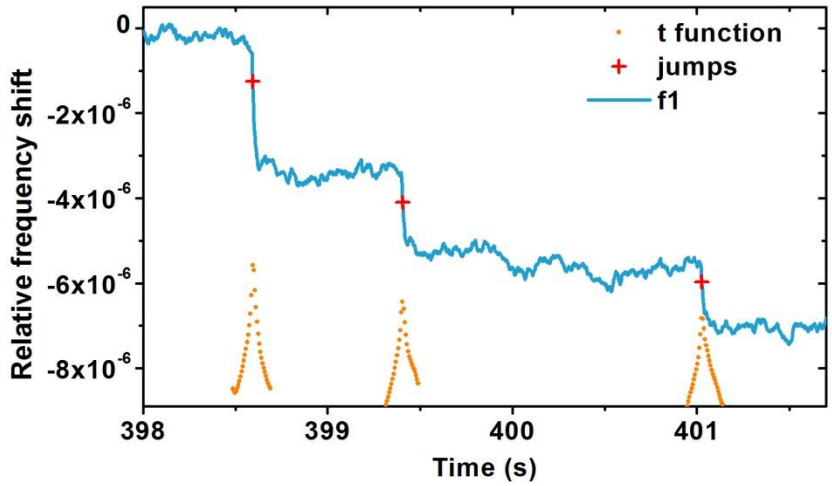

Fig. III.13: Center of the frequency jumps found with the maximum of the student t-test. The t function isn't computed over ranges where no events occur.

For each mode, we now have a list of timestamps for potential mass landing events. Thousands of events are processed in less than a few seconds. The two lists are merged into a new list where frequency jumps on mode 1 and mode 2 whose timestamp difference is smaller than τ_{AVG} are considered to be induced by the same mass landing event (Fig. III.14).

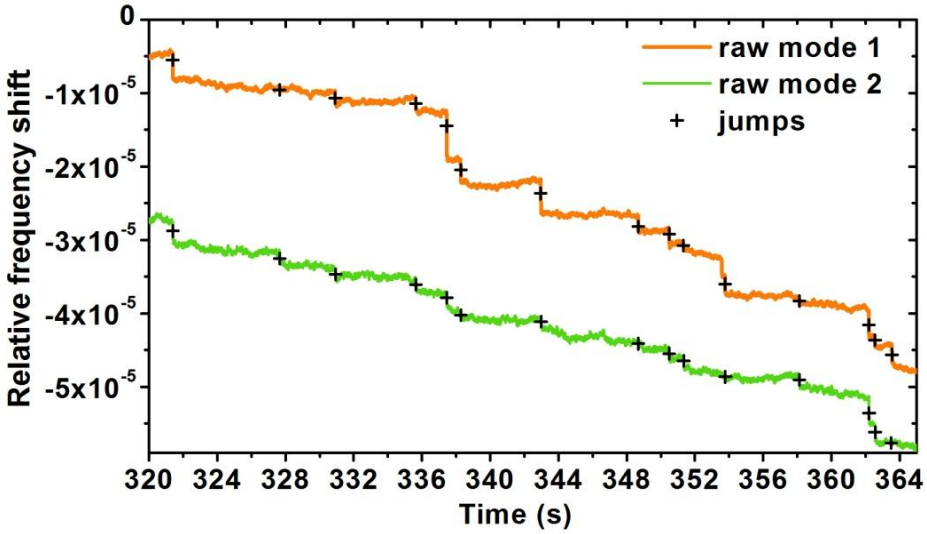

Fig. III.14: Automated frequency jump detection result.

2.8. Jump quantification

For both modes the frequency jumps are evaluated at these timestamps. For each jump occurring at time t_0, the data range before the jump at $[t_0 - 1.5\tau_{AVG}\ ,\ t_0 - 0.5\tau_{AVG}]$ and the data range after the jump at $[t_0 + 0.5\tau_{AVG}\ ,\ t_0 + 1.5\tau_{AVG}]$ are integrated over τ_{AVG} before being subtracted (Fig. III.15).

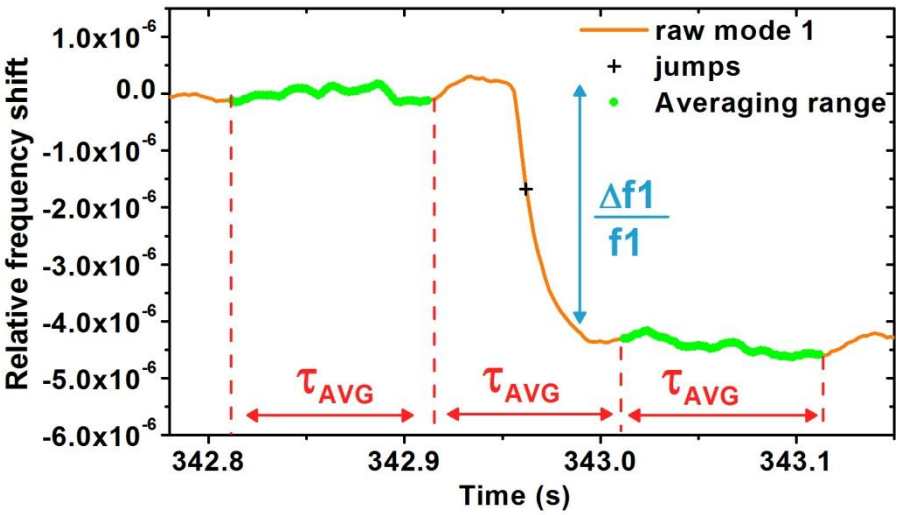

Fig. III.15: Relative frequency jump evaluation example on a mode 1 frequency jump

The jump timestamp list becomes a list of frequency shift pairs $[\delta f_1, \delta f_2]$ that can be translated to mass/position pairs$[\delta m, x]$.

2.9. Mass and position computation

For each frequency shift pairs $[\delta f_1, \delta f_2]$, the ratio $\frac{\delta f_2}{\delta f_1}$ yields the particle position using equation (III.3). Equation (III.4) yields the particle mass. A filter is then applied to rule out particles that landed on portions of the beam where mode responses are too weak: precise mass determination is obtained on portions of the beam where both mode 1 and mode 2 response are high enough. However, reducing the portion of the beam decreases the resonator sensing area hence the probability to detect a particle. Thus, a trade-off needs to be made and we defined a sensing interval on x=[0.25-0.74] and by symmetry x=[0.53-0.75] (Fig. III.16).

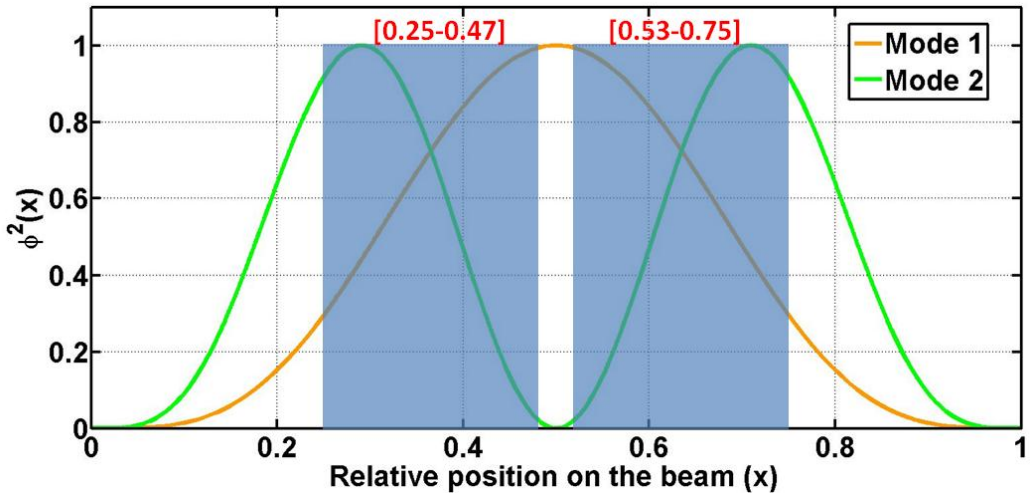

Fig. III.16: Mode 1 and mode 2 response functions with chosen sensing interval in blue.

The general idea for sensing interval determination is as follows:

- Sensing area should be maximized
- Response function of both modes should be as high as possible

We ruled out [0, 0.25], [0.75, 1] and [0.47, 0.53] because below 0.25 (or above 0.75), both response function are low while between 0.47 and 0.53, response function of mode 2 is almost null. The reasons for these precise numbers are empirical and detailed further in Section 5. As the SNR decreases, it is sometimes preferable to decrease the sensing area but a trade-off must be made with the desired number of detected particles, especially in experiments where the particle statistics is important.

When the list of frequency shift pairs$[\delta f_1, \delta f_2]$ has been translated to$[\delta m, x]$ and filtered according to particle position on the beam, a first idea of a mass spectrum can be obtained thanks to a simple histogram as shown in Fig. III.17.

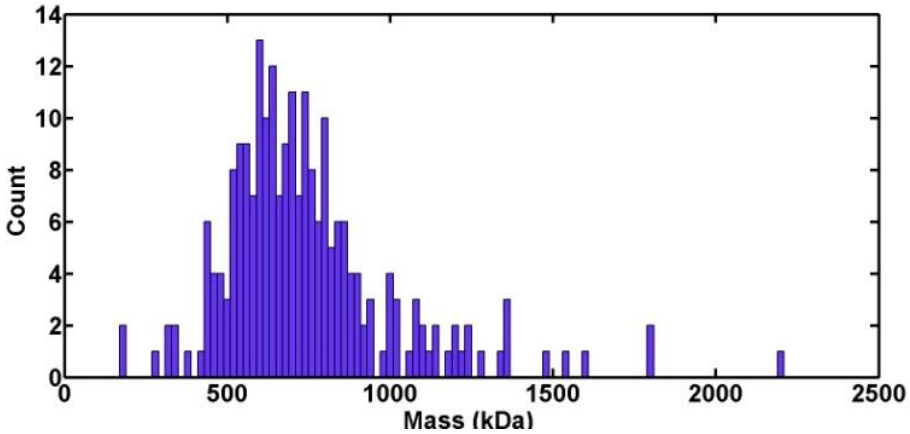

Fig. III.17: Mass histogram produced with fractional frequency jump pairs extracted from an experimental acquisition of metallic nanoclusters with a mean mass centered on 600kDa

We have successfully constructed a mass spectrum from our raw multimode frequency data. However, this simple representation where each measured mass is represented as a dirac does not take into account the measurement uncertainties. Indeed, the resonator frequency fluctuations generate uncertainty on the values of the measured frequency shifts that directly translates to uncertainty on mass and position of the particles. An elegant way to represent this uncertainty has been developed by Dr. Selim Hanay at Caltech [1]. It consists in characterizing the NEMS frequency fluctuations and fitting them to a bivariate gausian distribution law. We already performed this for the denoising step when we extracted ρ, σ1 and σ2. The distribution, represented in the $[\delta f_1, \delta f_2]$ plane, is associated with an experimental frequency jump pair and translated in the $[\delta m, x]$ plane using transfer matrices. Integration along the x dimension of the Joint Probability Function $JPDF_{\delta m,x}(\delta m, x)$ followed by normalization yield a mass event represented by a Probability function (PDF) accounting for the measurement incertitude. The final mass spectrum is built by successive addition of all events (Fig. III.18).

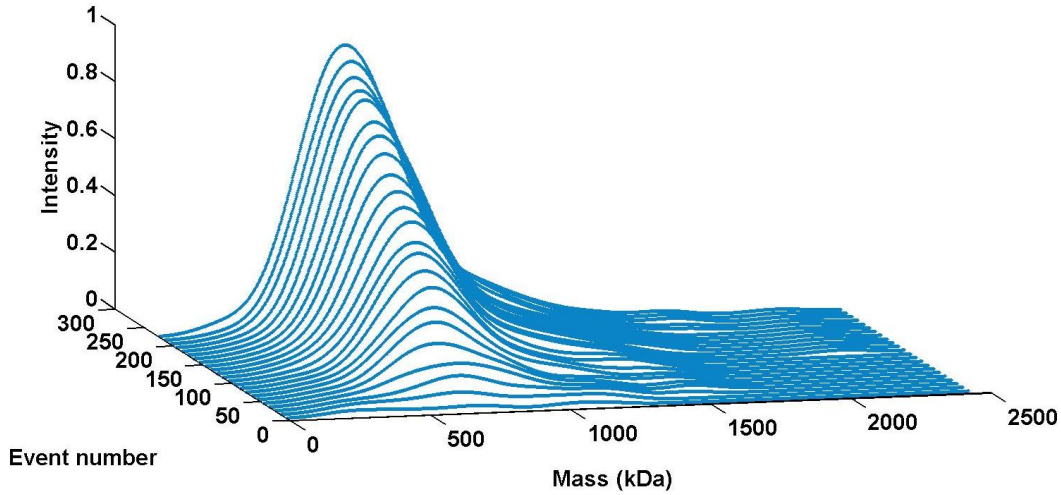

Fig. III.18: Event-per-event built mass spectra of tantalum nanoclusters centered on 600kDa.

More complete details on the complex error analysis are provided in Appendix C. The algorithm was implemented in a Matlab code optimized for ultra-fast computation allowing for a future implementation of actual real time NEMS-MS where the experimenter will be able to follow the mass spectrum evolution in real time during the acquisition. By removing all unnecessary computation where the JPDF can be neglected and distributing the code processing workload to 8 CPU operating in parallel (i.e. optimizing the code for multicore CPUs), we were able to process a 4 min multimode mass acquisition featuring 1500 events in 40 seconds whereas it took around 30 minutes before optimization. The possibility to quickly build mass spectra has made a significant difference for simulations and experiments where results could be accessed almost instantaneously.

In summary, we have built a PLL-based circuitry to monitor the frequency shifts on vibrational modes 1 and 2 of a doubly clamped nanomechanical resonator using a custom electronic equipment fast enough for event rates down to the millisecond. An algorithm has been developed to automatically detect mass induced frequency jumps and translate them to a mass spectrum. This system has been evaluated in a dedicated setup where the mass spectrum of metallic nanoclusters can be acquired by either NEMS-MS or conventional ion MS, here Time Of Flight (TOF) Mass Spectrometry.

3. Experimental setup

The comparison of NEMS-MS and conventional ion MS requires a setup featuring:

- A stable mass source
- Mass collimation and deposition in vacuum
- A Mass Spectrometer able to produce a mass spectrum of the produced mass flux

- The possibility to insert a NEMS sensor with its electrical connections in the mass flux.

Hence, we decided to introduce the NEMS in the deposition chamber of a sputtering-gas aggregation setup able to produce nanometric metallic clusters whose deposition rate and mass distribution can be measured by a Quartz Crystal Microbalance (QCM) and a Time-Of-Flight (TOF) Mass Spectrometer respectively [11]. The deposition is performed in high vacuum (1×10^{-5} mbar). The original setup was built by Robert Morel, Lucien Notin and Ariel Brenac from the department DSM/INAC/SP2M in CEA-Grenoble. Its initial purpose was to generate nanometric metallic clusters with remarkable magnetic properties and deposit them on a substrate for further study of their size-dependent attributes or to create novel devices exploiting the nanoclusters properties. The setup is shown in Fig. III.19.

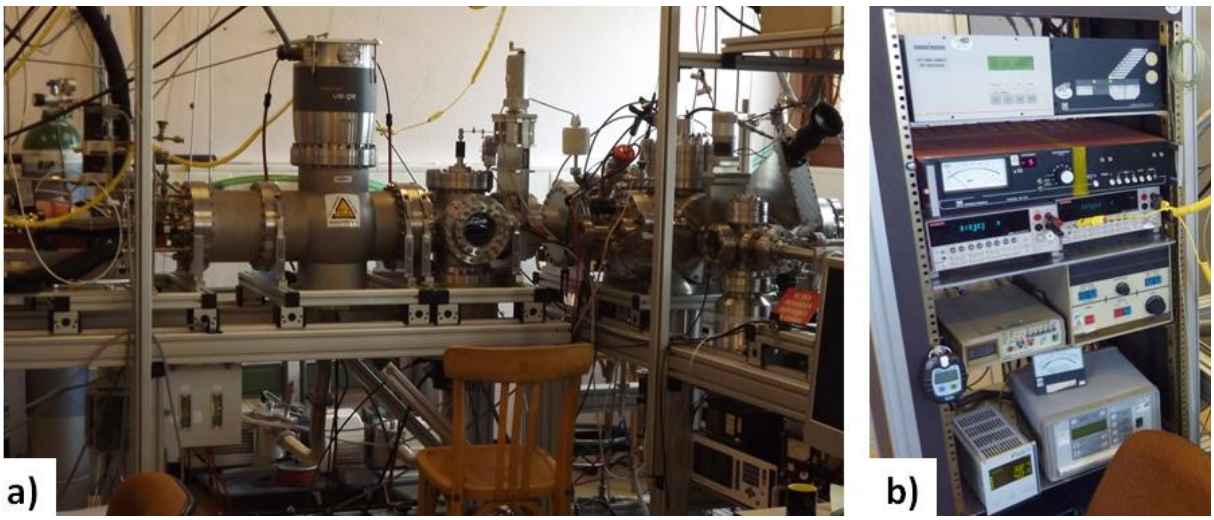

Fig. III.19: Photo of the setup (a) and its instrumentation rack (b).

The bench is composed of four main chambers:

- A cluster source where metallic clusters are generated
- A shutter chamber where the cluster flux can be reduced if necessary
- A deposition chamber where the cluster flux hits either the substrate or the QCM. Both substrate holder and QCM are set on a translational stage that allows to quickly switch from mass deposition rate measurement to mass deposition on the substrate
- An in-line Time-Of-Flight Mass Spectrometer (principle detailed in Chapter I). When both QCM and substrate holder are retracted, the cluster flux enters the final chamber where particles are accelerated before measurement of their mass-to-charge ratio.

The metallic nanoclusters are generated by using the sputtering gas-aggregation technique [11], [12], [13]. The cluster growth is performed by sputtering a metallic target with a magnetron head inserted in a liquid nitrogen cooled chamber. Argon is chosen as the carrier gas because of its high atomic number and low chemical reactivity. Positives Argon ions generated in plasma bombard at high speed a metallic target polarized at -300V, ejecting metallic atoms and secondary electrons that further maintain the plasma. The permanent

magnet traps the secondary electrons in helical paths around the magnetic lines hence provoking confinement of the plasma on the target surface. This results in higher ionizing collision rates with Argon leading to higher sputter rates and lower pressure operation.

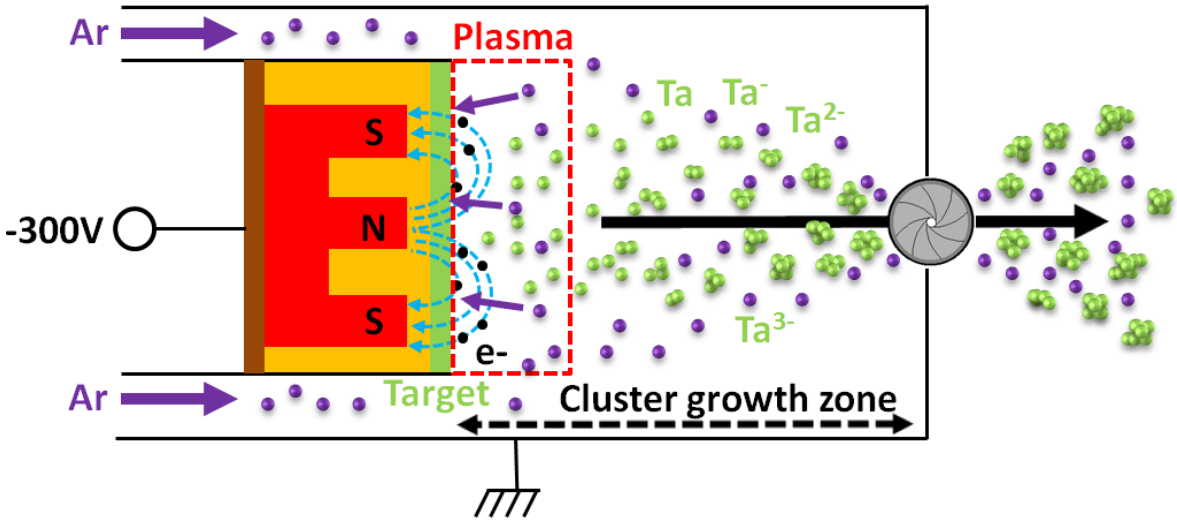

Fig. III.20: Schematic of the cluster source. A permanent magnet (red) confines a plasma on the metallic target (green), for example Tantalum. Positive ions are accelerated toward the target by a high negative voltage on the backside electrode. Atoms aggregate in the cluster growth zone before exiting the source through a tunable diaphragm.

By collisions with the cold argon gas, the sputtered atoms aggregate in the growth zone before being expelled into the high vacuum deposition chamber through a differential pumping stage. The metallic cluster sizes as well as the cluster deposition rate depend on the following parameters:

- Properties of target material
- DC power on the backside electrode
- Argon inlet flux
- Pressure in the cluster growth zone
- Length of the cluster growth zone

DC power and Argon flux are controlled by electronic equipments while pressure in the cluster growth is tuned with the diameter of the diaphragm at the output of the cluster source. The magnetron head is set on a translational stage enabling adjustment of the growth zone length.

Hence by proper control of the parameters, the source can produce metallic nanoclusters with tunable deposition rate and diameter (mean diameter: approximately 2 to 9.5 nm depending on the target material) which proves to be ideal for studies and calibration of our resonant mass sensors. Thus, the bench was modified to replace the substrate by a NEMS, the difficulty being to bring electrical connections and NEMS cryogenic cooling in the high vacuum chamber. A schematic of the modified setup is presented in Fig. III.21.

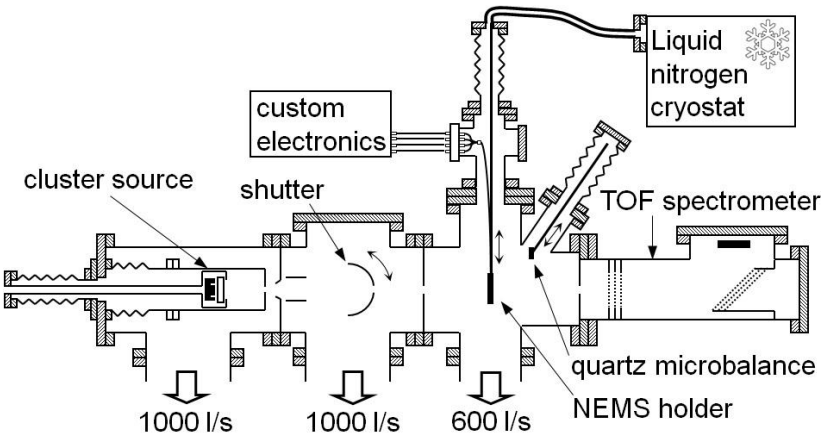

Fig. III.21: Schematic of the modified experimental setup. From left to right: cluster source, shutter chamber, deposition chamber and Time Of Flight Mass Spectrometer

A 4 way standard cross is set on a translational stage with one flange joined to the bench deposition chamber, the opposite one connected to the liquid nitrogen inlet/outlet system while the two remaining flanges are combined with vacuum feedthroughs for the electrical connections (Fig. III.22).

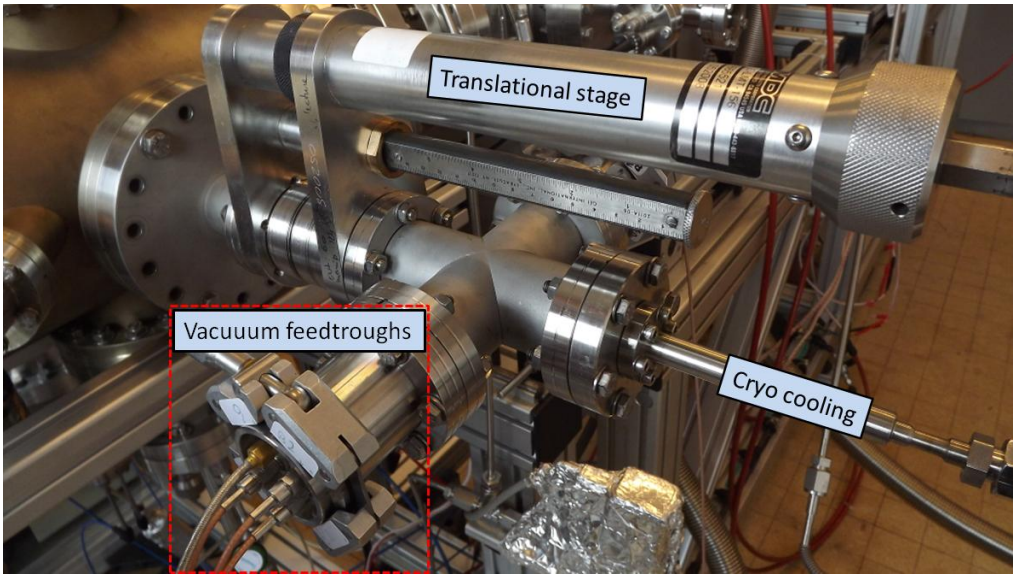

Fig. III.22: Photo of the assembly built to reach the NEMS holder inserted in the deposition chamber with electrical connections and liquid nitrogen cooling

The vacuum feedthroughs are custom built and have been assembled by Lucien Notin (DSM/INAC/SP2M) from a peek strip (Polyetheretherketone) and SMA jack to jack bulkhead hermetic seals. This enabled us to obtain 4 compact SMA feedtroughs per flange: a total of 8 electrical connections are available in the deposition chamber. In addition, unlike commercial feedthroughs, our custom ones keep the ground signals isolated from the bench virtual ground. The liquid nitrogen cryostat cools the NEMS holder at theoretically 77K but without any direct possible measurement of the actual NEMS temperature, we estimate the NEMS temperature of the order of 100K. Cooling the NEMS at these temperatures generally reduces its frequency fluctuations by a factor of two.

A NEMS holder, designed to optimize the thermal transfer from the holder itself to the NEMS chip, has been machined in brass by André Poinard and Henry Blanc (LETI/DCOS/SCMC/LCMS). In the old version the only thermal path toward the NEMS ran through the interconnecting pins between the motherboard and the PCB. Here, a small brass piece, used as a thermal contact, fills the physical gap present in previous holder versions between the motherboard and the PCB. To keep the NEMS isolated from the bench virtual ground, the system motherboard-thermal contact-PCB is sandwiched with kapton sheets which are electrical isolators with good thermal conductance.

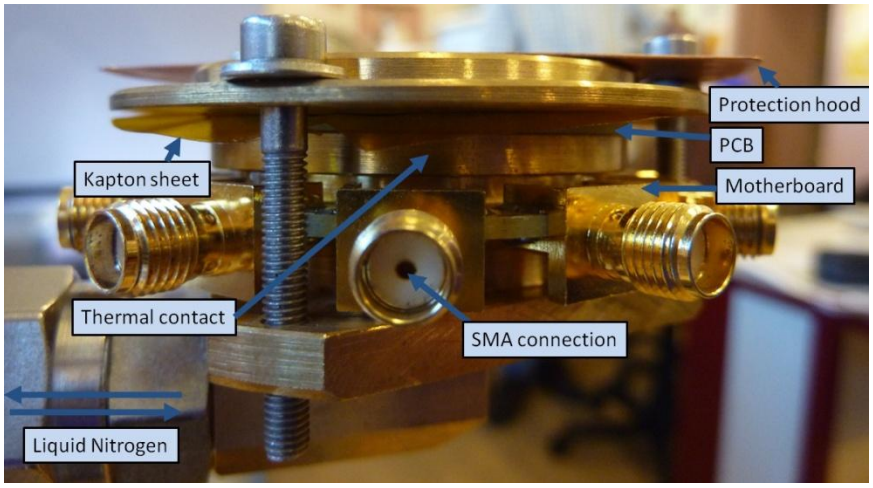

Fig. III.23: Old (top) and new (bottom) NEMS holder. In the old version the only thermal path toward the NEMS ran through the interconnecting pins between the motherboard and the PCB.

The NEMS holder also features a protection hood (usually a copper sheet) to localize cluster deposition on the wirebonded device, keeping most of the other devices and the PCB intact for subsequent experiments (Fig. III.24).

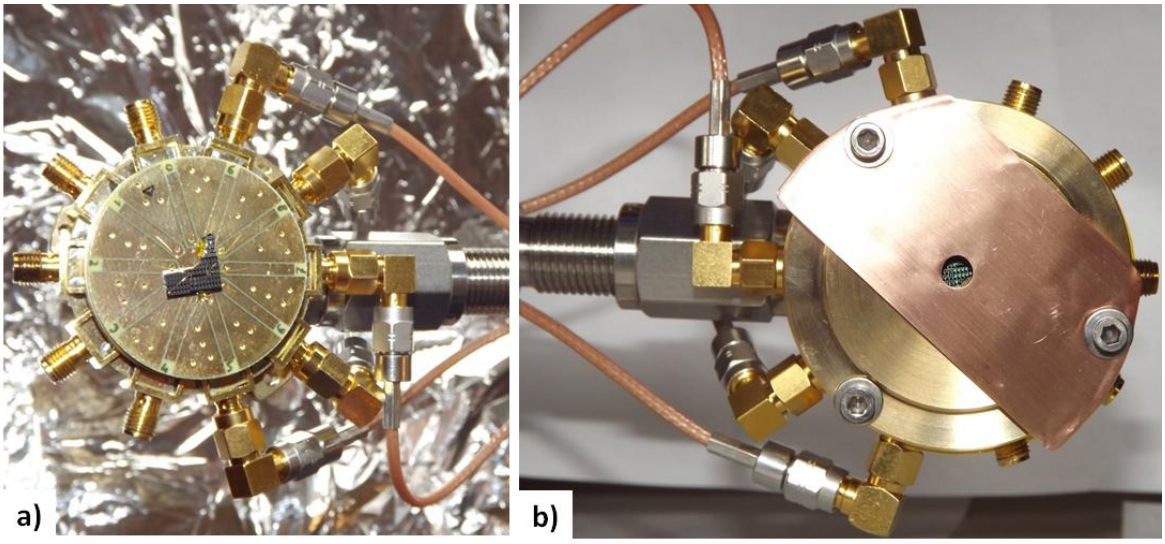

Fig. III.24: NEMS holder before (a) and after (b) protection hood mounting.

Three operating modes are eventually possible with the resulting modified setup in the deposition chamber where the cluster flux can either hit the NEMS sensor or the QCM or

enter the TOF module: in addition to the mass deposition rate provided by the QCM, we are able to measure the nanocluster mass distribution by both TOF-MS and NEMS-MS in vacuum in the same experimental conditions (Fig. III.25).

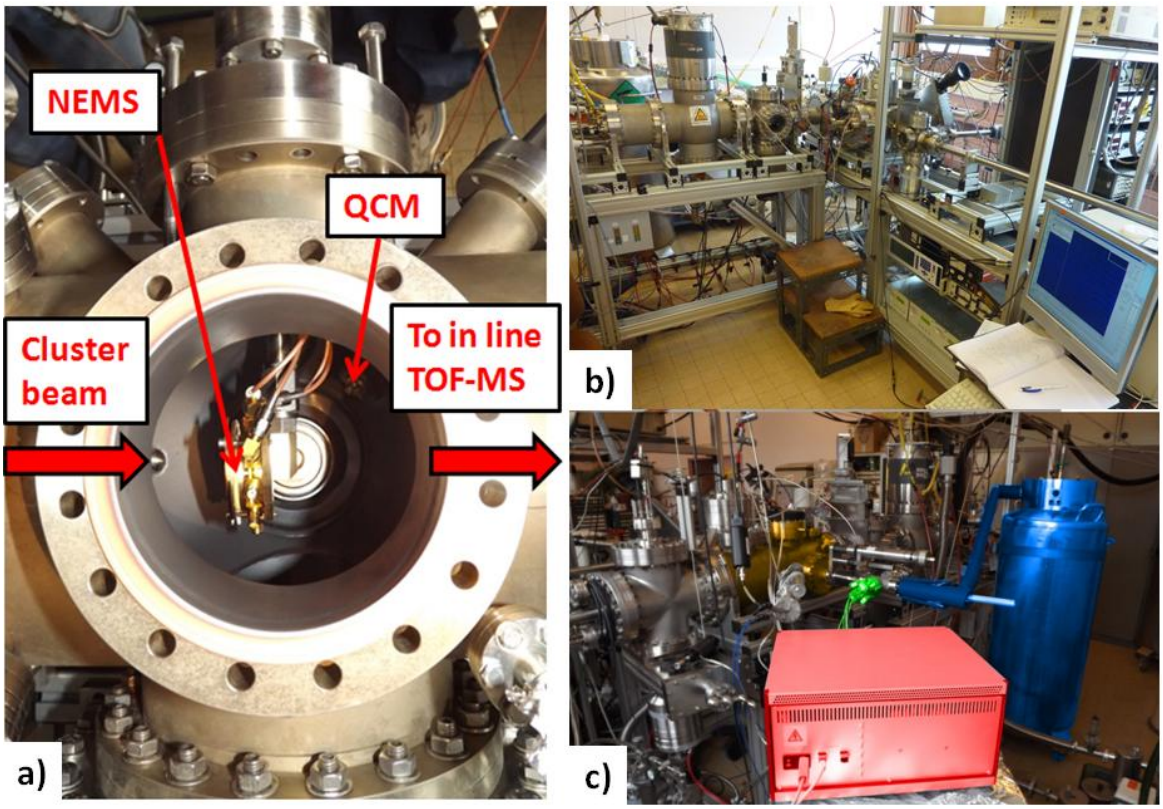

Fig. III.25: Top view of the deposition chamber showing both retractable NEMS holder and QCM (a), general front view of the setup (b) and colorized view of the setup (c) featuring the electronics (red), the vacuum feedthroughs and electrical connections (green), the cryostat cooling (blue) and the deposition chamber (orange).

A doubly clamped beam was inserted in the bench for NEMS-MS measurements. Before each run, a calibration of the sensor mass sensitivity was carried out before acquisition of nanocluster mass spectra.

4. Mass sensitivity calibration

Mass landings on the resonant beam induce frequency shift pairs $[\delta f_1, \delta f_2]$ that can be translated to pairs $[\delta m, x]$, with $\delta m = \frac{\Delta m}{M}$. Thus precise determination of M is essential for accurate estimation of the particles' masses. However, while the nominal resonance frequencies f_1, f_2 or the mass induced frequency shifts $[\delta f_1, \delta f_2]$ can be obtained experimentally, we have no direct measurement of M. The total resonant mass is usually calculated as:

$$M = \rho_{Si} \cdot t \cdot w \cdot L \qquad \textbf{(III.9)}$$

ρ_{Si} is the density of silicon while t, w and L are the beam thickness, width and length respectively.

We propose experimental determination of this value by characterizing the linear frequency response to uniform mass deposition along the beam. The theoretical frequency response of a resonator to a uniform deposition along the beam of mass $\Delta m \ll m_0$ is [14]:

$$\frac{\Delta f_n}{f_n} = \frac{\Delta m}{2 \times M} \qquad \textbf{(III.10)}$$

where f_n is the resonance frequency of mode n and M is the total mass of the resonator.

Thus the total mass deposited on the sensor is:

$$\Delta m = \varphi_{QCM} \times L \times w \times 10^{12} \qquad \textbf{(III.11)}$$

where φ_{QCM} is the QCM deposition rate in g/s/µm²

Combined with (III.10) the relationship between the measured fractional frequency shift rate and φ_{QCM} is:

$$\frac{\Delta f_n}{f_n} = \frac{\varphi_{QCM} \times 10^{12}}{2 \times \rho_{Si} \times t} \qquad \textbf{(III.12)}$$

Therefore, we have an experimental determination of $\rho_{Si} \times t$ and assuming w and L are known, we have access to the experimental resonator mass. As detailed in Chapter I, the resonator length is taken between the two nanogauges. Indeed, FEM simulations showed that the beam length between the anchors and the nanogauges showed negligible displacement. SEM images confirmed the 300nmwidth of our resonators.

A typical doubly clamped beam inserted in the bench resonates at 24.6MHz and 66.8Mhz for mode 1 and 2 respectively and has the following dimensions:

	Thickness	Width	Length
Resonant mass	160nm	300nm	9.2µm
Nanogauges	160nm	80nm	400nm

Table III.1: device dimensions

This yields a total resonator mass of 1.03pg. The theoretical mass sensitivity of the nth mode can be deduced as:

$$S_n = \frac{\Delta f_n}{\Delta m} = \frac{f_n}{2 \times M} \qquad \textbf{(III.13)}$$

Hence typical theoretical mass sensitivities of our resonators are $S_1 = 12\ Hz/ag$ and $S_2 = 32.5\ Hz/ag$.

Experimental values of S_1 and S_2 can be obtained by simultaneously measuring the frequency shift rates of modes 1 and 2 during uniform deposition of metallic clusters and

comparing them to the QCM mass deposition rate. In this experiment, the focus is not on frequency shifts caused by individual events but rather on the average slope of the frequency drifts during mass deposition. Low cluster diameters and high flux rates are used to ensure uniform mass deposition along the beam. Different mass deposition rates are obtained by tuning the parameters of the cluster source while monitoring the result with the QCM before frequency shift acquisition on the NEMS. Then the NEMS frequency shift rate is extracted from each acquisition and compared to the QCM. A linear fit yields the experimental mass sensitivities. The method is illustrated in Fig. III.26 with copper clusters deposition.

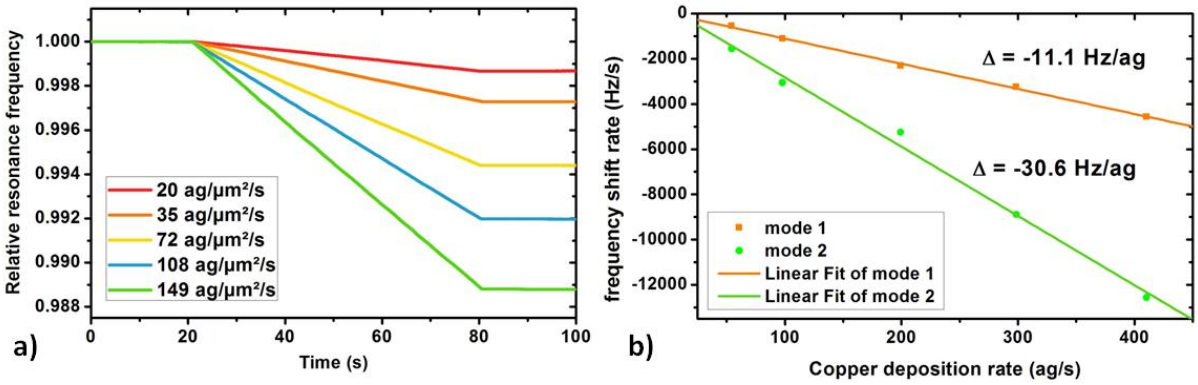

Fig. III.26: Sensitivity calibration method: frequency response to five different deposition rates given by the QCM (mode 1 shown here) is acquired (a). The NEMS frequency shift rates are linearly fitted and plotted versus the mass deposition rate on the device deduced from the QCM to obtain the experimental mass sensitivities (b).

The obtained mode 1 and mode 2 experimental sensitivities are 11.1 Hz/ag and 30.6 Hz/ag respectively. The experimental vibrating mass, needed for the NEMS-MS measurements is deduced:

$$M_{\text{exp}} = \left\langle \frac{f_1}{2 \times S_1} \middle| \frac{f_2}{2 \times S_2} \right\rangle = 1.12 \text{ pg} \qquad \textbf{(III.14)}$$

In this specific case, the experimental resonator mass is found bigger than the theoretical one since the device underwent many copper mass deposition experiments before we eventually performed the calibration. Nevertheless, the experimental mass was generally found from 0 to 15% smaller than the theoretical resonant mass. This discrepancy may be caused by device thickness variation or may originate from the uncertainties on the boundary conditions.

This calibration method, applied for all NEMS-MS experiments, reduces the measurements uncertainties by experimental determination of the sensor sensitivity and enabled us to get great mass accuracy performances

5. Theoretical limit of detection and mass resolution

The minimum detectable mass of our calibrated resonators depends on the ability to discriminate mass induced frequency jumps from the noise floor, here the resonator's frequency fluctuations. Our jump detection algorithm relies on efficient denoising usually requiring a removal of noise within a 5 sigma interval. Deriving from equation (III.4) and attributing a 5 sigma detection limit it comes out that the minimum detectable mass landing on an antinode of mode n is:

$$\Delta m_{min} = 5 \times \sigma_{\delta f} \times 2 \times M \times \alpha_n \qquad \textbf{(III.15)}$$

where δf is the resonator's relative frequency and $\sigma_{\delta f}$ the resonator's relative frequency fluctuations.

This minimum detectable mass will be denoted as the Limit Of Detection (LOD) throughout this document. It may be lowered using more advanced step detection techniques that does not rely on 5 sigma noise removal such as those mentioned in the jump detection section or by using statistical Bayesian inference [15].

The mass resolution, defined here as the standard deviation of a measured mass, relies on the uncertainty of the measured frequency jump hence the resonator's frequency fluctuation:

$$\sigma_m = \sigma_{\delta f} \times 2 \times M \times \alpha_n \qquad \textbf{(III.16)}$$

The experimental NEMS stability of δf is measured using the Allan deviation estimator [16]. Fractional resonance frequencies of both modes are monitored in closed loop when the cluster beam is blocked. The device is cryogenically cooled and under argon flux. A typical Allan deviation plot is presented in Fig. III.27.

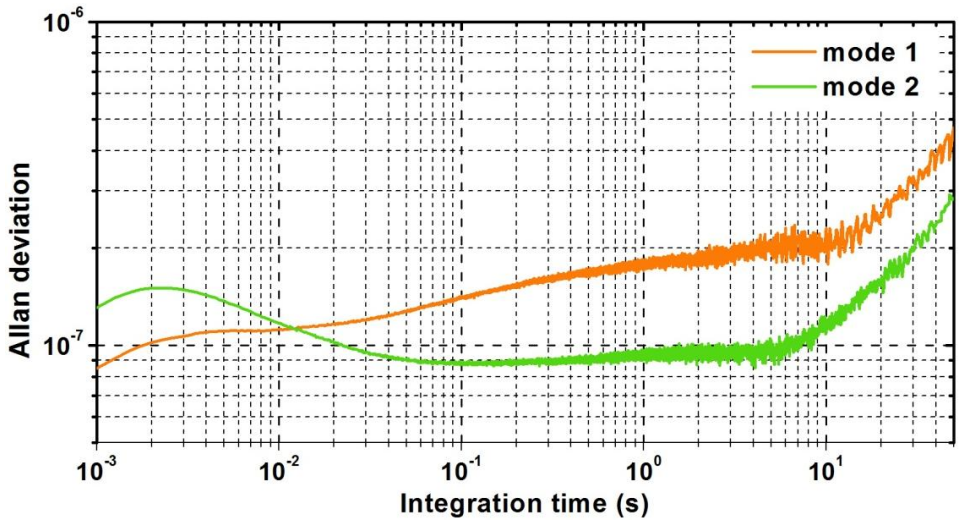

Fig. III.27: Typical Allan Deviations of mode 1 and 2 at optimum operating points from a single NEMS resonator in vacuum and cooled with liquid nitrogen.

Allan deviations of 1.2×10^{-7} and 9.5×10^{-8} are obtained at 30ms integration time for mode 1 and mode 2 respectively. According to equation (III.15) and (III.16), this yields a minimum detectable mass around 330 kDa (1 dalton=1.66×10^{-27} kg) and a 70 kDa mass resolution. The Allan deviation plot helps in choosing the appropriate integration time for our acquisition and getting a first estimation of the expected LOD and mass resolution. However we looked for more direct ways to estimate the actual values encountered in our experiments.

We were able to experimentally determine our actual LOD by applying our NEMS-MS postprocess algorithm on an acquisition without mass-induced frequency jumps. Doing so, we observed the effect of the denoising ellipse with respect to different denoising thresholds. As shown in Fig. III.28, the noise is translated to a so called "low mass noise peak" that defines our LOD.

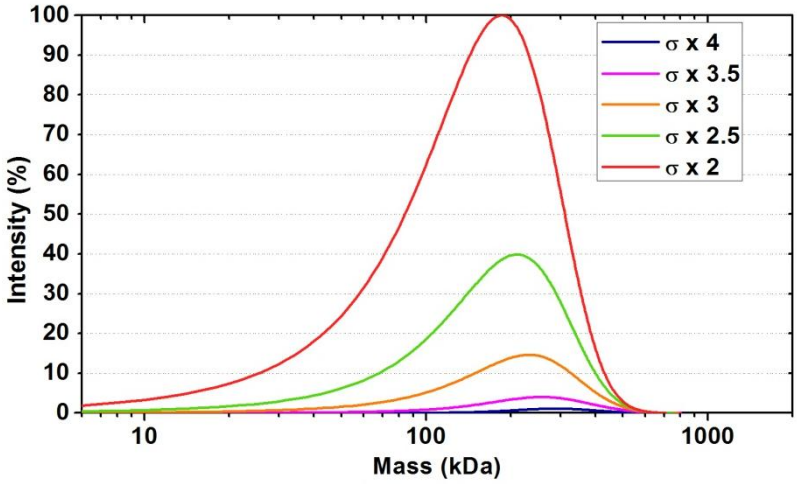

Fig. III.28: Low mass peak artifact caused by the NEMS frequency fluctuations. The filtering starts from 0 to increasing masses as the denoising ellipse gets larger. A filtering at σ x 5 rules out all false positives.

The LOD is defined as the maximum mass value where the "low mass noise peak" is present. We find that the LOD is around 500kDa: any particle over 500kDa landing on our sensing interval can be confidently attributed to an actual mass landing events. Experiments below this limit may be attempted with lower denoising ellipses but will unavoidably feature some noise induced false positives. The theoretical value of 330kDa previously calculated was under evaluated as the clusters positions were assumed to be at the maximum deflection of the mode shape which is rarely the case.

The experimental mass resolution is estimated with the standard deviation of the PDF associated with a mass landing by our error analysis (Fig. III.18). An acquisition of metallic nanoclusters centered on 1090kDa was simulated using the characterized NEMS frequency fluctuations properties: σ1 = 2.2e-7, σ2 = 1.3e-7 and ρ = 0.21. The simulation procedure is detailed in Section 6.2 of this chapter. We studied the influence of the particles position and mass on the standard deviation σ_{mass} of the assigned PDF. We found out that the particle position can influence σ_{mass} to a large extent as shown in Fig. III.29.

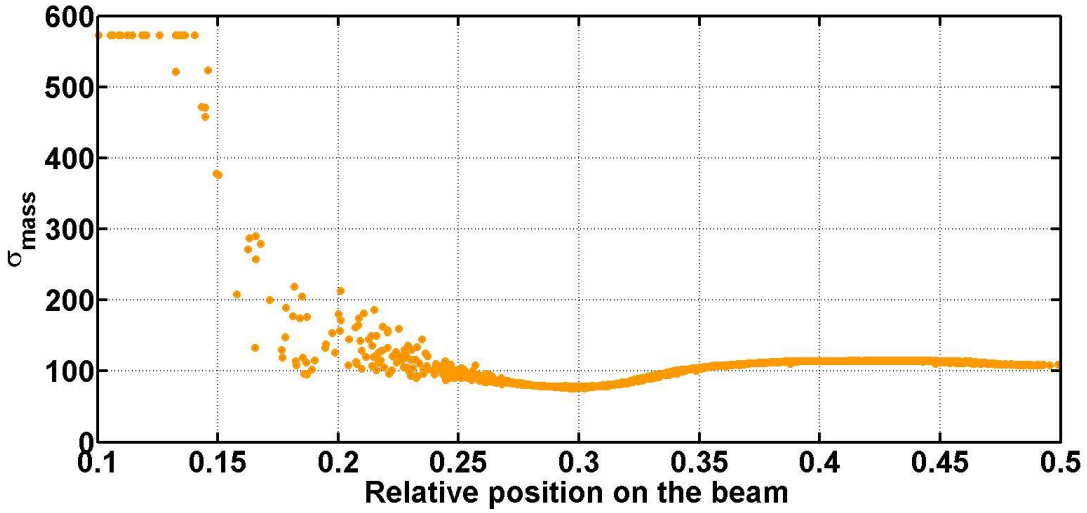

Fig. III.29: Standard deviation of the PDF assigned to an individual particle respect with its relative position on the beam.

Three main regimes are observed. The interval [0.1, 0.25] shows a large degradation of σ_{mass} as we get closer to the resonator's mechanical anchors. Intervals [0.25, 0.36] and [0.36, 0.5] feature a σ_{mass} around 80kDa and 115kDa respectively. These three regimes can be understood by reporting them on the response functions of mode 1 and 2 (Fig. III.2). We observe that mode 1 response is dominant in the [0.36, 0.5] interval while the mode 2 response is stronger in [0.25, 0.36]. Given that the mode 2 frequency fluctuations are slightly inferior with respect to mode 1, a slightly better mass resolution is obtained in the interval where mode 2 dominates. Below 0.25, both modes response are weak and quickly decrease when getting closer to the anchors: the SNR decreases and σ_{mass} reaches 570kDa. This plot shows the importance of ruling out detected particle at positions below 0.25 where poor mass resolution is achieved. It also seems to indicate that the region close to the beam center (0.5) is reliable. However, given that mode 2 response is very poor here and that we filter out the noise with a 5σ standard error ellipse, most particles landing in a region empirically determined as [0.47, 0.5] have a null δf2 and a strong δf1 and are therefore assigned to the position 0.5: it is impossible to determine if the null mode 2 frequency shifts come from an actual particle position at the middle of the beam or a weak δf2 that was filtered out. In addition, keeping the position 0.5 showed an increased influence of the low mass noise peak previously discussed. For all these reasons, the sensing interval we used for most of our experiments was [0.25, 0.47] as previously mentioned in of this chapter.

We confirmed the absence of influence of the particle mass on σ_{mass} by simulating particles ranging from 500kDa to 10MDa. A 3D scatter plot of $\sigma_{mass}$with respect to mass and position shows that on the interval [0.25, 0.47], σ_{mass}does not depend on the particle mass, as expected (Fig. III.30).

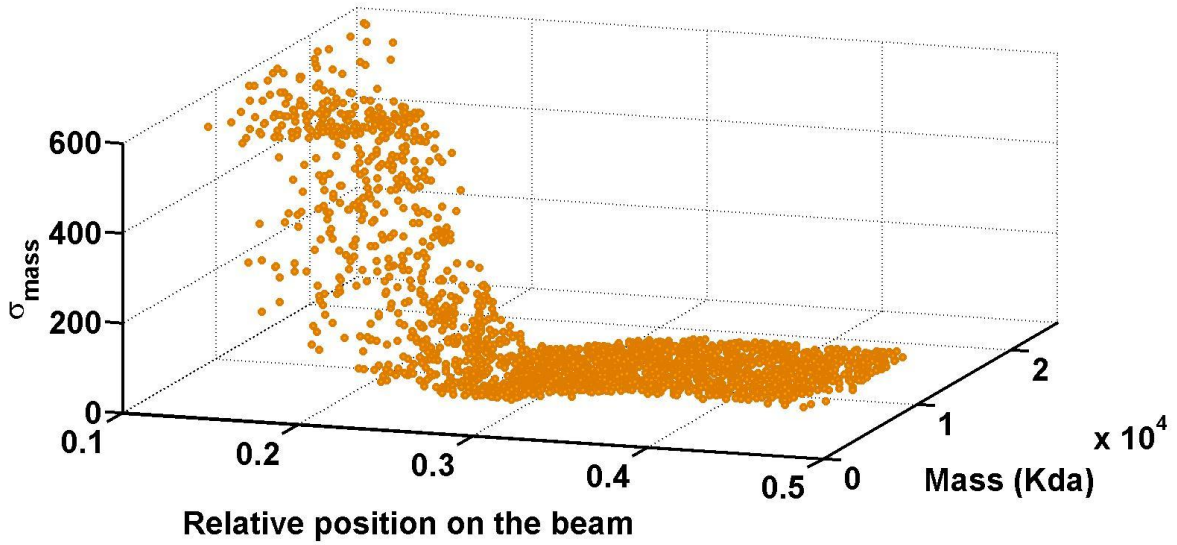

Fig. III.30: 3D scatter plot of σ_{mass} versus particle mass and position from simulated particles ranging from 500kDa to 100MDa.

In summary, we can expect a constant mass resolution around 100kDa for any measured mass. For confident detection, we need to generate nanoclusters as heavy as possible, at least above 500kDa.

6. Mass spectra comparison

6.1. Experimental preparation

Using our NEMS-MS postprocess algorithm along with the characterized mass sensitivity and noise properties of our nanomechanical sensors, we built NEMS-MS spectra of metallic nanoclusters that we compared to those of the conventional TOF present in our setup. Mass deposition rates and mass spectra were acquired with the QCM and the TOF before and after each NEMS-MS run. This was easily done as the TOF is mounted in line with the particles path and both QCM and NEMS holder are retractable. Given that low deposition rates are sought, the deposition rate provided by the QCM is integrated over 100 seconds to provide accurate readings. We assume that the TOF gives a reliable description of the actual nanocluster distribution and that the ionized clusters measured by the TOF are representative of the total cluster distribution. This was verified by nanocluster deposition on carbon-coated microscopy grids for High Resolution Transmission Electronic Microscopy (HRTEM) to evaluate their size distribution [11]. Deducted mass distributions confirmed the TOF mass spectra.

To obtain an acceptable mass SNR (i.e. $\frac{M}{mass\ LOD}$) the clusters masses need to be over the mass LOD and as heavy as possible i.e. in the MDa range. Several metals were tested. Copper (Cu) density is 8.96 g.cm^{-3} and the typical cluster mean diameters were around 4.5nm

while a maximum diameter of 6nm was reached. This corresponds to 260kDa and 610kDa respectively. Given our 500kDa LOD and our 100KDa mass resolution, it leaves us with poor leeway for experimentations. We found out that tantalum was an excellent candidate for our experiments as it is both dense (16.65 $g.cm^{-3}$) and easily condensates into clusters for mean cluster diameters up to 9.5nm. We obtained cluster populations following a log normal distribution law with mean masses from 50kDa to 4500kDa (diameter of 2 to 9.5nm).

Tantalum clusters were deposited with low flux rates so our fast Phase Lock Loop could detect all frequency jumps due to individual particle landings. Since we chose a PLL response time of 10ms, we aim at depositing one cluster approximately every 100ms. The expected event rate can be roughly estimated from the cluster mean mass Δm_{mean} given by the TOF spectrum and the mass deposition rate φ_{QCM} (g/s/µm²) given by the QCM:

$$Event\ rate = \frac{\Delta m_{mean}}{\varphi_{QCM} \times L \times w \times 10^{12}} \qquad \textbf{(III.17)}$$

A maximum of detected events is desired to reproduce with fidelity the actual nanocluster distribution of the population.

In a NEMS-MS acquisition, a few tens of seconds without mass events (shutter blocks the mass flux) are kept at the beginning and end of the measurement. These are useful to observe any false positive detection in the jump detection process. If a non negligible amount of false positives is found, the standard deviation ellipse used for denoising can be made bigger than 5-sigma until all false positives are ruled out.

We successively acquired NEMS-MS spectra of various nanocluster populations in a large range of average mass from 470kDa (mean diameter = 4.5nm) to 4500kDa (mean diameter = 9.5nm) to check the reliability of NEMS-MS respect with TOF-MS within this range.

6.2. Preliminary results & simulations

The first confrontations of NEMS-MS spectra and conventional TOF MS are shown in Fig. III.31. The mass spectra were directly obtained as shown below and we did not need to fit any curve. A first observation can be made on the TOF spectra: while an additional bump at half the main mass peak is observed for the 610kDa centered spectrum, it becomes a separate secondary peak at higher mass ranges such as seen on the 1090kDa centered spectrum. These peaks represent doubly charged particles and will be left aside for now but are further discussed in Section 6.4 of this chapter. TOF and NEMS-MS spectra are normalized with respect to the singly charged particles mass peak.

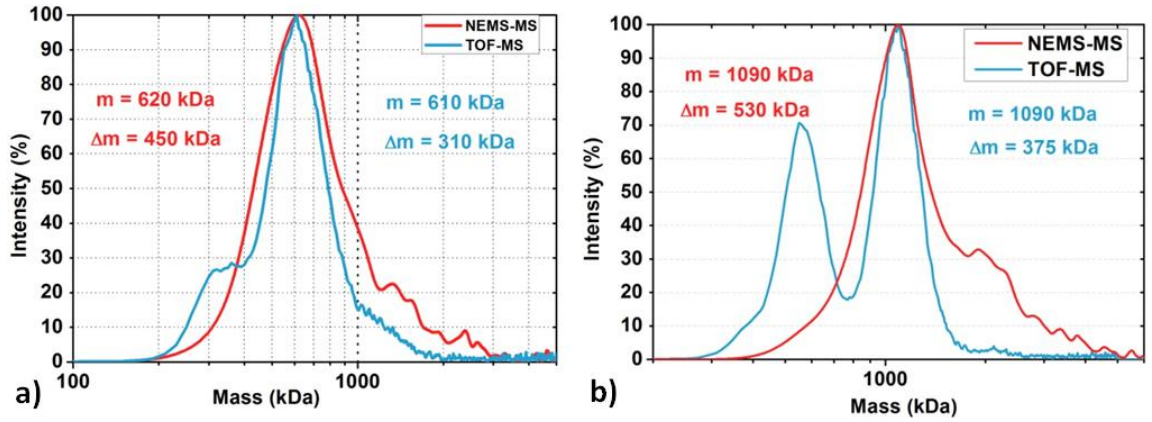

Fig. III.31: Superposition of normalized mass spectra from TOF-MS and NEMS-MS of tantalum clusters. 324 clusters with a 4.85 nm mean diameter were acquired in 4 minutes (a) and 1383 clusters with a 5.9 nm mean diameter were acquired in 4 min (b). m denotes the center of the spectrum while Δm is the Full Width at Half Maximum (FWHM).

It can be noted that NEMS-MS provides a fairly accurate evaluation of the clusters mean masses with errors generally well below 100kDa which can be surprising given our predicted 100kDa mass resolution. The large number of detected events probably improves the probability to accurately evaluate the mean mass. In addition, the importance of the NEMS mass sensitivity calibration detailed in section 4 is highlighted here as uncalibrated NEMS-MS spectra are generally shifted upward (from 0 to 15%) respect with the TOF. We can also observe on the NEMS-MS results broader spectra than TOF-MS and an additional bump at twice the mean mass. Simulations were carried out to understand these phenomena.

The simulation's inputs are the NEMS dimensions and resonance frequencies, the TOF spectrum and the characterized noise properties of the NEMS' bivariate Gaussian noise i.e. σ1, σ2 and ρ. The simulations consist in generating tantallum nanoclusters with a distribution well-matched with the TOF spectrum that land randomly on the NEMS. We did not simulate the frequency trace affected by mass events here and we directly considered frequency jumps. The expected frequency jumps $[\delta f_1, \delta f_2]$ are calculated and a bivariate Gaussian noise characterized from the NEMS' frequency fluctuations is added. Effect on the noise on simulated data is amplified or nulled with a multiplier X_n. The list of frequency jumps $[\delta f_1, \delta f_2]$ is filtered for jumps below 5*σ1 or 5*σ2 and translated to $[m, x]$ before construction of the final spectrum. A block diagram of the procedure is shown in Fig. III.33.

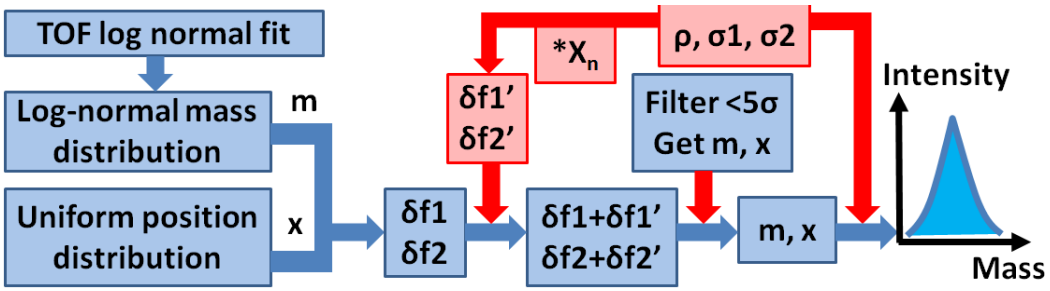

Fig. III.32: Block diagram of simulation procedure. The idea is to simulate noisy frequency jumps and process them just like regular NEMS-MS data. The amount of frequency noise δf1' and δf2' can be varied with the multiplier X_n. The log-normal law of the nanocluster

distribution is extracted from the TOF spectrum.

In a first step, no noise (X_n=0) was added on the frequency jumps to check whether our noise analysis broadens our spectrum. Then, the influence of the frequency noise on $[\delta f_1, \delta f_2]$ was studied by increasingX_n.

We detail here simulations performed to study the results of Fig. III.31 (right).

The TOF gives us a distribution centered on 1090kDa with a FWHM at 375kDa that we fitted with the PDF of the log normal law:

$$f(x;\mu,\sigma) = \frac{1}{x\sigma\sqrt{2\pi}} e^{-\frac{(ln(x)-\mu)^2}{2\sigma^2}} \qquad \textbf{(III.18)}$$

with $\mu = 7.01$ and $\sigma = 0.135$

The experiment we studied yielded 1383 events. Since we kept the events comprised in the interval [0.25, 0.47] of the beam, only 44% of the total number of cluster landing on the device was detected. Hence we evaluated the total number of clusters that landed of the resonator to be 3450. The fitted PDF was used to generate a vector of 3450 masses following a log normal law. A second vector of equal length with values drawn from a standard uniform distribution on the open interval [0, 1] is generated to simulate the clusters' relative landing positions on the beam. A list of relative masses and landing positions $[\delta m, x]$ is formed and the expected relative frequency shifts on mode 1 and mode 2 $[\delta f_1, \delta f_2]$ are calculated using equation (III.1). Frequency noise is applied on each frequency jumps using the characterized NEMS frequency fluctuations properties: σ1 = 2.2e-7, σ2 = 1.3e-7 and ρ = 0.21. A frequency jump is evaluated as the difference of the relative frequencies before and after the jump, $\frac{\Delta f'}{f}$ and $\frac{\Delta f''}{f}$. Given that their respective incertitude σ' and σ'' are equal and assuming a stationary and ergodic noise, the incertitude of $\frac{\Delta f''}{f} - \frac{\Delta f'}{f}$ is given by:

$$\sigma(\delta f) = \sqrt{2}\,\sigma' \qquad \textbf{(III.19)}$$

Hence according to the principles of uncertainty calculus, we should use $X_n = \sqrt{2}$. However various values of X_n were applied on the noise to study its effect on the final mass spectrum. Fig. III.33 (left) shows a simulated NEMS-MS spectrum without added noise (X_n = 0) compared with the TOF while Fig. III.33 (right) presents the mass spectra obtained with $X_n = 0, 1, \sqrt{2}$ and 2.

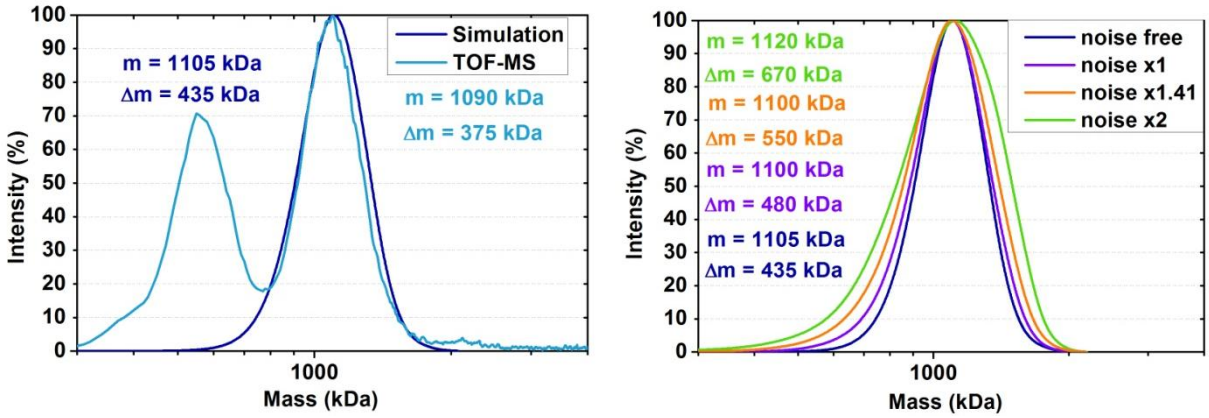

Fig. III.33: Comparison of the TOF spectrum with a simulation of NEMS-MS without incertitude on the frequency jumps (left) and simulated effect of increasing frequency jumps noise on the produced NEMS-MS spectrum (right).

We can observe in Fig. III.33 (left) that the simulated spectrum already presents a minor broadening of several tens of kDa even with no added incertitude on the frequency shifts. This is caused by the underlying error analysis present in our postprocess algorithm that attributes a probability density function to each mass landing event with a given dispersion. Hence, the true central mass of each cluster has been correctly found but the PDFs that model frequency noise inherently broaden the spectrum.

A more important source of spectral broadening is the inaccurate determination of each cluster central mass. We can notice in Fig. III.33 (right) that adding increasing frequency noise on the frequency jumps broadens to a larger extent the mass spectrum (hundreds of kDa). Frequency noise depends solely on the NEMS frequency fluctuations and its influence decrease as we measure higher masses generating higher frequency jumps: $\frac{\delta f1}{\delta f1'} \gg 1$ and $\frac{\delta f2}{\delta f2'} \gg 1$.

On some spectra, we observe an additional bump at twice the mean mass, more or less present according to the experiment. We found out that these bumps become more important during experiments where the expected event rate is high. For instance, the expected event rate in Fig. III.33 (right) is 1 cluster every 37ms .We can model the probability of mass events with a Poisson distribution:

$$f_p(X = k, \lambda) = \frac{\lambda^k e^{-\lambda}}{k!} \qquad \textbf{(III.20)}$$

where k is the number of events and λ the expected value of x.

The jump detection algorithm was processed with $\tau_{AVG} = 20ms$. Therefore more than one event within 60ms (three data points) will generate a single long jump instead of two abrupt frequency jumps. Using equation (III.20), the probability to have more than 1 mass event within 60ms is 48%. We simulated the effect of double landings by simulating various double landing proportions and plotting the resulting mass spectra. The multiplier on the frequency jumps noise is √2. We plotted the simulated spectra with increasing proportion of

double landing events and confronted one of them with our experimental results as presented in Fig. III.34.

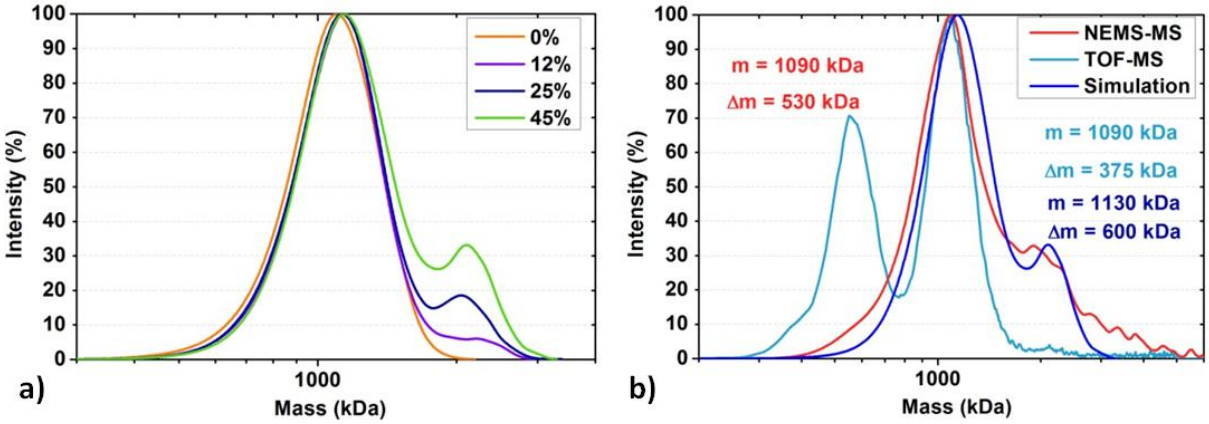

Fig. III.34: Effect of double cluster landings on the mass spectrum with varying proportions (a) and comparison of TOF-MS, NEMS-MS and a simulation with a √2 multiplier on the added noise and a 45% proportion of double landings (b).

Our simulations seem to indicate that a proportion of double landing events close to 45% close to the 48% expected from the Poisson distribution. It underlines the importance of a ratio $\frac{\tau_{PLL}}{mass\ landing\ events}$ over 10 to avoid this kind of behavior. We also note that simulations tend to produce mass spectra slightly shifted upward (≈5%) with respect to the TOF. However, our measurements did not chronically display upward shifts of this scale and this discrepancy between results and simulations is yet unexplained.

The simulations evidenced an additional phenomenon: if we remove the noise filtering from the postprocess of the simulated frequency jumps (Fig. III.32), a low mass peak similar to the one described in Section 5 (defining the mass LOD) reappears as shown in Fig. III.35.

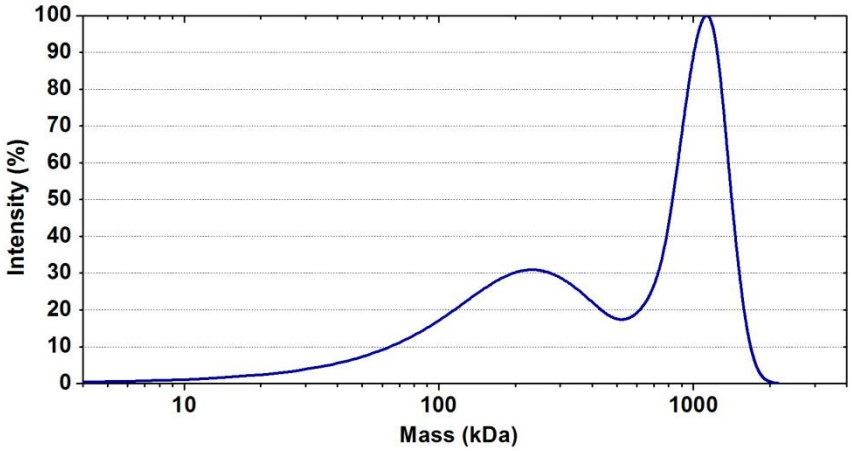

Fig. III.35: Simulated NEMS-MS spectra without noise filtering in the postprocess algorithm

This is unexpected as we generated each event as a metallic nanocluster: no frequency jumps caused by sole frequency fluctuations were created. Hence, no filtering should be required to postprocess our simulated particles. We investigated the origin of this peak and studied the properties of detected events below 530kDa. We found out these events were generated from high mass particles landing in the low sensitivity region of the resonator i.e. at

relative positions on the beam between 0 and 0.2. Hence they produced low frequency shifts pairs at a scale comparable with the NEMS frequency fluctuations. However, combined with frequency noise the ratio $\frac{\delta f_2}{\delta f_1}$ that we use for position determination (equation (III.3)) is altered and becomes almost random. A fair amount of these frequency shifts pairs are then wrongly assigned a position on the sensitive portion of the beam ([0.25-0.5]). Therefore these low frequency shifts attributed with a position on a sensitive portion of the beam are mistaken for low masses as shown in Fig. III.36.

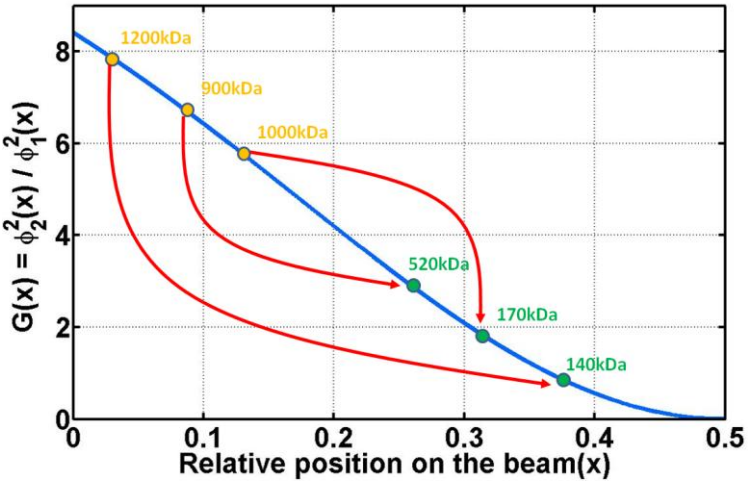

Fig. III.36 : Low mass peak induced by mass events: noise perturbs the ratio $\frac{\delta f_2}{\delta f_1}$ and attributes wrong landing positions on more sensitive areas. The small frequency shifts are then mistaken for small masses.

Translating a cluster position from the anchors to the center of the beam requires decreasing the ratio $\frac{\delta f_2}{\delta f_1}$ which is why the noise incriminated with low mass noise has generally features a positive δf_1 shift (Fig. III.37).

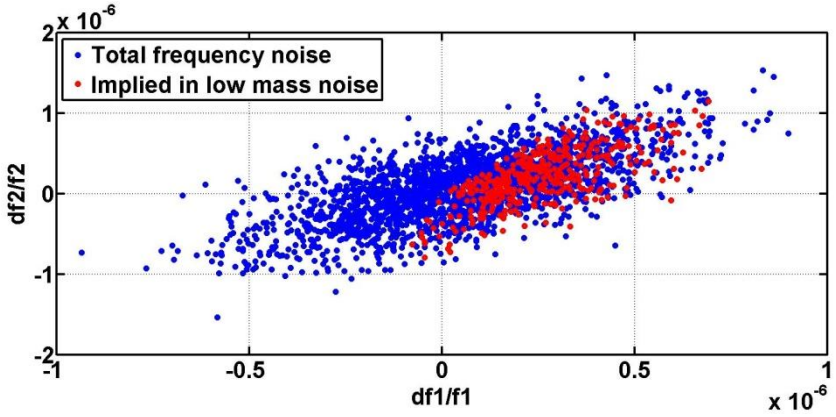

Fig. III.37: Scatter plot of the frequency noise we applied in our simulation (referred to as δf1' and δf2' in Fig. III.32). We show in red the noise that wrongly translated an event that landed close to beam anchors.

The effects of this phenomenon are very similar to the "low mass noise peak" discussed in Section 5 resulting from pure frequency noise. It can be seen as a frequency shot noise with amplitudes depending on the mass of the clusters being acquired. Thus, we could

expect the low mass peak to shift toward higher masses when we project larger masses onto the NEMS. Hopefully wrong position attribution appears only when the mass-induced low frequency shifts are in the same order of magnitude than frequency-noise: for higher mass-induced low frequency shifts, correct position is found and a high mass is attributed. Yet, this additional frequency noise may amplify slightly our basic frequency noise. This may explain why some of our NEMS-MS acquisitions feature some noise despite the 5-sigma denoising procedure. Nevertheless denoising at 5σ and a sensing beam interval [0.25, 0.47] showed excellent results on most of our experiments.

6.3. Experimental mass range influence

We tested the limit of NEMS-MS by attempting to measure masses close to the LOD. We performed a NEMS-MS acquisition on a tantalum nanocluster population with a 470kDa mean mass (diameter = 4.5nm). A standard postprocess yields a NEMS-MS spectra that does not match with TOF-MS (Fig. III.38).

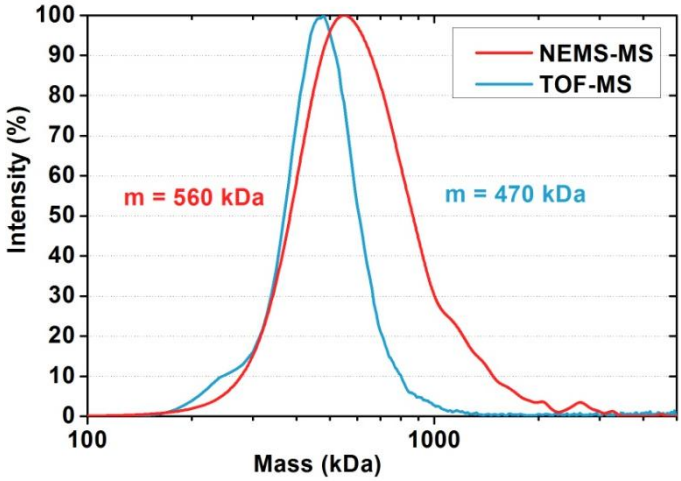

Fig. III.38: NEMS-MS spectra of metallic nanoclusters with mean masses close to LOD using standard postprocessing parameters.

Being close to the LOD, the NEMS-MS spectra is most probably affected by the denoising procedure using a standard deviation ellipse at 5σ. On the other hand, decreasing too much the denoising ellipse size introduces false positive events generated by the NEMS noise. We proceeded by gradually lowering the denoising ellipse until the actual mass peak and the "low mass noise peak" (see Section 5) could be separated. The number of detected events for each spectrum is recorded (Fig. III.39).

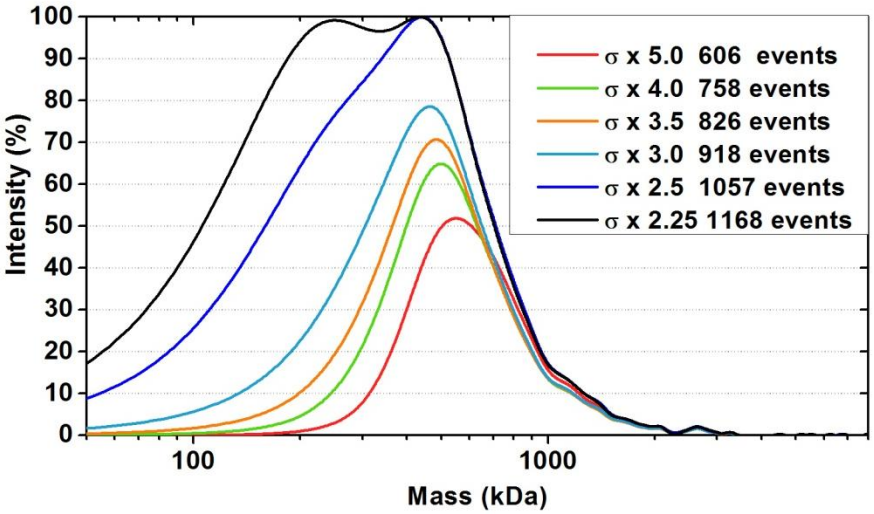

Fig. III.39: NEMS-MS spectra of metallic nanoclusters with mean masses close to LOD using a gradually decreasing denoising ellipse. At σ x 2.25, the mass induced peak can be separated from the low mass noise peak.

In this situation, denoising too much would shift the mean mass upward as we delete the lighter nanoclusters of the population. On the other hand, low denoising introduces more false positives in ranges overlapping with the nanocluster spectra: the mean mass is shifted downward.

We used the part of the frequency trace acquisition where no mass is sent onto the NEMS (2x20s without mass deposition) to evaluate the proportion of false positives. For σ x 2.25, 49 false positives are found which yields 1.225 false positive per second. We increased the denoising ellipse up to σ x 3.5 where no false positives are observed. The MS spectrum is compared to the TOF in Fig. III.40.

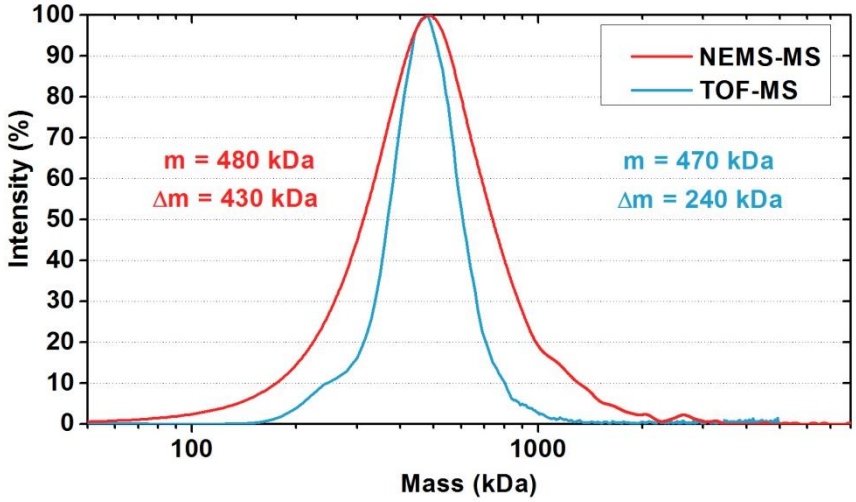

Fig. III.40: Superposition of normalized mass spectra from TOF-MS and NEMS-MS of tantalum clusters. 826 clusters with a 4.5 nm mean diameter were acquired in 4 minutes

The final spectrum probably features a few false positives. However we obtained a fair estimate of the particle distribution in spite of the very low signal to noise ratio. This was made possible by the much higher rates of mass induced events than false positives rates.

The noise of our mass sensor is governed by the resonator frequency noise and is independent of the measured mass. Therefore we expect higher signal to noise ratios and better matching with the TOF with measurements at increased mass ranges. We modified the parameters of our cluster source to obtain larger clusters as shown in Fig. III.41.

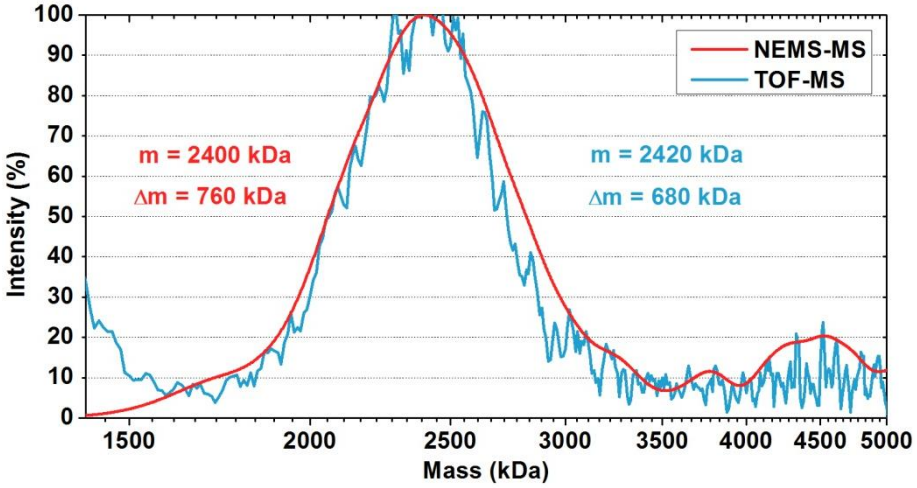

Fig. III.41: Superposition of normalized mass spectra from TOF-MS and NEMS-MS of tantalum clusters. 818 clusters with a 7.7 nm mean diameter were acquired in 5 minutes

We observe a much better matching between TOF-MS and NEMS-MS since we are operating in a mass range where the incertitude on each particle mass becomes negligible. Therefore our sensor is well adapted for the measurement of large proteins, virus and biomolecules in the MDa range and above whether there are ionized or not.

6.4. Muticharged and neutral particles

We previously mentioned in Section 6.2 that the TOF spectra of the measured nanoparticles can feature not one but several mass peaks. Given that the TOF mass spectrometer measures mass to charge ratios, additional peaks correspond to particles having more than one charge. This is more easily observable as the cluster population grows in size. We observed additional peaks in the extended mass spectra of Fig. III.42 whose centers are integer quotients of the highest mass peak (Fig. III.42).

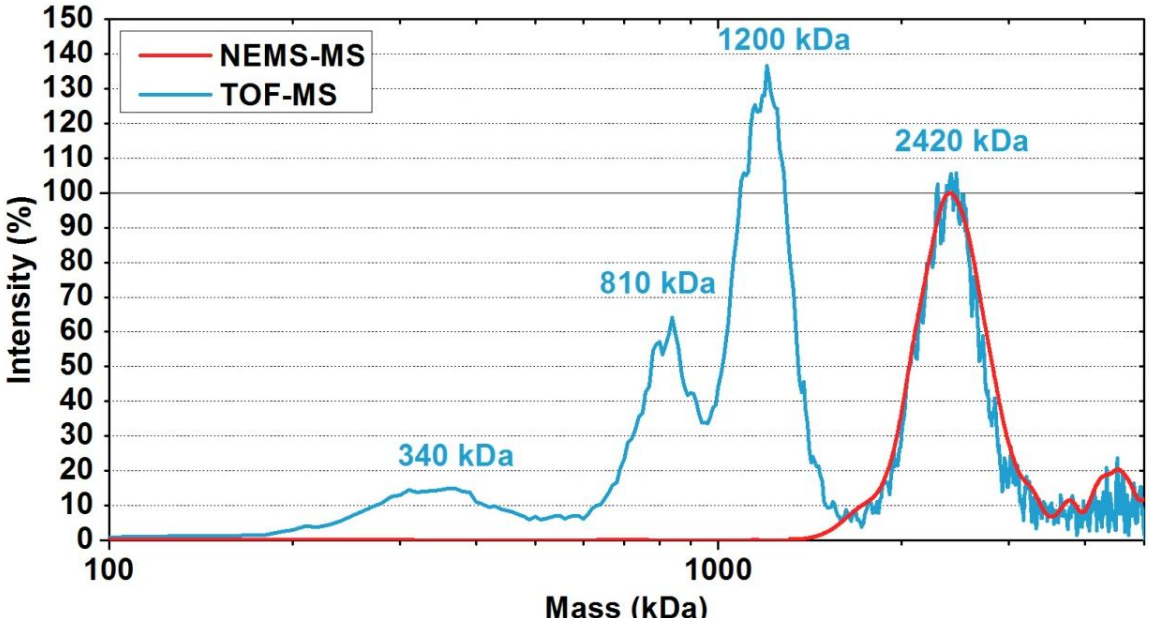

Fig. III.42: Extended mass spectrum of clusters with a 7.7 nm mean diameter showing the TOF multicharged peaks. Spectral normalization is done according to the main peak with singly charged particles.

In the acceleration grid of the TOF, particles with X charges get X times more acceleration than singly charged particle and are henceforth detected as X times lighter. We observe here four mass peaks given by the TOF-MS at 2420, 1200, 810 and 340 kDa. The 1200 kDa and 800 kDa peaks most probably correspond to clusters having 2 or 3 charges respectively. As it is known that with electric and magnetic fields the trajectories of particles having the same mass to charge ratio cannot be distinguished, the assignation of these peaks to 2 and 3 charge states cannot be proved with the TOF spectrometer. On the other hand, we frequently observed that peaks at m/2 and m/3 are present in spectra peaked at m. Moreover, when the source works in conditions where these peaks appear, after any change of the source conditions modifying the central mass m, the satellite peaks systematically change with 1/2 and 1/3 mass ratios. This is a strong presumption that they correspond to multicharged states. The peak at 340 kDa is suspected to be an artifact related to the operation of the spectrometer.

With this “peak forest” obtained with a single particle population, it is easy to understand that the analysis of a complex mixture can be somewhat problematic as multicharged peaks from one compound can hide single charged peaks of other compounds [17]. On the other hand, the multiple charge states are also one of the great assets of MS as algorithms produce more accurate mass evaluation with these additional informations. However, the FWHM of the peaks need to be lower that the separation between two charge states which become more complicated for large molecules with a high number of charges. Therefore, parallel measurements of the inertial mass would be extremely beneficial for spectra clarification.

NEMS-MS gives a direct measurement of the inertial mass and is insensitive to the charge of particles: none of the TOF peaks corresponding to multiple charged particles is displayed by our NEMS mass sensor. The absence of those peaks cannot be attributed to the NEMS LOD (limit of detection) as we showed that NEMS-MS spectra down to 470 kDa

could be produced. This feature bestows NEMS-MS a significant asset over traditional ion MS as the analysis of complex chemical mixture can be extremely intricate when multiples of the base mass peaks are produced. Mass spectrometry of proteins is often performed by tandem MS where the proteins are weighed after undergoing fragmentations to identify the peptides composing the protein. The obtained spectra can become extremely confusing with a multitude of peaks with unknown charge states and extensive research has been developed for the sole interpretation of these spectra [22-23-24]. This is why large-scale protein screening where thousands of spectra coming from a single experiment have to be deciphered is still considered as a challenge with traditional ion-MS. In addition some peptides obtained after fragmentation might never be observed as they don't ionize easily or at all.

So far, no mass spectra of neutral molecules have been reported. Secondary Neutral Mass spectrometry (SNMS) used in surface science, analyzes neutral molecules after post-ionization processes using lasers with ionization rates around 10% [20]. This falls into the same ionization rate issues of other conventional MS

Without use of post-ionization processes, we have evidenced the ability of nanomechanical mass spectrometry to perform neutral particles mass spectra by removing all charged particles from the cluster flux with deflector plates placed at the output of the cluster source. The deflector plates are shown in Fig. III.43.

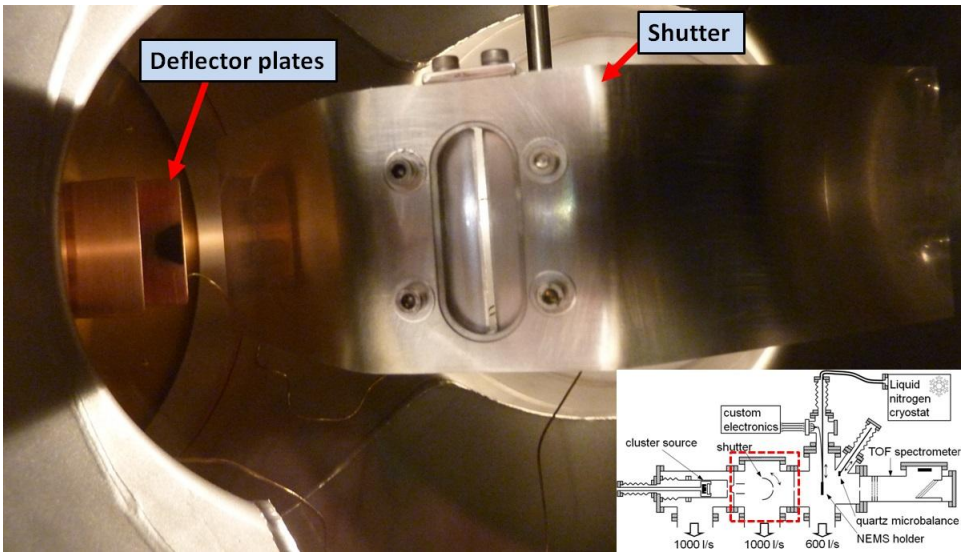

Fig. III.43: Photo of the shutter chamber showing the shutter and the deflector plates. The black spot on the deflection plates is caused by ionized clusters attracted on the polarized plates. Inset: schematic of the complete setup where the shutter chamber is delineated.

When the potential on the deflector plates is set to 0V, all particles enter the deposition chamber regardless of their charge state but only charged particles are measured by the TOF. When the potential is set to 40V, charged particles hit the plates or the chamber walls and the no ion reaches the TOF to be measured. While the TOF becomes blind when confronted to a flux of neutral particles, NEMS-MS can still build a mass spectrum.

We demonstrated the acquisition of neutral particles spectra on three different cluster populations as listed in Table III.2.

Central mass of clusters	Equivalent diameter	Potential on deflector plates	Deposition rate (ag/s/µm²)
1250kDa	6.2nm	0V	6.66
		40V	5.38
2300kDa	7.6nm	0V	10.2
		40V	6.83
3340kDa	8.6nm	0V	13.8
		40V	8.49

Table III.2: Cluster populations and their deposition rate with and without deflection

The QCM readings give us the ratio of neutral particles over the total population: 80.8%, 67% and 61.5% for the populations centered on 1250kDa, 2300kDa and 3340kDa respectively. We believe that higher ionization rates are correlated with higher particle sizes because heavy nanoclusters are obtained with higher power applied to the cluster source. Therefore, to evaluate the particles distribution, TOF-MS can use only a fraction of the actual total particle distribution and we have to assume that charged particles are representative of the total population. This can prove to be quite problematic when trying to figure out proportions between different biomolecules found in a complex mixture as each biomolecule may have a different ionization yield. This phenomenon is known as charge competition [22-26].

In addition this reduced number of "useful" particles for TOF-MS underlines the difficulty to acquire spectra of high mass nanoclusters: as the sputtered target material aggregates to form bigger nanoclusters, the number of nanoclusters leaving the source is getting low. Hence losing more than 50% percent of the information forces us to acquire the spectrum on very long integration times which yields poor looking spectra. So far, no TOF spectra over 4000kDa could be observed. Needless to say, the measurement of some biological particles, whose ionization rate is below 1%, is very challenging.

By contrast, NEMS-MS can weigh both neutral and ionized particles while the TOF is blind when all charged particles are deflected as shown in Fig. III.44.

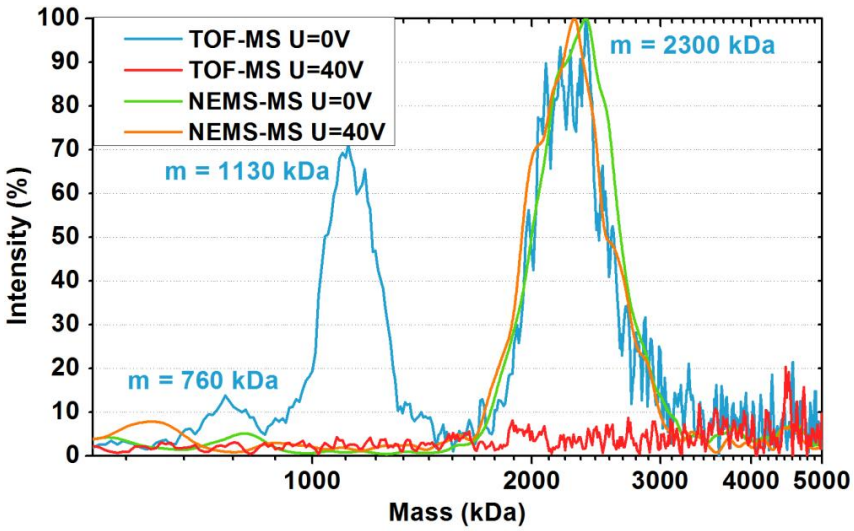

Fig. III.44: NEMS-MS and TOF-MS spectra with and without charged particles removal using a 40V deflection.

Plus the great similarity of the NEMS-MS spectra with neutrals or neutrals+ionized partially confirms our assumption that the mass distributions of neutral and charged particles are the same. Full confirmation could be obtained by placing the sensor on the trajectory of deflected ionized particles.

The number of detected events and total relative frequency shifts are listed in Table III.3.

Central mass of clusters	Potential on deflector plates	$\delta f1$/s	$\delta f2$/s	count
1250kDa	0V	9.867e-6	1.001e-5	676
	40V	7.233-6	7.533e-6	506
2300kDa	0V	1.534e-5	1.574e-5	702
	40V	9.003e-6	9.680e-6	441
3340kDa	0V	2.045e-5	2.067e-5	523
	40V	1.349e-5	1.240e-5	308

Table III.3: Mode 1 and mode 2 total relative frequency shifts and number of detected events for different cluster populations with or without ion deflection

The ratio of neutrals, whether obtained by QCM deposition rates, NEMS relative frequencies shifts (averaged between the two modes) or counted events from NEMS-MS are consistent as shown below in Table III.4.

	QCM	δf average	count
1250kDa	80.8	74.3	74.8
2300kDa	67	60.1	67
3340kDa	61.5	62.9	58.9

Table III.4: Percentage of neutral particles in a population obtained from QCM, NEMS frequency shift rate or number of detected particles on the resonator.

As expected, the quality of TOF spectra gets lower at higher masses whereas NEM-MS, on the contrary, gets better and detects neutral particles as well.

7. Conclusion

This chapter presents an important milestone in the development of NEMS-MS being the first comparison of this technique with conventional ion-MS and the development of ultra-fast detection. Indeed, the Alliance made great progress in 2012 with a first step toward practical application of NEMS-MS with real time nanomechanical spectrometry of single proteins and this first success of ESI-NEMS-MS engendered the initiation of new setups combining NEMS-MS with different mass source such as Matrix-Assisted Laser Desorption/Ionization (MALDI). However, the possibility to evaluate the performance of these measurements and further understand the phenomena at work was still lacking. Hence we have developed in parallel an additional setup exclusively dedicated to NEMS-MS evaluation and comparison with traditional ion-MS. Knowledge gained from this setup can

then benefit all existing or future setup designed purely for biomolecules and other applications.

The developed setup proved to be practical for experimentations as the gas-aggregation source allowed for the formation of a flux of nanoclusters with tunable mean size and deposition rate. A Quartz Crystal Microbalance and a Time Of Flight Mass Spectrometer played the role of reference measurements. We were able to obtain a mass range overlap of both MS technique from 470kDa to 4500kDa by sputtering tantalum clusters with mean diameters from 4.5 to 9.5nm. Given the mass spread of the cluster population, a large number a mass events had to be recorded which required ultra-fast measurements.

In this chapter, we presented the equipment and the circuitry developed to perform simultaneous closed loop acquisition of the first two resonance frequencies of a doubly clamped nanomechanical resonator with potential response times down to 1ms. We covered as well the developed automated frequency shift detection technique that evaluates the thousands of events before conversion to mass spectra using an optimized complex error analysis. As the computation time of a single event went down to 25ms, implementation of actual real time NEMS-MS is now possible.

Combined with simulations, the acquisition of cluster populations with varying mean mass highlighted the performance increase of NEMS-MS as the weighted masses got heavier: the mass resolution of a resonant mass sensor is constant regardless of the weighted molecules. On the other hand, while traditional ion-MS performs very well in the very low mass range (below 100kDa), difficulties arise with heavier molecules that require very high voltages to be accelerated properly: the mass resolution drops down. Hence the constant mass resolution of NEMS-MS is a great advantage over traditional MS as very large mass dynamic range can be obtained. Assuming that the NEMS response to mass adsorption is linear up to 1/100 of its own mass, the device presented in this experiment has a dynamic range from 100kDa to 6GDa. The few hundred kDa LOD was demonstrated by postprocessing a mass event free acquisition as a regular mass acquisition and this limit was later confirmed by a successful mass spectrum construction of a cluster population centered on 470kDa provided a few tweaks with the denoising algorithm. No spectra below this limit could be obtained in spite of the different filtering techniques applied on the data. But the excellent performance at high mass ranges makes NEMS-MS an excellent tool for proteomics: while some MS techniques require the fragmentation of proteins into smaller analytes for peptide sequencing or multi-charging with an ESI to bring the analytes below a m/z ratio of 1000 [22], NEMS-MS can fill in the gap in the supramolecular range and provide masses of the initial molecules before fragmentation in tandem MS for instance.

Finally, we have successfully made the very first demonstration of mass spectra acquisition of neutral particles. To the best of our knowledge NEMS-MS is currently the only technique able to provide mass distribution of neutral molecules. This asset can make a difference in many applications. In our setup, TOF-MS seemed to struggle to acquire clean spectra above 3MDa as measurable particles rarefied whereas NEMS-MS could use all landed particles, neutrals and ionized, to provide both the mass distribution and the mass deposition

rate: NEMS-MS has the potential to become a two-in-one tool replacing TOF-MS and the QCM found in this setup. Moreover NEMS-MS appears like an interesting tool to study ion sources: using deflector plates, one can study which compounds found in a mixture are ionized or not, determine ionization rates, and optimize the ion source accordingly.

As far as protein mass spectrometry is concerned, the absence of multi charged peak makes mass peak interpretation much simpler and remove any possible peak overlap caused by multiple charge states that may be found in ion-MS [17]. Plus, in ion-MS, the peak intensity proportion between compounds depends their ionization rate [21]. Worse, information loss caused by neutrals particles makes peptide sequencing even more difficult. NEMS-MS does not miss any information and display the actual compounds proportion regardless of ionization rates or charge states. These claims hold true if we are able to weight the totality of the molecules or at least a very representative fraction of the analyzed mixture.

Obviously there is still long way to go until we can measure every single particle: the nanocluster beam from the setup had an approximate 5cm diameter surface cross-section whereas the resonant beam surface is 9µm*300nm. In addition the actual sensing area is 44% of this surface as particles can be accurately detected in the interval [0.25, 0.47] only. A scale factor of 10^8 is found between the sensing area and the particles flux. Given the promising results obtained with such a tiny capture cross-section, one can only imagine the potential of NEMS-MS with a large capture area. Leeways to do so are still large as we can use:

- Additional modes tracking for extension of the sensing area. 4 modes can probably extend the useful surface to 80% of the beam.

- Mass beam focusing using quadrupoles for ionized molecules or aerodynamic lenses for neutral ones.

- Dense arrays of resonant NEMS to cover a much larger surface

While tracking additional modes can be relatively easily implemented, the surface gain is less than a factor of two while a mass beam focusing on a 1mm² surfaces would gain two orders of magnitudes. Mass beam focusing is currently being developed at CEA-Leti, Grenoble to focus particles into a 1mm² surface. In parallel, efforts are carried out to match the NEMS surface to this 1mm² surface using arrays of NEMS. The design, fabrication, electrical characterization and addressing technique of small arrays, as a first step toward larger arrays, are the object of Chapter 4.

Bibliography

[1] M. S. Hanay, S. Kelber, A. K. Naik, D. Chi, S. Hentz, E. C. Bullard, E. Colinet, L. Duraffourg, and M. L. Roukes, “Single protein nanomechanical mass spectrometry in real time,” *Nature nanotechnology*, vol. 7, pp. 602–608, 2012.

[2] J. Chaste, A. Eichler, J. Moser, G. Cballos, R. Rurali, and A. Bachtold, “A nanomechanical mass sensor with yoctogam resolution,” *Nature nanotechnology*, vol. 7, pp. 301–304, 2012.

[3] E. Mile, “Systèmes électromécaniques nanométriques à base de nanofils de silicium et nanotubes de carbone,” 2010.

[4] C. Kharrat, E. Colinet, and A. Voda, “H∞ Loop shaping control for PLL-based mechanical resonance tracking in NEMS resonant mass sensors,” *IEEE Sensors*, no. 4716641, pp. 1135–1138, 2008.

[5] “www.asygn.com.” .

[6] Y. Whang, “Jump and sharp cusp detection by wavelet,” *Biometrika*, vol. 82, no. 2, pp. 385–397, 1995.

[7] A. Antoniadis and I. Gijbels, “Detecting abrupt changes by wavelet methods,” *J. Nonparametr. Stat.*, vol. 14, no. 1–2, pp. 7–29, 2002.

[8] K. Bleakley and J.-P. Vert, “The group fused Lasso for multiple change-point detection,” *Technical report HAL-00602121*, 2011.

[9] B. Kalafut and K. Visscher, “An objective, model-independent method for detection of non-uniform steps in noisy signals,” *Computer Physics Communications*, vol. 179, no. 10, pp. 716–723, 2008.

[10] N. J. Carter and R. A. Cross, “Mechanics of the kinesin steps,” *Nature*, vol. 435, pp. 308–312, 2005.

[11] R. Morel, A. Brenac, P. Bayle-Guillemaud, C. Portemont, and F. La Rizzo, “Robert Morel & Ariel Brenac Growth of Cobalt.pdf,” *European Physical Journal D*, vol. 24, no. 1, pp. 287–290, 2003.

[12] A. Marek, J. Valter, S. Kadlec, and J. Vyskcil, “Gas aggregation nanocluster source - Reactive sputter deposition of copper and titanium nanoclusters,” *Surface & Coatings Technology*, vol. 205, pp. S573–S576, 2011.

[13] H. Haberland, M. Mall, M. Moseler, Y. Qiang, and T. Reiners, “Filling of micronsized contact holes with copper by energetic cluster impact,” *Journal of Vacuum Science and Technology A*, vol. 12, p. 2925, 1994.

[14] K. Jensen, K. Kim, and A. Zettl, “An atomic-resolution nanomechanical mass sensor.,” *Nature nanotechnology*, vol. 3, pp. 533–537, Sep. 2008.

[15] C. M. Bishop, *Pattern Recognition and Machine Learning*. Springer, 2007.

[16] D. W. Allan, “Statistics of Atomic Frequency Standarts,” *Proceedings of the IEEE*, vol. 54, no. 2, pp. 221–230, 1966.

[17] B. Ma, “Challenges in computational analysis of mass spectrometry data for proteomics,” *Journal of Computer Science and Technology*, vol. 5, no. 1, pp. 107–123, 2010.

[18] J. B. Cunniff and P. Vouros, “Mass and Charge State Assignement for Proteins and Peptide Mitures Via Nanocovalent Adduction in Electrospray Mass Spectrometry,” *Journal of the*, vol. 6, pp. 1175–1182, 1995.

[19] C. Fah, “Characterization and de novo sequencing of multi-charge MS/MS spectra,” 2010.

[20] K. Vad, A. Csik, and G. Langer, “Secondary neutral mass spectrometry--A powerful technique for quantitative elemental and depth profiling analyses of nanostructures,” *SpectroscopyEurope*, vol. 21, no. 4, pp. 13–16, 2009.

[21] K. Tang, J. Page, and R. Smith, “Charge competition and the linear dynamic range of detection in electrospray ionization mass spectrometry,” *Journal of the American Society for Mass Spectrometry*, vol. 15, no. 10, pp. 1416–23, 2004.

[22] S. Banerjee and S. Mazumdar, “Electrospray ionization mass spectrometry: a technique to access the information beyond the molecular weight of the analyte,” *International journal of analytical chemistry*, vol. 2012, no. Article ID 282574, p. 40 pages, 2012.

[23] S. Dohn, W. Svendsen, A. Boisen, and O. Hansen, “Mass and position determination of attached particles on cantilever based mass sensors.,” *The Review of scientific instruments*, vol. 78, no. 10, p. 103303, Oct. 2007.

[24] S. Dohn, S. Schmid, F. Amiot, and A. Boisen, “Position and mass determination of multiple particles using cantilever based mass sensors,” *Applied Physics Letters*, vol. 97, p. 044103, 2010.

Chapter IV: Frequency-addressed NEMS arrays

This chapter presents the concept of frequency-addressed NEMS arrays. The motivation and principle of these arrays will be exposed before presenting their design and fabrication. Then, a simple resistance model of these arrays is compared to experimental resistance measurements. Characterizations in open loop and closed loop are presented to evaluate any performance degradation with respect to single devices. Finally, the implantation and performances of the frequency addressing technique is explained and experiments highlighting the potential of NEMS arrays for gas and mass sensing are detailed and discussed for future promising implementations.

1. Rationale of NEMS arrays

Resonant NEMS have recently demonstrated promising results for gas sensing [1] or mass sensing [2-3] with extremely low mass resolutions. The extreme sensitivity of resonant NEMS mass sensors is bestowed by their inherent low dimensions. Indeed, the relative frequency shifts induced by uniform mass adsorption is proportional to the resonator mass:

$$\frac{\Delta f}{f} = \frac{\Delta m}{2M} \qquad \textbf{(IV.1)}$$

where Δf is the detected frequency shift, f is the nominal frequency, Δm is the adsorbed mass and M the resonator mass.

However, this extreme sensitivity comes at the cost of an extremely reduced proportion of the resonant area versus the inactive regions: 10^{-6} is the typical ratio between the sensing area and the total device layout (Fig. IV.1).

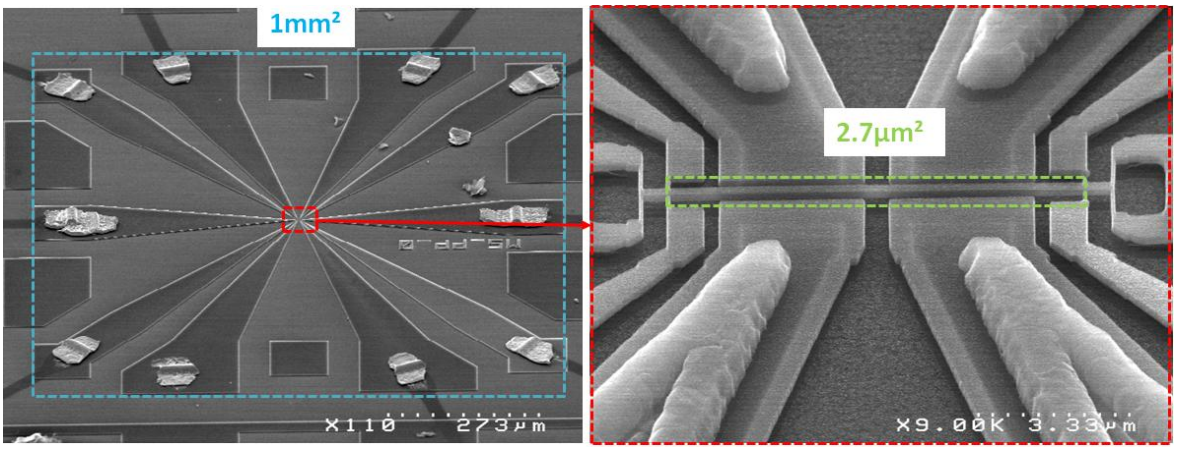

Fig. IV.1: SEM image of the device layout showing the wirebonding pads, electrical accesses

and the resonant beam. The beam represents 2.7ppm of the total layout surface.

The capture cross-section becomes extremely small, in the µm² scale, making the detection of a molecule of a particle beam highly unlikely as ion or mass sources usually produce mass beams with cross sections in the mm² or cm² scale. However, increasing the device cross-section (hence the device mass) would inevitably lead to a loss of sensitivity. A solution to keep both high sensitivity and large capture surface is to multiply the number of sensors and pack them as densely as possible as schematized in Fig. IV.2.

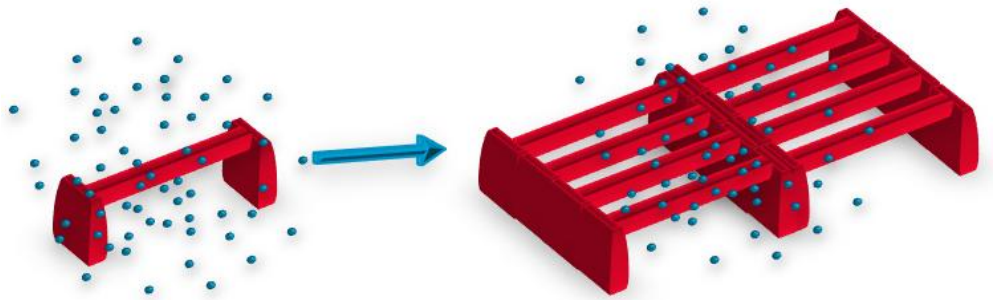

Fig. IV.2: Multiplication of the particle detection probability by multiplication of resonant sensors.

However, providing individual electrical accesses to each resonator within a large array is extremely challenging as we need a minimum of 4 electrical connections per device: an array of 100 NEMS would then require 400 electrical accesses, each associated with a bonding pad of 150µm*150µm. This would lead to a complex and lengthy wirebonding of these pads to an external multiplexer. In addition, the issue of the low sensing surface versus the total layout surface is not addressed.

A recent attempt to extend the sensing surface and the mass sensitivity for gas sensing applications consisted in realizing large arrays of interconnected, identical NEMS with metallic piezoresistive devices to obtain both a large capture area and high sensitivity for gas sensing applications [4]. Arrays up 6800 resonators have been achieved yielding a device density around 6 million NEMS/cm² (Fig. IV.3). The concept relied on the collective coherent response of these thousands of devices with identical geometry and resonance frequency interconnected both in series and in parallel providing natural noise averaging, high output signal and high power handling.

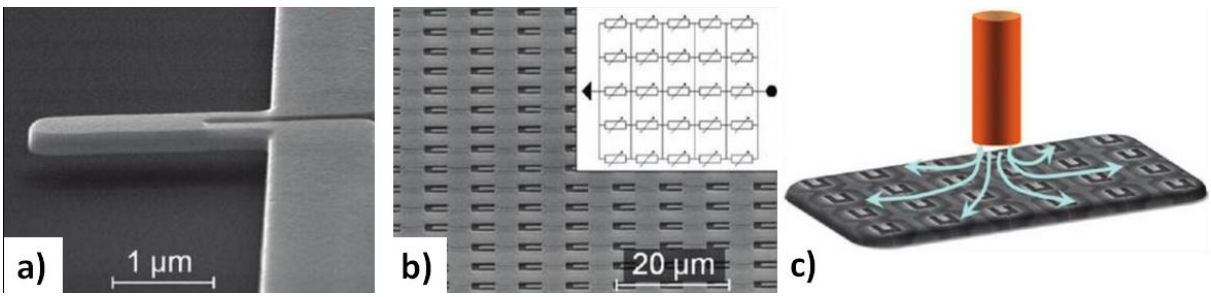

Fig. IV.3: Large scale integration of resonant NEMS for gas sensing applications: SEM image of an individual piezoresistive cantilever (a), SEM image of a section of a VLSI cantilever array (b) and schematic of the integration of the array with gas a chromatography system (c)

While the useful signal would add coherently over the array, noise from individual cantilevers would add incoherently leading to a SNR increase of $\sqrt{N}$, N being the number of cantilevers:

$$SNR = \frac{\sum_{i=1}^{N} Signal_i}{\sum_{i=1}^{N} Noise_i} = \frac{N.Signal}{\sqrt{N.Noise^2}} = \sqrt{N}\frac{Signal}{Noise} \qquad \textbf{(IV.2)}$$

where $Signal_i = Signal$ and $Noise_i = noise$ for all i.

However, averaging the coherent signals of all NEMS did not yield the desired noise reduction as the array suffered from fabrication uncertainties, leading to spread in individual nominal frequencies and decrease in overall quality factor. Moreover, the thermoelastic actuation and bias for piezoresistive detection of thousands of cantilevers caused large power consumption and the design of those arrays was inherently aimed at applications where the perturbation to be measured is homogeneous over the whole array such as gas concentration sensing. On the other hand, access to every single device in the array is necessary for NEMS-MS as molecules land on only one resonator: with these arrays, the signal information of a single device would be drowned in the array output.

We propose here to use arrays of NEMS resonators with different resonant frequencies that we can address and read sequentially over time [5]: provided there is sufficient spacing between each resonant frequency, the fabrication uncertainties issue is circumvented and the information of each individual resonant sensor becomes accessible. The frequency of each resonator becomes its address, which is the reason why the term “frequential addressing” was coined. While it can lead to noise reduction for gas concentration sensing applications the same way as in [4], it allows for real time monitoring of every single resonator within the array for NEMS-MS applications.

2. Principle of Frequency addressed NEMS arrays

The NEMS arrays we propose are composed of individual resonators being either cantilevers designed for gas sensing in air or doubly clamped beams for mass sensing in vacuum (Fig. IV.4). The resonant beams typical dimensions are 160nm thick, 300nm wide and several micrometers long. Actuation is electrostatic and in-plane motion transduction is performed thanks to piezoresistive nanogauges disposed in a bridge configuration for background cancellation [6]. Hence each device possesses five electrical connections.

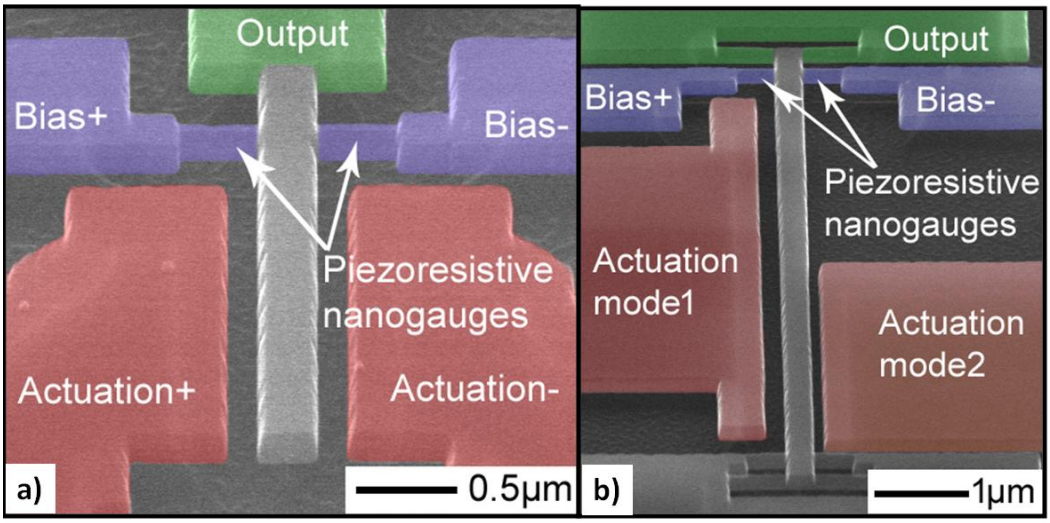

Fig. IV.4: Colorized SEM image of typical suspended in-plane resonators found in our NEMS arrays: cantilevers are designed for gas sensing (a) while doubly clamped beams are designed for NEMS-MS (b). Actuation pads are in red or orange, bias gauges in blue and output in green.

Our architecture uses two additional metal layers to interconnect all individual devices in parallel: the array has the same input/output (I/O) ports as a single device and the provided input signal is applied to the whole set of NEMS while the output signal is the sum of all individual NEMS' contributions. The layout of an array composed of three cantilevers is schematized in Fig. IV.5.

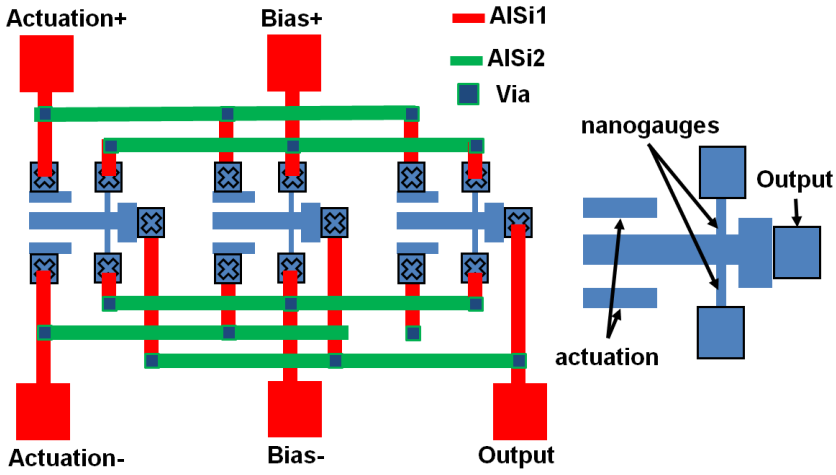

Fig. IV.5: NEMS array layout interconnecting in parallel all input/outputs electrical connections of three cantilevers using two level of metal layers (AlSi)

While [4] (Fig. IV.3) was aiming at obtaining one "super device" having one response composed of added up coherent response from identical resonators, we are rather looking for individualized resonators whose response can be retrieved within the array. The resonance frequency of a beam is calculated as:

$$f_n = \frac{{\lambda_n}^2}{4\pi}\sqrt{\frac{E}{3\rho_{Si}}}\frac{w}{L^2} \qquad \textbf{(IV.3)}$$

where E is Young's modulus, ρ_{Si} the silicon density, w the beam width, L the beam length and λ_n the eigenvalue of mode n.

On the other hand, the beam mass sensitivity is proportional to the resonator mass hence L, w and t. Since f_n is inversely proportional to L^2, the best option to engineer a range of resonance frequencies along a population of beam resonators is to gradually change their lengths. Doing so with w would lead to an increased spread of mass sensitivities within the array.

Therefore each resonator has a different length hence a different resonance frequency that will be used for identification. The expected open loop response to a frequency sweep is a succession of Lorentzian peaks, each corresponding to a different resonator as shown in Fig. IV.6.

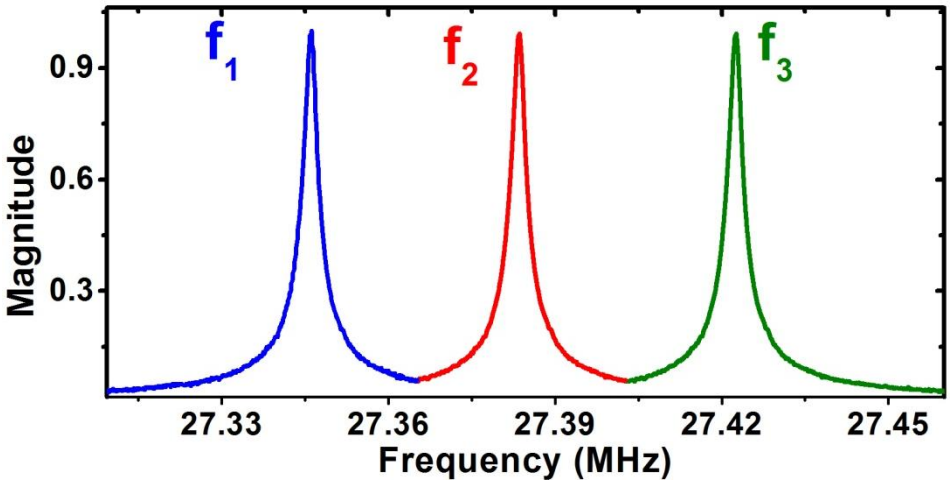

Fig. IV.6: Expected open loop response of three resonators interconnected in parallel with three well separated resonance frequencies.

Thus, assuming all devices' backgrounds are additive, when actuating and reading the device number #x found within an array of N NEMS, the output is composed of the amplified response of the x^{th} device at resonance plus the off-resonance responses of the other N-1 devices:

$$Output\ @\ f_x = S_x + \sum_{i=1}^{N} BGD_i \qquad \textbf{(IV.4)}$$

where f_x is the frequency address, S_x the pure signal and BGD_x the background signal of NEMS number #x

Therefore, this architecture requires using individual resonators whose Signal to Background Ratio (SBR) is initially very high. Our group has demonstrated that our devices motion transduction based on doped nanowire gauges achieved SBRs up to 67dB which makes them excellent candidate for this architecture [6].

Once the frequency address of each resonator is known, any of them can be interrogated individually if the information of a specific NEMS is desired. Plus, the complete array can be probed by switching between each resonator as quickly as possible: the PLL is instructed to measure the resonance frequency of one device and switch to the next NEMS as soon as the information is obtained. If we switch quickly enough, we get a virtually simultaneous monitoring of all NEMS at long time scales. While theoretically possible in open loop, the concept is better implemented in closed loop operation. The notion is illustrated in Fig. IV.7.

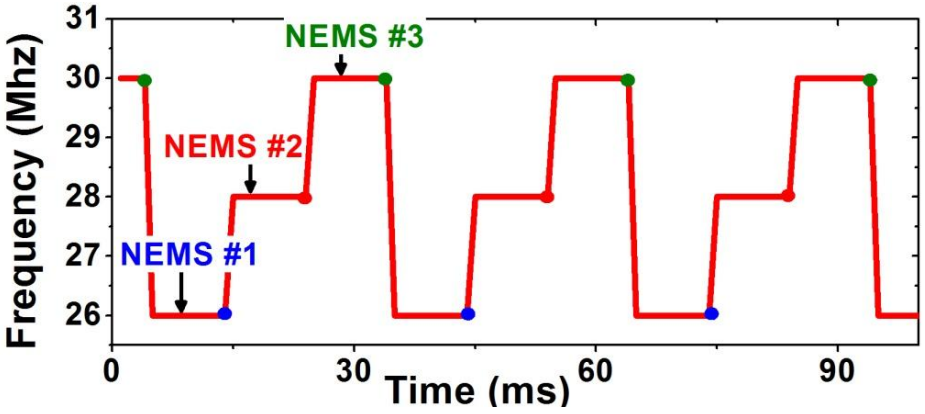

Fig. IV.7: Array probing by sequentially switching from one NEMS to the following one over time. The individual signal of each resonator can then be reconstructed by keeping each data points found before each switch.

We wait for the PLL response time to acquire a data point before switching to the next NEMS. Probing the complete array comes at the cost of a reduced sampling rate as it follows:

$$SR = \frac{1}{\tau_{PLL} \times N} \qquad \textbf{(IV.5)}$$

where N is the number of NEMS in the array and τ_{PLL} the time we need to wait for to obtain a point before switching to the next NEMS

In the literature, mass resolution of mass sensors are generally evaluated with the Allan Deviation (ADEV) [7] of the resonator's nominal frequency taken at the integration time of the measurement. Using a PLL response time of 10ms, we would be interested in the ADEV in the 10ms range for single resonators. However, for arrays featuring tens of resonators with a higher sampling time, we will be interested in the ADEV at higher integration times, for instance 200ms for a τ_{PLL} of 10ms in an array of 20 devices.

3. Fabrication

The fabrication follows a top-down approach on a 200mm silicon-on-insulator (SOI) with a p-doped top silicon layer (5.10^{19} cm^{-3}) using standard CMOS VLSI processes [6]. The NEMS area is realized by a hybrid deep UV/electron beam lithography on the Si TOP of a SOI wafer. The first oxide level is deposited and patterned for interconnections contacts Si TOP/metal1. Then metal1 layer (AlSi) is deposited and etched before deposition of a second oxide layer. Vias are patterned for metal1/metal2 interconnections and the second level of metal is deposited and etched. The array of resonant structures is finally released by vapor HF (Fig. IV.8).

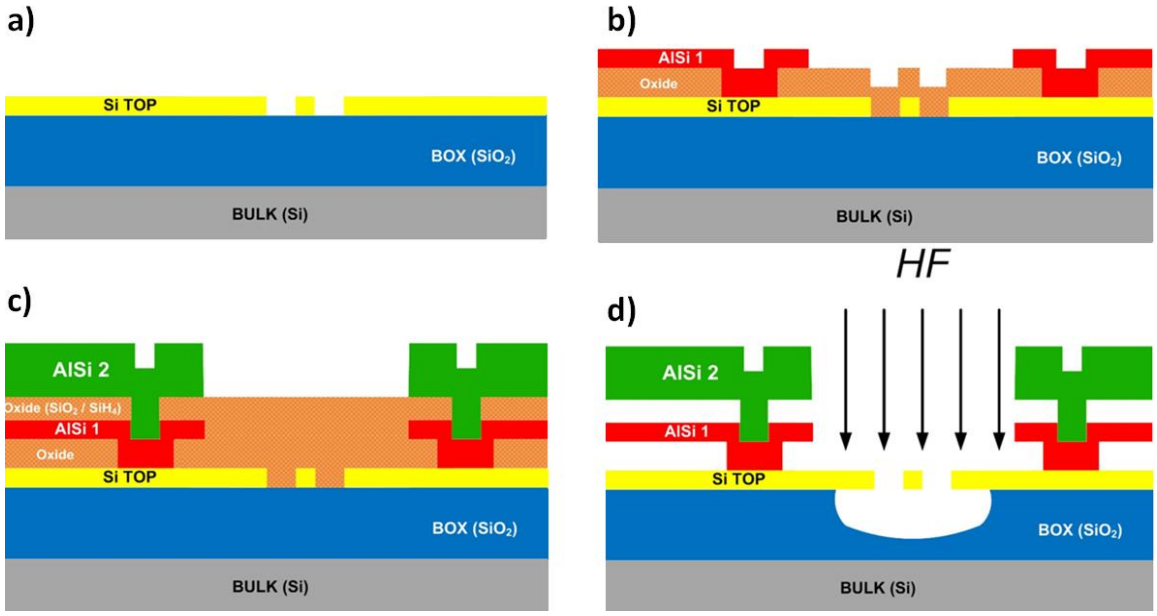

Fig. IV.8: Wafer level processes to build NEMS arrays: patterning of the resonant structure on the Si TOP of a SOI wafer (a), deposition and patterning of first levels of oxide and metal (b), deposition and patterning of second levels of oxide and metal (c) and final release with vapor HF.

The two levels of metals are necessary to interconnect properly all five electrical connections of each resonator with those of the other NEMS in the array. Metal1 and metal2 lines carry the signals vertically and horizontally respectively while vias enable to realize the desired interconnections as shown in Fig. IV.10. The signal always transit trough two vias from the device to the pad.

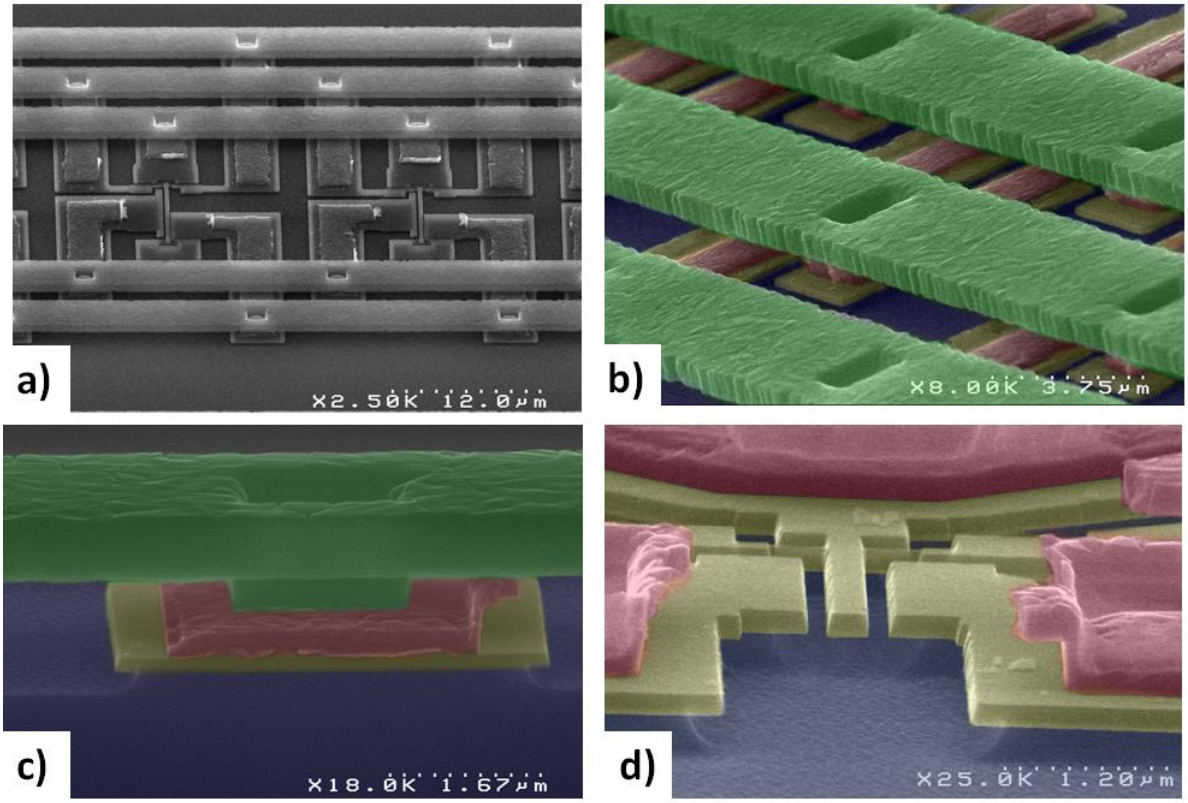

Fig. IV.9: SEM image of two doubly clamped beams within a 5x4 array showing parallel interconnections (a); colorized SEM image of dense intersecting metal1 and metal2 lines (b), interconnection via (c) and released cantilever (d).

Simple arrays of 20, 49 or 100 interconnected nanoresonators have been designed. There are two types of array designs according to the application. Doubly clamped beams used for mass sensing are arranged in a square shape forming an elementary capture surface (5x4, 7x7 or 10x10) while cantilevers designed for gas sensing are aligned in columns that can be easily integrated in fluidic channels (1x20 or 2x10). Fig. IV.10 presents SEM images of both designs.

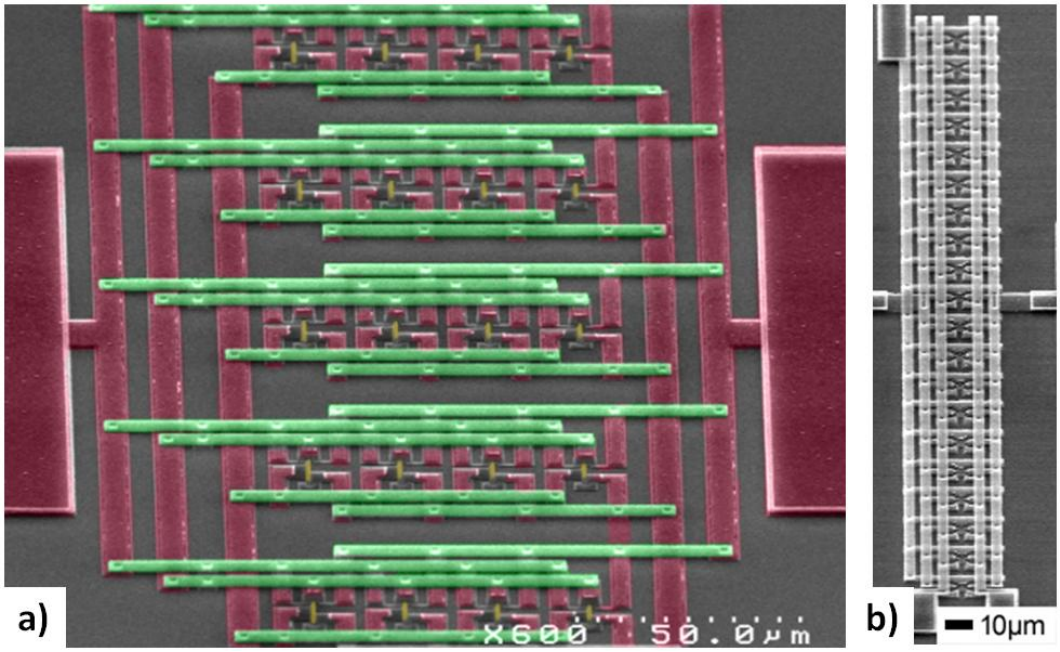

Fig. IV.10: Colorized SEM image of square shaped array (5x4) of doubly clamped resonators designed for NEMS-MS (a) and SEM image of an array of cantilevers disposed in line (1x20) for gas sensing. Resonators are colorized in yellow, metal1 in red and metal2 in green.

Typical pitches between the resonators are 20µm and 57µm in the horizontal and vertical direction respectively. The NEMS' resonance frequencies range approximately from 20MHz to 70MHz. The frequency pitches of the resonance peaks range from 150 kHz to 1MHz according to the design and the number of resonators within the array: for a given measurable bandwidth, a higher number of NEMS within the array requires lower frequency pitches while small arrays can extend this pitch.

4. Equivalent circuit

The resistance model of a resonator can be schematized as in Fig. IV.11.

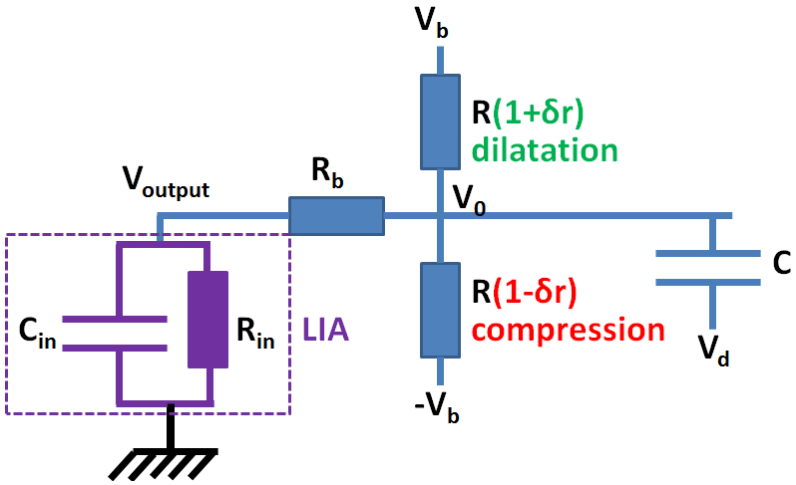

Fig. IV.11: Electrical model of single resonant NEMS. Nanogauges resistances are modeled by R while Rb is the resistance from the Bias pad to the middle of the nanogauge bridge. A capacitor models the electrostatic actuation. δr is the piezoresistive resistance variation. The input impedance of the LIA is modeled by a resistance and a capacitor in parallel.

The LIA input impedance is $Z_{in} = \left(\frac{1}{R_{in}} + jC_{in}\omega\right)^{-1}$.

4.1. Impact of arrays of resistances

When considering an array of N NEMS devices, the potential Vdrive is applied on all capacitors modeling the actuation: the surface for charge accumulation is added and the equivalent capacitor of the array is:

$$C_{array} = \sum_{i=1}^{N} C_i \qquad \textbf{(IV.6)}$$

where C_{array} is the equivalent capacitance of the array and C_i the equivalent capacitance of the individual resonator number #i

Assuming Rb, and R are identical in the N devices, identical currents flow in the resistances regardless of the device. Hence, without beam motion, we can model the array's resistances as a parallel combination of individual resonators' resistances:

$$R_{array} = \left(\sum_{i=1}^{N} \frac{1}{R_i}\right)^{-1} = \frac{R}{N} + R_{access} \qquad \textbf{(IV.7)}$$

where R_{array} is the equivalent nanogauge array, R_{access} the array access resistance and R_i the equivalent resistance R of the individual resonator number #i

Hence we expect the equivalent resistance of NEMS arrays to drop as the number of resonators increase. Resistance measurements were performed between the output pads and the bias pad to deduce R and Rb of different NEMS arrays and singe devices [8]. Typical values are listed in Fig. IV.12.

NEMS number	1	20	49	100
R	2kΩ	200Ω	105Ω	60Ω
Rb	1.5kΩ	150Ω	80Ω	55Ω

Fig. IV.12: Resistance measurements on single devices and NEMS arrays

While the resistances scale down with the number of devices, we don't get exactly the expected values. Taking the single resonators as a reference, the expected values would be:

NEMS number	1	20	49	100
R	2kΩ	100Ω	41Ω	20Ω
Rb	1.5kΩ	75Ω	31Ω	15Ω

Fig. IV.13: Expected resistances on NEMS arrays

The discrepancies might be caused by different access resistances as well as the dispersion on the resistance measurements since single device exhibited a standard deviation on R around 600Ω. Plus, we have few resistance measurements on NEMS array rending these values vulnerable to random errors.

4.2. Impact of arrays on the output signal

Using the Millman theorem, we calculated in Chapter 1 the value of the voltage sensed by the Lock In amplifier when the beam is in motion is:

$$V_{output} = \frac{V_b \times \delta r}{1 + \frac{R_b}{Z_{in}} + \frac{R}{2Z_{in}}} \quad \textbf{(IV.8)}$$

where V_0 is the voltage at the middle of the nanogauge bridge, V_b the polarization voltage, R the nanogauge nominal resistance and δr the relative resistance variation in a nanogauge subjected to mechanical strain.

In the ideal case with infinite LIA input impedance we have:

$$V_{output} = V_b \times \delta r \quad \textbf{(IV.9)}$$

When one resonator within an array is in motion, the following resistance model can be used to describe the effect of its resistances variations:

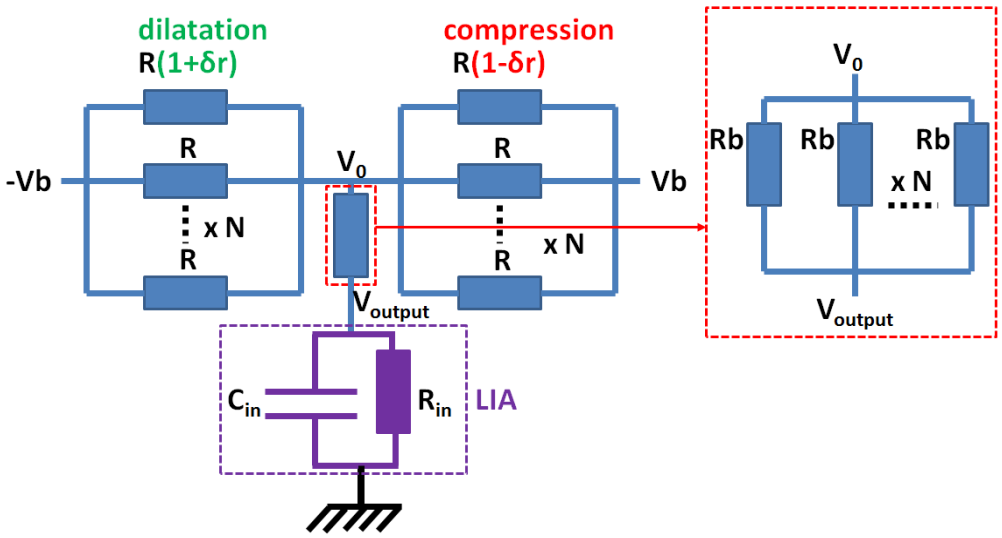

Fig. IV.14: Resistance model of a NEMS array when only one device is in motion

The equivalent nanogauge resistance for the left branch is calculated as:

$$Z_+ = \left(\frac{1}{R(1+\delta r)} + \sum_{i=1}^{N-1}\frac{1}{R}\right)^{-1} = \frac{R(1+\delta r)}{N+(N-1)\delta r} = \frac{R}{N-\dfrac{\delta r}{1+\delta r}} \qquad \textbf{(IV.10)}$$

Similarly, the nanogauge resistance for the right branch is calculated as:

$$Z_- = \left(\frac{1}{R(1-\delta r)} + \sum_{i=1}^{N-1}\frac{1}{R}\right)^{-1} = \frac{R(1-\delta r)}{N-(N-1)\delta r} = \frac{R}{N+\dfrac{\delta r}{1-\delta r}} \qquad \textbf{(IV.11)}$$

Therefore, the voltage V_0 is calculated as:

$$V_0 = \frac{\dfrac{V_b}{Z_+} - \dfrac{V_b}{Z_-}}{\dfrac{1}{Z_+} + \dfrac{1}{Z_-} + \dfrac{1}{Z_{in} + \dfrac{R_b}{N}}} = \frac{V_b \times \delta r}{\delta r^2 + \left(N + \dfrac{R}{2\left(Z_{in} + \dfrac{R_b}{N}\right)}\right)(1-\delta r^2)} \qquad \textbf{(IV.12)}$$

$$\cong \frac{V_b \times \delta r}{N + \dfrac{R}{2\left(Z_{in} + \dfrac{R_b}{N}\right)}}$$

The approximation can be made as the relative resistance change is extremely small ($\approx 10^{-3}$-10^{-4}) compared to N.

The output voltage is written as:

$$V_{output} = \frac{V_0 \times Z_{in}}{Z_{in} + \frac{R_b}{N}} = \frac{V_b \times \delta r}{N + \frac{R_b}{NZ_{in}} + \frac{R}{2Z_{in}}} \quad \textbf{(IV.13)}$$

In the ideal case with infinite LIA input impedance we have:

$$V_{output} = \frac{V_b \times \delta r}{N} \quad \textbf{(IV.14)}$$

Therefore the output voltage is inversely proportional to the number of devices in the array. If we reason in term of dissipated power, a single device dissipates:

$$P_{single} = \frac{2{V_b}^2}{R} \quad \textbf{(IV.15)}$$

An array of parallel devices dissipates:

$$P_{array} = \frac{2N{V_b}^2}{R} \quad \textbf{(IV.16)}$$

Therefore arrays consume N times more power than single devices.

4.3. Impact of arrays on noise

The thermomechanical noise is proportional the white noise force applied on the beams times the piezoresistor gauge factor (GF) [8]:

$$S_{th} \propto \frac{4M_{eff}\omega_0 k_B T}{Q} \frac{GF^2.{V_b}^2}{M_{eff}^2\left((\omega^2 - {\omega_0}^2)^2 + \frac{\omega^2{\omega_0}^2}{Q}\right)} \quad \textbf{(IV.17)}$$

Thermomechanical noise is filtered out for frequencies away from the resonance frequency of the beam. Therefore, when probing a specific device, we only see thermomechanical noise of this device. Since both the signal of the array and the thermomechanical noise is divided by N, the SNR is the same as with a single device.

The Johnson noise picked up by our devices is calculated as:

$$J = \sqrt{4k_b TR} \quad \textbf{(IV.18)}$$

where k_b is Boltzmann constant, T the temperature and R the equivalent resistance

Hence a single device picks up:

$$J_{single} = \sqrt{4k_bT\left(\frac{R}{2} + R_b\right)} \qquad \textbf{(IV.19)}$$

While an array obtains:

$$J_{array} = \sqrt{4k_bT\frac{\left(\frac{R}{2} + R_b\right)}{N}} \qquad \textbf{(IV.20)}$$

Hence a Johnson noise reduction of √N is to be expected. Therefore, for Johnson noise and for the same polarization voltage, the SNR of an array is decreased by a factor √N with respect to a single device.

In summary, at equal polarization voltage, the SNR of arrays with respect to single devices remains the same for thermomechanical noise while it decreases by √N for Johnson noise. SNR reduction is mainly caused by the signal reduction by a factor of N caused by the parallel resistances of inactive devices. Hence, if we can deliver $\sqrt{N}$ times more voltage, we should obtain similar performances from a device within an array with respect to a single device.

5. Characterizations

Open loop measurements were performed on the NEMS arrays: when the drive frequency of the array is swept over the complete range, all individual resonances appear in the array frequency response as expected (Fig. IV.15).

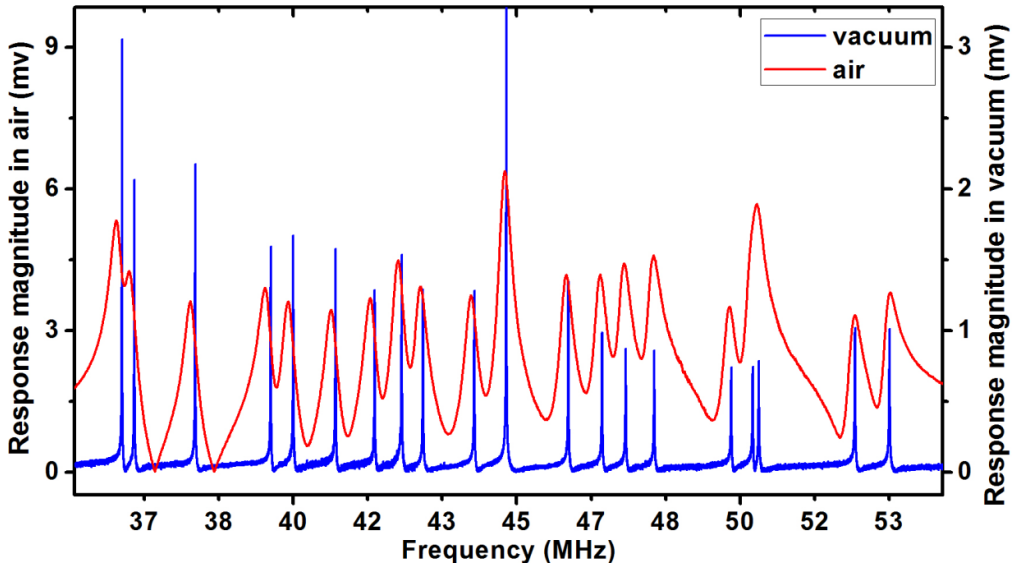

Fig. IV.15: Frequency sweep of an array of 20 cantilevers in air and vacuum (First mode response)

Because of fabrication uncertainties, the frequency spacing can somewhat differ from the designed one. While it is usually a minor concern for vacuum measurements, it may lead to peak overlap in air where the quality factor is low. For instance, we can observe in Fig. IV.15 that NEMS #17 and #18 are very close one to another. While they can be separated in vacuum where their Q is roughly 7000, it is impossible to tell them apart in air where Q is roughly 100. This implies that further care must be taken with frequency spacing for arrays designed to operate in air environment. Yet, large frequency spacing also implies a larger operating frequency range and a larger spread of mass sensitivities. Hence a trade-off must be made on the base of the estimated process variability related variance of nominal resonance frequency [9].

Signal to Background Ratios (SBR) were extracted from arrays of 20 devices and compared to those of individual devices resonating at 25MHz and 45MHz for doubly-clamped beams and cantilevers respectively. Typical values are presented in Table 1.

Cantilever	Single device	NEMS array
SBR (air)	18dB	15dB
Phase jump (air)	170°	60-85°
Q (air)	145	65-125
SBR (vacuum)	47dB	38dB
Phase jump (vacuum)	180°	180°
Q (vacuum)	7000	7000
Doubly-clamped beam	Single device	NEMS array
SBR (air)	33dB	30dB
Phase jump (air)	160°	65-105°
Q (air)	90	55-105
SBR (vacuum)	42dB	40dB
Phase jump (vacuum)	180°	180°
Q (vacuum)	6000	6000

Table IV.1: Typical open loop characteristics of single devices and NEMS arrays

In vacuum, the characteristics of a NEMS within an array are almost those of an individual resonator: quality factors and phase jumps are not degraded and the SBR retains a very good value. While -13dB with respect to single devices were expected, we multiplied the polarization voltage by 2 or 3 (+6dB or +9.5dB respectively) to get a SBR close to those of single devices. In air however, we observe a spread in quality factors and phase jumps. This is mainly due to the varying beam lengths resulting in different amounts of viscous damping [10]. Because of lower quality factors in air, most resonant peaks overlap each other thus reducing phase jumps and the SBRs but they remain excellent and sufficient for PLL tracking.

As explained in Chapter III, the frequency stability of a resonant sensor is a critical parameter for optimum mass sensing performances. Therefore, although the open loop characteristics of NEMS arrays are excellent, we need to characterize the potential degradations of the frequency stability brought by the NEMS array architecture.

Locking a Phase-Locked-Loop to each resonator within a doubly clamped beam array, we characterized the frequency stabilities of both mode 1 and mode 2 as shown in Fig. IV.16. The array features 19 NEMS whose first resonance mode range from 26.3MHz to 41.8MHz.

Given that we plan to monitor the complete array in real time by sequentially switching from one device to another, the sampling rate decreases (details in Section 2 of this chapter) and our integration time range of interest shifts from 10ms to 100ms.

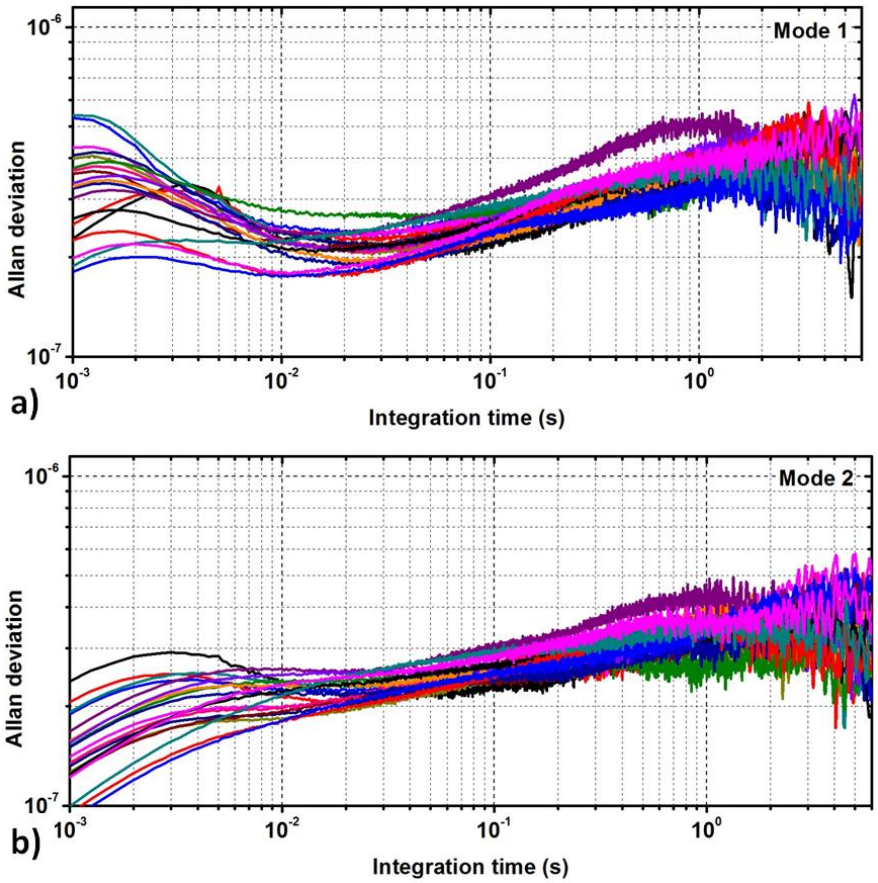

Fig. IV.16: Relative frequency stability of mode 1 (a) and mode 2 (b) from 19 NEMS of an array of 20 doubly-clamped beams.

We observe that although the 19 devices within the array have different lengths and therefore different resonance frequencies, relative frequency stabilities are very similar. At 100ms integration time we obtain an ADEV ranging from 2.2×10^{-7} to 3×10^{-7} for both modes. Comparatively, ADEV around 2×10^{-7} and 1.25×10^{-7} for mode 1 and mode 2 respectively can be found for a traditional single resonator coming from the same chip batch (Fig. IV.17).

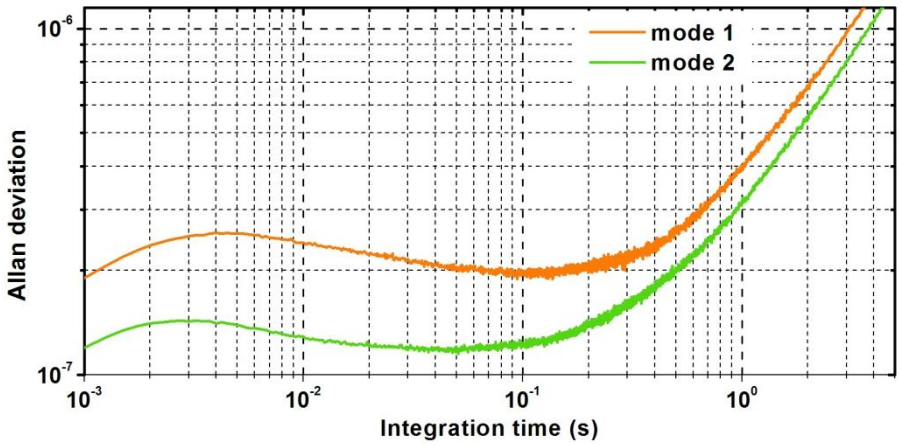

Fig. IV.17: Relative frequency stability of mode 1 and mode 2 from a single resonator. The single device comes from the same chip batch as the NEMS arrays. Mode 1 and mode 2 resonates at 26.5MHz and 72.2MHz respectively.

The discrepancies between the array ADEVs and the single device ADEVs are inferior to the statistical variations of relative frequency stabilities observed in our population of single devices. Therefore the inclusion of the single resonator within an array does not seem to degrade its frequency stability in a large extent. This is excellent news for potential applications such as concentration gas sensing and NEMS-MS.

To obtain similar performances with respect to single devices, the polarization voltage applied on the piezoresistive nanogauges must be increased: while bias voltages of 1.25Vpp are generally used for single devices, 2.5Vpp is applied on 20 NEMS arrays. Arrays of 49 NEMS (7x7) require 6Vpp but we still keep and excellent SBR of 40dB. An open loop sweep is shown in Fig. IV.18.

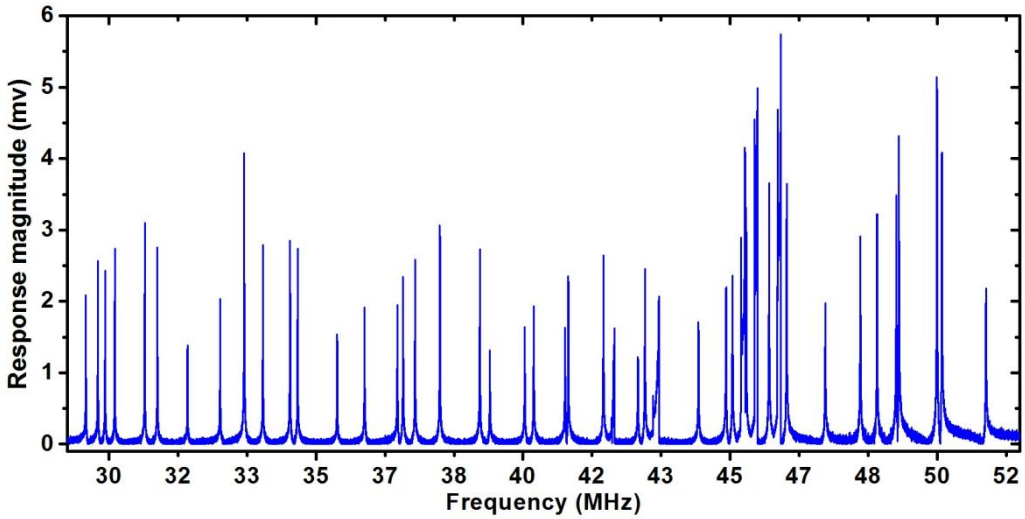

Fig. IV.18: Open loop sweep of an array of 49 doubly clamped resonators (7x7).

However, preliminary results on the relative frequency stabilities measured on one resonator of a 7x7 array seemed to point out degradations respect with single devices since values of roughly 5×10^{-7} were obtained. Nevertheless, the measurements were performed on only one device within the array in different vacuum conditions. Open loops on a 10x10

arrays showed a very weak signal that did not allow for acceptable frequency stabilities. Additional measurement should be carried out to confirm these early results. Nevertheless, the development of the first demonstration of mass sensing applications was focused on the smallest fabricated arrays i.e. arrays of 20 NEMS for the sake of simplicity of implementation. Once validated, the concept can then be extended to larger arrays. In this work, the reader may encounter details of experiments where arrays have of 19 or 18 devices for instance: this is due to unfortunate NEMS destructions, usually at the nanogauge level, caused by static discharges as depicted in Fig. IV.19.

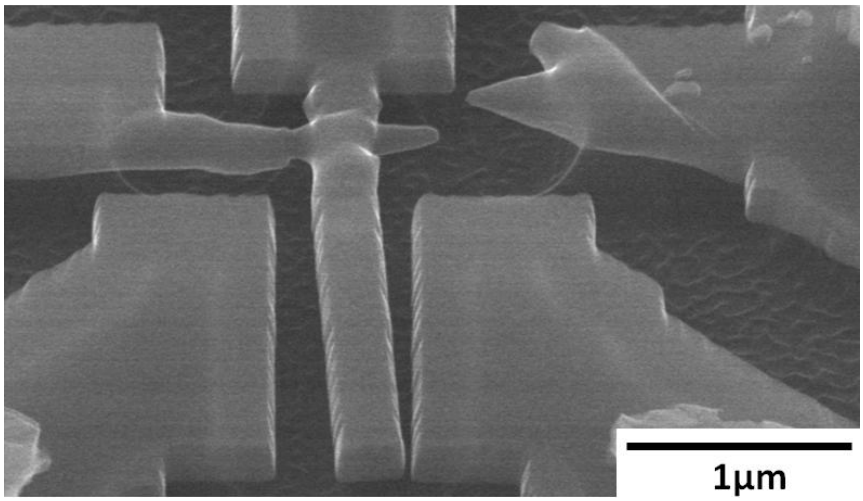

Fig. IV.19: Nanogauge melting caused by electrostatic discharges on a cantilever embedded in an array of 20 resonators.

As the number of devices in the array increases, the equivalent resistance decreases leading to a higher weakness to electrostatic discharge. Nevertheless it is interesting to see here an additional advantage of our array design insofar as the "death" of a single device let us use the remaining devices with minor incidences. The "dead" resonator is then the equivalent of a dead pixel on a LCD screen. Hence, our architecture is robust towards isolated defects and is especially pertinent in the frame of VLSI integration

6. Frequency-addressing technique

In this section, we cover the implementation of the frequency-addressing technique that was previously mentioned in Section 2. The complete process required for successful monitoring of NEMS arrays using the frequency-addressing technique has been fully implemented in a custom Labview instrument control software. The code controls the "D-Box" electronic boards presented in Chapter III via an Ethernet connection. A large array of commands can be sent to the equipment such as actuation and polarization voltage amplitudes, frequencies, phase references or the LIA low pass filter integration time, sampling rates etc. In addition the developed software can handle different actuation and polarization voltages required by each single resonator. This seemingly optional feature happened to be of paramount importance for homogeneous performances over the whole array. Indeed,

fabrication variabilities induce a wide range of required actuation and polarization voltages that need to be properly tuned for each resonator. Besides, the custom electronics delivered lower voltages as the commanded frequency increased (for a constant commanded voltage). Consequently, the mode 2 resonance peaks in the 80-115MHz range were often almost indistinguishable and attempting to switch over the whole array with voltage parameters taken from the first NEMS was bound to fail. Fortunately, individual device operating points solved this issue.

Measurements have been focused on an array of 20 cantilevers. It is first necessary to identify each NEMS' own resonant frequency and phase reference needed for PLL operation (Fig. IV.15). Recorded resonances frequencies are the NEMS' "addresses" that we can use to interrogate any of them while the phase reference allow for proper LIA phase reference setting to null out the phase at resonance for optimal PLL operation. Once the matrix of 20 pairs $[f_n, \varphi_n]$ is stored in memory, the software allows navigating through the array by automatically setting the sweep parameters of the open loop module corresponding to the selected NEMS. The open loop resonance of the selected NEMS can be acquired and may be used update $[f_n, \varphi_n]$ for this NEMS (if necessary) and move on to its closed looped monitoring. The corrector coefficients of the PLL transfer function are calculated from the quality factor of any resonator: quality factors found within the array are identical in vacuum and very similar in air. In closed loop operation, actuation and polarization voltages are tuned for maximization of the resonator's frequency stability characterized by the ADEV and kept in memory in an additional matrix of pairs$[V_{drive}, V_{bias}]$. This procedure must be repeated for every functional device of the array.

Once the preparatory steps have been dealt with, the PLL is sequentially locked onto each NEMS of the array as quickly as possible over time as illustrated in Fig. IV.20.

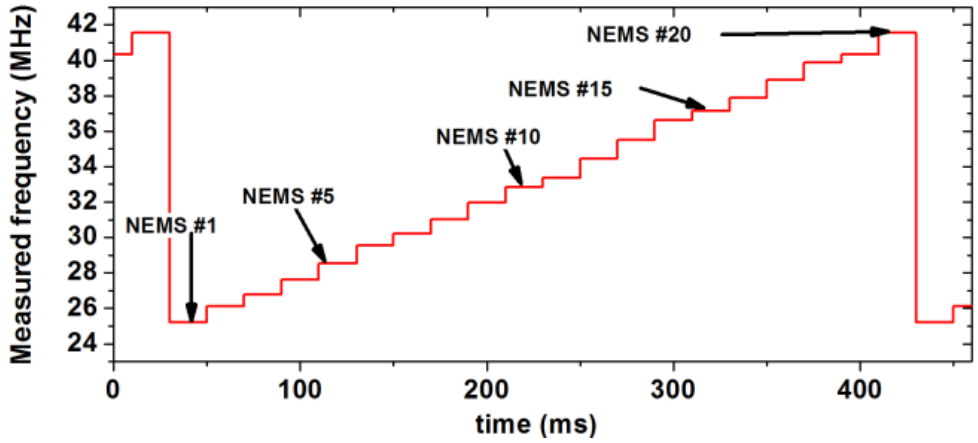

Fig. IV.20: Frequency addressing technique. The PLL successively locks onto each NEMS over time based upon resonance frequency and phase reference of each NEMS gathered previously in Open Loop.

Practically, switching from NEMS #N to N+1 implies to open the loop, change the operating frequencies and phase references according to NEMS #N+1, change the actuation and polarization voltage adapted for NEMS #N+1 and close the loop. Since we are looking for a sampling rate as low as possible, the PLL is instructed to lock onto the next NEMS when

the PLL response time is reached, yielding a sampling time for each resonator equal to the number of resonator in the array times the PLL response time. A typical switch is presented in Fig. IV.21.

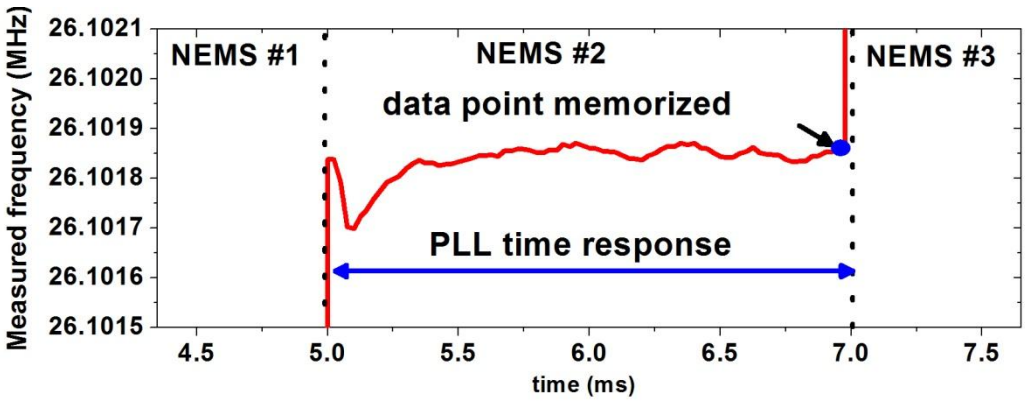

Fig. IV.21: Zoomed in view of an acquired data point of NEMS #2. After switching from NEMS #1, the full response of the PLL is awaited before switching to the next NEMS. Data points before each switch are memorized.

While sweeping the array, the frequency addresses are continuously updated to ensure that the PLL switches to the latest known frequencies. After an acquisition, the raw data is postprocessed with a Matlab algorithm that detects data points found before switches and automatically reconstruct the frequency trace of every individual resonator as shown in Fig. IV.22.

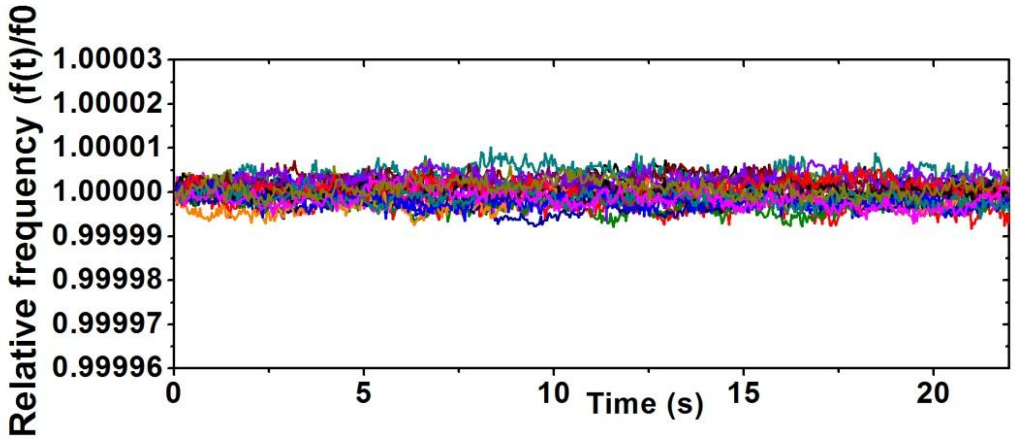

Fig. IV.22: Frequency trace of 20 resonators reconstructed from frequency-addressing technique based measurements like in Fig. IV.20.

The major concern resides now in the impact of the frequency addressing technique on the frequency stability of resonators. We found out that the frequency stability found with a conventional scheme is not degraded by our technique. A typical comparison of the mode 1 ADEV of one cantilever within the array is presented in Fig. IV.23.

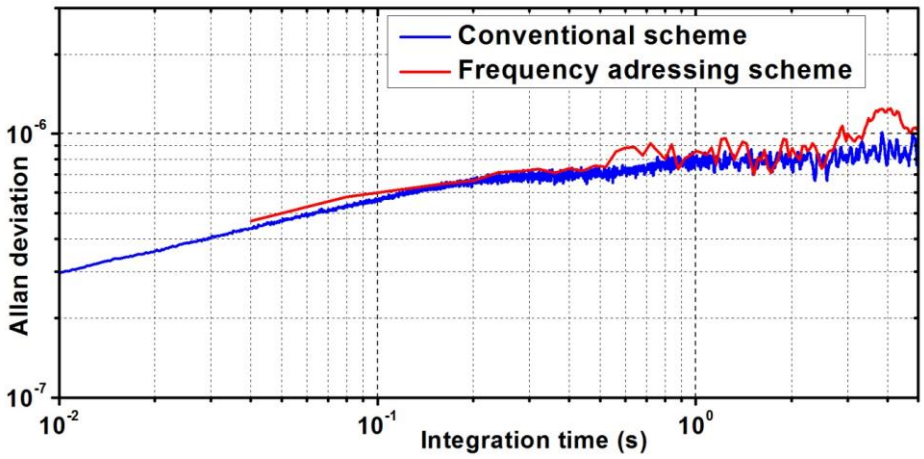

Fig. IV.23: Comparison of the frequency stability of one resonator (#10) in vacuum when readout as a single device or within the array using the frequency addressing technique. Strictly speaking, the definition of the Allan deviation is not satisfied for the frequency-addressed measurement as there is dead time between data points.

We have proved that we can monitor a complete array of resonators without sizeable degradation of their performances and we can now demonstrate their applications for potential use in gas sensing or NEMS-MS.

7. Potential applications in mass and gas sensing

7.1. Gas sensing

In air, 19 NEMS were tracked using a PLL response time of 25ms. We couldn't track all 20 NEMS because of peak overlap (Fig. IV.15). We obtained ADEVs ranging from 9×10^{-7} to 2×10^{-6}, i.e. excellent stabilities in air environment. When plotting the typical ADEV curve, i.e. the mean ADEV obtained by a single resonator, we obtain a typical ADEV at 1.3×10^{-6}. Then the array was viewed as one "superdevice" with a single mean resonance frequency obtained by averaging all 19 signals. This is very similar to [4] except that signal averaging isn't done electrically in-situ but rather by numerical postprocess. Provided that the frequency noise is uncorrelated between each device and that the noise is stationary and ergodic, averaging over the 19 NEMS is equivalent to averaging the acquisition repeated 19 times and should provide a noise reduction of $\sqrt{19}$. However, this inevitably leads to lower sampling times which means a trade-off on noise reduction and bandwidth must be made according to the desired sensing application. The mean frequency of the array was computed and its frequency stability was found to go down to $3.4.10^{-7}$, yielding a noise reduction of around 3.8, a value close to $\sqrt{19}$ (4.36). The experiment is more easily visualized in Fig. IV.24.

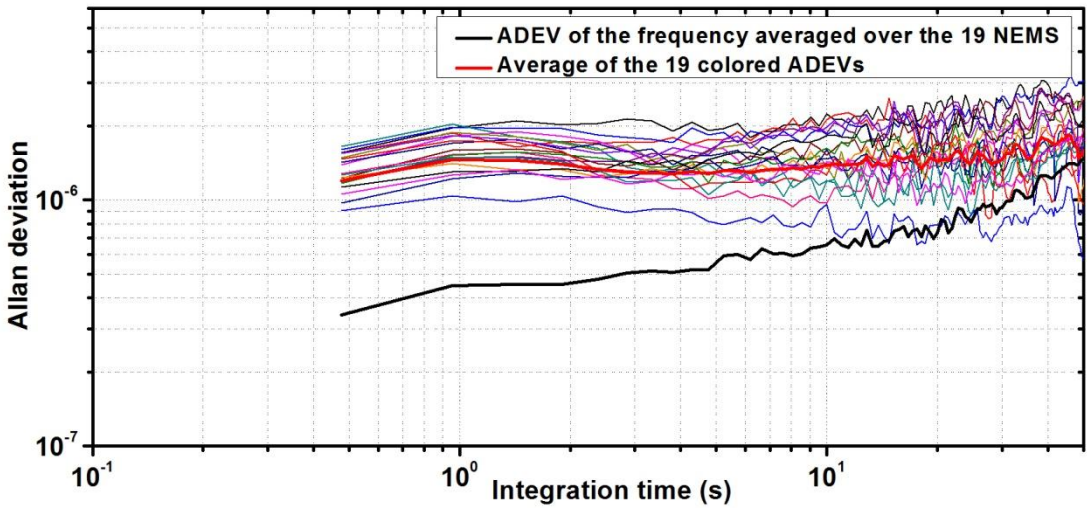

Fig. IV.24: Allan deviation versus integration time for the frequencies of 19 cantilevers within an array (colored) and for the average frequency of the 19 NEMS (thick black line). For comparisons purposes, the average ADEV of the 19 NEMS is computed (thick red line).

The slight discrepancy with respect to the expected noise reduction probably comes from the resonance peaks overlapping and better results are expected from arrays with larger frequency spacing. Plus, no further investigation was performed on the subject as the work of this thesis is mainly focused on NEMS-MS applications. Nevertheless, ADEV values as low as $3.4.10^{-7}$ in air are promising for excellent performances for homogeneous concentration detection of gas over the array.

7.2. Mass sensing

Using a PLL response time of 2ms we successfully tracked 20 cantilevers in vacuum, yielding a sampling time of 40ms for all NEMS within the array. This is the fastest sampling time achievable with the currently available electronic equipment. Indeed, switch commands are externally sent by a Labview code from a personal computer. Yet Labview codes speed can't handle submillisecond speed except if compiled on a Real-Time Target and switching every 1ms showed extreme instability as latencies would cumulate yielding randomly time spaced switch commands. Higher switch rates will be obtained with newer versions of the "D-Box" equipment that will include internal switching functions independent of the command software speed.

While tracking the array, we simulated mass adsorption-induced frequency shifts by applying DC voltage steps on the entire array using the unused second actuation pad; connected to the 20 NEMS in parallel as well. The experiment is presented in Fig. IV.25 .

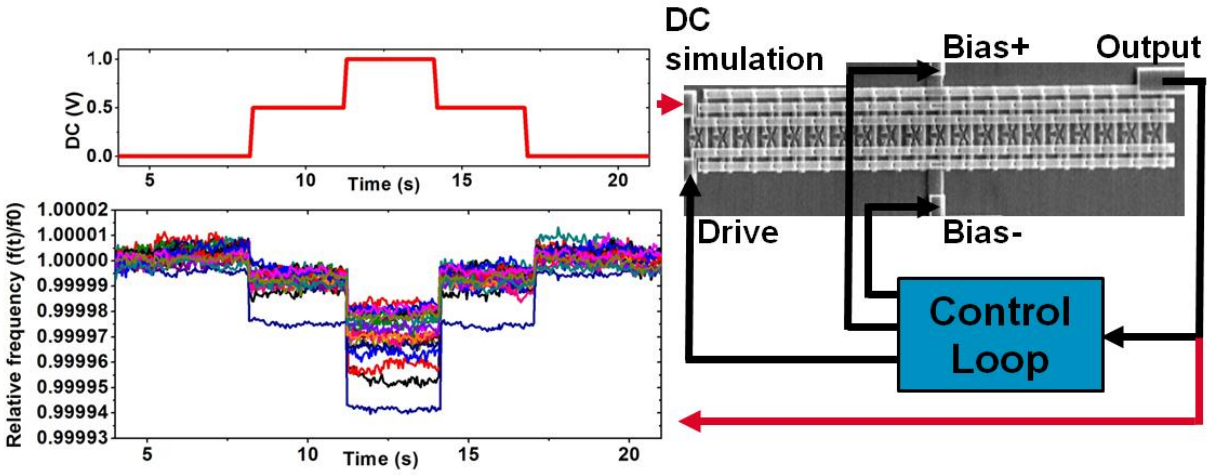

Fig. IV.25: Reconstructed relative resonance frequencies of 20 NEMS tracked using the frequency addressing technique. All NEMS respond to negative stiffness induced by DC voltage steps applied on all resonators using the second actuation electrode (Fig. IV.4). Every 3 seconds, we applied +0.5V DC twice then -0.5V DC twice.

We demonstrated that we could track the frequency shifts on all 20 NEMS: the capture area for mass detection applications is multiplied by 20. The spread in frequency shift magnitudes can be explained by the unequal access resistances caused by interconnections and the different NEMS lengths leading to a spread of resonator stiffness and actuation electrostatic force.

8. Conclusion

A new approach to significantly increase the active area of extremely small NEMS sensor with a simple routing scheme that keeps the number of electrical connections low was presented. It consists in using arrays of NEMS with different resonance frequencies sequentially addressed in time. All devices are interconnected in parallel thanks to two levels of metal and their lengths are gradually changed. This gives them a unique resonance frequency which becomes their "address". By using a PLL that locks to a different NEMS down to every 2ms, the closed loop monitoring of a full array of 20 NEMS down to a 40ms time scale has been demonstrated in both air and vacuum almost without noise increase.

The advantages of this system over individual devices for concentration gas sensing is evidenced by the reduction of the signal noise by a factor close to $\sqrt{N}$, N being the number of averaged NEMS signal and allowed to obtain Allan Deviations down to $3.4.10^{-7}$ range in air.

The successful monitoring of 20 NEMS in vacuum in a 40ms time scale also holds great promise for future NEMS mass spectrometry applications as it may lead to MS imaging when combined to a MALDI or LIAD ([11], [12]) ion source and a much larger mass event detection probability for ESI-NEMS-MS where event rates of 1 particle/30min may go down to more acceptable rates (around 1 particle/1min30s for an array of 20 devices).

We presented an application of the frequency-addressing technique where each device is successively read over time. While still viable for small arrays, very low sampling rates are to be expected for very large arrays. Hence one can consider combining this technique with multispectral signal generators. Indeed, similarly to the multimode tracking presented in chapter III, one can simultaneously drive multiple NEMS within the array as long as the electronics is able to provide a sufficient number of drive and detection signals. Hence one can imagine arrays of NEMS where columns are read sequentially over time while lines are read simultaneously using multispectral tracking: an array of 100 devices may be monitored with a 40ms sampling time with a 5 mode multispectral electronics switching to 20 different columns over time.

For concentration gas sensing another option can consist in realizing frequency addressed arrays of classical arrays i.e. combine the NEMS array architecture presented in [4] with our frequency-addressing scheme: an array of 1000 NEMS can be realized by designing 100 arrays of 10 NEMS with identical frequencies: provided trade-offs can be made on the sampling rate, the power consumption respective to an array of 1000 identical NEMS is divided by 10. Plus, small arrays where the spread in frequency is too large can be considered as a dead pixel and be ignored: this would reduce the noise averaging gains but improve the sampling rate. Hence, studies can be extended to the optimal combination of arrays for different applications requiring different trade-offs between noise reduction, sampling rate, or power.

NEMS-MS applications, on the other hand, cannot use arrays of identical NEMS and the priority is to achieve extremely dense frequency-addressed NEMS arrays. The two metal lines used to interconnect in parallel each device spend a significant area of layout space leading to device spatial pitch of the order of 10s of µm. Extremely dense arrays may be obtained with CMOS co-integration where interconnections are routed below the sensing surface that can then be designed much denser.

Nevertheless, before achieving such complex wafer level systems, their viability needs to be assessed with first proofs of concept of sensing applications with 2D arrays. While the first demonstrations of gas concentration sensing have been already reported, the following Chapter IV presents the first demonstration of NEMS-MS based on arrays of oscillating nanostructures.

Bibliography

[1] J. Arcamone, A. Niel, V. Gouttenoire, M. Petitjean, N. David, R. Barattin, M. Matheron, F. Ricoul, T. Bordy, H. Blanc, J. Ruellan, D. Mercier, N. Pereira-Rodrigues, G. Costa, V. Agache, S. Hentz, J. Gabriel, F. Baleras, C. Marcoux, T. Ernst, L. Duraffourg, E. Colinet, E. B. Myers, M. L. Roukes, P. Andreucci, E. Ollier, and P. Puget, "VLSI silicon multi-gas analyzer coupling gas chromatography and NEMS detectors," in *International Electron Devices Meeting (IEDM)*, 2011, pp. 29.3.1–29.3.4.

[2] J. Chaste, A. Eichler, J. Moser, G. Cballos, R. Rurali, and A. Bachtold, "A nanomechanical mass sensor with yoctogam resolution," *Nature nanotechnology*, vol. 7, pp. 301–304, 2012.

[3] M. S. Hanay, S. Kelber, A. K. Naik, D. Chi, S. Hentz, E. C. Bullard, E. Colinet, L. Duraffourg, and M. L. Roukes, "Single protein nanomechanical mass spectrometry in real time," *Nature nanotechnology*, vol. 7, pp. 602–608, 2012.

[4] I. Bargatin, E. B. Myers, J. S. Aldridge, C. Marcoux, P. Brianceau, L. Duraffourg, E. Colinet, S. Hentz, P. Andreucci, and M. L. Roukes, "Large-Scale Integration of Nanoelectromechanical Systems for Gas Sensing Applications," *Nano letters*, vol. 12, pp. 1269–1274, 2012.

[5] E. Sage, O. Martin, C. Dupré, T. Ernst, G. Billiot, L. Duraffourg, E. Colinet, and S. Hentz, "FREQUENCY-ADDRESSED NEMS ARRAYS FOR MASS AND GAS SENSING APPLICATIONS," in *Transducers*, 2013.

[6] E. Mile, G. Jourdan, I. Bargatin, S. Labarthe, C. Marcoux, P. Andreucci, S. Hentz, C. Kharrat, E. Colinet, and L. Duraffourg, "In-plane nanoelectromechanical resonators based on silicon nanowire piezoresistive detection.," *Nanotechnology*, vol. 21, no. 16, p. 165504, Apr. 2010.

[7] D. W. Allan, "Statistics of Atomic Frequency Standarts," *Proceedings of the IEEE*, vol. 54, no. 2, pp. 221–230, 1966.

[8] E. Mile, "Systèmes électromécaniques nanométriques à base de nanofils de silicium et nanotubes de carbone," 2010.

[9] O. Martin, E. Colinet, C. Dupré, E. Sage, P. Villard, S. Hentz, L. Duraffourg, and T. Ernst, "Impact of process variability on a frequency-addressed NEMS array sensor used for gravimetric detection," in *European Solid-State Device Research Conference*, 2013.

[10] K. Yum, Z. Wang, A. O. Suryavanshi, and M. Yu, "Experimental measurement and model analysis of damping effect in nanoscale mechanical beam resonators in air," *Journal of Applied Physics*, vol. 96, p. 3933, 2004.

[11] M. Karas, D. Bachmann, U. Bahr, and F. Hillenkamp, “Matrix-assisted ultraviolet laser desoprtion of non-volatile compounds,” *Journal of Mass Spectrometry and Ion Processes*, vol. 78, pp. 53–68, 1987.

[12] A. R. Dow, M. Wittrig, and H. I. Kenttämaa, “Laser-induced acoustic desoprtion mass spectrometry,” *European Journal of Mass Spectrometry*, vol. 18, pp. 77–92, 2012.

[13] E. Ollier, C. Dupre, G. Arndt, J. Arcamone, C. Vizioz, L. Duraffourg, E. Sage, A. Koumela, S. Hentz, G. Cibrario, P. Meininger, K. Benotmane, C. Marcoux, O. Rozeau, G. Billiot, E. Colinet, F. Andrieu, J. Philippe, F. Aussenac, D. Mercier, H. Blanc, T. Ernst, and P. Robert, “Ultra-scaled high-frequency single-crystal Si NEMS resonators and their front-end co-integration with CMOS for high sensitivity applications,” *Micro Electro Mechanical Systems (MEMS)*, pp. 1368–1371, 2012.

Chapter V: Nanomechanical mass spectrometry with arrays of resonant NEMS

While the setup to compare NEMS-MS and conventional ion MS was presented in Chapter III along with the associated results and conclusions, Chapter IV covered the concept and preliminary results of frequency-addressed NEMS arrays for gas and mass sensing. In this chapter, we demonstrate the first proof of concept of NEMS-MS with arrays of resonant NEMS by inserting an array in our mass deposition setup. This is a first, simple effort towards scaling the technology, mainly in terms of capture area and throughput. Extremely fast and robust readout and control schemes had to be developed to this aim. The performances are evaluated with different cluster populations and the ability to produce a spectrum with each device is investigated by positioning the array in different positions of the cluster beam.

1. Experimental design

For the first demonstration of NEMS-MS with arrays, we implemented the concept on the smallest arrays available i.e. array of 20 devices. The procedure can then be translated to bigger arrays. An array of 20 doubly clamped NEMS was selected to perform NEMS-MS measurements in the deposition chamber of our gas-aggregation setup. The primary objective was the building of mass spectra of tantalum clusters out of the detected relative frequency shifts on mode 1 and mode 2 obtained from the 20 NEMS of the array.

An additional interest of the NEMS array resides in the ability to produce a mass spectra on each individual NEMS: we dispose of an array of nanomechanical mass spectrometer that provides individual information, just like a CCD array, that we may read to know the mass distribution sensed along a specific spatial coordinate defined by the resonator position. For instance a very large array can be used to characterize a particle beam where NEMS at the center of the beam would measure higher particles than those in the periphery. Hence, a second objective was to demonstrate the possibility to perform spatial MS imaging with such arrays by building an individual mass spectrum on each resonator. Since we are using small arrays, actual spatial imaging of a complete beam is not within reach. A first step toward this long term objective consists in highlighting the spatial properties of arrays by evidencing mass detection of portions of array while low numbers of events are detected on the other side. This was achieved by placing the array at the periphery of the nanocluster beam.

Achieving those two objectives implied bringing the frequency-addressing technique covered in Chapter IV to a whole new level where two PLLs simultaneously monitoring mode

1 and mode 2 are instructed to sequentially switch from one NEMS to the next one with extremely low switching time.

2. Array characterization

The selected array was wirebonded on a round Printed Circuit Board (PCB) and characterized in air before and after introduction in the gas-aggregation setup chip holder. Unfortunately, we found out that the NEMS with the lowest resonance (NEMS #1) was missing after inclusion as shown in Fig. V.1: electrostatic charges accumulated in the holder had probably melted the nanogauges of one device. From now one, we refer to NEMS# from 1 to 19. Knowing precisely which NEMS is destroyed is of paramount importance given that the resonant beam dimensions, especially their widths and lengths, are necessary to compute their mass sensitivities (see Chapter III Section 4). Since the lengths within the array vary from 9.2µm to 7µm, a factor up to 1.31 difference in sensitivities can be obtained. Hence mistaking a resonator's dimensions can lead to poorly accurate spectra. In addition, when one or more NEMS devices are destroyed without a possible determination of their identity, resonance peaks can't be attributed to a spatial position in the array rending spatial MS imaging impossible.

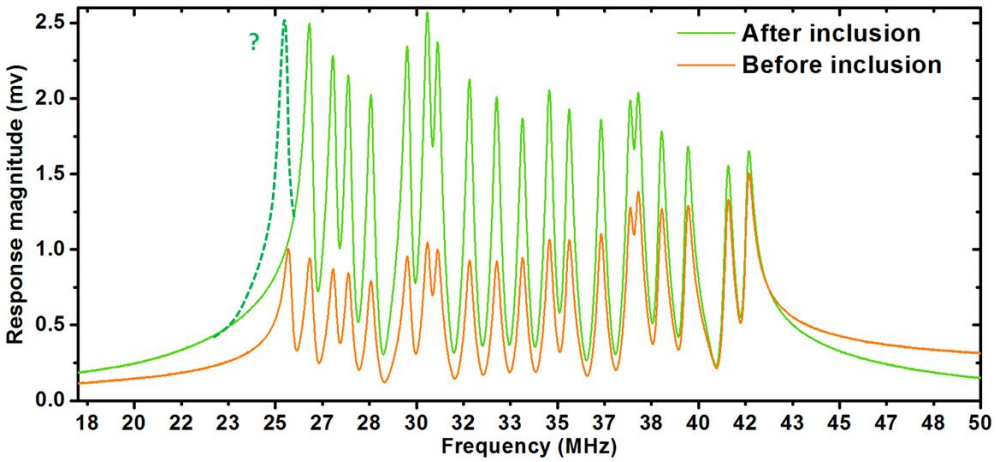

Fig. V.1: Open loop of the NEMS array before and after insertion in the chip holder underlining missing NEMS #1.

The electrical setup is identical to the multimode scheme detailed in Chapter III: two channels of the "D-Box", each associated with a given resonance mode, are combined with simple tees or power combiners to actuate and detect simultaneously modes 1 and 2. Once in vacuum, the array was cryogenically cooled with liquid nitrogen the same way we did with single devices in Chapter III. We performed a multimode open loop acquisition to identify all remaining resonance peaks resonance frequency and phase for both modes (Fig. V.2).

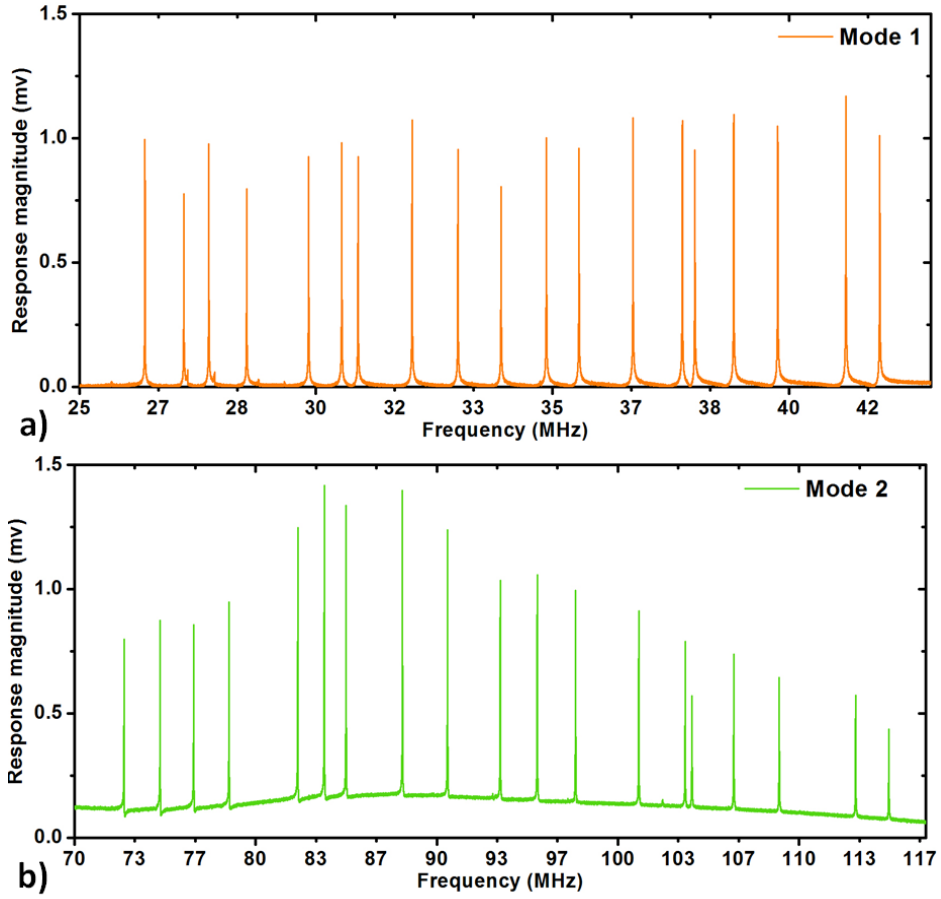

Fig. V.2: Mode 1 (a) and mode 2 (b) open loop response of an array of 19 NEMS.

Very clean resonance peaks can be observed for both modes and average quality factors of 8500 and 7500 are obtained for mode 1 and 2 respectively. At this point, it is important to check good correspondence of mode 1 peaks with mode 2 peaks. We demonstrated in Chapter I that the ratio $\frac{f_2}{f_1}$ of a doubly clamped beam is 2.75. The experimental ratios found over the array are presented in Table V.1.

NEMS#	**1**	**2**	**3**	**4**	**5**	**6**	**7**	**8**	**9**	**10**
Ratio	2.757	2.747	2.749	2.752	2.758	2.743	2.751	2.750	2.746	2.757
NEMS#	**11**	**12**	**13**	**14**	**15**	**16**	**17**	**18**	**19**	**/**
Ratio	2.740	2.746	2.755	2.748	2.739	2.740	2.739	2.745	2.742	

Table V.1: Ratios $\frac{f_2}{f_1}$ of resonators within the array

Excellent matching of ratios with respect to theory assures us confidently that f_1 and $f_2$of each pair refer to the same resonator.

We characterized the Allan deviations one-by-one of each cooled resonator within the array in multimode operation as presented in Fig. V.3.

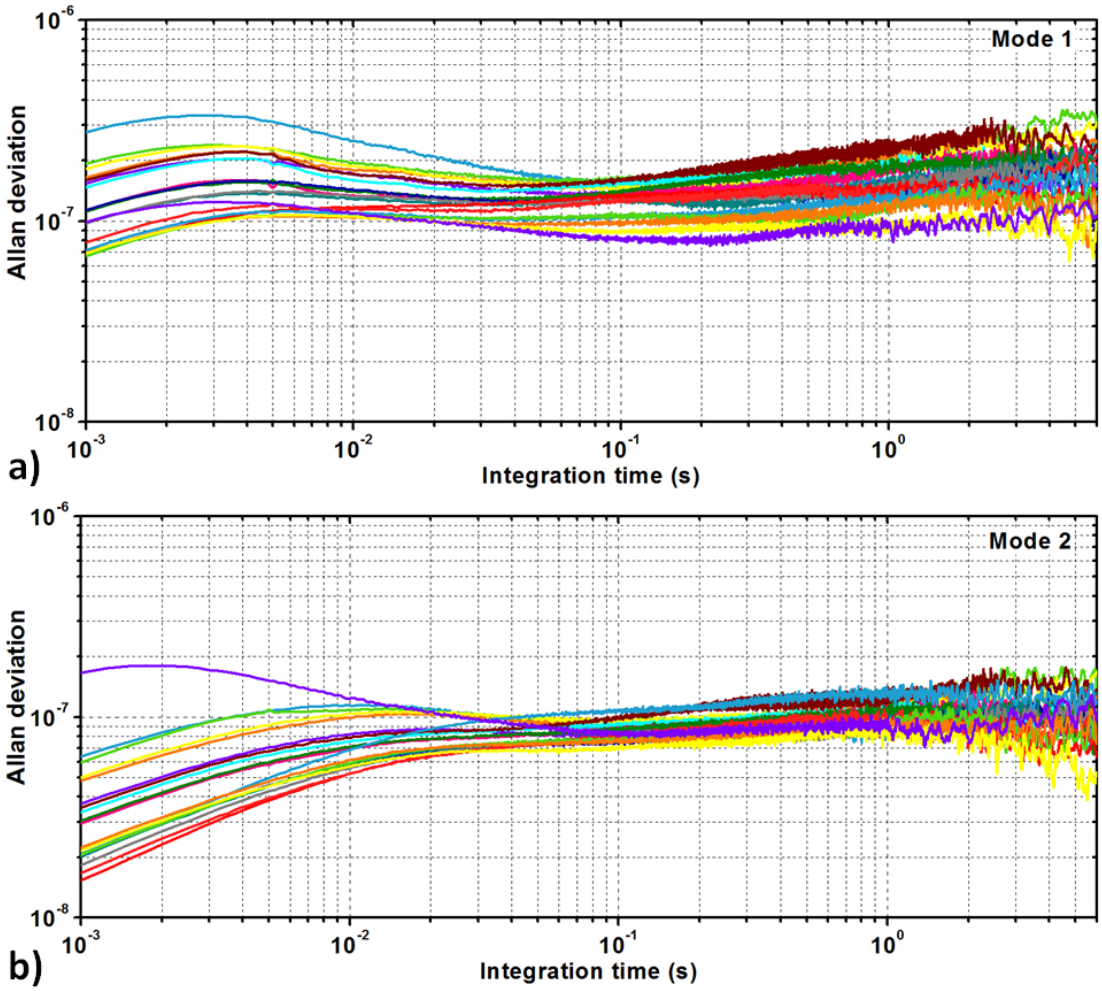

Fig. V.3: Allan Deviations (ADEV) of mode 1 (a) and mode 2 (b) measured individually on all 19 resonators cooled by liquid nitrogen.

While the ADEVs at 100ms previously found at room temperature ranged from 2.2×10^{-7} to 3×10^{-7}, the liquid nitrogen cooled devices featured ADEVs at 100ms ranging from 8×10^{-8} to 1.6×10^{-7} and 7×10^{-8} to 1.1×10^{-7} for mode 1 and mode 2 respectively. Hence, cooling the device yielded a frequency noise reduction factor around 2.

We applied the frequency-addressing scheme simultaneously on both modes using a PLL response time as low as possible. Unfortunately, we couldn't replicate the 2ms switching time we used on array of cantilevers in Chapter IV as it appeared to induce very high frequency instabilities. The sources of instabilities are not yet fully understood and require further studies. Nevertheless, given proper time to respond and reach a stable state, excellent performances with a 8ms switching time are obtained as shown in Fig. V.4 when devices are operated with frequency addressing scheme.

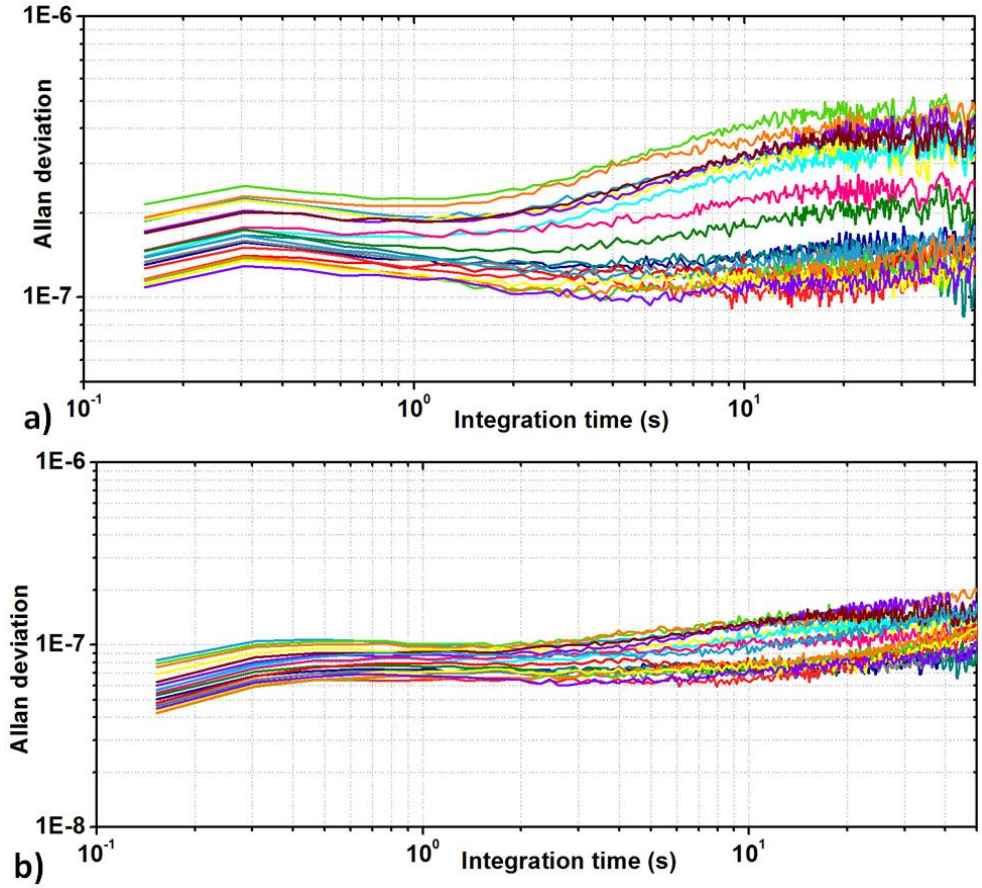

Fig. V.4: Allan deviation of mode 1 (a) and mode 2 (b) using the frequency-addressing scheme.

We obtained ADEVs from 1.3×10^{-7} to 2.5×10^{-7} and 6×10^{-8} to 1×10^{-7} for mode 1 and mode 2 respectively.

3. Mass sensitivity calibration

An important step for accurate mass measurement is the mass sensitivity calibration of each resonant device found in the array. The mass sensitivity yielding the absolute resonator frequency shift per mass unit ($Hz.g^{-1}$) is defined as:

$$S_n = \frac{f_n}{2M} = \frac{f_n}{2\rho_{Si}.t.w.L} \qquad \textbf{(V.1)}$$

where f_n is the nominal frequency of mode n, ρ_{Si} the density of silicon, t the beam thickness, w the beam width and L the beam length.

Equation (V.1) can be rewritten in term of geometric properties as:

$$S_n = \frac{\Delta f}{\Delta m} = \frac{f_n}{2\rho_{Si} w.t.L} = \frac{{\lambda_n}^2}{8\pi}\sqrt{\frac{E}{3{\rho_{Si}}^3}}\,\frac{1}{t.L^3} \qquad \text{(V.2)}$$

where λ_n is the eigenvalue of mode n

Experimental determination of sensitivities is performed in an analogous way as with a single device (details in Chapter III): the cluster source is tuned to deliver tantalum clusters as small as possible with different deposition rates measured by both the QCM and the NEMS array. The latter is monitored with the frequency-addressing scheme in multimode operation. We obtain 19 response curves that yield the mass sensitivity when linearly fitted (Fig. V.5).

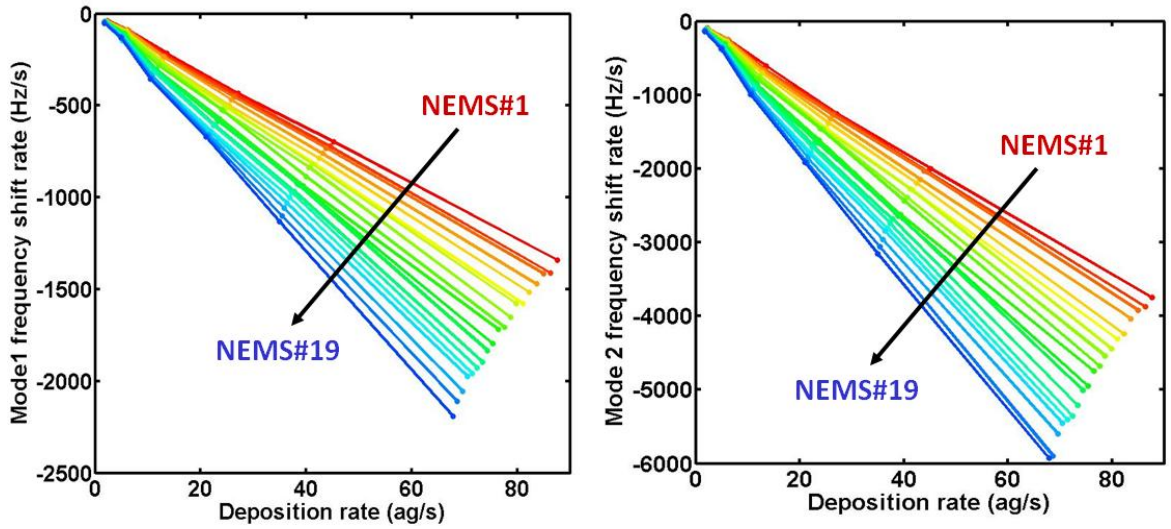

Fig. V.5: Mode 1 and mode 2 frequency shift rates of all 19 NEMS of the array with respect to the deposition rate on their surface deducted from the QCM readings. Red curve corresponds to NEMS#1 and the color progressively turn to blue for smaller devices until dark blue for NEMS#19. We deposited a maximum mass of ~4fg≪~1pg (resonator mass) to remain in the linear regime.

The extracted mass sensitivities are listed in Table V.2 for mode 1 and Table V.3 for mode 2.

NEMS#	1	2	3	4	5	6	7	8	9	10
S (Hz/ag)	15.3	16.3	16.6	17.6	18.4	19.3	19.8	21	22	22.5
NEMS#	11	12	13	14	15	15	16	18	19	/
S (Hz/ag)	23.7	24.6	25.9	26.6	27.24	27.8	29.6	30.8	32.5	/

Table V.2: Mode 1 experimental mass sensitivities

NEMS#	1	2	3	4	5	6	7	8	9	10
S (Hz/ag)	42.9	44.9	46.1	48.4	51.5	52.9	55.6	57.9	60.2	62.3
NEMS#	11	12	13	14	15	15	16	18	19	/
S (Hz/ag)	65.6	67.3	71	74	75.4	77	80.8	86.2	87.8	/

Table V.3: Mode 2 experimental mass sensitivities

According to equation (V.2), we can observe a dependence of the absolute mass sensibility on $\frac{1}{L^3}$, L being the beam length.

We observe that experimental values are roughly 1.0525 times higher than theoretical ones. The discrepancy can be attributed to fabrication process related variations. Provided division by this factor for all devices, we obtain an excellent fit and observe the predicted dependence on $\frac{1}{L^3}$ (Fig. V.6).

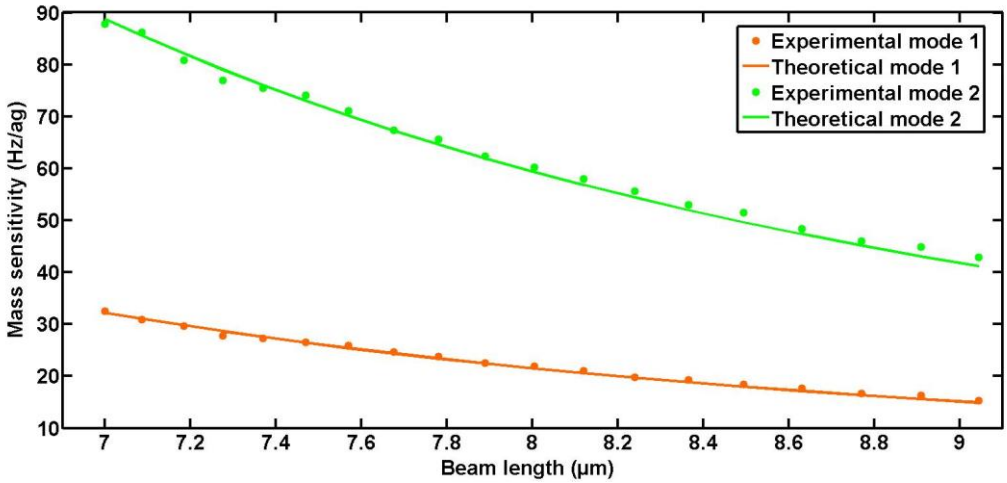

Fig. V.6: Experimental mass sensitivities divided by a factor 1.025 and fitted by theoretical values.

We have been able to perform mass sensitivity calibration for every individual device within the array with a procedure that takes the same amount of time with respect to a single device calibration. This has been made possible thanks to a reliable frequency-addressing scheme that was able to track strong and continuous frequency shifts on all devices.

4. Mass resolution and Limit Of Detection (LOD)

Given the spread of mass sensitivities and frequency stabilities within the array, we expect different LODs for each mass sensor. Similarly as what we did with single devices (Chapter III), we postprocessed a noise acquisition as if it were a mass measurement. A denoising ellipse at $2 \times \sigma$ is used to voluntarily let appear mass events generated by frequency noise. Each device's experimental LOD is found as the maximal mass value of the generated spectra as shown in Fig. V.7.

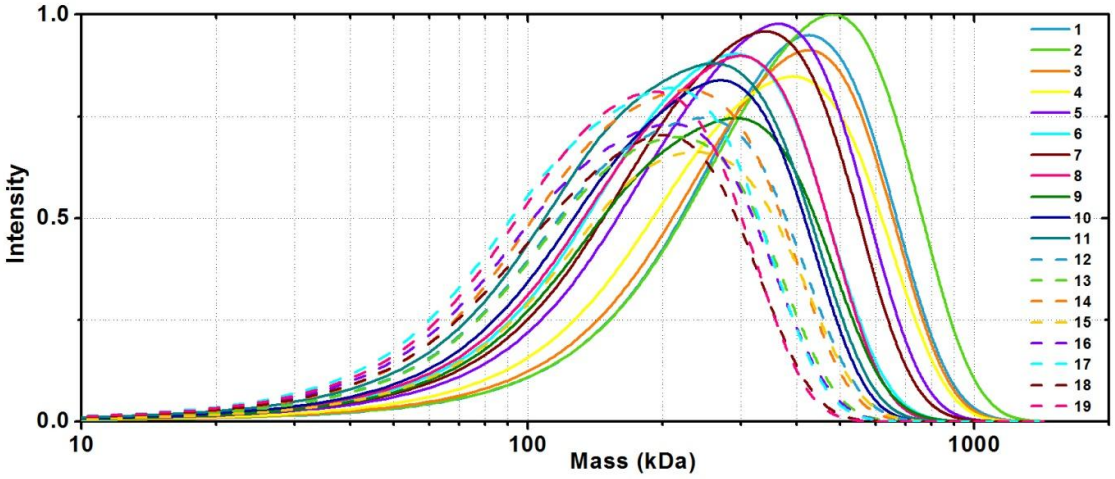

Fig. V.7: "low mass noise" with a denoising at $2 \times \sigma$ for all 19 NEMS. The maximal mass value of the generated spectra defines the LOD. A tendency toward lower LOD with smaller resonators is observed.

The resonators' LODs are listed in Table V.4.

NEMS#	1	2	3	4	5	6	7	8	9	10
LOD(kDa)	1100	1200	1070	1050	940	760	910	760	760	660
NEMS#	11	12	13	14	15	15	16	18	19	/
LOD(kDa)	700	650	570	660	660	560	560	520	510	/

Table V.4: LOD of mass sensors within the array.

On the hand, we extracted the experimental mass resolution out of standard deviations of the Probability Density Function (PDF) attributed for each mass landing events (details in Chapter III and Annex A). As detailed in Chapter III Section 5, the mass resolution may vary according to the particle landing position. We chose to keep the worst (highest) mass resolution found in our sensing interval and listed in Table V.5.

NEMS#	1	2	3	4	5	6	7	8	9	10
S (Hz/ag)	188	205	185	177	160	154	166	136	136	122
NEMS#	11	12	13	14	15	15	16	18	19	/
S (Hz/ag)	126	117	112	113	121	102	101	95	93	/

Table V.5: Mass resolution of the sensors within the array.

The LOD can vary from 500kDa to 1200kDa while the mass resolution goes from 93kDa to 205kDa. Thus, different performances are to be found between each NEMS: a trend in lower LOD with smaller devices is observed. This isn't surprising as the frequency stabilities seemed relatively similar within the array while the mass sensitivity scales like $\frac{1}{L}$.

5. Building a mass spectrum with frequency-addressed NEMS arrays in multimode operation

Because of the inherent higher sampling rate of arrays with respect to single devices, we need to reduce the particle flux impinging on the sensors. To do so, we used a mechanical shutter to let the particle flux trough a 2mm slit at short time intervals. The particle flux was measured to be roughly divided by 20 when the shutter is on. More detailed effects of the shutter of the particle flux is discussed in Annex B. The following procedure is applied to acquire a mass spectrum: using the shutter, the array is hidden from the cluster flux during 20s; then the shutter is set in rotation during the desired acquisition time (usually 4min) before finally hiding the array for another 20s and stop the acquisition.

Before and after each mass acquisition, we make sure to measure:

- The cluster deposition rate with the QCM
- The reference mass distribution with the TOF
- A noise acquisition: the array is monitored with the frequency-addressing scheme in multimode operation when the array is hidden from the cluster flux

A mass acquisition yields 19 relative frequency time traces featuring frequency shifts between the two 20s time periods when the array is protected from the cluster flux as shown in Fig. V.8.

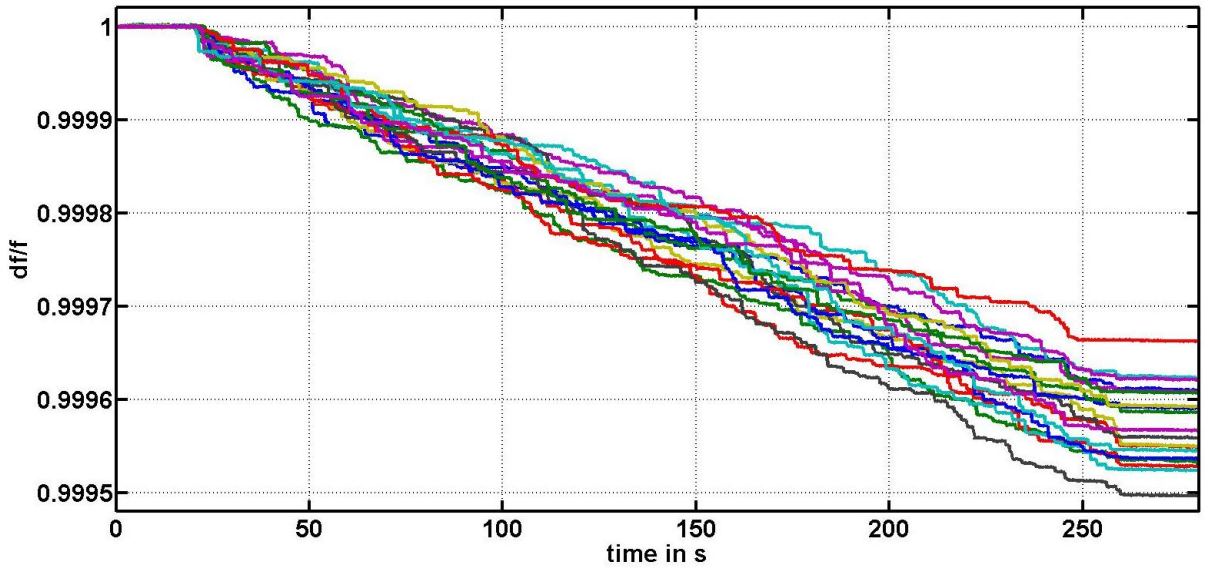

Fig. V.8: Mode 1 relative frequency time traces of an array of 19 NEMS exposed to a flux of tantalum nanoclusters with a mean diameter of 7.2nm. Acquisition starts at t=0s and stops at t=280s. Exposure to nanoclusters starts at t=20s and stops at 260s.

Zooming in, we can observe a multitude of mass induced frequency jumps detected by all 19 resonators as presented in Fig. V.9.

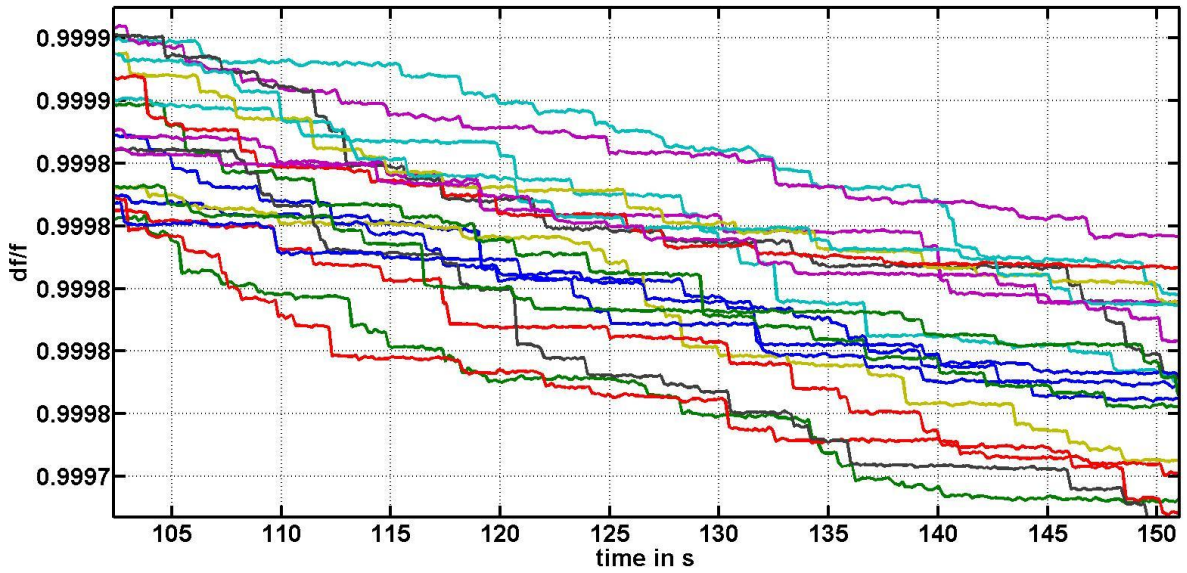

Fig. V.9: Zoomed in view of Fig. V.8. Each frequency jump is induced by a cluster landing on one of the resonators.

Although we switched sequentially in time over the NEMS within the array, the time traces look like all NEMS within the array are tracked simultaneously: this is the result of the ultra-short switching time (here 8ms) obtained with our scheme and our fast custom electronics. Once the relative frequency time traces of both mode 1 and mode 2 for all 19 NEMS have been reconstructed, we can proceed to the construction of a mass spectrum just like detailed in Chapter III.

A noise acquisition is acquired for denoising purposes and easier identification of mass induced frequency jumps. Since the frequency noise can differ from one device to the other, the standard deviation ellipse is extracted individually for all 19 NEMS as shown in Fig. V.10.

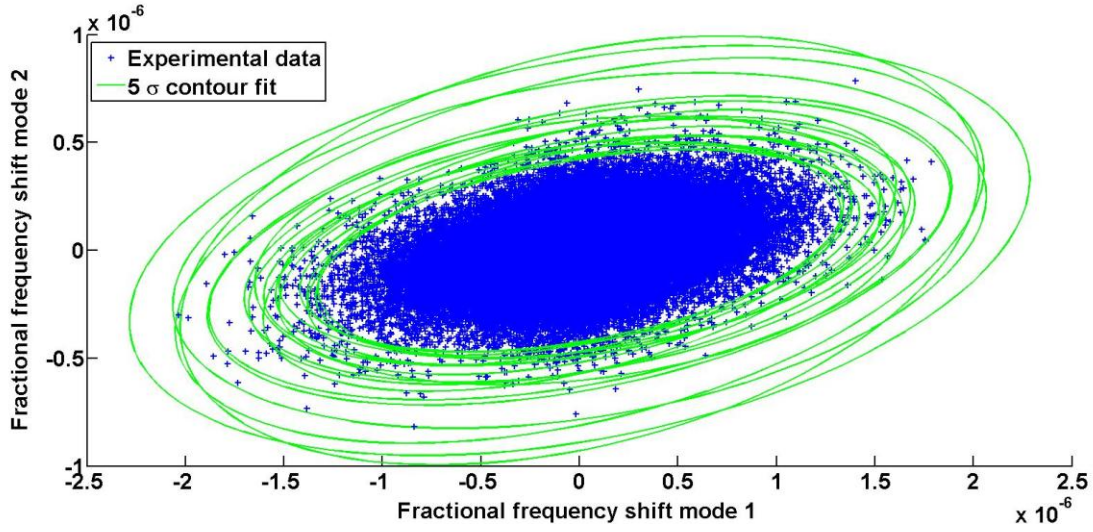

Fig. V.10: Superposed fractional frequency noise scatter plot of mode 1 and mode 2 and their associated 5 sigma contour fit for all 19 NEMS.

In Chapter III, we have seen that with a single device, we proceeded to data averaging over a integration time τ_{AVG}. This integration time is generally a multiple of τ_{PLL} to ensure the system has fully responded between two data points.With respect to an acquisition with a single device, no averaging needs to be done with arrays as it has been already "naturally" done by our algorithm to extract each individual NEMS signal: we have a sampling time of 8ms (250µs for a single device). Once the denoising ellipses have been acquired, they can be used to remove inherent NEMS noise from the acquisitions of tantalum nanoclusters as presented in Fig. V.10.

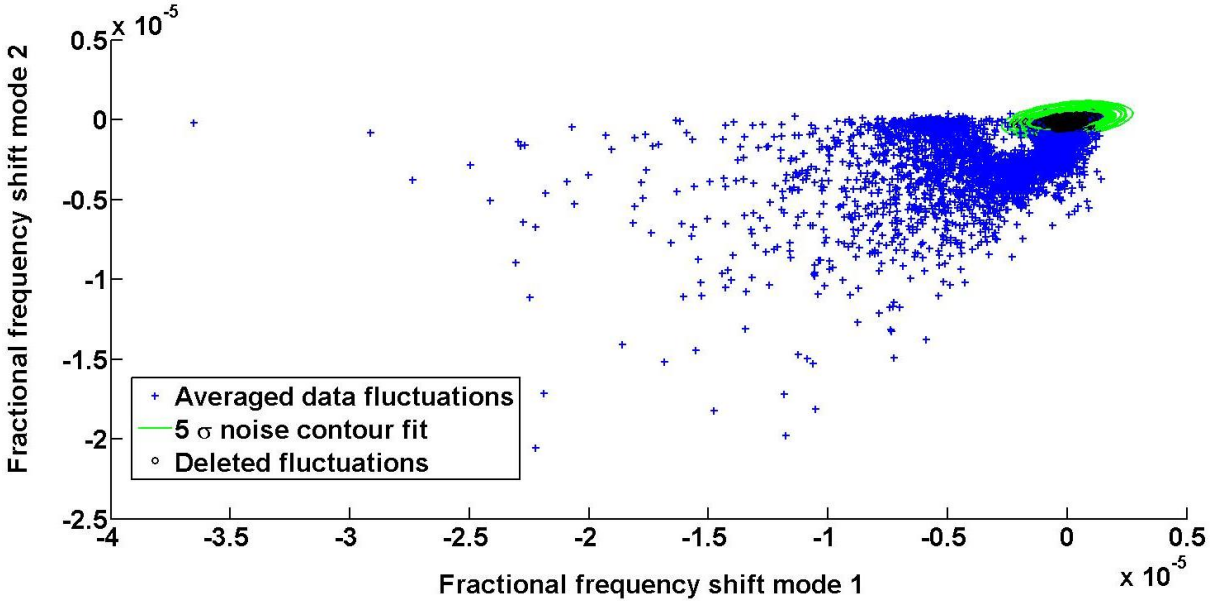

Fig. V.11: Superposed fractional frequency scatter plot of averaged data from a cluster deposition run from all 19 NEMS. Fluctuations comprised within the contour fit are "deleted" i.e. set to 0. Most points outside the ellipse are probably involved in mass induced frequency jumps.

Denoising the data highlights a succession of abrupt frequency jumps that we consider as induced by a mass landing event provided the jump is observed on both modes (Fig. V.12).

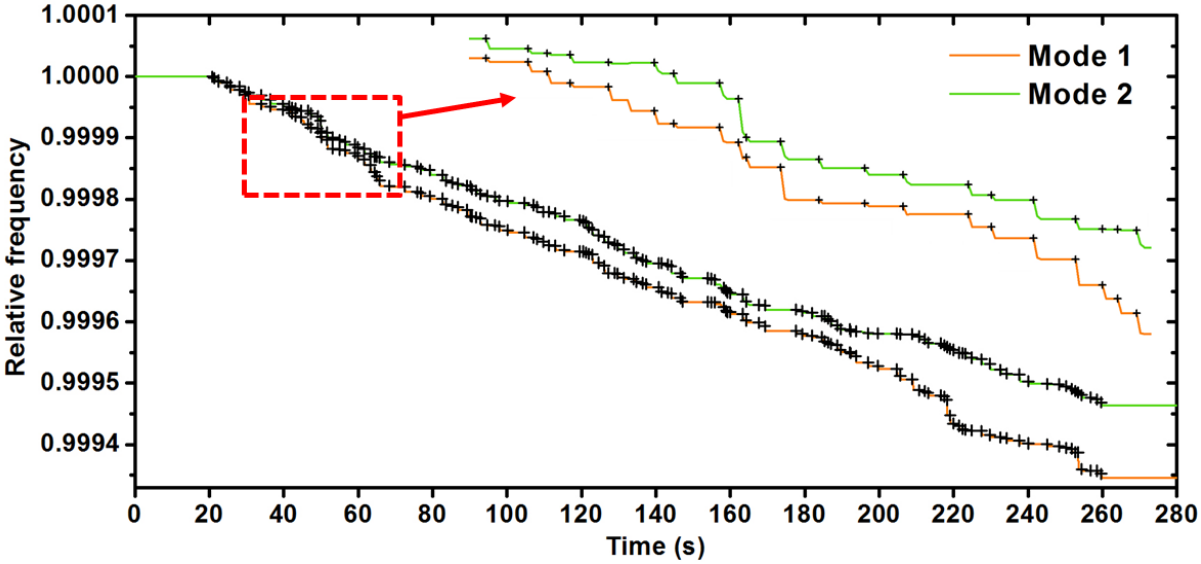

Fig. V.12: Relative frequency time trace of NEMS#1. Detected frequency jumps are indicated by black crosses.

Jump detection cannot be done the same way as with single devices (details in Chapter III) as the sampling rate is very low and a frequency jump is usually seen on two or three data points. Jumps are identified with a negative derivative of the relative frequency observed on both modes. While jump detection and evaluation is made much simpler, we might obtain values of frequency jumps less precise than those obtained with an individual device with a large data sampling rate.

For each NEMS resonator, a list of frequency shift pairs $[\delta f_1, \delta f_2]$ is formed and translated to mass/position pairs$[\delta m, x]$. Mass spectra are built for each individual resonator using the error analysis detailed in Annex A and an addition of these spectra pondered by their event number over the complete array yields a mass spectrum of the tantalum clusters that landed on any of the resonators embedded in the array.

6. Comparison of NEMS array-MS with TOF-MS

Tuning the cluster source, we have exposed the NEMS array to a variety of different cluster populations with mean cluster masses ranging from 530kDa to 2400kDa (mean diameter of 4.65nm to 7.7nm). This allowed us to check the good consistency of our NEMS-MS results. We remind that the TOF spectrum is considered to be representative of the actual mass distribution of projected nanoclusters. Four typical comparisons are presented in Fig. V.13.

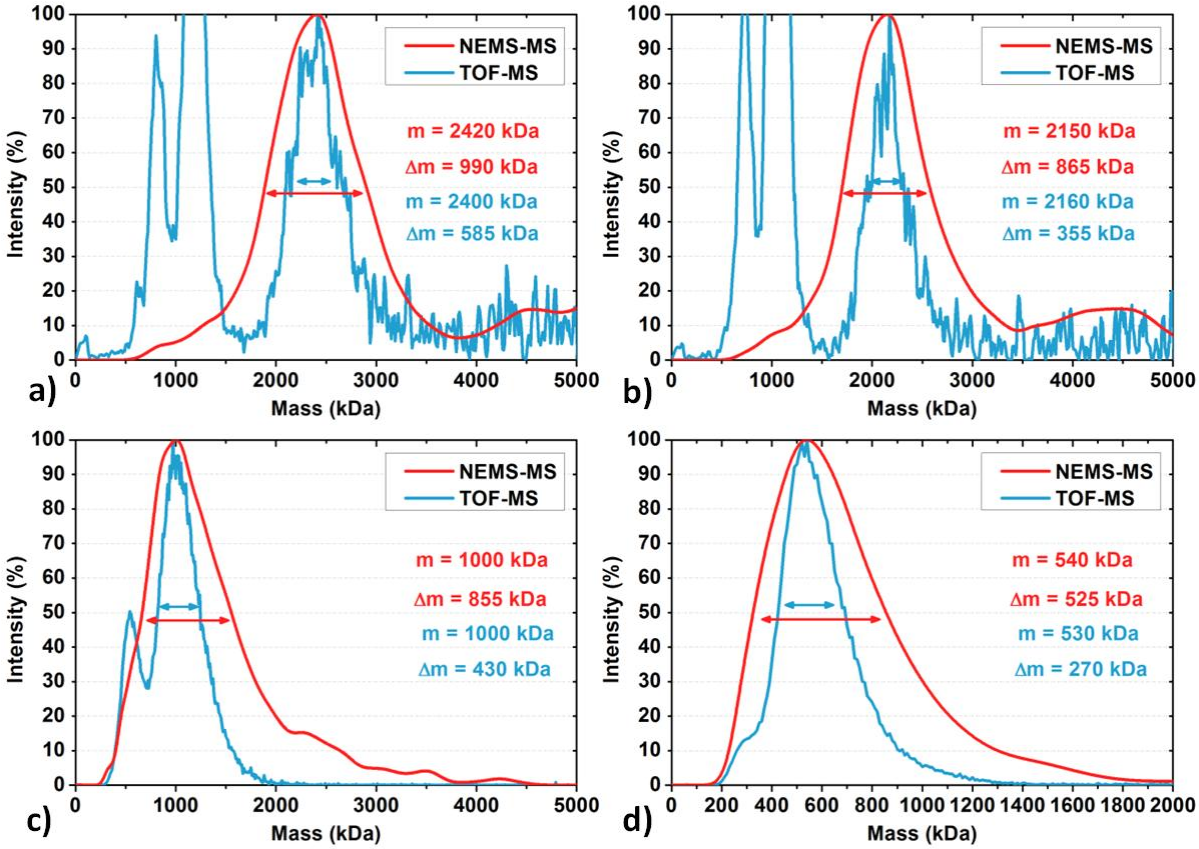

Fig. V.13: Comparison of TOF and NEMS-MS with populations of nanoclusters with a mean diameter of 7.7nm (a), 7.45nm (b), 5.8nm (c) and 4.65nm (d). Spectral normalization for TOF-MS is performed according to singly charged particles. m denotes the center of the spectrum while Δm is the Full Width at Half Maximum (FWHM).

We observe that NEMS-MS provides the actual particle mass distribution while TOF-MS displays additional peaks corresponding to multicharged particles (details in Chapter III). Each NEMS-MS spectra was acquired in 4 minutes and yielded approximately 1000 events. This gives us around 52 events per device which is unfortunately rather low to measure a statistical distribution. However, we note that the contribution of all devices to build a common spectrum gives excellent accuracies. The spectrum centered on 530kDa (Fig. V.13 d) was obtained by restraining the sensing portion of the beam where mode 2 response is high. Our results demonstrated strong consistency along a mass range from 530kDa to 2400kDa and gave pretty fair evaluations of the cluster mass distributions.

Even so, we observe larger spectra obtained with NEMS arrays with respect to single devices. To highlight this, an array acquisition was performed with similar conditions than a NEMS-MS measurement previously done with a single device. As evidenced by the TOF, we succeeded in producing quasi identical cluster populations which allowed us to confront single device NEMS-MS with array NEMS-MS (Fig. V.14).

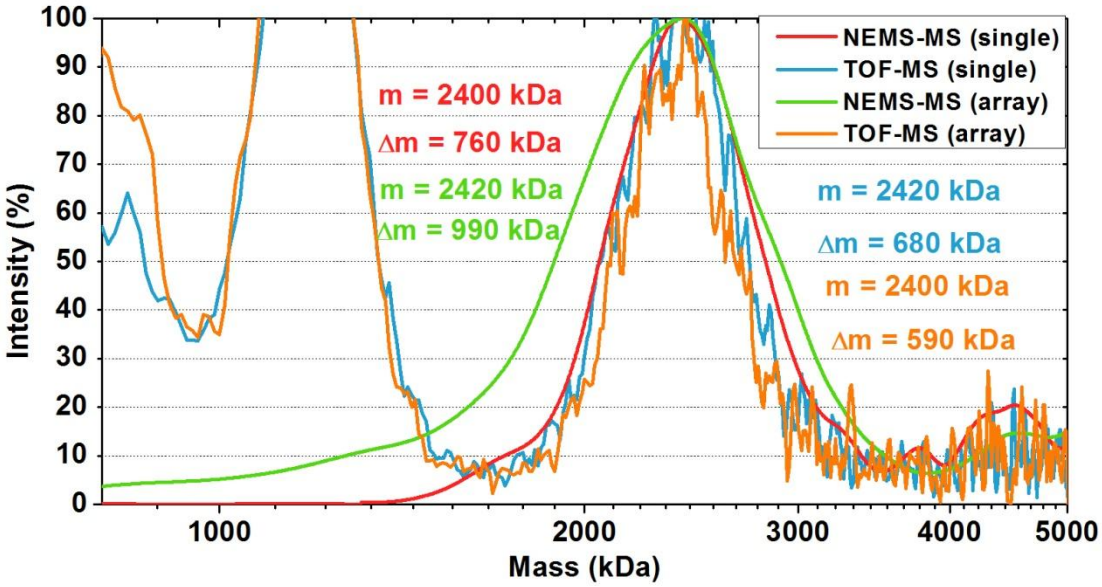

Fig. V.14: Comparison of NEMS-MS with a single device and an array. Cluster populations during both experiments are very similar.

While array NEMS-MS provide a correct mean mass, the spectrum is relatively larger with respect to a single device. Yet, the NEMS-MS spectrum of an array is composed of spectra provided by 19 different devices. They calibration in mass sensitivity requires prior knowledge of their surface that may differ from theory because of process related variabilities. Adding up the signal from the 19 resonator with a spread of responses might lead to larger spectrum. Plus, while NEMS-MS with a single device featured a 100kDa mass resolution, a range of the mass resolution from 150kDa to 300kDa is found within the array for this experiment. In addition, devices with higher mass resolution are generally those at lower frequencies: they have higher lengths and thus a bigger capture surface that contributes more to the final spectrum than smaller devices. Therefore, if we are willing to use every resonator in the array, it should be assumed that the highest mass resolution found among the resonators should be considered as the limiting one.

Nevertheless, we have made the demonstration of the viability of NEMS-MS with arrays: we have been able to realize a mass spectrum with frequency jumps measured on 19 different resonators hence extending our capture surface from 2.76µm² to 45.264µm². This is a tremendous gain for setups with a low event rate such as ESI-NEMS-MS where acquisition usually taking hours can now be realized in about ten minutes or so. Applying the very same protocol with larger arrays, we can further extend our capture surface with arrays of 49 or 100 devices with sampling times of 392ms and 800ms respectively.

7. Mass spectrometry imaging

While resonant arrays can provide multiplied capture surface by merging information coming from all sensors, we can also keep the individualized data of each resonator and consider our system as an array of resonant nanomechanical mass spectrometers. The arrays give us the opportunity to realize a spatial mapping, even crude, of the cluster beam mass

distribution. For our first demonstration of array NEMS-MS, we used an array with 5 rows and 4 columns. The pitches for the rows and columns are 57µm and 20µm respectively which yields a rectangular surface studded with sensors around 0.14mm². Therefore we cannot use it to map a cluster beam whose diameter is estimated at 4cm. Nevertheless, we decided to place the array at different positions in the cluster beam to find potential differences of mass distribution. The spatial sweep was performed on a horizontal axis by retracting the holder progressively from its initial position at the centre of the cluster beam to a position where no events are detected. We are particularly interested in positions at the rim of the cluster beam where we can evidence particle detection on a fraction of the array only. The different positions within the beam are shown in Fig. V.15.

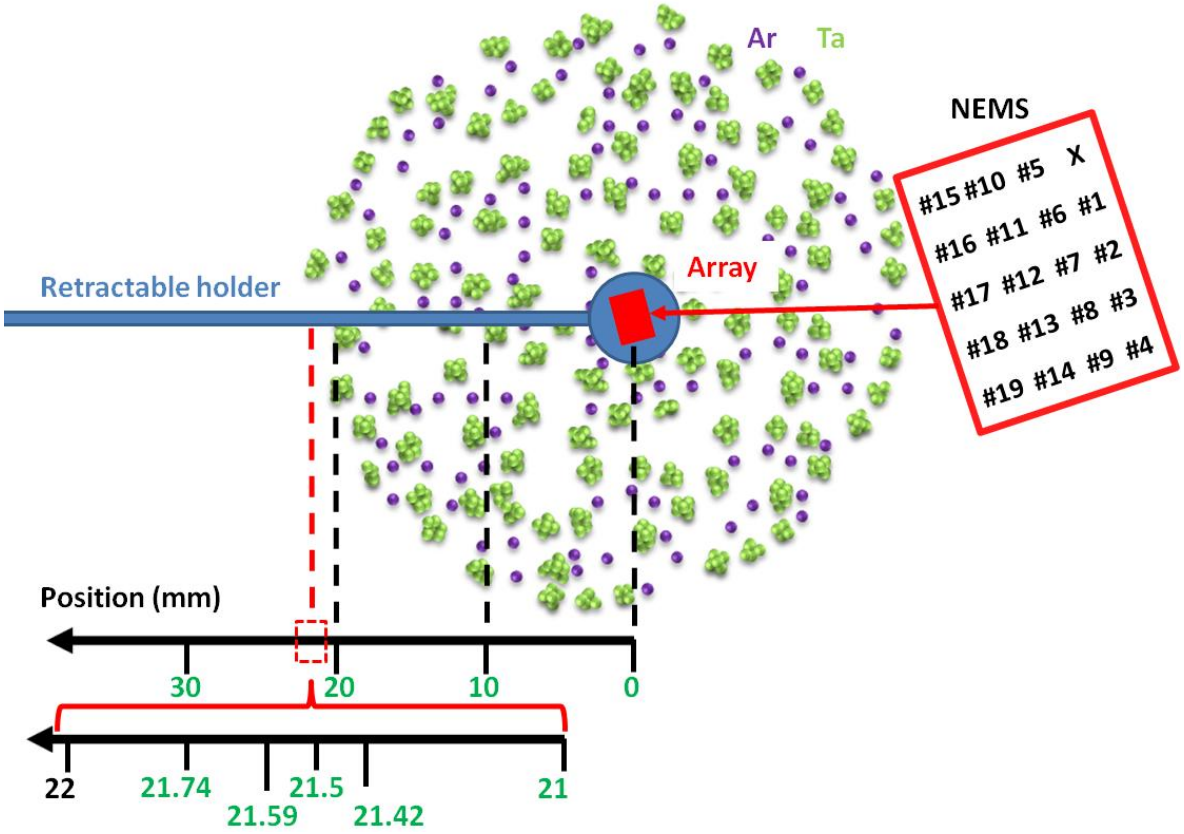

Fig. V.15: Schematic not-to-scale cross-section of the cluster beam from the cluster source point of view. The array is progressively retracted from the beam centre considered as the 0 position. Values in green are positions where we made array NEMS-MS acquisitions. With respect to layout, the array is upside down and slightly tilted.

We tuned the cluster source to obtain a cluster population centered on 7nm (1800kDa) with a deposition rate measured by the QCM around 25ag/s/µm².

For each position, assuming a uniform mass deposition along the resonators, an evaluation of the mass deposition rate per µm² ϕ_m can be made as:

$$\phi_m = \frac{\partial f}{f} \frac{2\rho_{Si} t}{T.10^{12}} \qquad \textbf{(V.3)}$$

where ϕ_m is the mass deposition rate par µm², ρ_{Si} the silicon density, t the resonator thickness, T the acquisition time and $\frac{\partial f}{f}$ the measured relative frequency shift.

Given that we can access the same information with both mode 1 and mode 2, averaging on the two modes provides noise reduction.

The mass beam shutter was on when we performed each acquisition. We plotted the average $\square_m$ found within the array with respect to position in the beam to get a first glimpse at the beam profile as presented in Fig. V.16.

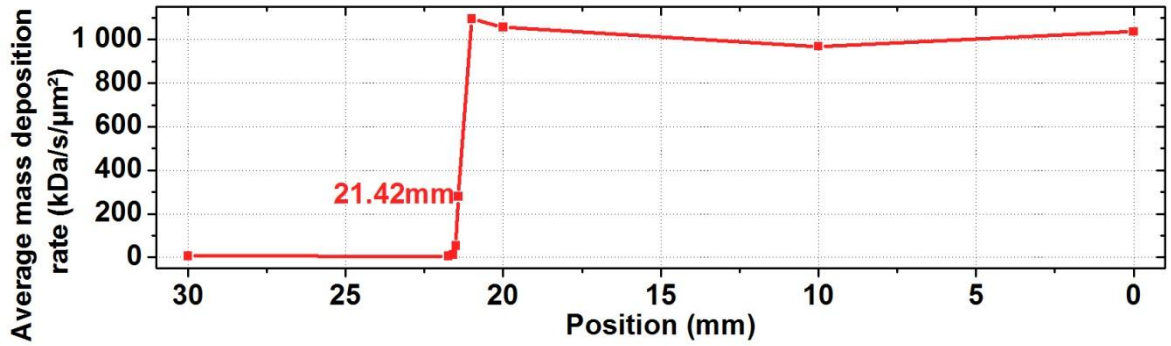

Fig. V.16: Cluster beam profile as the mean ϕ_m of the array with respect to position.

The cluster beam seems to have a homogeneous deposition rate on a 4.2cm diameter beyond which ϕ_m radically drops. We found an intermediate position at 21.42mm where only a fraction of the array sees substantial mass events: we observe a spatial dissymmetry in the frequency shift rates measured among the array as shown in Fig. V.17.

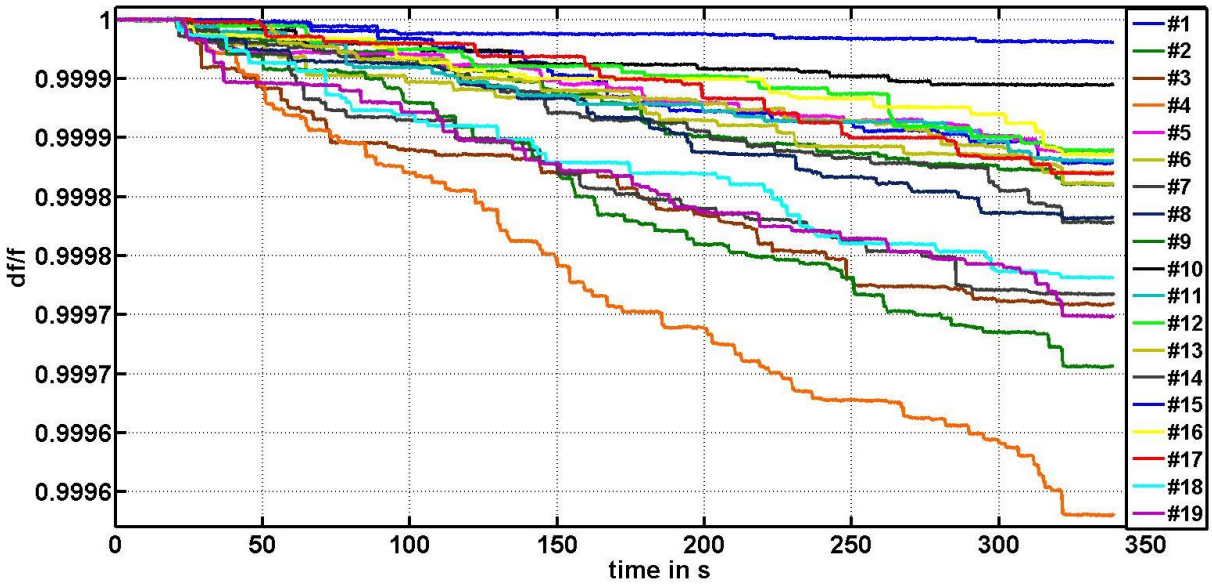

Fig. V.17: Relative frequency shifts of resonators within the array placed at 21.42mm from the beam centre. NEMS are numbered according to increasing resonance frequency (hence decreasing beam length). While frequency shifts are usually almost the same among the array when placed at the center of the beam, a dissymmetry is observed here.

We can clearly see that NEMS#4 and #9 receive way more clusters than NEMS#1 and #10. For better visualization we mapped ϕ_m along the array and interpolated the data in a matrix with 1µm² pixels. The resulting mapping is presented in Fig. V.18.

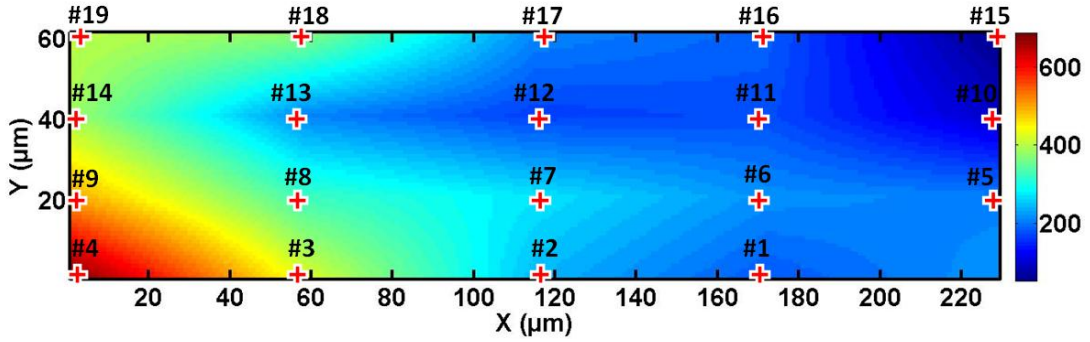

Fig. V.18: $\square_m$ (kDa/s/µm²) mapping along the array placed at 21.42mm from the beam centre with the shutter on. Red crosses indicate positions of the NEMS where experimental data is gathered. The rest of the matrix is obtained by interpolation.

It is clearly visible that the array is tilted and that the bottom left corner is closer to the beam center than to right corner. When going further away from the beam centre at 21.59mm, we have very few jumps but the dissymmetry still appears:

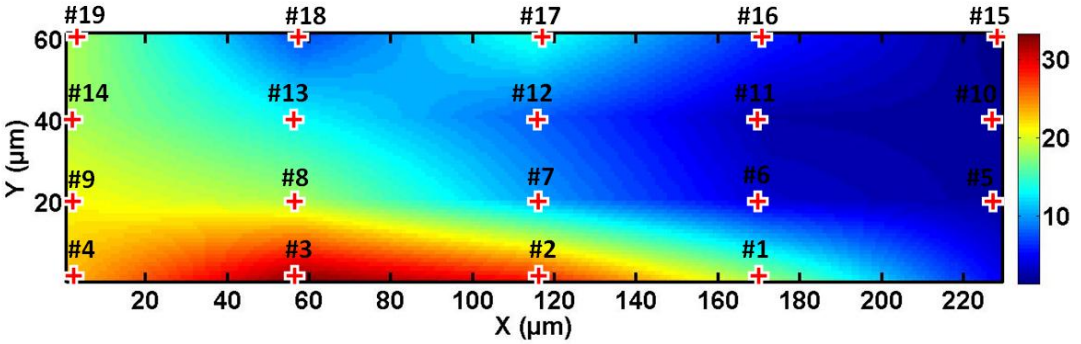

Fig. V.19: $\square_m$ (kDa/s/µm²) mapping along the array placed at 21.59mm from the beam centre with the shutter on.

Given the low event rate, we removed the shutter to obtain a higher particle flux and moved the array 0.4mm toward the beam centre to obtain the following mapping:

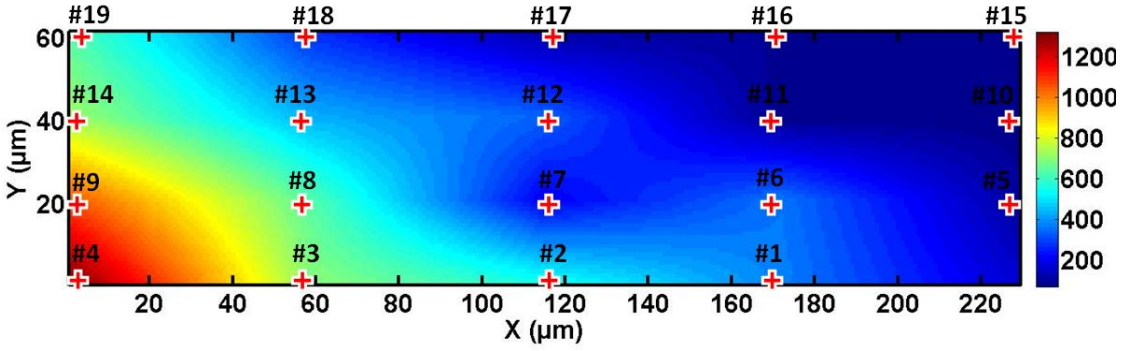

Fig. V.20: $\square_m$ (kDa/s/µm²) mapping along the array placed at 21.55mm from the beam centre without shutter.

We get a high ϕ_m and a strong dissymmetry along the array. We proceeded to cluster detection and mapped the number of detected event per µm² (Fig. V.21):

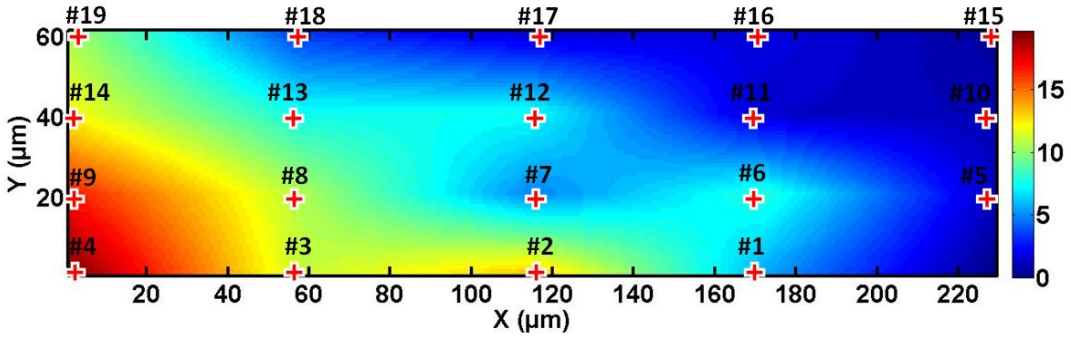

Fig. V.21: Number of events per µm² mapping along the array placed at 21.55mm from the beam centre without shutter.

Without surprise the highest number of events per µm² is found on NEMS#4. The final step consists in producing every NEMS-MS spectra associated with "pixel" resonators as shown in Fig. V.22.

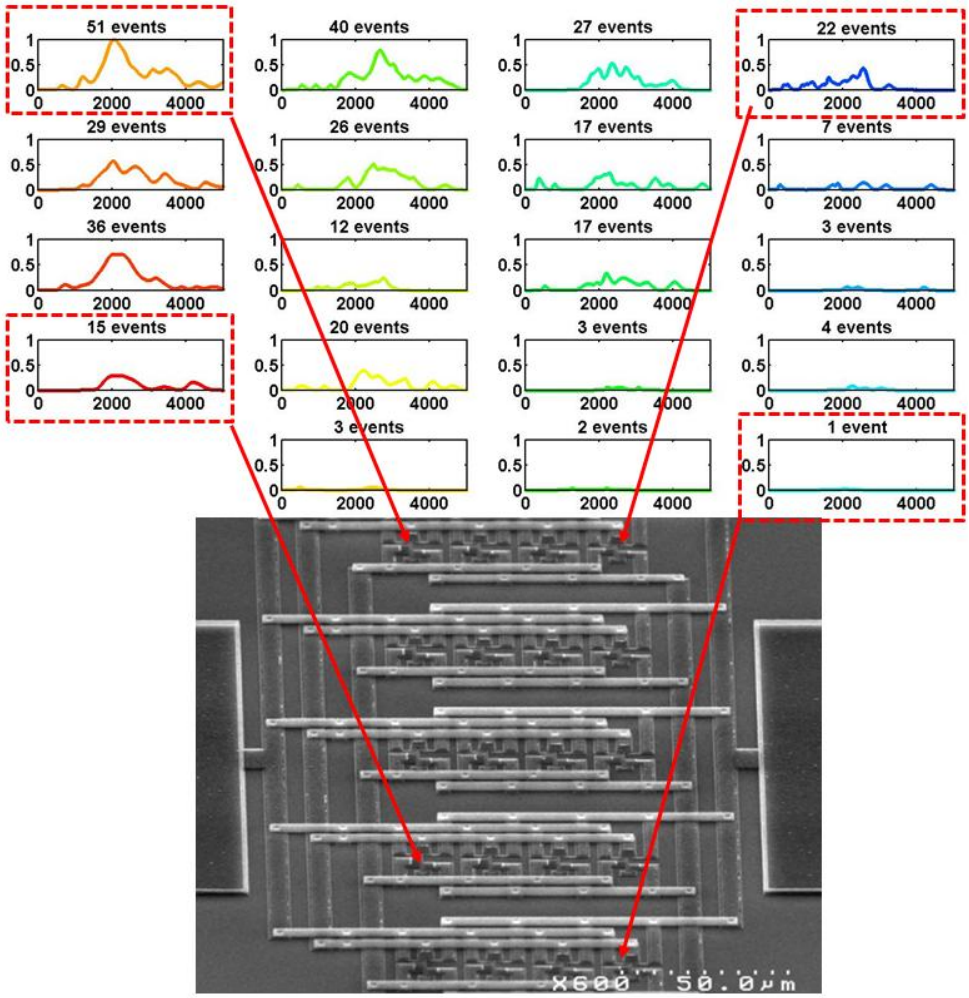

Fig. V.22: Mass spectra obtained with an array displayed as a matrix pattern reproducing the devices physical layout (5x4). Each figure represents the intensity with respect to mass (kDa). The array is 21.55mm away from the beam centre and the shutter is off.

Except for NEMS#4 that detected enough clusters, most mass spectra are rather poor as a few tens of events isn't very reliable to measure a mass distribution. We repeated the measurement at the centre of the beam (with the shutter on). A total of 1378 events were gathered to produce a common spectrum:

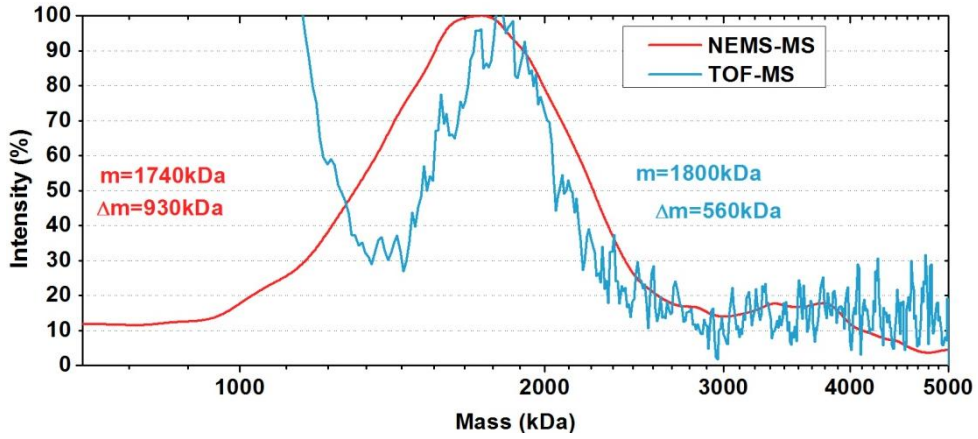

Fig. V.23: Comparison of TOF and array NEMS-MS with populations of nanoclusters with a mean diameter of 7nm when the array is at the beam centre.

The spectrum is composed of the 19 individual spectra:

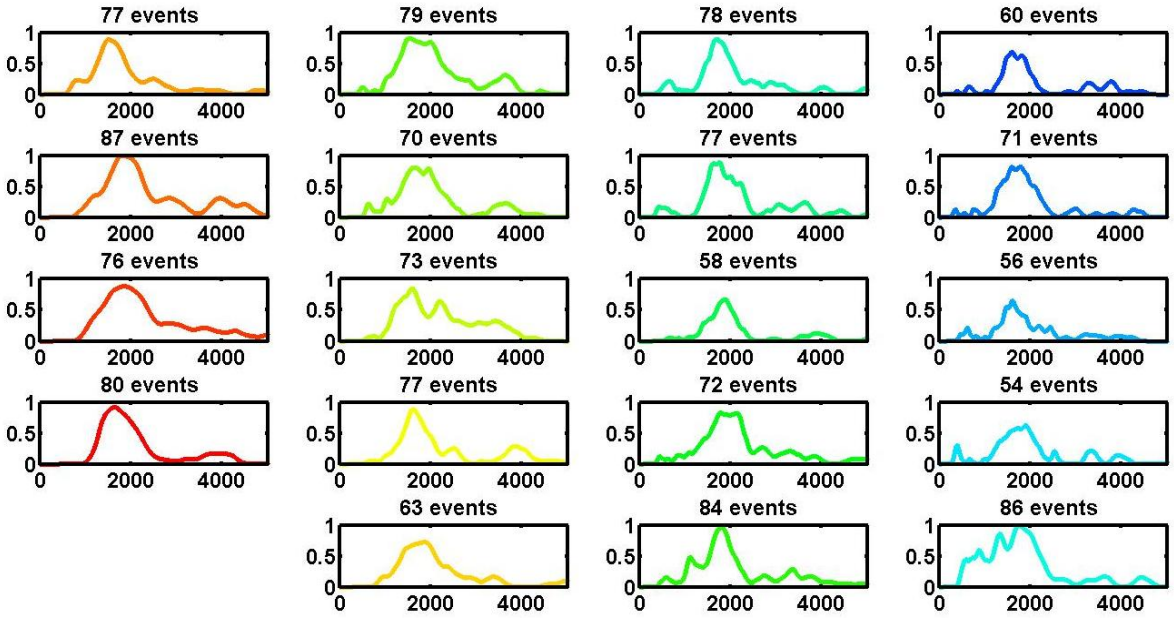

Fig. V.24: Mass spectra obtained with an array displayed as a matrix pattern reproducing the devices physical layout (5x4). Each figure represents the intensity with respect to mass (kDa). The array is placed at the beam centre and the shutter is on.

While most spectra are correctly centered, they aren't as smooth as the "array spectrum".

The array NEMS-MS spectra 10mm and 20mm away from the beam center are shown is Fig. V.25.

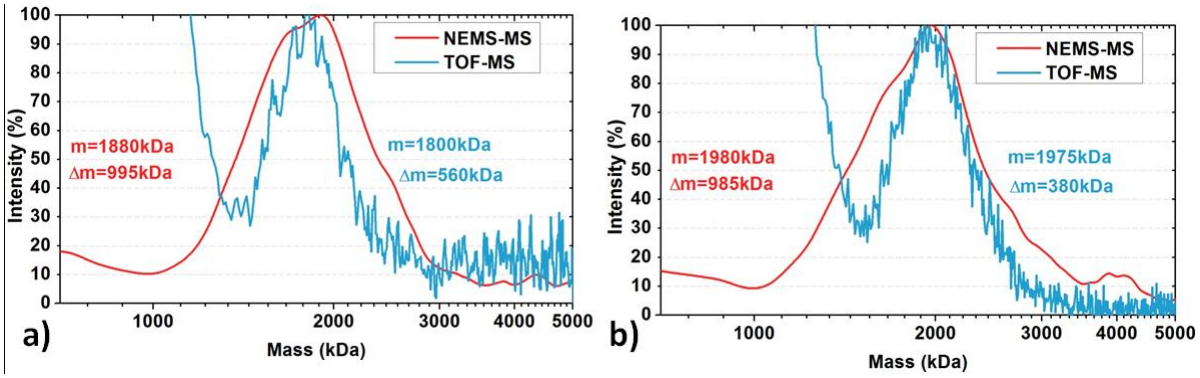

Fig. V.25: Comparison of TOF and array NEMS-MS with populations of nanoclusters with a mean diameter of 7nm (a) and 7.2nm (b) when the array is 10mm away from beam centre (a) and 20mm away (b).

The slight increase of mass observed by both NEMS and TOF-MS is attributed to the cluster source whose internal pressure may drift causing a drift in the mass distribution as well. Yet, we can conclude that no significant difference in mass distribution is observed along the cluster beam profile.

Since NEMS-MS performances are proportional to the mass of the weighted particles, we increased the cluster mean mass size to 7.7nm to obtain nice spectra on all 19 resonators. The main spectrum is shown in Fig. V.13 a) while the individual spectra are presented in Fig. V.26. Each spectrum was built with roughly 60 events.

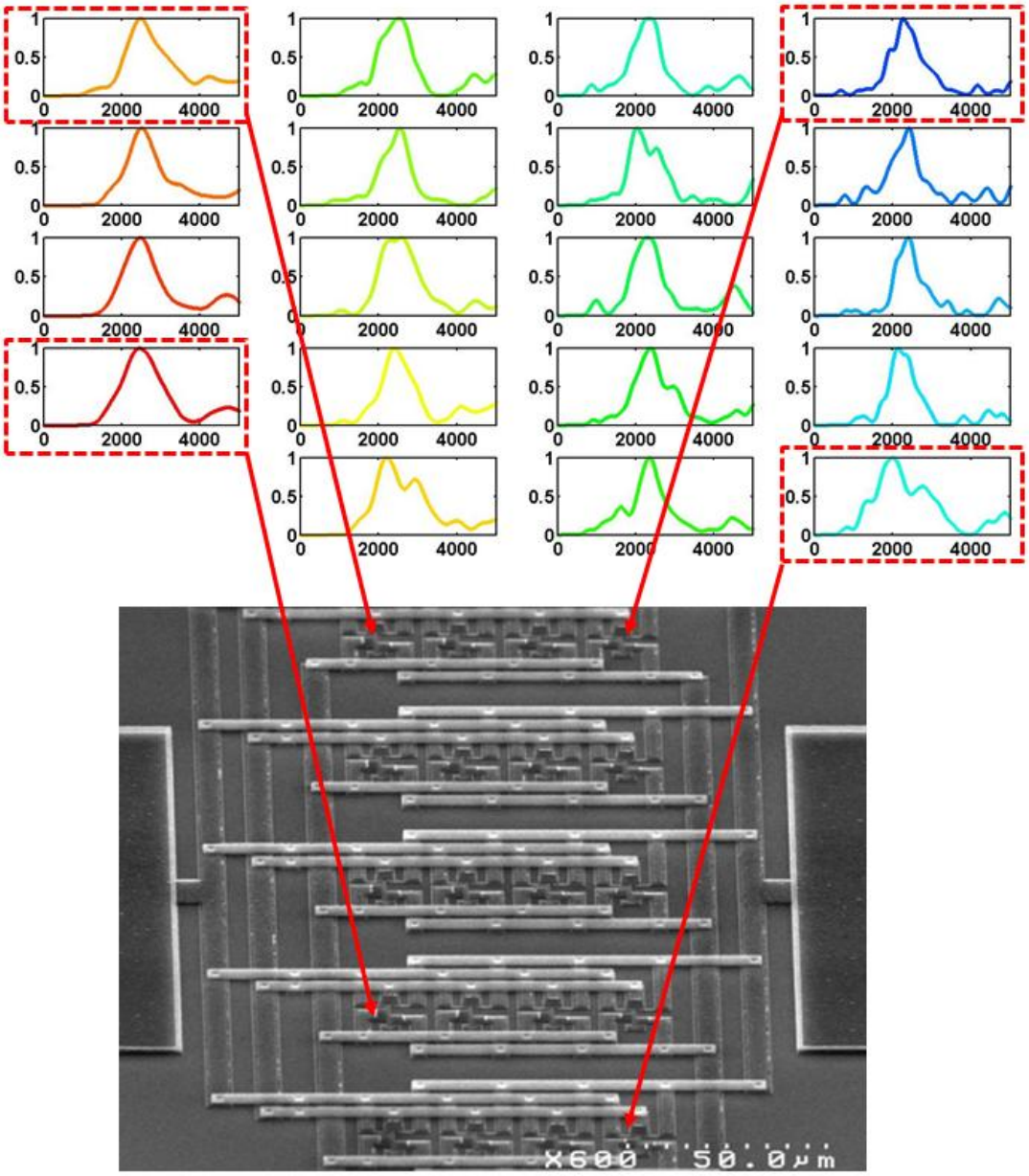

Fig. V.26: Mass spectra obtained with an array displayed as a matrix pattern reproducing the devices physical layout (5x4). Each figure represents the intensity with respect to mass (kDa).

We demonstrate 19 individual spectra with good individual properties. While m and Δm of the array spectrum is 2420kDa and 990kDa respectively, each device features very similar spectra as listed in Table V.6.

NEMS#	1	2	3	4	5	6	7	8	9	10
m	2392	2508	2468	2448	2110	2348	2608	2526	2576	2350
Δm	978	832	716	978	1350	810	1106	704	900	504
NEMS#	11	12	13	14	15	15	16	18	19	/
m	2422	2432	2034	2486	2646	2360	2496	2426	2406	
Δm	1176	808	1152	854	1384	516	504	382	584	/

Table V.6: Spectra properties of each individual resonator of the array

The central mass has mean of 2423kDa and a standard deviation of 150kDa along the array: the spectra obtained within the array are relatively homogeneous given the low number

of events. Dispersion on the central mass may be lowered with a higher number of events i.e. with longer acquisitions or higher deposition rate combined with faster array sampling rate. If not, we may face dispersion on the geometric length and width of the devices with respect to the layout that may lead to dispersion of the estimated mass sensitivity. Indeed, as mentioned in Chapter III, our resonator mass calibration based on comparison with the QCM requires prior knowledge of the beams length and width. However, by comparison of TOF and NEMS-MS of a large number of events for each device we could adjust the geometric parameters for equal ass spectra outputs. Combining both techniques may yield an optimal calibration where an identical spectrum on each device is ensured.

8. Conclusion

In this Chapter, we have presented the first demonstration of a functional array of mass spectrometer. Spectra produced by arrays generally have a larger FWHM than single devices as a spread of performances and exact response to mass is found within the array. Nevertheless, we have proved that a spectrum produced with an NEMS array produces accurate estimation of the generated cluster mean masses on a range from 530kDa to 2400kDa. This is a great progress for low event rate NEMS-MS setups such as ESI-NEMS-MS since the acquisition time can be approximately divided by the number of devices in the array: one can imagine quasi instantaneous acquisitions with VLSI 3D co-integrated arrays of 10000 NEMS.

In addition, the possibility to read a unique mass spectrum of every “pixel” of an array of sensor is a unique property unreported so far. Currently mass spectrometry imaging techniques such as MALDI [1], DESI and SIMS imaging rely on a localized desorption of the analyzed sample. Desorbed particles are then focused into a mass analyzer regardless of their spatial position. NEMS-MS is the only technique that allows in situ mass spectrometry as it does not require collimation for time of flight measurement, or deflection by sector instruments: the spectrum is produced as long as the particles hit the NEMS. Information on the spatial mass distribution of particles would be a great benefit to many MS domains such as aerosol science. Aerosol technologies are used to generate and focus particles (either charged or neutrals) [2-3], whose size are estimated by laser scattering and mass composition obtained by Rapid Single Particle Mass Spectrometry (RSPMS) [4]. Beam collimation is a challenge in aerosol science and aerodynamic lenses have been developed to obtain mass beams as small as possible [2-5]. The mass beams are generally evaluated with a knife edge particle beam stop and a detector connected to an electrometer downstream the lens exit nozzle: as the knife is progressively advanced forward, the detected charges on the electrometer is monitored to evaluate the beam profile. As beam diameters now reaches dimensions down to the millimeter, a simple array of 10x10 resonators spaced by 100µm would provide precise beam profiling, MS imaging and would replace or complete RSMS. This kind of setup could demonstrate that high mass particles would seem to stay focused in the middle of the trajectory while smaller particles influenced by Brownian motion would spread spatially. Different particle beam can be reconstructed according to particle size and

evidence different beam diameters. Plus, unlike RSMS, no ionization is required which maintains the initial nature of the mass beam.

In-situ MS, MS imaging and neutral MS are advantages of NEMS-MS that makes it truly unique and the great potential of this novel technique of mass spectrometry is further discussed in Chapter VI.

BIBLIOGRAPHY

[1] R. T. McIver, Y. Li, and R. L. Hunter, “High-resolution laser desorption mass spectrometry of peptides and small proteins.,” *Proceedings of the National Academy of Sciences of the United States of America*, vol. 91, no. 11, pp. 4801–5, May 1994.

[2] P. Liu, P. J. Ziemann, D. B. Kittelson, and P. H. McMurry, “Generating Particle Beams of Controlled Dimensions and Divergence: II. Experimental Evaluation of Particle Motion in Aerodynamic Lenses and Nozzle Expansions,” *Aerosol Science and Technology*, vol. 22, no. 3, pp. 313–324, 1995.

[3] K.-S. Lee, S.-W. Cho, and D. Lee, “Development and experimental evaluation of aerodynamic lens as an aerosol inlet of single particle mass spectrometry,” *Journal of Aerosol Science*, vol. 39, pp. 287–304, 2008.

[4] P. G. Carson, K. R. Neubauer, M. J. Johnston, and A. S. Wexler, “ON-LINE CHEMICAL ANALYSIS OF AEROSOLS BY RAPID SINGLE-PARTICLE MASS SPECTROMETRY,” *Journal of Aerosol Science*, vol. 26, no. 4, pp. 535–545, 1995.

[5] X. Wang and P. H. McMurry, “An experimental study of nanoparticle focusing with aerodynamic lenses,” *International Journal of Mass Spectrometry*, vol. 258, pp. 30–36, 2006.

Conclusion & perspectives

Nanomechanical mass spectrometry represents a new paradigm in the field of mass spectrometry: it is the only technique that not does rely on mass-to-charge separation of the analytes. While ionization yield and correct charge states assignment are important in conventional ion-MS, NEMS-MS directly weigh the mass of any particle, ionized or not. This leads to significantly simpler mass spectra, especially for complex mixtures. Plus, since the measurement uncertainty does not depend on the weighed mass, the resolving power increases with higher masses whereas it decreases for conventional ion-MS instruments. This advantage can make the difference in MS analysis for proteomics where biological objects of interest such as macromolecular complexes, protein machinery, bacteria and viruses are found in the MDa-GDa range [1]. Indeed, routine MS of heavy molecules over 100kDa is performed with difficulty as most peaks remain unresolved because of weak ion acceleration and mass analyzers' low resolving powers [2]. While the first demonstration of single protein nanomechanical mass spectrometry has been successfully performed in the MDa range with a single resonator [3], it featured a relatively high mass resolution (~100kDa) and a very low event rate. In addition, no direct comparison of NEMS-MS with conventional ion-MS has been shown so far, leaving NEMS-MS without possible calibration or chance to highlight its advantages over ion-MS.

In the framework of this dissertation, we have studied the mechanisms limiting the mass resolution of the resonant sensors before aiming at scaling the technology for a fast and robust MS system. After comparison of a single resonator's mass sensing performance with a TOF mass spectrometer in a dedicated setup, we implemented a frequency-addressing technique on a small array of 20 resonators as a first step toward very large scale integration before validation of the concept by successfully building mass spectra of nanoclusters from data provided by all functional sensors within the array.

First, we focused on the study of individual resonator's mass resolution. A low mass resolution may be achieved with high mass sensitivity and low resonator relative frequency fluctuations. While high mass sensitivity is obtained by device scale reduction, the scaling laws of the resonator relative frequency fluctuations are not well understood. Assuming white additive amplitude noise, relative frequency fluctuations should be limited by thermomechanical noise yielding expected relative deviations in the 10^{-9} the range. We performed experimental measurements of the Allan Deviation, the correlation function and the Power Spectral Density. As we progressively decreased the white noise with larger SNR, we encountered a 1/f noise limit yielding a frequency stability limit around 1.5×10^{-7}, orders of magnitude above the expected one, regardless of drive and polarization voltages. After ruling out instrumentation and transduction-related limitations, we evidenced the presence of a frequency noise lying in the mechanical domains: as the quality factor increases, phase noise

increases in proportion. A correlation of 1 on the frequency fluctuations sampled at two different frequencies in the sensor bandwidth confirmed this hypothesis. Thus, beyond a certain point, improving transduction efficiencies or resonator quality factors does not provide better sensor resolution: the limit comes from the resonator frequency fluctuation caused by some physical variations. Additional facts gathered on this excess noise points out to a correlation between two positions on the resonator but none between two different resonators. Temperature is the only parameter we found that could influence the magnitude of this noise. Our measurements are in agreement with thermally activated local Young's modulus variations caused by defects motion in the crystalline lattice producing a $\frac{k_b T}{f}$ noise spectrum. We hope that this work will be a base for further investigations. Future research should investigate any correlation between the resonator frequency noise and point defects, surface effects like trapped charges and material-induced effects. Hopefully, this might lead to optimized fabrication processes to reduce the sensors' mass resolution.

Once we identified the operating points for the ultimate mass resolution achievable by our mass sensors, we decided to compare their performances with ion-MS. We introduced our device in a bench of metallic nanoclusters deposition equipped with a QCM and a Time-of-Flight mass spectrometer. The setup was modified to allow for introduction of the NEMS holder, electrical connections and liquid nitrogen cooling. We designed a multimode tracking electrical scheme using a custom board providing PLL responses times down to 1ms. Combined with an ultra-fast post-processing algorithm, the system was able to handle the high flux of nanoclusters hitting the NEMS and actual real time NEMS-MS is now only a matter of implentation. The NEMS' mass sensitivity per surface unit was extracted from curves of frequency shifts vs mass deposition per surface unit given by the QCM before acquiring mass spectra of nanocluster populations with a mean mass ranging from 470kDa to 4500kDa. Through simulations, we were able to explain the shapes of NEMS-MS spectra in term of discrepancies with TOF-MS at low masses (~below 2MDa), additional peak for very high event rates and apparitions of noise-induced peaks at low masses. We observed an experimental limit of detection around 500kDa and increasingly good matching with TOF-MS as the mass range increases. Beyond 2.4MDa, both techniques provided similar spectra although the TOF seemed to struggle, requiring longer acquisitions times. Plus, we evidenced the singularity of NEMS-MS in acquisitions where TOF mass spectra featured multiple peaks induced by multicharged particles whereas NEMS-MS directly gave a single peak unambiguously representative of the particles mass distribution. Lastly, we produced the first unequivocal evidence of neutral particle nanomechanical mass spectrometry: a deflector removed all charged particles from the particle beam, leaving a population of neutral particles detected by NEMS-MS only. This setup, dedicated to NEMS-MS comparison with respect to TOF-MS, provided calibration and validation of our technique: benefits of NEMS-MS over ion-MS such as constant resolution along the mass range, simple spectra and detection of neutrals have now been experimentally demonstrated. The following step consisted in increasing the capture cross-section via NEMS arrays.

We produced NEMS arrays where all devices are interconnected in parallel yielding an equal number of electrical connections with respect to a single device. All devices lengths

differ by a small amount to obtain a spacing of their respective resonance frequencies. The latter form a series of "frequency addresses" that can be used to interrogate a given device. Open loop measurements displayed a succession of lorentzian resonance peaks, as expected. For small arrays of 20 devices, we were able to measure similar SBRs and similar frequency fluctuations with respect to single devices, provided an increase of polarization voltage. We were able to monitor the NEMS array in closed loop by successively switching from one NEMS to the other as quickly as possible. Signal reconstruction by post-processing yielded the individual signals of each device with sampling times down to 40ms and frequency fluctuations unaffected by the scheme. Two simple experiments demonstrated that frequency-addressed arrays provided a noise reduction of roughly the square root of the device number for gas sensing applications while mass induced events could be tracked quasi-simultaneously on all devices of the array for NEMS-MS applications. The next natural step is solid proof of concept of NEMS-MS with arrays by producing a mass spectrum.

The new concept of nanomechanical mass spectrometry based on arrays of oscillating nanostructures was validated in our nanocluster deposition setup. After characterization, optimal operating voltage settings and collective calibration of individual mass sensitivities per surface unit thanks to the QCM, we deposited nanoclusters on a 20 devices array while monitoring it. Our system was able to handle the mass adsorptions events occurring over the whole array and provided an effective surface multiplication by the number of functional devices. We built mass spectra from the mass events detected among the devices of the array and compared them with TOF-MS and single NEMS-MS. While good mean mass matching is observed, arrays seem to have a slightly higher mass resolution than single devices, probably caused by a spread of the mass sensing responses throughout the array and the lower performances of the lower frequencies resonators. Yet, our results demonstrated strong consistency along a mass range from 530kDa to 2400kDa and gave pretty fair evaluations of the cluster mass distributions. We highlighted another interesting feature of arrays by placing one at the rim of the nanocluster beam: we evidenced a dissymmetry of mass event rate while still being able to obtain the mass spectrum at each "pixel" of the array. This is a first step toward MS imaging with larger arrays.

In summary, this thesis describes the advent of a new generation of nanomechanical mass spectrometry setup. While the previous generation tracked a single resonator with a 500ms response time, we are now able to monitor quasi-simultaneously 20 devices, each featuring a 160ms response time. This was made possible through further comprehension of the important phenomena and parameters in our system and thanks to an efficient control scheme of NEMS arrays. These enhanced performances in terms of speed and capture surface will greatly benefit to existing NEMS-MS setups producing large-area particle beams. Yet, there is still room for much larger arrays and the next step could make the most of our VLSI approach with arrays beyond thousands of devices.

Another aspect of this work lies in the deeper understanding of our resonators' mass resolution, the experimental evaluation of our mass sensing performances as well as the experimental demonstration of NEMS-MS advantages over ion-MS. We now know that we are limited by the so called "MFN", mechanical frequency noise, which induces fluctuations

of the resonator frequency. The physical fluctuations behind this frequency noise limit the Allan Deviation of our sensors around 1.5×10^{-7} at room temperature. This is translated to a LOD around 500kDa and a mass resolution around 100kDa. This would lead to resolving powers around 10^4 in the GDa range. For now, NEMS-MS is unlikely to outperform any ion-MS technique below 1MDa, especially with respect to ultra-high resolution instruments such as FTICR or the emerging orbitrap technique. Nevertheless, with the current performances, it complements very well ion-MS by becoming highly efficient for very large biomolecules (>20MDa) and by providing the singly charged base peaks down to 500kDa, making charge state assignment much more straightforward for complex mixtures. Hence, hybrid ion-NEMS-MS bench where advantages of both techniques are well exploited should be considered. On the other hand, one major property of NEMS-MS lies in neutral particles detection. Since ionization yields are not a concern anymore, benches with mass injection sources abandoned by conventional ion-MS because of low yields should be explored.

At this point, we believe the next important issues to tackle are:

- Further progression toward identification of the limiting noise source and lower mass resolutions.
- Faster event rate handling to avoid artifacts caused by adsorption of several particles in timescales shorter than the system response time.
- Very large capture surface with VLSI arrays with more than thousands of devices
- Better exploitation of NEMS-MS unique properties with neutral mass introduction or combination with high mass ion-MS instruments.
- Demonstration of NEMS-MS advantages by solving precise issues that remain unresolved in the MS field.

Lower mass resolutions can be attempted with ultralow temperature using liquid Helium or by further scaling down the devices. While all the resonators used in this work are 160nm thin, new 80nm thick chips are now available and should be tested in the near future. Future work on the MFN may provide process fabrication guidelines for lower noise.

While NEMS-MS combined with ESI featured a very low mass adsorption rate (1 particle per 30 minutes), we have been confronted to effects of multiple particle landings caused by very high mass flux in the nanocluster deposition setup. Both experiments and simulations showed that double adsorptions generate an additional mass peak roughly around twice the main base peak. This issue can be solved by decreasing the mass flux, hence the particle adsorption event rate but in the frame of extended applications of NEMS-MS, techniques must be developed in order to at least rule out multiple landings or ideally allow for simultaneous measurement of different particles. Monitoring a third mode would give us a way to rule out these effects while higher modes could provide us determination of multiple masses. So far, we have been able to separately track the fourth first harmonics of in-plane resonance. Given that some designs of our doubly clamped beams possess electrical connections for both pairs of nanogauges found across the device, it would seems rather

straightforward to duplicate the multimode tracking of mode 1 and 2 detailed in Chapter III for mode 3 and 4 tracking on the second pair of nanogauges found at the opposite extremity of the beam. NEMS-MS with resonance mode tracking extended to higher number of harmonics seems to be the obvious next step for experimentations of NEMS-MS in the present setup. We can expect demonstration of uncertainty reduction on single particles' position and mass, extended useful capture surface, suppression of peaks caused by multiple landings (for very high event rates) and even determination of two simultaneously landed particles.

For an ultra fast MS system, the priority is to achieve extremely dense frequency-addressed NEMS arrays. The two metal lines used to interconnect in parallel each device occupy a significant area of layout space leading to device spatial pitch of the order of 10's of µm. Extremely dense arrays may be obtained with CMOS co-integration where interconnections are routed below the sensing surface.

This dissertation did not address the issue of system architecture for true biological NEMS Mass Spectrometry. One path would consist in getting rid of ionization and directly introducing particles from the liquid phase to the gas phase towards the NEMS detector in vacuum. Provided that we are able to cover a large area with extremely dense arrays of NEMS resonators, we can expect detection of hundreds of thousands of events within a few tens of seconds. Since no high ionization yield is needed in this case, any buffer solution can be used. This enables the vaporization and analysis of species that are unsolvable or tend to aggregate in traditional buffer solutions.

The second strategy relies on the introduction of NEMS-MS in an ion-MS setup optimized for MDa ranges. Heck *et al.* measured a 18MDa virus assembly with a modified Q-TOF, proving that large biomolecules could be transmitted with quadrupoles [4]. Doussineau *et al.* also showed how MDa particles could be studied with a charge detector [5]. However, the presence of multi charged peaks can make mass peak interpretation much more complex and possible peak overlaps caused by multiple charge states may hide some compounds [6]. Plus, since ion-MS rely on charged particles to build a spectrum, the peak intensity proportion between compounds can vary according to their ionization rate [7]. Worse, many peptides resulting from fragmentation in tandem MS may be not ionized resulting in information loss rending peptide sequencing even more difficult. On the other hand, NEMS-MS does not miss any information and display the actual compounds proportion regardless of ionization rates or charge states. The NEMS detector can be placed right after the mass analyzer or the charge detector to provide the singly charged peaks and masses over 20MDa before being retracted and proceeding to regular ion-MS. Complementary data of both techniques would simplify mass spectra and reduce information loss whether caused by >20MDa molecules, neutral molecules or overlapping peaks of two different analytes multicharge states. An additional interesting property of NEMS-MS comes from its ability to perform in-situ MS: both analysis and detection are simultaneously performed as long as the particle lands on the resonator. The sensor can then be easily introduced anywhere in an existing setup: for instance, while some protein identification techniques rely on tandem MS where fragmentation yields pieces of proteins amenable to mass analyzers' mass range, it cannot weigh the complete complex before fragmentation: one could think of inserting the NEMS sensor before the collision cell.

Disposing of the mass of information of both precursor and product ions would be greatly beneficial for this type of analysis.

The benefits of NEMS-MS can be highlighted in various situations where biomolecules are hard to ionize, precipitates in the buffer solution or too heavy for mass analyzers. For instance, membrane proteins are very difficult to analyze as they have a tendency to precipitate. This may be avoided with detergent introduction but leads to low ionization yields and may form abducts with the protein, yielding poor mass spectra. One challenging experiment could consist in protein vaporization with detergent followed by detergent desolvation during transport before NEMS-MS analysis. Others proteins of interest include chaperonins such as GroEl or Thyroglobulin (660kDa) that remains difficult to study with conventional MS [8], [9]. Thanks to its single-molecule capability, NEMS-MS has the potential to measure a fingerprint of different isoforms. A change in such a fingerprint of IgM human antibody could be used to diagnose Waldenström disease for example. The technology could have tremendous advantages in the clinical area for bacteria profiling at the bed of the patient for example. Also, it is possible to consider scaling up the whole system and in the future obtaining cheap and handheld devices.

In its current state, NEMS-MS already has the potential to offer solutions to yet unmet challenges as thousands of particles may be acquired in a few minutes. However, its full potential is still to be developed. Clearly, realization of arrays of thousands of NEMS monitored with more than two harmonics, co-integrated with transistors and with mass resolutions below the kDa will probably make a difference in the way MS is currently done and announce the advent of a mature technology.

BIBLIOGRAPHY

[1] H.-C. Chang, "Ultrahigh-mass mass spectrometry of single biomolecules and bioparticles.," *Annu. Rev. Anal. Chem. (Palo Alto. Calif).*, vol. 2, pp. 169–85, Jan. 2009.

[2] K. Breuker, M. Jin, X. Han, H. Jiang, and F. W. McLaffertey, "Top-down identification and characterization of biomolecules by mass spectrometry," *J. Am. Soc. Mass Spectrom.*, vol. 19, pp. 1045–1053, 2008.

[3] M. S. Hanay, S. Kelber, A. K. Naik, D. Chi, S. Hentz, E. C. Bullard, E. Colinet, L. Duraffourg, and M. L. Roukes, "Single protein nanomechanical mass spectrometry in real time," *Nat. Nanotechnol.*, vol. 7, pp. 602–608, 2012.

[4] J. Snijder, R. J. Rose, D. Veesler, J. E. Johnson, and A. J. R. Heck, "Studying 18 mda virus assemblies with native mass spectrometry," *Angew. Chemie*, vol. 52, pp. 4020–4023, 2013.

[5] T. Doussineau, M. Kerleroux, X. Dagany, C. Clavier, M. Barbaire, J. Maurelli, R. Antoine, and P. Dugourd, "Chargin megadalton poly(ethylene oxide)s by electrospray ionization. A charge detection mass spectrometry study.," *Rapid Commun. Mass Spectrom.*, vol. 25, pp. 617–623, 2011.

[6] B. Ma, "Challenges in computational analysis of mass spectrometry data for proteomics," *J. Comput. Sci. Technol.*, vol. 5, no. 1, pp. 107–123, 2010.

[7] K. Tang, J. Page, and R. Smith, "Charge competition and the linear dynamic range of detection in electrospray ionization mass spectrometry," *J. Am. Soc. Mass Spectrom.*, vol. 15, no. 10, pp. 1416–23, 2004.

[8] R. H. H. Van den Heuvel, E. van Duijn, H. Mazon, S. Synowsky, K. Lorenzen, C. Versluis, S. J. J. Brouns, D. Langridge, J. van der Oost, J. Hoyes, and A. J. R. Heck, "Improving the Performance of a Quadrupole Time-of-Flight Instrument for macromolecualr Mass Spectrometry," *Anal. Chem.*, vol. 78, pp. 7473–7483, 2006.

[9] N. M. Karabacak, L. Li, A. Tiwari, L. J. Hayward, P. Hong, M. L. Easterling, and J. N. Agar, "Sensitive and Specific Identification of Wild Type and Variant Proteins from 8 to 669 kDa Using Top-down Mass Spectrometry," *Mol. Cell. proteomics*, vol. 8, no. 4, pp. 846–856, 2009.

Appendix A: Frequency noise for additive white noise limited resonant systems

For sensing applications, the resonant mechanical devices are driven at resonance and the phase is monitored with a Phase Locked Loop (PLL). Fig. A.1 presents an experimental open loop of a doubly clamped resonator with a null phase at resonance:

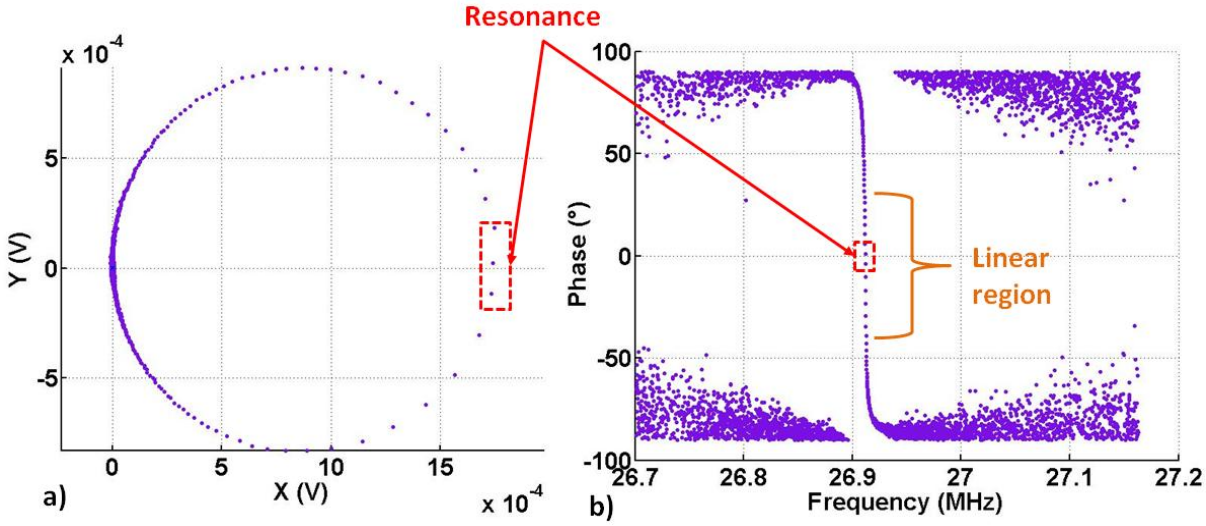

Fig. A.1: Experimental open loop on a doubly clamped beam. Quadrature component with respect to in-phase component of the detected signal during a frequency sweep (a) and corresponding phase response ($\tan^{-1}\left(\frac{Y}{X}\right)$) with respect to frequency (b). Since the LIA provides a phase comprised within [-90°, +90°], the random phase outside of resonance fluctuates between -90 and 90°.

Using a PLL to track the mechanical resonance frequency is especially pertinent insofar as the phase response of a harmonic oscillator is linear with respect to driving frequency close to resonance. In this region the relationship between phase and frequency can be linearized. The phase response of a harmonic oscillator is obtained with the argument of the system transfer function:

$$\varphi(\omega) = arg\left(\frac{F}{\left(\omega_0^2 - \omega^2 + j\frac{\omega\omega_0}{Q}\right)}\right) \qquad \textbf{(A.1)}$$

Since $\frac{\omega\omega_0}{Q}$ is positive, we have:

$$\varphi(\omega) = -\frac{\pi}{2} + tan^{-1}\left(\frac{Q(\omega_0^2 - \omega^2)}{\omega\omega_0}\right) \quad \textbf{(A.2)}$$

When $\omega \to \omega_0$, given $\omega \gg \omega - \omega_0$ we obtain:

$$\varphi(\omega) \approx -\frac{\pi}{2} + 2Q\frac{\omega_0 - \omega}{\omega} \quad \textbf{(A.3)}$$

Defining $\Delta\omega = \omega - \omega_0$, a phase variation $\Delta\varphi$ around ω_0 is equal to:

$$\Delta\varphi \approx -2Q\frac{\Delta\omega}{\omega} = -2Q\frac{\Delta f}{f} \quad \textbf{(A.4)}$$

Therefore we can link relative frequency fluctuations to phase fluctuations as:

$$\frac{\Delta f}{f} \approx -\frac{\Delta\varphi}{2Q} \quad \textbf{(A.5)}$$

When the resonator is driven at resonance with a phase value centered on zero, the phase undergoes random fluctuations because of noise on the signal. The signal can be represented in term of amplitude R and phase φ or in phase signal (X) and quadrature signal (X). When the phase is centered on 0, $X \cong R$ and $\varphi \cong \tan^{-1}\frac{Y}{X}$ as shown in Fig. A.2.

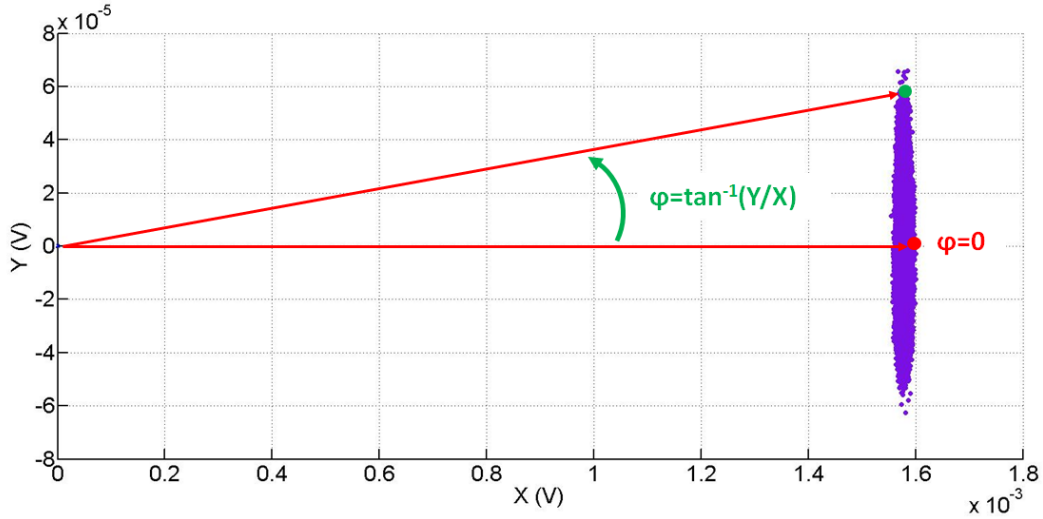

Fig. A.2: Quadrature versus in-phase signal of a closed loop acquisition at resonance. The phase is calculated as the cone angle formed with the X axis from the origin.

Thus, white noise on Y will translate in phase noise. For very small phase variations, equation (A.5) can be approximated by:

$$\frac{\Delta f}{f} = -\frac{\Delta\varphi}{2Q} = \frac{-\tan^{-1}\left(\frac{Y}{X}\right)}{2Q} \approx -\frac{Y}{2QX} \quad \textbf{(A.6)}$$

where Y is the quadrature signal and X the in-phase signal.

For a measurement bandwidth B and given that the signal is carried by the in-phase signal component when the phase is centered on 0, we can estimate the fluctuation of the relative frequency:

$$\sigma_{\delta f} = \frac{1}{2Q}\frac{S_n(\omega_0)\sqrt{B}}{S_0} = \frac{1}{2Q.SNR} \qquad \textbf{(A.7)}$$

where ω_0 is the angular resonance frequency, $S_n(\omega)$ the noise spectral density, S_0 the measured output signal, B is the measurement bandwidth and SNR the signal to noise ratio on this bandwidth.

Therefore, frequency noise should decrease as Q or the signal X increase i.e. with high quality factor resonators driven at their maximum amplitude for optimum Signal to Noise Ratio (SNR).

Appendix B: The Allan Deviation

The Allan Deviation is the square root of the Allan Variance (AVAR), also called the two-sample variance as it is a special case of the more general M-sample variance defined as:

$$\sigma_y^2(M,T,\tau) = \frac{1}{M-1}\left\{\sum_{i=0}^{M-1} \bar{y}_i{}^2 - \frac{1}{M}\left[\sum_{i=0}^{M-1} \bar{y}_i\right]^2\right\} \quad \textbf{(B.1)}$$

where M is the number of samples, T the sampling time, and $\bar{y}_i$ the ith fractional frequency average observed over a time τ.

Therefore the Allan variance can be written as:

$$\sigma_y^2(\tau) = \langle \sigma_y^2(2,\tau,\tau)\rangle = \frac{1}{2}\langle(\bar{y}_{n+1} - \bar{y}_n)^2\rangle \quad \textbf{(B.2)}$$

To understand how the fractional frequencies are calculated, a few items need to be properly defined before proceeding further on.

A real oscillator V_{re} can be described as:

$$V_{re} = V_0\, sin(\Phi_{\mathrm{re}}(\mathrm{t})) = V_0\, sin\big(2\pi f_n t + \varphi(t)\big) \quad \textbf{(B.3)}$$

where f_n is the nominal frequency, $2\pi f_n = \omega_n$ the angular frequency, $\varphi(t)$ the phase fluctuations away from the nominal phase cycle, Φ_{id} the ideal oscillator phase and the Φ_{re} real oscillator phase.

The frequency function $f(t)$ is defined as:

$$f(t) = \frac{1}{2\pi}\frac{\delta\Phi(\mathrm{t})}{\delta t} \quad \textbf{(B.4)}$$

We define the time error X(t) as the time difference between an ideal harmonic signal and the real noisy signal as illustrated in Fig. B.1.

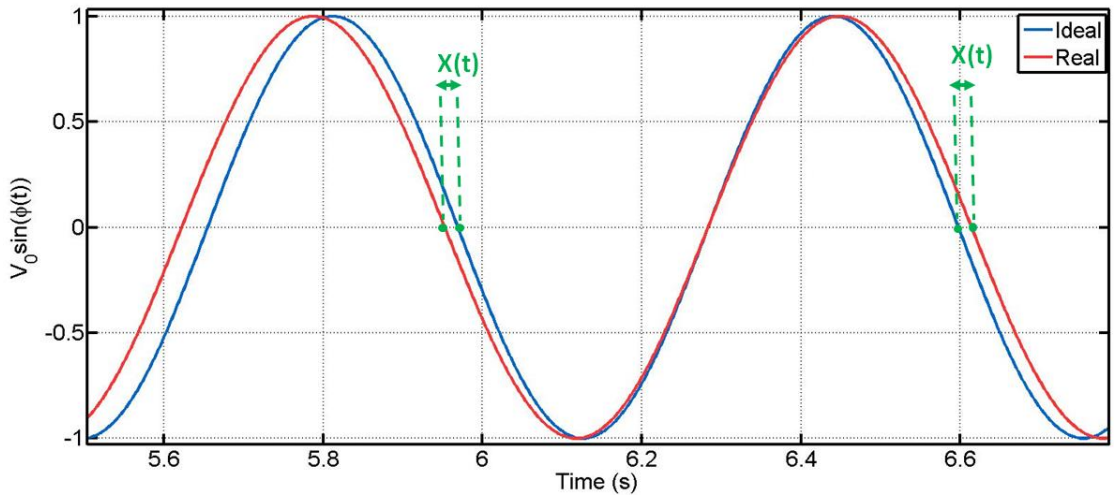

Fig. B.1: Illustration of the time error definition. The time error is the difference between ideal nominal time and real time.

Thus, it can be seen as the time deviation from an ideal periodic time reference produced by an ideal harmonic oscillator. It is calculated as:

$$X(t) = T_{re}(t) - T_{id}(t) = \frac{2\pi f_n t + \varphi(t)}{\omega_n} - \frac{2\pi f_n t}{\omega_n} = \frac{\varphi(t)}{2\pi f_n} \qquad \textbf{(B.5)}$$

The fractional frequency $y(t)$ is the normalized frequency fluctuation:

$$y(t) = \frac{f(t) - f_n}{f_n} = \frac{\frac{1}{2\pi}\frac{\delta\Phi(t)}{\delta t} - f_n}{f_n} = \frac{\frac{1}{2\pi}\left(2\pi f_n t + \frac{\delta\varphi(t)}{\delta t}\right) - f_n}{f_n} \qquad \textbf{(B.6)}$$

$$y(t) = \frac{1}{2\pi f_n}\frac{\delta\varphi(t)}{\delta t} = \frac{\delta X(t)}{\delta t}$$

The average fractional frequency is defined as:

$$\bar{y}(t,\tau) = \frac{1}{\tau}\int_0^{\tau} y(t + t_{int})dt_{int} = \frac{X(t+\tau) - X(t)}{\tau} \qquad \textbf{(B.7)}$$

Once the fractional frequency series of M data points $[\bar{y}_1, \ldots, \bar{y}_M]$ have been obtained, the Allan Deviation of a frequency acquisition is computed as:

$$\sigma_y(\tau) = \sqrt{\frac{1}{2(M-1)}\sum_{i=1}^{M-1}(\bar{y}_{i+1} - \bar{y}_i)^2} \qquad \textbf{(B.8)}$$

where $\bar{y}_i$ are consecutive.

One single set of frequency data over time can be used to compute the Allan deviation for many different observation times:

$$\sigma_y(n\tau_0, M) = \sqrt{\frac{1}{2n(M-1)} \sum_{i=1}^{\frac{M-1}{n}} (\bar{y}_{i+1} - \bar{y}_i)^2} \qquad \textbf{(B.9)}$$

where n is an integer inferior to M-1

Appendix C: NEMS-MS Error analysis

An error analysis, detailed here [1], has been developed by Selim Hanay from Caltech to represent a mass adsorption event with a Probability Density Function (PDF). It consists in characterizing the NEMS frequency fluctuations and fitting them to a bivariate distribution law. Then this distribution, represented in the $[\delta f_1, \delta f_2]$ plane, is associated with an experimental frequency jump pair and translated in the $[\delta m, x]$ plane using transfer matrices. This produces a mass event represented by a Probability function (PDF) accounting for the measurement incertitude as shown in Fig. C.1.

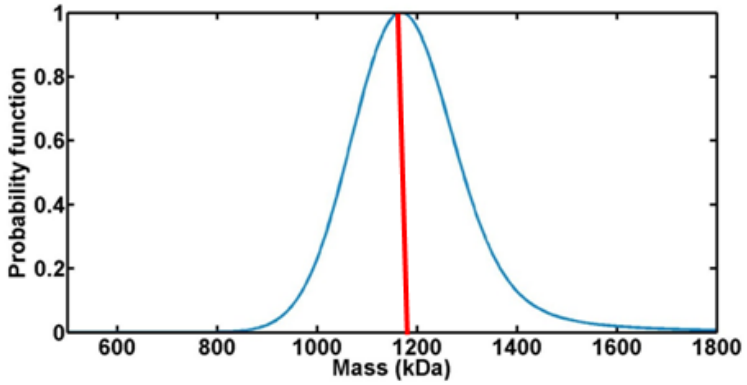

Fig. C.1: Representation of a particle mass as a dirac (red) and as a probability density function (blue) centered at 1200Da

First, the resonance frequencies of mode 1 and 2 are monitored at normal operating conditions without particle adsorption. In an analogous way as for the denoising procedure detailed in the jump detection section, the data is averaged over τ_{AVG} and fractional frequency shift differences y_1 and y_2 are computed. Their distribution can be reasonably well fitted by a Gaussian function (Fig. C.2:).

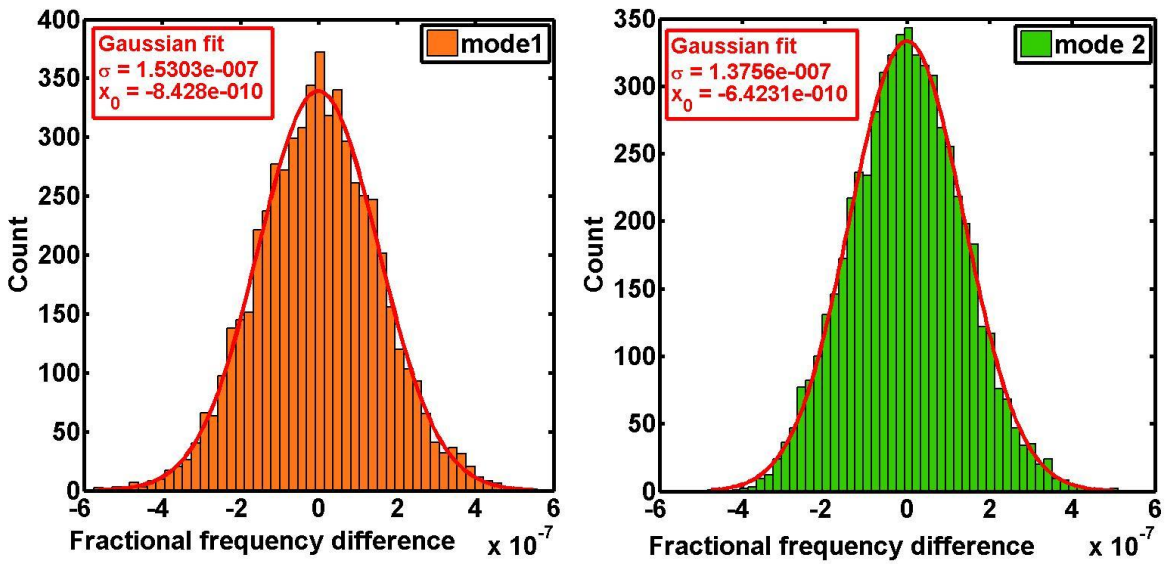

Fig. C.2: Histogram of experimental fractional frequency differences and associated Gaussian fits

Hence we can describe their distribution with a normal law whose PDF is:

$$PDF(y = x) = \frac{1}{\sqrt{2\pi}} e^{\frac{(x-\mu)^2}{\sigma^2}} \qquad \textbf{(C.1)}$$

with $\mu = -8.4 \times 10^{-10}$ and $\sigma = 1.5 \times 10^{-7}$ for mode 1

and $\mu = -6.4 \times 10^{-10}$ and $\sigma = 1.4 \times 10^{-7}$ for mode 2

However, as detailed in the jump detection section, the frequency noise of mode1 and mode2 are correlated (correlation factor ρ=0.3 here). Thus the frequency noise can be modeled by a bivariate Gaussian distribution whose Joint Probability Function (JPDF) is written as:

$$JPDF_{\delta f_1, \delta f_2}(\delta f_1, \delta f_2) = \frac{1}{2\pi\sigma_1\sigma_2\sqrt{1-\rho^2}} e^{-\frac{z}{2(1-\rho^2)}} \qquad \textbf{(C.2)}$$

where:

$$z = \frac{(\delta f_1 - \mu_1)^2}{\sigma_1^2} - \frac{2\rho(\delta f_1 - \mu_1)(\delta f_2 - \mu_1)}{\sigma_1\sigma_2} + \frac{(\delta f_2 - \mu_1)^2}{\sigma_2^2} \qquad \textbf{(C.3)}$$

where δf_1 and δf_2 are mode 1 and mode 2 fractional frequency differences. μ_1 and μ_2 are the characterized mean frequency fluctuations, σ_1 and σ_2 the frequency fluctuations standard deviations and ρ their correlation factor.

This distribution, centered on μ_1 and μ_2, models our NEMS frequency noise that we can relocate on a measured frequency jump pair $[\delta f_1', \delta f_1']$ caused by mass adsorption by writing:

$$\mu_1 = \delta f_1{}' \text{ and } \mu_2 = \delta f_2{}' \qquad \textbf{(C.4)}$$

We now have a distribution describing the JPDF of a mass induced frequency jump that we need to translate to a JPDF of mass and position of the adsorbed particle i.e. we need to transition from $JPDF_{\delta f_1,\delta f_2}(\delta f_1, \delta f_2)$ to $JPDF_{\delta m,x}(\delta m, x)$ using bivariate transformations [2].

We can describe the transformations from $[\delta f_1, \delta f_2]$ to $[\delta m, x]$ as:

$$\begin{aligned} \delta m &= g_1(\delta f_1, \delta f_2) \\ x &= g_2(\delta f_1, \delta f_2) \end{aligned} \qquad \textbf{(C.5)}$$

and the corresponding inverse transformations:

$$\begin{aligned} \delta f_1 &= h_1(\delta m, x) \\ \delta f_2 &= h_2(\delta m, x) \end{aligned} \qquad \textbf{(C.6)}$$

where:

$$\begin{aligned} h_1(\delta m, x) &= -\delta m \, \frac{\varphi_1(x)^2}{2 \times \alpha_1} \\ h_2(\delta m, x) &= -\delta m \, \frac{\varphi_2(x)^2}{2 \times \alpha_2} \end{aligned} \qquad \textbf{(C.7)}$$

The transformation requires the calculation of the Jacobian:

$$J = \begin{vmatrix} \frac{\partial \delta f_1}{\partial \delta m} & \frac{\partial \delta f_1}{\partial x} \\ \frac{\partial \delta f_2}{\partial \delta m} & \frac{\partial \delta f_2}{\partial x} \end{vmatrix} \qquad \textbf{(C.8)}$$

where $\frac{\partial \delta f_1}{\partial \delta m} = \frac{\partial h_1(\delta m,x)}{\partial \delta m}$, $\frac{\partial \delta f_1}{\partial x} = \frac{\partial h_1(\delta m,x)}{\partial x}$, $\frac{\partial \delta f_2}{\partial \delta m} = \frac{\partial h_2(\delta m,x)}{\partial \delta m}$, and $\frac{\partial \delta f_2}{\partial x} = \frac{\partial h_2(\delta m,x)}{\partial x}$

We obtain:

$$J = \frac{2\delta m}{\alpha_1 \alpha_2} \, \varphi_1(x)\varphi_2(x) \, [\varphi_1(x)\varphi_2{}'(x) - \varphi_2(x)\varphi_1{}'(x)] \qquad \textbf{(C.9)}$$

where $\varphi'(x) = \frac{\partial \varphi(x)}{\partial x}$

The JPDF of the particle position is then written as:

$$JPDF_{\delta m,x}(\delta m, x) = JPDF_{\delta f_1,\delta f_2}(h_1(\delta m, x), h_2(\delta m, x))|J| \qquad \textbf{(C.10)}$$

which yields:

$$JPDF_{\delta m,x}(\delta m, x) = |J| \frac{1}{2\pi\sigma_1\sigma_2\sqrt{1-\rho^2}} e^{-\frac{\gamma}{2(1-\rho^2)}} \quad \textbf{(C.11)}$$

where:

$$\gamma = \frac{(-\delta m \ \frac{\varphi_1(x)^2}{2\times\alpha_1} + \delta f_1{}')^2}{\sigma_1^2} + \frac{(-\delta m \ \frac{\varphi_2(x)^2}{2\times\alpha_2} + \delta f_2{}')^2}{\sigma_2^2} + \frac{2\rho}{\sigma_1\sigma_2}\left(-\delta m \ \frac{\varphi_1(x)^2}{2\times\alpha_1} + \delta f_1{}'\right)\left(-\delta m \ \frac{\varphi_2(x)^2}{2\times\alpha_1} + \delta f_2{}'\right) \quad \textbf{(C.12)}$$

where $\delta f_1{}'$ and $\delta f_2{}'$ are the positive values of measured frequency shifts

Since we are mostly interested in the mass of the weighted particle, the final step consists in obtaining the marginal PDF of δm by integration of $JPDF_{\delta m,x}(\delta m, x)$ with respect to x.

Practically, the transformation of $\left[\delta f_1^{'}, \delta f_2{}'\right]$ to a mass PDF is implemented in a Matlab code generating a matrix $JPDF_{\delta m,x}(\delta m, x)$ where the probability needs to be calculated for each coordinates $(\delta m, x)$. Fig. C.3 presents a superposition of 227 mass events attributed with a $JPDF_{\delta m,x}(\delta m, x)$.

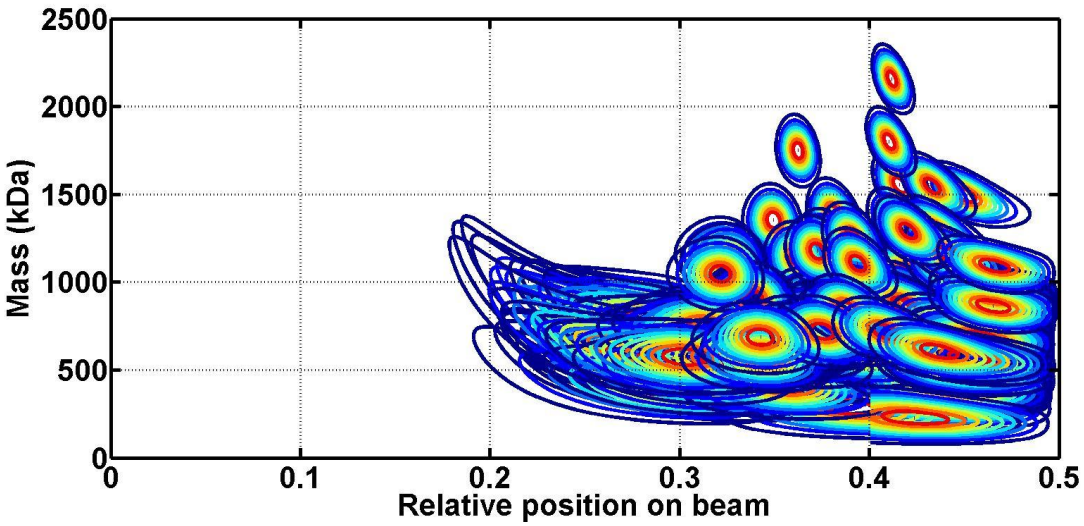

Fig. C.3: Superposed JPDFs of 227 events in the $(\delta m, x)$ plane

Then the JPDF of each event is integrated over the position and normalized to obtain the marginal PDF of the mass similar as in Fig. C.1. We can now build the final mass spectra by successive addition of all events (Fig. III.18).

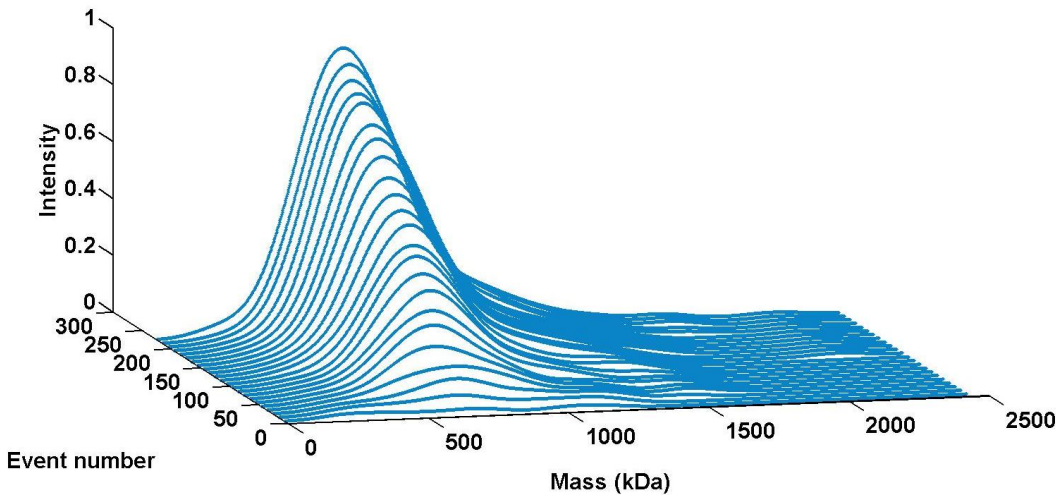

Fig. C.4: Event-per-event built mass spectra of tantalum nanoclusters centered on 600kDa.

This post-process procedure can prove to be extremely lengthy. Hence the code has been optimized for fast computation to allow for a future implementation of actual real time NEMS-MS where the experimenter will be able to follow the mass spectrum evolution in real time during the acquisition.

The $JPDF_{\delta m,x}(\delta m, x)$ isn't calculated over the whole matrix but on coordinates centered on the first evaluation of $[\delta m, x]$ done before the error analysis. Indeed, far from the $[\delta m, x]$ estimate, the JPDF becomes quickly negligible and thus does not need to be computed. Then, given that the mass PDF is normalized, all proportional terms of equation (C.11) that does not depend on $[\delta m, x]$ is removed. Finally, the matlab code has been optimized for multicore processing: events are processed in parallel. On an 8 cores processor cadenced at 2.4 GHz, a 4 min mass acquisition featuring 1500 events that took around 30 minutes to post-process before optimization is now obtained in 40 seconds. The possibility to quickly build mass spectra has made a significant difference for simulations and experiments where results could be accessed almost instantaneously.

BIBLIOGRAPHY

[1] M. S. Hanay, S. Kelber, A. K. Naik, D. Chi, S. Hentz, E. C. Bullard, E. Colinet, L. Duraffourg, and M. L. Roukes, “Single protein nanomechanical mass spectrometry in real time,” *Nat. Nanotechnol.*, vol. 7, pp. 602–608, 2012.

[2] G. Casella and R. L. Berger, *Statistical Inference*, 2 edn. Duxbury Press, 2008.